Universität Hamburg

Doctoral Thesis

Measure cosmic magnetic fields with extreme astrophysical messengers

Dissertation with the aim of achieving a doctoral degree
at the Faculty of Mathematics, Informatics and Natural Sciences
Department of Physics
at the University of Hamburg

by

Stefan Hackstein

Hamburg

2020

Referees:	Prof. Dr. Marcus Brüggen Prof. Dr. Franco Vazza
Examination comission:	Prof. Dr. Marcus Brüggen Prof. Dr. Franco Vazza Prof. Dr. Günter Hans Walter Sigl Prof. Dr. Robi Banerjee Prof. Dr. Jochen Liske
Chairman:	Prof. Dr. Jochen Liske
Date of disputation:	22.09.2020
Chairman of PhD-board PHYSIK:	Prof. Dr. Günter Hans Walter Sigl
Director of department of physics:	Prof. Dr. Wolfgang Hansen
Faculty director of MIN:	Prof. Dr. Heinrich Graener

Declaration of Authorship

I, Stefan HACKSTEIN, declare that this thesis titled, "Measure cosmic magnetic fields with extreme astrophysical messengers" and the work presented in it are my own. I confirm that:

- This work was done wholly or mainly while in candidature for a research degree at this University.
- Where any part of this thesis has previously been submitted for a degree or any other qualification at this University or any other institution, this has been clearly stated.
- Where I have consulted the published work of others, this is always clearly attributed.
- Where I have quoted from the work of others, the source is always given. With the exception of such quotations, this thesis is entirely my own work.
- I have acknowledged all main sources of help.
- Where the thesis is based on work done by myself jointly with others, I have made clear exactly what was done by others and what I have contributed myself.

Signed:

Date:

Eidesstattliche Versicherung / Declaration on oath

Hiermit versichere ich an Eides statt, die vorliegende Dissertationsschrift selbst verfasst und keine anderen als die angegebenen Hilfsmittel und Quellen benutzt zu haben.

Die eingereichte schriftliche Fassung entspricht der auf dem elektronischen Speichermedium.

Die Dissertation wurde in der vorgelegten oder einer ähnlichen Form nicht schon einmal in einem früheren Promotionsverfahren angenommen oder als ungenügend beurteilt.

_____

Unterschrift des Doktoranden

Hamburg, den 10.07.2020

"*The origin of galactic and extragalactic magnetic fields is one of the most fascinating and challenging problems in modern astrophysics.*"

Lawrence M. Widrow

"*If I have seen further it is by standing on the shoulders of giants.*"

Isaac Newton

"*Prediction is difficult for us for the same reason that it is so important: it is where objective and subjective reality intersect. Distinguishing the signal from the noise requires both scientific knowledge and self-knowledge: the serenity to accept the things we cannot predict, the courage to predict the things we can, and the wisdom to know the difference*"

Nate Silver

UNIVERSITÄT HAMBURG

Abstract

Fakultät für Mathematik, Informatik und Naturwissenschaften
Sternwarte Hamburg

Doctor of Physics

Measure cosmic magnetic fields with extreme astrophysical messengers

by Stefan Hackstein

Magnetic fields are a ubiquitous phenomenon observed in all kinds of astrophysical objects throughout the entire Universe. Their omnipresence requires a common cosmic origin or universal processes of magneto-genesis. However, observations of magnetic fields are increasingly difficult at larger distances, especially in the low-density regions of cosmic voids. These are most informative on the history of cosmic magnetic fields, since dynamo activity in denser environments leaves little trace of the initial seed field. In this thesis, I focus on high-energy astrophysical messengers, namely ultrahigh-energy cosmic rays and fast radio bursts. These are modified during propagation in magnetic fields and hence potentially deliver information on the magnetic fields outside the dense structures of the Universe and consequently on the cosmic origin of magnetic fields. With the use of constrained cosmological models of the intergalactic medium, I simulate the propagation of these messengers and predict the statistics of their signal observed at terrestrial telescopes and compare to observations.

The propagation of cosmic rays is computed using the CRPropa code, that entails all energy-loss and decay processes. Combining possible source catalogues with different models of intergalactic magnetic fields and their Lorentz deflections, I predict measures of large-scale anisotropy and compare to results reported by the Pierre Auger Collaboration. However, no fitting catalogue of sources with uniform emission properties could be identified. Still, my results suggest that a heavy source composition is required in order to explain the dipole anisotropy observed at the Pierre Auger Observatory.

For the investigation of fast radio bursts, I produced the open-source python software package PrEFRBLE, whose purpose is to enhance communication between theoretical models and observational data. This code uses approximate Bayesian computation to quantify the contribution of different regions along the line-of-sight: the intergalactic medium, the local environment of the source, the host as well as intervening galaxies. These are combined to full line-of-sight scenarios in order to predict the expected distribution of observables in the most realistic modelling available. These statistical predictions are compared to observations of fast radio bursts in order to investigate long-standing cosmological questions. I show that in order to constrain the location of missing baryons and the redshift distribution of fast radio bursts, the discrepancy between results of different instruments, especially CHIME and ASKAP, needs to be explained, unless the bursts can be localized in great numbers.

Finally, I show that linearly polarized fast radio bursts can be used to constrain the intergalactic magnetic field. Current upper limits can be improved on with a minimum of 10^3 FRBs. Furthermore, an increasing sample size of up to 10^5 FRBs will allow to probe the whole range of possible IGMF strengths down to the current lower limits. In my work I have investigated new ways to learn about the cosmic origin of magnetic fields and established useful tools already in use by other scientists to continue this endeavour.

Zusammenfassung

Messen kosmischer Magnetfelder mithilfe extremer astrophysikalischer Boten

von Stefan Hackstein

Magnetische Felder sind ein allgegenwärtiges Phänomen, welches wir in nahezu jedem Himmelskörper beobachten. Ihre Omnipräsenz kann nur durch einen gemeinsamen Ursprung oder universale Prozesse der Magnetogenese erklärt werden. Allerdings wird die Beobachtung von Magnetfeldern in größerer Distanz zunehmend schwieriger, besonders in Voids wo Materie nur in sehr geringer Dichte vorhanden ist. Diese Bereiche enthalten die meisten Informationen über die Entstehung kosmischer Magnetfelder, da Dynamoaktivität in Bereichen höherer Dichte die Spuren des ursprünglichen Feldes verwischt. In der vorliegenden Arbeit erforsche ich hochenergetische astrophysikalische Botschafter, ultrahochenergetische kosmische Strahlung sowie schnelle Radioblitze. Deren Signal erfährt eine Änderung beim Durchqueren von Magnetfeldern und liefert uns möglicherweise Information über magnetische Felder außerhalb der Dichten Strukturen des Universums und so über der Herkunft dieser Felder. Mithilfe von kosmologischen Modellen des intergalaktischen Mediums im lokalen Universum simuliere ich die Auswirkungen des Magnetfelds auf diese astrophysikalischen Botschafter und erstelle Vorhersagen für die statistische Verteilung derer Signale, welche ich mit Beobachtungsdaten vergleiche.

Zur Simulation der kosmischen Strahlung verwende ich die Software "CRPropa", welche alle relevanten Energieverlust- und Zerfallsprozesse beinhaltet. Durch Kombination möglicher Kataloge von Quellen dieser Strahlung mit verschiedenen Modellen des intergalaktischen Magnetfelds und der implizierten Ablenkung ermittle ich das erwartete Maß an Anisotropie auf großen Skalen, welche ich mit den Beobachtungen der Pierre Auger Kollaboration vergleiche. Dabei konnte kein passender Quellenkatalog mit einheitlichen Emissionseigenschaften gefunden werden. Dennoch liefert meine Arbeit hinweise darauf, dass die emittierte kosmische Strahlung vornehmlich aus schweren Elementen bestehen muss, um die beobachtete Dipolanisotropie zu erklären.

Um schnelle Radioblitze näher zu erforschen, habe ich das quelloffene python Software Paket PrEFRBLE entwickelt, mit dem Ziel die Kommunikation zwischen theoretischen Modellen und Beobachtungsdaten zu verbessern. Diese Software verwendet die approximative Bayesianische Methode für die Berechnung der Beiträge verschiedener Regionen entlang der Sichtlinie: das intergalaktische Medium, die lokale Umgebung der Quelle, die Ursprungsgalaxie sowie mögliche weitere Galaxien zwischen Quelle und Beobachter. In Kombination liefern diese die bisher realistischsten Abschätzungen für die erwartete Verteilung von Observablen. Diese statistischen Vorhersagen werden mit Beobachtungsdaten von schnellen Radioblitzen verglichen, um seit Langem bestehende kosmologische Fragen zu untersuchen. Ich zeige, dass die Beobachtungen verschiedener Instrumente zu unterschiedlichen Schlussfolgerungen führen. Insbesondere muss der Unterschied zwischen Ergebnissen von ASKAP und CHIME aufgeklärt werden, um eine gemeinsame Identifikation der fehlenden Baryonen und der Verteilung der Quelldistanzen zu ermöglichen, solange die Radioblitze nicht in großer Zahl lokalisiert wurden. Abschließend zeige ich, das linear polarisierte Radioblitze genutzt werden können, um das intergalaktische Magnetfeld zu messen. 10^3 dieser Radioblitze reichen aus um die derzeitige Obergrenze zu

verbessern. Mit Erreichen einer Datenmenge von 10^5 Radioblitzen wird es möglich die gesamte Bandbreite möglicher Feldstärken zu messen. In meiner Arbeit habe ich neue Wege erforscht, um mehr über die kosmische Herkunft von Magnetfeldern zu lernen und habe dabei nützliche Werkzeuge errichtet, welche schon jetzt von anderen Wissenschaftlern genutzt werden, um dieses Unterfangen fortzuführen.

Acknowledgements

This work was funded by the Deutsche Forschungsgemeinschaft (DFG) under grant BR2026/25. I thank my supervisor Marcus Brüggen for providing me with this interesting project, encouraging me to work independently as well as for a lot of fruitful discussions and guidance throughout my whole studies. Many thanks go to Franco Vazza, whose simulations of magnetic fields in the local Universe were necessary to enable this study and who guided me to become acquainted with the simulation software. I further thank Günter Sigl for many worthwhile discussions. Thanks to Rafael Alves-Batista and Andrej Dundovic for guidance in the use of CRPropa as well as for many interesting discussions. I also thank Robi Banerjee and Pranjal Trivedi for interesting collaboration on the cosmic evolution of magnetic fields.

Finally, I thank my fiancée Nadine Klipp for standing by me through all this time.

Contents

List of Figures

List of Abbreviations

MW	**M**ilky**W**ay
LoS	**L**ine **o**f **S**ight
PMF	**P**rimordial **M**agnetic **F**ield
CMF	**C**osmic **M**agnetic **F**ield
IGM	**I**nter**G**alactic **M**edium
IGMF	**I**nter**G**alactic **M**agnetic **F**ield
CMB	**C**osmic **M**icrowave **B**ackground
MHD	**M**agneto-**H**ydro**D**ynamics
CR	**C**osmic **R**ay
UHECR	**U**ltra**H**igh-**E**nergy **C**osmic **R**ays
PAO	**P**ierre **A**uger **O**bservatory
TA	**T**elescope **A**rray
GZK	**G**reisen **Z**atsepin **K**uzmin
FRB	**F**ast **R**adio **B**urst

List of Symbols

F_L	Lorentz force	N
q	charge	C
$\vec{v}$	velocity	m s^{-1}
$\vec{E}$	electric field	N C^{-1}
$\vec{B}$	magnetic field	G
$B_\perp$	perpendicular magnetic field component	G
$B_\parallel$	parallel magnetic field component	G
B_0	average field strength of PMF	G
Θ_F	Farady rotation angle	deg
RM	Farady rotation measure	rad m^{-2}
λ	wavelength	m
ν	frequency	Hz
n_e	free electron density	cm^{-3}
ρ	gas density	g cm^{-3}
d	distance	pc
z	redshift	-
E	energy	eV
k	wave number	1/pc
r	scale of eddy	pc
L_0	outer scale of turbulence	pc
l_0	inner scale of turbulence	pc
l_c	coherence length	pc
$X_{\max}$	penetration depth of EAS	
A	mass number	-
Z	atomic number	-
r_g	gyro radius	pc
L	scale	pc
t	time	s
DM	dispersion measure	pc cm^{-3}
f_{IGM}	fraction of baryons in the ionized IGM	-

To my love, family and friends. But mostly to enthusiasts of cosmic magnetism.

Chapter 1

Introduction

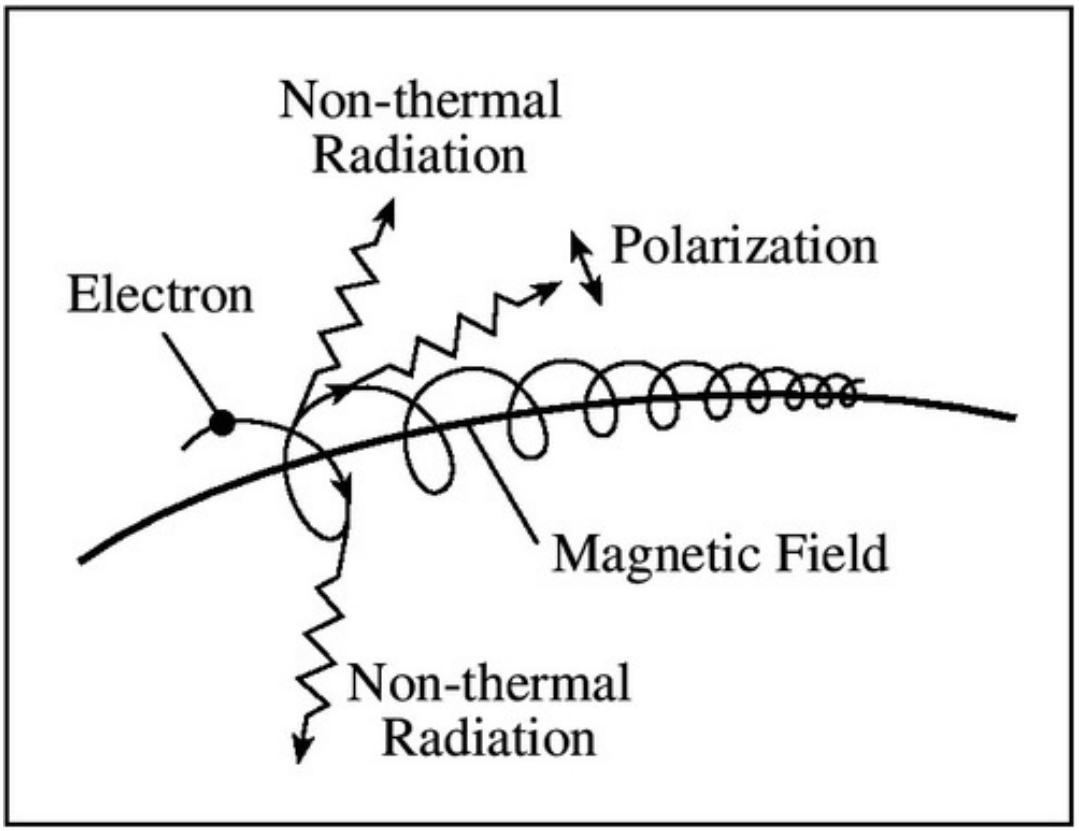

FIGURE 1.1: Visualizations of synchrotron radiation emitted by charged particles gyrating around magnetic field lines (Lang 2010).

1.1 Cosmic Magnetic Fields

The Universe is magnetized. Observations of virtually all astrophysical structures, be they as small as neutron stars ($\approx$ 10 km) or as big as clusters of galaxies ($\gtrsim 3 \times 10^{19}$ km), show evidence of residual magnetic fields. How do we know such fields exist? What is their origin? How can we explain that magnetic fields are so common around the Universe?

1.1.1 How to measure CMFs?

Magnetic fields interact with the magnetic moment of orbital electrons, split their energy levels and thus spectral absorption lines into several components. This Zeeman effect allows to measure magnetic field strengths e. g. of stars in our own Galaxy, the Milky Way (MW).

Due to Lorentz force,

$$\vec{F}_L = q \cdot (\vec{E} + \vec{v} \times \vec{B}) \tag{1.1}$$

particles of charge q in a magnetic field $\vec{B}$ are deflected perpendicular to their velocity $\vec{v}$ and thus gyrate around field lines. For most parts of the Universe, the electric field $\vec{E} \approx 0$, due to the high conductivity of interstellar plasma. The acceleration of charged particles causes them to emit coherent electromagnetic waves, known as synchrotron radiation, see Fig. 1.1. The spectrum and polarization angle of the synchrotron emission, respectively, deliver information about the strength and direction of the residual magnetic field perpendicular to the line-of-sight (LoS), $B_\perp$. Synchrotron

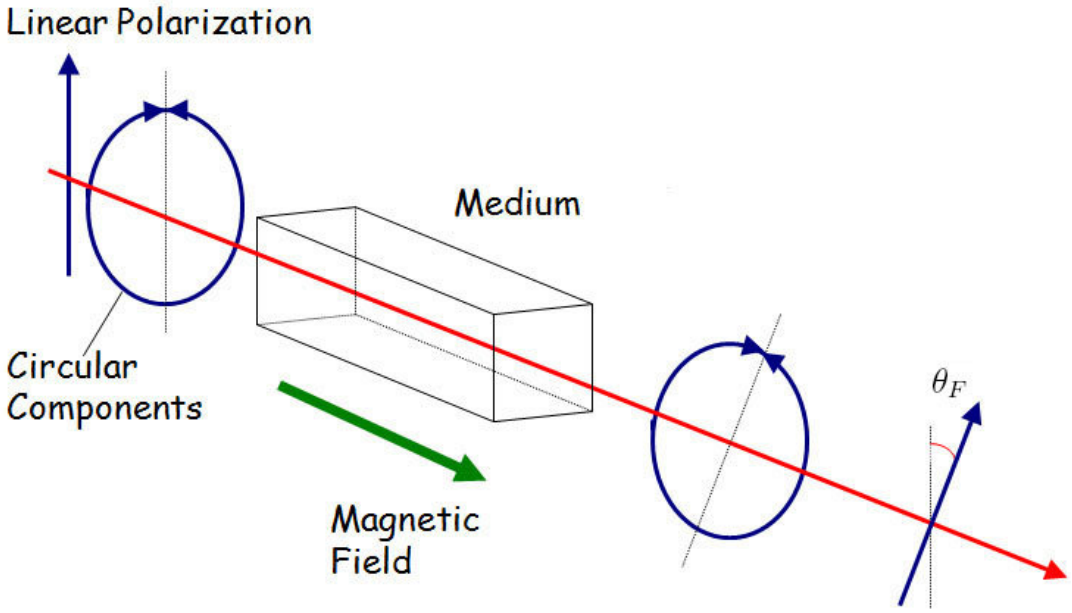

FIGURE 1.2: Visualizations of Faraday rotation that changes the angle of polarization according to the magnetic field along the LoS (Villarraga-Gómez 2010).

emission enables to measure magnetic fields $\vec{B}$ in the MW and beyond, e. g. in elliptical galaxies or lobes of radio galaxies.

Linear polarized light can be understood as the superposition of two light beams with left- and right-circular polarization. In circularly polarized radiation, the electric field rotates, causing gyration of free electrons and thus induces a magnetic field along the path of propagation. This interferes with an external magnetic field, causing a difference in the energy budget of the two beams. They thus see different refraction indices, are slowed down to different speeds, causing a phase difference. After the phase-shift, the superposition of the two beams is linearly polarized again, but with a rotated direction of polarization, see Fig. 1.2. Thus, propagation along magnetic field lines changes the polarization angle of linearly polarized radiation by angle

$$\Theta_F = \mathrm{RM}\ \lambda^2, \tag{1.2}$$

which depends on the squared wavelength λ^2. The frequency independent rotation measure RM is the path integral over number density of free electrons n_e times the LoS magnetic field $B_\parallel$,

$$\mathrm{RM} \approx 0.81\ \mathrm{rad\ m^{-2}} \int_d^0 \left(\frac{n_e}{\mathrm{cm^{-3}}}\right) \left(\frac{B_\parallel}{\mu\mathrm{G}}\right) \left(\frac{\mathrm{d}l}{\mathrm{kpc}}\right). \tag{1.3}$$

Together with a model for n_e, Faraday rotation allows to measure $B_\parallel$ along the LoS to distance d of a radio source by comparing their rotation angle at different frequencies. However, for radiation with wavelength shorter than radio the effect is too subtle to be measured. Investigation of RM allows to measure large-scale magnetic fields of well-resolved galaxies and other regions along the LoS.

The large-scale properties of galaxies and clusters are not influenced significantly by magnetic fields. However, they play an important role in many astrophysical processes. For example, magnetic fields can influence star formation, drive jets and

affect accretion rate of stars (e. g. Price, 2004). There are also some suggestions that primordial magnetic fields (PMFs) influenced the thermal history of the Universe in the epoch of recombination (Jedamzik et al., 1998). Excellent reviews on cosmic magnetic fields (CMFs), their measurement, observations and theory can be found in Vallée (1997), Widrow (2002) and Beck (2009).

1.1.2 What do we know about astrophysical magnetic fields?

Numerous observations of magnetic fields in the structured Universe and their comparison to model predictions have let to remarkable insights into their strength and shape in many structures. The properties of a stars magnetic field depend on many parameters, resulting in a huge range of surface magnetic field strengths observed in stars. While some stars show no trace of a significant residual magnetic field, others reach several thousand times the field strength of our Sun at 1 G. It was long time believed that the magnetic field of stars, like that of the Earth, is dominantly dipolar. However, observation of the field around our Sun shows that the structure of solar magnetic fields is much more complicated (e. g. Zwaan, 1987).

Stellar plasma is highly conductive and, according to Alfvén's theorem, every motion of the fluid perpendicular to the field is forbidden, since it would cause infinite eddy currents. Thus, the magnetic field is frozen into the ionized fluid and has to move along with it. Hence, when a star collapses to form a neutron star, the magnetic field gets compressed and thus amplified to reach strengths up to $10^{14} - 10^{16}$ G. Such neutron stars are called magnetars and have the strongest magnetic fields in the Universe.

At small scales, astrophysical magnetic fields dissipate, e. g. due to turbulent diffusion by irregular velocity fluctuations, transforming magnetic energy into heat and kinetic energy (e. g. Piddington, 1981). Hence, in order to explain the strong magnetic fields observed in old stars, we require a mechanism that amplifies and sustains the solar magnetic field. In the magnetic dynamo model, electrically conducting matter moves in a magnetic field, such that the induced currents amplify and maintain the field (Shukurov, 2004).

Our planet does have such a dynamo that sustains the 0.5 G terrestrial magnetic field. Heat flow from the Earth's inner core drives convection currents of fluid metal in the outer core, which are organized into rolls by the Coriolis force. These create circulating electric currents, which generate a coherent magnetic field along the rotation axis, forming a dipole field around the Earth.

The α-Ω-dynamo active in stars is the combination of two effects. These transform poloidal magnetic field components into toroidal ones and vice versa in order to generate and maintain the field on cost of rotational or kinetic energy. Poloidal magnetic field lines are frozen into the plasma and carried along by rotation. Since the stars' equator revolves at faster pace than the poles, the magnetic field lines get twisted, bringing them closer together, thus increasing the field strength. Further, the field lines get wrapped around the sun and align with the equator, transforming magnetic energy from poloidal to toroidal component. This is called the Ω-effect. Observations show the emergence of magnetic bipolar regions which by Coriolis force are systematically tilted with respect to the equator (e. g. Cameron et al., 2017). This transforms the toroidal field back into a poloidal component. Furthermore, in any rotating turbulent system, electric currents flow along the regular magnetic field lines, which can be shown using mean-field approximation to describe the effects of turbulence (Steenbeck et al., 1966). Current along toroidal field lines is always accompanied by a poloidal field. Such α-effects transform magnetic energy from toroidal to

poloidal field component, closing the loop and maintaining the magnetic field against Ohmic diffusion (Parker, 1979).

The magnetic field of the MW has been studied extensively using synchrotron emission, Faraday rotation, optical polarization and Zeeman splitting (summarized e. g. in Haverkorn, 2015). There were several attempts to model the free electron distribution and magnetic field structure of our Galaxy, in order to fit theoretical predictions to observations (e. g. Cordes and Lazio, 2002; Jansson and Farrar, 2012; Yao et al., 2017). However, all of these models use different parametrization and consider the different observables separately. The IMAGINE consortium (Boulanger et al., 2018) attempts to combine the information of several available observables together with sophisticated Bayesian emulation methods in order to provide a converged model for the MW magnetic field, also making use of knowledge obtained from observation of similar other galaxies.

Many pieces of information about the magnetic field of our Galaxy could only be acquired by comparing to other galaxies, where the structure of large-scale magnetic fields can be observed more easily (e. g. Beck, 2009). Typical magnetic field strengths observed in galaxies are of order $1 - 10$ μG. Magnetic fields in spiral galaxies like the MW are well described by a superposition of turbulent and regular components, where the latter are coherent on length-scale of the visible disk. The regular field lines are aligned with the spiral arms and often exhibit patterns or symmetries with respect to both, the spin axis and equatorial plane of the galaxy. Both field components carry similar amounts of energy density. In contrast, the dominant scale of the random magnetic fields in elliptical galaxies, i. e. the coherence length l_c, is much smaller than the galaxy itself. There is usually an increase in field strength in the centre of any galaxy. Magnetic fields have also been observed in barred and irregular galaxies. Mao et al. (2017) investigate the polarization of a radio background source and report evidence for a coherent galactic magnetic field in a galaxy at redshift $z = 0.44$. This is the highest redshift galaxy with clear evidence of magnetic fields with similar strength and geometry as for galaxies in the local Universe, in agreement with expectations from the dynamo paradigm. At higher redshift, observation of coherent magnetic fields in galaxies is increasingly difficult, due to limited sensitivity and angular resolution. Still, there are hints for coherent μG magnetic fields in galaxies at high redshift up to $z \gtrsim 2$ (Athreya et al., 1998; Bernet et al., 2008).

Due to turbulent diffusion, the large-scale magnetic field of a galaxy would be destroyed within a fraction of the galactic lifetime. In order to explain the existence of regular magnetic fields in galaxies with old stellar populations, a dynamo process is required that sustains the galactic magnetic field. The α-Ω-dynamo active in disk galaxies is a combination of differential rotation, which transforms poloidal to toroidal magnetic fields, and turbulent motion, driven e. g. by stellar winds or supernovae. Loops of toroidal magnetic field lines are carried out of the plane of the disk and twisted into the poloidal plane by Coriolis force. This dynamo requires dissipation processes, e. g. turbulent diffusion or magnetic reconnection, to eliminate magnetic fields that pile up at the equatorial plane. Still, the mean-field dynamo discussed for stars provides an excellent model to sustain the magnetic field of rotating galaxies. However, due to their short life-time, the strong magnetic fields observed in galaxies at high redshift might better be explained by amplification due to compression during collapse of the protogalactic cloud. Still, without a dynamo at play, these fields would be destroyed on rather short timescale by turbulent diffusion (Parker, 1971). Overviews on dynamo theories can be found in Kulsrud (1999), Shukurov (2004) and Rincon (2019).

Clusters of galaxies are the largest virialized objects in the Universe, can contain several thousands of galaxies and reach masses up to $\sim 10^{15} M_{\odot}$. Observation of diffuse cluster-wide synchrotron radio emission demonstrated the existence of magnetic fields in the intergalactic medium (IGM) of galaxy clusters (Giovannini et al., 1991, 1993; Feretti et al., 2012). An excellent review on recent observational results is provided in van Weeren et al. (2019). The magnetic field that permeates the IGM in clusters of galaxies is found to be of order ~ 1 μG, dominated by a turbulent component with $l_c =$ few 10 kpc, usually assumed to be characterized by a Kolmogorov spectrum, $E(k) \propto k^{-5/3}$ (Kolmogorov, 1991b,a), though simulations suggest that it might not follow a power law at all (Domínguez-Fernández et al., 2019). A turbulent flow can be seen as the composition of eddies of different length scale r, characterized by wavenumber $k = \frac{2\pi}{r}$. The energy cascades from larger to smaller scales down to the dissipation scale, where viscous shear stress converts kinetic to internal energy. The integrated power spectrum equals the mean turbulent kinetic energy of the flow. Assuming that the eddy characteristics are universal and uniquely determined by length scale, rate of energy dissipation and kinematic viscosity, Kolmogorov derived the spectral index of $-\frac{5}{3}$ from dimensional analysis of this equation. In conclusion, a turbulent system is dominantly driven by some process that provides turbulent energy on outer scale L_0, which determines the largest scale associated with the turbulence and, for a perpetual energy source, also marks l_c. Subsequently, the energy cascades to lower scales, converging to a Kolmogorov spectrum, which describes the natural state for a fully developed turbulence. The power law continues down to the inner scale l_0, which is determined by dissipation and marks the end of the spectrum.

Slowly or non-rotating objects, such as elliptical galaxies and clusters, show turbulence with characteristic l_c below the size of the system. Those systems obviously lack differential rotation and thus cannot sustain their magnetic field with an α-Ω- nor mean-field-dynamo. However, the rather strong magnetic fields observed in clusters require a dynamo to sustain the field against dissipation. Local turbulent dynamos are believed to sustain these fields, which do not organize on large scales. The fluctuation dynamo process amplifies magnetic fields via random shears in a background velocity field. A magnetic flux tube embedded in an eddy is sheared and eventually rolls up on itself. The magnetic field lines are thus folded, which causes an increase in magnetic energy but does not generate large-scale fields.

Upper limits on the magnetic field strength in cosmic filaments of < 0.1 μG have been deduced from the non-observation of synchrotron emission (Brown et al., 2017). A summary of observational findings on CMFs can be found in de Gouveia Dal Pino (2006).

1.1.3 What is the cosmic origin of magnetic fields?

Dynamo activity can amplify and sustain the magnetic field, however, requires a seed field in order to commence. The strength and shape of that seed field has low impact on the field generated by the dynamo, complicating identification of its origin. One possible explanation is the Biermann effect (Biermann, 1950), where magnetic fields are induced by electric currents due to misalignment of electron density and temperature profile, e. g. due to pressure gradients in stars. The necessary conditions for Biermann batteries can also be met during collapse of a protogalactic cloud or even during phase transitions in the early Universe, providing a possible origin for CMFs. Furthermore, the Harrison mechanism (Harrison, 1970) generates magnetic fields by electric currents due to different photon drag on ions and electrons in vortical

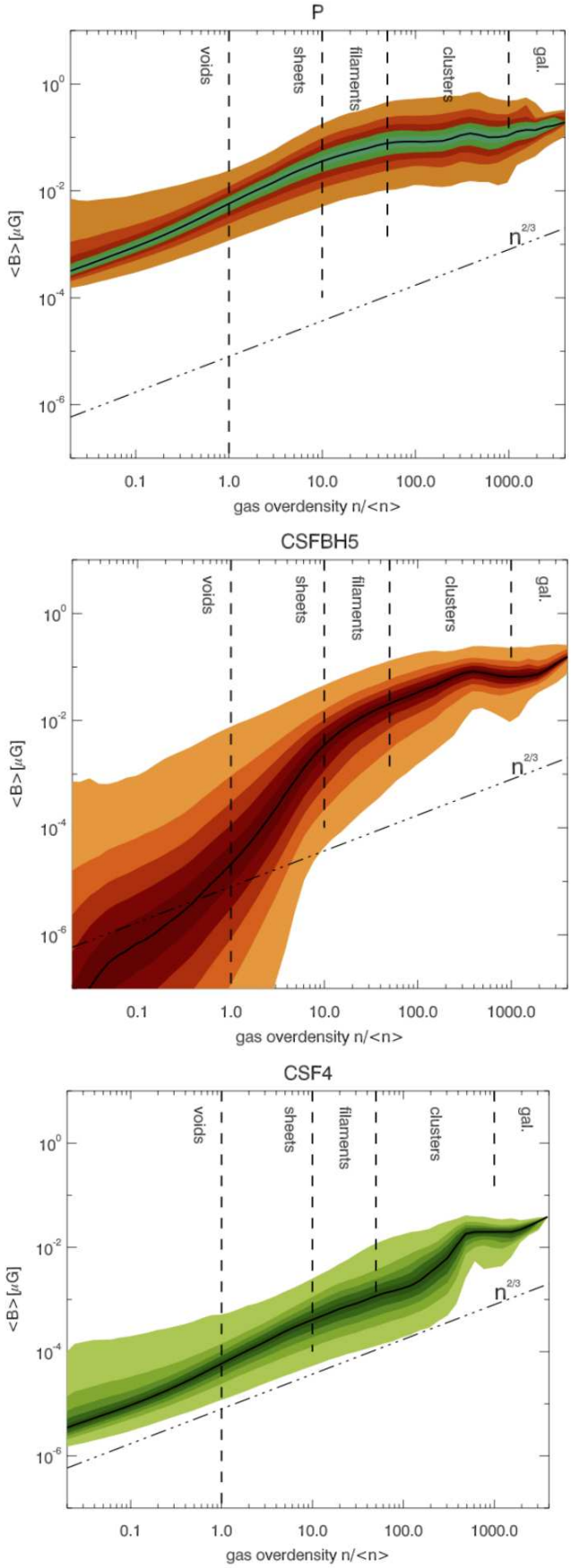

FIGURE 1.3: Relation of average magnetic field strength to gas over-density from a small set of MHD simulations from Vazza et al. (2017) assuming different scenarios of magneto-genesis. The dashed lines indicate the regions of different over-density in the IGM.

motions in the early Universe. Hutschenreuter et al. (2018) show that this process suggests a minimum magnetic field of 10^{-20} nG in the IGM today.

Scenarios of magneto-genesis can roughly be divided into two classes, *primordial* processes that generate magnetic fields throughout the entire Universe prior to formation of the first stars at redshift $z \approx 20$ and *astrophysical* processes, where the first galaxies expel their fields and magnetize the low-density regions. While the primordial processes generate magnetic fields that permeate the entire observable Universe, fields expelled by astrophysical sources tend to be focussed on the large-scale structure. A review on the different possible scenarios of magneto-genesis can be found in Durrer and Neronov (2013) and Subramanian (2019).

Magnetic fields generated in the primordial Universe are carried along by the accumulating gas, hence are compressed and enhanced by structure formation. The fields are further amplified by the astrophysical dynamos explained above and partly expelled into the IGM. Dynamo processes in active galactic nuclei can amplify the magnetic fields on rather short timescale and, even when born with zero magnetic fields, easily meet the conditions for Biermann battery mechanisms. The jets transport magnetic energy away from the central object, thus magnetizing the IGM. Further, it has been proposed that galactic winds of the first dwarf galaxies can transport the magnetic field, generated and amplified by stellar activity, into the IGM. However, far outside the large-scale structure, these astrophysical contributions are negligible while the comoving PMF is basically conserved. Hence, measuring the shape and strength of magnetic fields in voids is a direct measure of the PMF. Regions with gas densities that are associated with neither clusters nor voids are of similar interest. Their magnetic fields are probably dominated by astrophysical processes and hence deliver information on the recent history of magnetization. The slope of the magnetic field strength - density relation varies strongly with different scenarios of magneto-genesis, see Fig. 1.3. Constraining this slope with observations would yield valuable information on the cosmic origin of magnetic fields.

The lack of stars outside of high-density structures complicates measuring the magnetic field in between clusters and especially in cosmic voids. The only accepted lower limits on the magnetic field strength in voids were derived by Neronov and Vovk (2010). On their way to Earth, γ-rays from a TeV-blazar produce pairs of charged particles, which in turn emit γ-rays in the GeV-range. A potential intergalactic magnetic field (IGMF) would deflect the charged particles, causing angular broadening compared to unscattered emission. This broadening has not been observed by Fermi, nor any GeV-rays associated with the blazar. In conclusion, the IGMF has to be strong enough to deflect the charged particles away from the LoS, providing a lower limit of $B_0 \gtrsim 10^{-7}$ nG. Their results suggest that the entire Universe is permeated by magnetic fields. However, Neronov and Vovk (2010) consider a homogeneous turbulent IGMF. A more thorough investigation considering inhomogeneities in the IGMF shows that the Fermi observations are in agreement with the hypothesis of vanishing magnetic fields in voids (Arlen et al., 2014).

Blasi et al. (1999) investigate RM of distant quasi-stellar objects and derive limits on the IGMF strength of the order of ~ 1 nG by modelling the inhomogeneous IGM with a Lyman-α forest, assuming that the magnetic field is a function of density. Grasso and Rubinstein (2001) propose that a strong PMF present during big bang nucleosynthesis would alter expansion rate of the Universe as well as produce fluctuations in the baryon to photon ratio and the relic neutrino temperature. They conclude an upper limit on the PMF strength of $B_0 \lesssim 7 \times 10^2$ nG. Furthermore, the cosmic microwave background (CMB) carries a signal of the PMF present at the

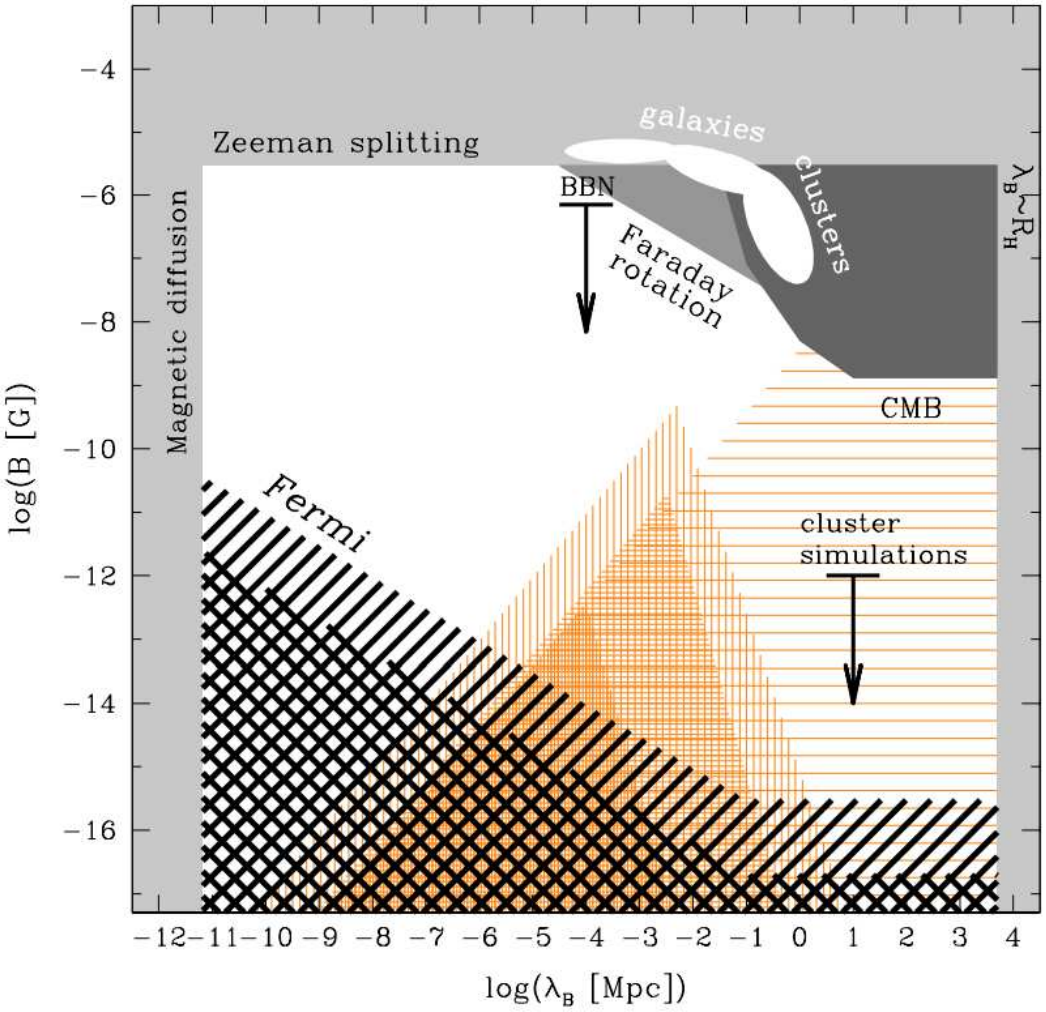

FIGURE 1.4: Current limits on field strength B and coherence length λ_B (or l_c) of the IGMF (Neronov and Vovk, 2010). The white regions in the top are mark magnetic field properties observed in galaxies and clusters.

epoch of recombination around redshift $z \approx 1100$. The PMF systematically deflects the pre-recombined plasma locally and induces small-scale baryonic density fluctuations leading to an inhomogeneous recombination process. This alters the peaks and heights of the CMB large-scale anisotropy power spectrum. The latest results of the PLANCK mission put an upper limit on the comoving strength of the PMF, $B_0 < 4.4$ nG (Ade et al., 2016a). Using the trispectrum of the CMB, Trivedi et al. (2014) derive even tighter upper limits on $B_0 < 0.05$ nG. Jedamzik and Saveliev (2019) derive similar upper limits using numerical magnetohydrodynamical (MHD) calculations and Monte-Carlo Markov chain analysis of the CMB power spectrum.

Apart from the strength of the magnetic field, l_c is of particular interest to characterize the shape of the field. The sparse constraints on l_c range from the size of the visible Universe, the Hubble radius of $\approx 4.4 \times 10^9$ pc, to the magnetic diffusion scale $\lesssim 10^{-5}$ pc. The current limits on B and l_c of the IGMF are summarized in Fig. 1.4 and in Neronov and Semikoz (2009).

1.1.4 How can we learn more about CMFs?

As discussed above, we can learn more about CMFs by measuring the magnetic field strength in the low-density regions of the Universe, using astrophysical messengers that are modified during propagation in magnetic fields. However, the weak fields associated with these regions only provide faint signals, which are likely to be overshadowed by other high-density regions along the path of propagation. In order to extract this information, we require statistical investigation of observations as well as comparison to predictions made by competing models. Since we can only observe one Universe and cannot change the input parameters like in a laboratory experiment, the use of Bayesian statistics is preferred (e. g. Trotta, 2008), which have lead to well established conclusions in interpretation of the CMB (Ade et al., 2016b).

In order to quantify the contributions from regions of different over-density in the IGM, we require detailed cosmological simulations, which start from a primordial Universe $z \gtrsim 20$ and consider different histories of magneto-genesis. At early times, the Universe was highly homogeneous and the structure formation is determined by gravity and small inhomogeneities that break symmetry. In a simulation, these inhomogeneities have to be chosen carefully in order to reconstruct the local Universe. We make use of results by Sorce et al. (2016), who describe a procedure to obtain the primordial inhomogeneities from observations of the local Universe by reverse-simulation of structure formation, enabling simulations that resemble the structure within 150 Mpc h^{-1}. Starting from the obtained initial conditions, the gravitational flow of dark matter and gas is computed while accounting for cosmic expansion, e. g. in comoving coordinates. Dark matter dominates gravitation and is usually followed using a N-body simulation of dark matter particles, that start uniformly distributed on a grid with random initial velocities. On top of that, the evolution of average gas-density, velocity, temperature and magnetic field is computed on scalar and vector field grids, following the equations of MHD (e. g. Bryan et al., 2014, used in this work). The magnetic field is amplified during structure formation by compression and stretching of field lines occurring during gravitational collapse. These processes occur prior to disk formation in spiral galaxies and can amplify a primordial seed field by several orders of magnitude. Where the necessary conditions are met, a phenomenological implementation of dynamo or other processes is triggered to further amplify the magnetic fields. In order to increase resolution only for the interesting parts of the simulation, some codes allow for adaptive mesh refinement. Cells that meet a certain condition, e. g. surpass a minimum density, are divided into sub-grids with better resolution, where the evolution of the field is followed in an increased number of cells. The output of such simulations at several redshifts represent the history of our Universe according to the assumed scenario. In further simulations, these can be used to obtain expectations of extragalactic observables that can be compared to observations.

In my thesis, I focus on extreme astrophysical messengers, namely ultrahigh-energy cosmic rays and fast radio bursts, and investigate how their recent observations can be used to improve our knowledge on magnetization of the low-density Universe. To this end, I investigate MHD simulations of the local Universe and its magnetic field, performed by Franco Vazza, assuming different scenarios for the cosmic origin of magnetic fields. With these, I simulate the propagation of messengers through the Universe and predict the properties we measure at Earth. Comparing these predictions to observations, I examine what we can learn about magnetic fields outside of galaxy clusters and their cosmic origin.

1.2 Ultrahigh-Energy Cosmic Rays

1.2.1 What are cosmic rays?

Apart from magnetic fields, the Universe is filled with freely moving particles. These were first discovered by Hess (1912, Nobel prize 1936), who found that the ionization rate increases with the altitude of his balloon, providing evidence for a constant stream of particles from outer space. Most of these are neutrons, protons and heavier elements, electrons, muons, pions and neutrinos. Astroparticles extended our view on astrophysical processes beyond electromagnetic radiation. For example, measurement of neutrinos from the Sun enhanced our knowledge on the fusion processes happening in the core, which cannot be probed otherwise. The history of astroparticle physics and the most prominent findings are reviewed in Cirkel-Bartelt (2008).

(Primary) Cosmic rays (CRs) exclusively describe fully ionized nuclei that travel the Universe close to the speed of light. CRs are expelled in stellar winds by our Sun and any other star. Still, most CRs in our galaxy probably are produced at the remnants of supernovae (Blasi, 2013). At the shock front, where fast expelled material impinges on colder gas, CRs can accelerate by travelling back and forth the discontinuity at the magnetic shock front. This type of acceleration was first proposed by Fermi (1949, 1954), which also includes a first estimate on the magnetic field of the MW of ≈ 6 μG, deduced from the isotropy of arrival directions of CRs. A general review on the history of CR detection and their implications can be found in Ginzburg (1996).

CRs arrive at Earth with energies above 10^{11} eV. Their energy spectrum, shown in Fig. 1.5, almost perfectly follows a power law over 9 orders of magnitude. The slope slightly changes at energies $E \lesssim 10^{16}$ eV and $E \lesssim 10^{19}$ eV. The features resemble a human leg and are hence called “knee” and “ankle”. The knee is believed to mark the maximum energy of Galactic accelerators of CRs. Some of the CRs measured at Earth have extreme energies beyond 10^{18} eV and up to few 10^{20} eV, more than 3 orders of magnitude above the highest energies obtained at the large hadron collider. These particles are named ultrahigh-energy cosmic rays (UHECRs). The ankle is believed to mark the energy, where UHECRs of extragalactic origin begin to dominate the spectrum. The sudden end of the spectrum at few 10^{20} eV either marks the maximum injection energy of UHECRs determined by their sources or a limitation of UHECRs due to energy loss processes. Excellent reviews on the history of UHECRs can be found in Blümer et al. (2009) and Kampert and Watson (2012).

1.2.2 How to measure cosmic rays?

At low energy, CRs can be measured by usual particle detectors on balloon and satellite experiments. But when CRs enter the atmosphere with energies above 10^{14} eV, their energy suffices to interact with the gas molecules and start an extensive air shower that impacts several km^2 on the ground, see Fig. 1.6. The flux of such particles is rather low, less than 1 particle per km^2 and year. Thus, observing a significant amount requires to measure air showers with a huge array of detectors, like the Pierre Auger Observatory (PAO) in Argentina (Collaboration et al., 2015) or the Telescope Array (TA) in Utah (Abu-Zayyad et al., 2012). Comparing these measures to air shower simulations allows to deduce the properties of the primary UHECR particle. The amount of secondary particles arriving at the stations is determined by the energy of the primary. The distribution of arrival times in the different detectors of the array allows for a geometrical reconstruction of the air shower and thus to deduce the

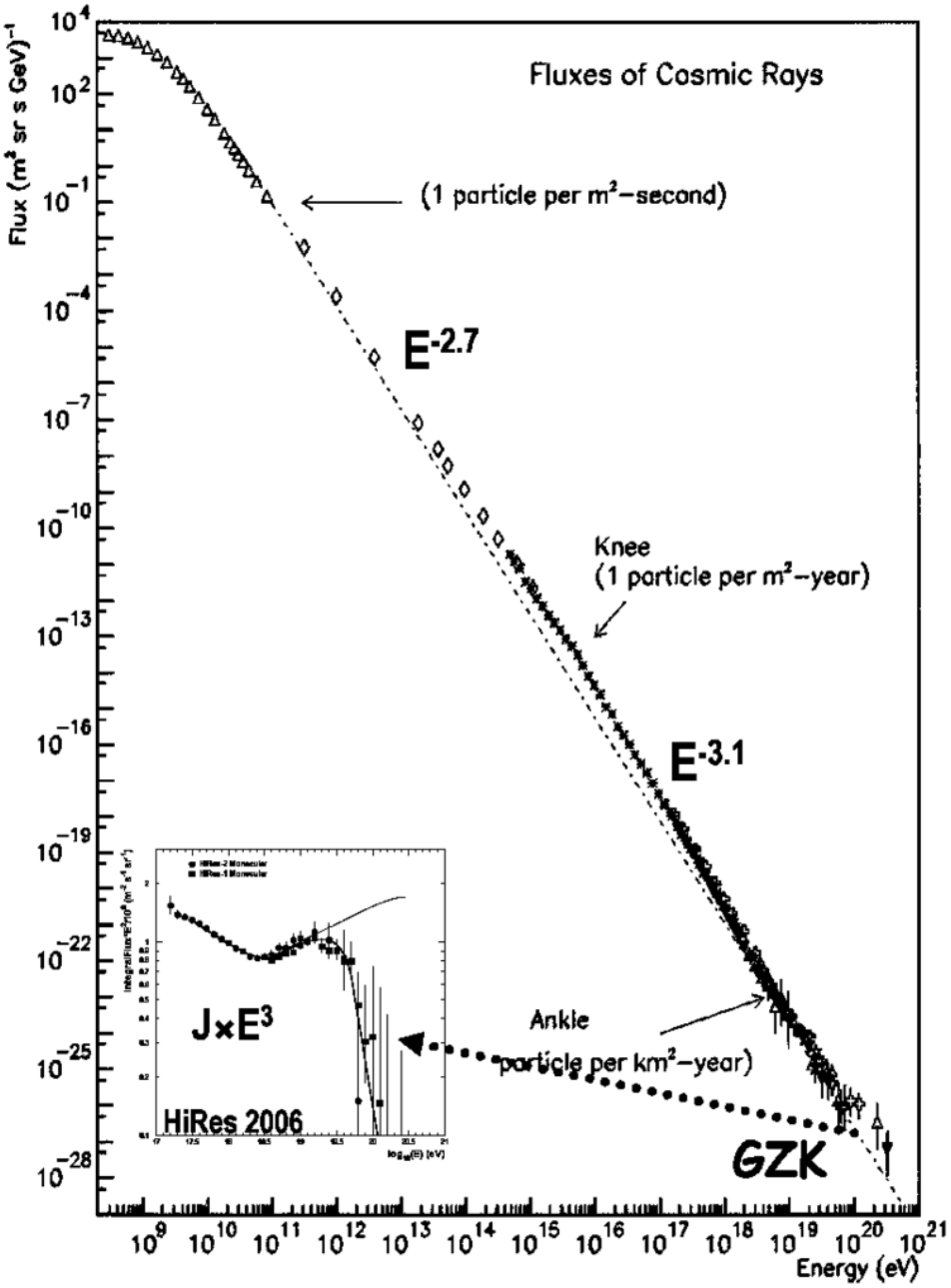

FIGURE 1.5: Energy spectrum of CRs observed by numerous observatories (Aharonian et al., 2011). The lower-left panel zooms the energy spectrum at high energies, multiplied by E^3 for clarity, revealing the GZK cut-off.

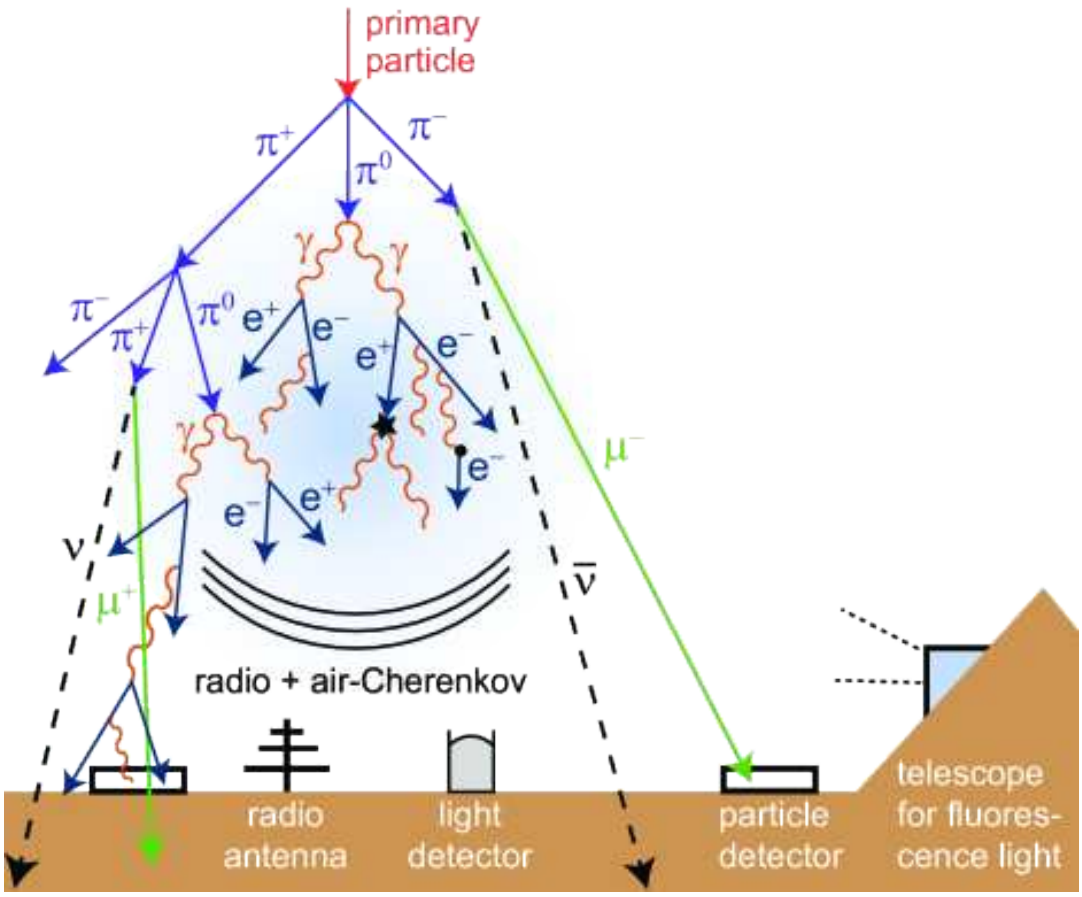

FIGURE 1.6: Extensive Air Shower (EAS) caused by high energy CRs that hit gas molecules in Earth's atmosphere (Schröder, 2017).

arrival direction of the primary. Additional telescopes surrounding the detector array can measure the fluorescence light emitted by excited gas in the atmosphere and give additional information about the air shower and its geometry. The shower increases in particle number, until the energy is completely distributed. The penetration depth into the atmosphere $X_{\max}$ at which that happens is determined by the number of nucleons in the primary nucleus. However, the large uncertainty ranges involved in measurement as well as air shower simulations, to which they are compared, only allow to derive the average atomic mass $\langle A \rangle$ for all UHECRs within an energy bin. The PAO has proposed an upgrade including additional muon detectors (Aab et al., 2016). The density of muons at the ground relative to the other secondaries is a much more precise measure of the particles composition and will allow to identify nuclei individually.

1.2.3 What do we know about UHECRs?

The PAO located in Argentina on the southern hemisphere reports a significant increase in average mass of nuclei $\langle A \rangle$ from helium-like at 10^{18} eV to nitrogen-like at 4×10^{19} eV (Aab et al., 2017), see Fig. 1.7. The results from TA in Utah on the northern hemisphere roughly agree with PAO for energies up to 10^{19} eV, but suggest substantially lower composition above this energy (Abbasi et al., 2019). This discrepancy might be explained by systematic differences between the two observatories or by the existence of a dominant nearby source in the southern hemisphere, e. g. Centaurus A, which is likely to be the closest source of UHECRs, since it correlates with a hotspot of increased flux of UHECRs (Collaboration et al., 2007). Particles from this source would have substantially lower travel time than particles from more distant sources.

During propagation, UHECRs interact with ambient photon fields, i. e. the CMB and infrared background emitted by stellar dust. Emitting secondaries, such as electron-positron pairs, neutrinos and γ-rays, the primary particles lose energy. The effect of these frequent events is well described by an adiabatic loss function. However, with energies above 5×10^{19} eV, UHECRs carry enough energy to produce pions in interaction with CMB photons, known as the GZK-effect, independently proposed by Greisen (1966) and Zatsepin and Kuzmin (1966). These rare events consume a significant amount of the particles energy and require sophisticated random modelling, e. g. using Monte-Carlo simulations. These repeatedly simulate individual events by picking random parameters, according to a reasonable distribution, in order to perform a numerical calculation of the expected result, which cannot be accessed analytically. The severe energy loss restricts the propagation of particles to within their energy-loss length, the GZK-horizon, at roughly 100 Mpc (Kachelriess et al., 2008). Thus, a GZK-cut-off in the observed energy spectrum is expected at $\approx 5 \times 10^{19}$ eV. UHECRs observed above that energy stem form sources within the GZK-horizon.

Furthermore, UHECRs lose nucleons due to nuclear decay or photo-disintegration, which have to be modelled by random generator simulations. A reduced travel time to a dominant nearby source like Centaurus A would hence suggest a heavier composition of arriving UHECRs, as observed by PAO. Due to the high Lorentz factor of UHECRs, the ejected protons and α-particles have a similar momentum as the primary particle, with about $1/A$ of the primaries energy, thus contribute to the flux of UHECRs at lower energy. See Allard (2012) for a review on the processes involved in propagation of UHECRs.

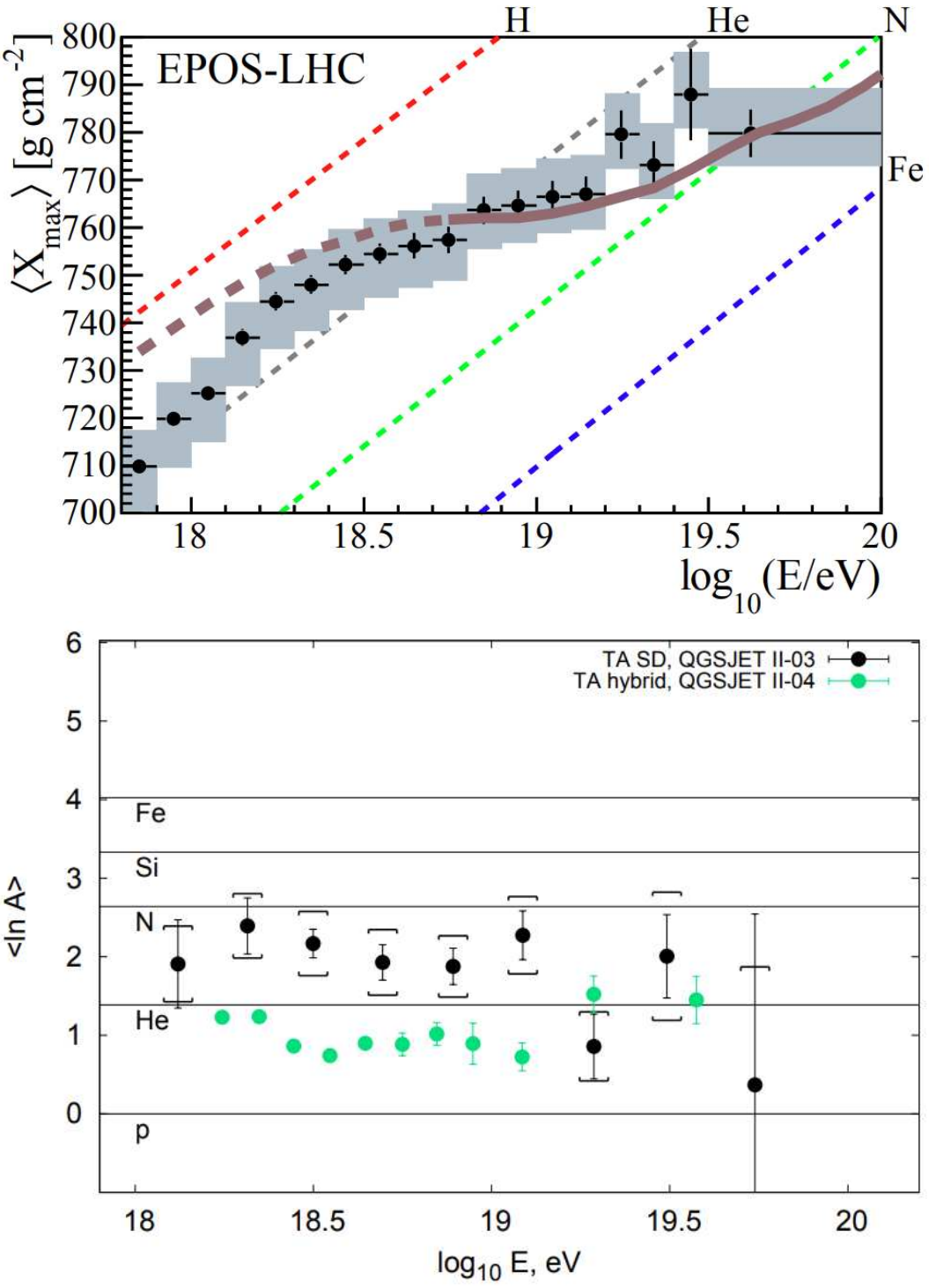

FIGURE 1.7: Composition measures of prominent UHECR telescopes for increasing energy E. Top: average maximum shower depth $\langle X_{\max} \rangle$ observed by PAO (Aab et al., 2017) and best fit (brown) together with expectations from Monte-Carlo simulations of air showers from different nuclei (dashed), assuming EPOS-LHC (Pierog et al., 2015) as hadronic model. Bottom: estimated average atomic mass A from reconstructions of air showers observed by TA (Abbasi et al., 2019) using only the particle detectors (black) or both, the particle and fluorescence detectors (green), assuming QGSJET-II (Ostapchenko, 2004) as hadronic model.

UHECRs are charged particles and thus deflected by CMFs. Hence, arrival directions do not point back on the sources, which hinders their identification. A nucleus with atomic number Z gyrates around a magnetic field line (cf. Fig. 1.1) at a distance called Larmor-radius, or gyroradius, given by (e. g. Mollerach and Roulet, 2013)

$$r_g = \frac{10}{Z} \left(\frac{E}{10^{19}\ \mathrm{eV}} \right) \left(\frac{B}{1\ \mu\mathrm{G}} \right)^{-1}\ \mathrm{kpc}, \tag{1.4}$$

obtained by equating Lorentz force with centripetal force. E/Z is also called rigidity and is used for a composition-independent estimate of deflection. For protons with $E > 10^{18}$ eV in a uniform magnetic field with strength $B \approx 10\ \mu$G, similar to the MW, $r_g \gtrsim 0.1$ kpc, comparable to the thickness of the stellar disk ≈ 0.6 kpc. Thus, such particles can hardly be confined within the Galaxy nor can their flux be isotropized by random motion. A Galactic origin of UHECRs would suggest a strong anisotropy in direction of the Galactic centre, which is not observed. Hence, the largely isotropic distribution in arrival directions of UHECRs suggests an extragalactic origin. However, the sources could not yet be identified.

In order to accelerate to higher energy, the particles need to be confined within the accelerating region. However, r_g increases with the particles energy E. For a possible accelerator with residual magnetic field B one can compare the gyro radius to the size of the structure L in order to derive a maximum injection energy possible by acceleration. This provides an exclusion criterion for sources of UHECRs of a certain energy, known as the Hillas criterion (Hillas, 1984), see Fig. 1.8. This only leaves the most powerful or extended astrophysical objects as potential sources for UHECRs above 10^{20} eV, i. e. neutron stars, γ-ray bursts, active galactic nuclei, radio lobes, colliding galaxies or galaxy clusters.

Aab et al. (2018a) report the observation of large-scale anisotropy in the flux of UHECRs with energies ≥ 8 EeV $= 8 \times 10^{18}$ eV, see Fig. 1.9. Since the weak dipole anisotropy is not aligned with the Galaxy, it clearly marks UHECRs to be of extragalactic origin and can be used to constrain possible source catalogues. Kim et al. (2019) report the presence of galaxy filaments connected to the Virgo cluster in direction of the TA hotspot (Abbasi et al., 2014). Furthermore, Aab et al. (2018b) found a correlation of UHECRs arrival direction with star burst galaxies. However, the significance is too low to rule out other sources. A summary of open questions in UHECR astronomy can be found in Batista et al. (2019).

1.2.4 What do UHECRs tell us about CMFs?

On their way to Earth, UHECRs are deflected by magnetic fields due to Lorentz force (Eq. 1.1). A significant amount of deflection is due to the relatively strong magnetic field of the MW. However, due to the larger scales involved, the halo of the MW probably dominates this deflection. This potentially makes UHECRs a unique measure of the magnetic field in the MW halo. The Galactic magnetic field has a strong regular component, thus Galactic deflection can shift the apparent position of sources in the sky (e. g. Farrar and Sutherland, 2019). Though these dispositions strongly depend on rigidity and arrival direction, Galactic deflections are too small to alter large-scale anisotropy.

Before entering the MW, UHECRs are further deflected by magnetic fields in the IGM. Though the magnetic field strength is at least 3 order of magnitude below the MWs, the opposite is true for travel distance. Thus, deflections in the IGMF potentially are of the same order as in the Galaxy. However, the IGMF is very likely to be

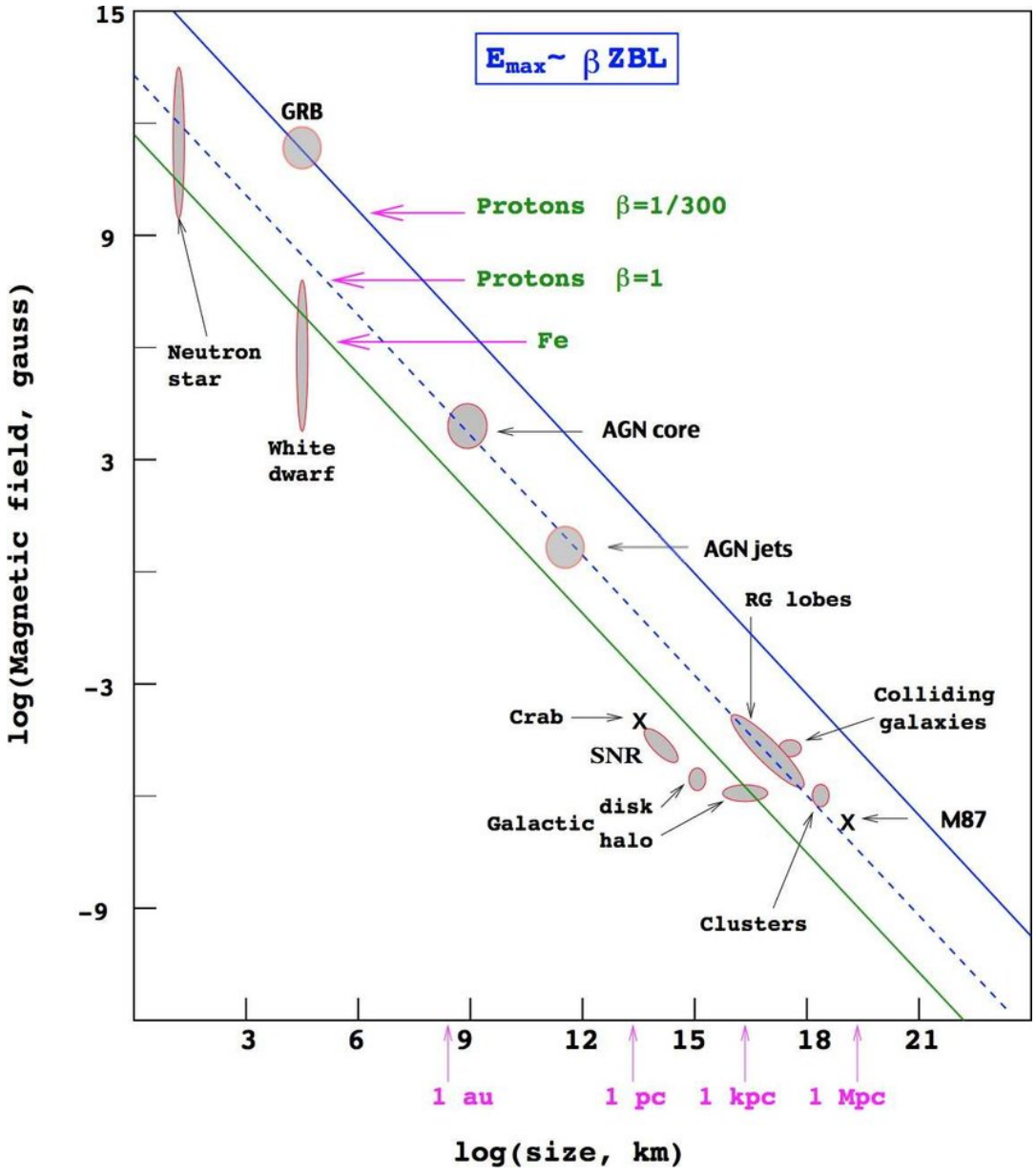

FIGURE 1.8: Hillas plot that shows the exclusion criterion for sources of UHECRs of charge Z with energy above 10^{20} eV according to their size L and residual magnetic field B (Letessier-Selvon and Stanev, 2011). β represents the efficiency of accelerators.

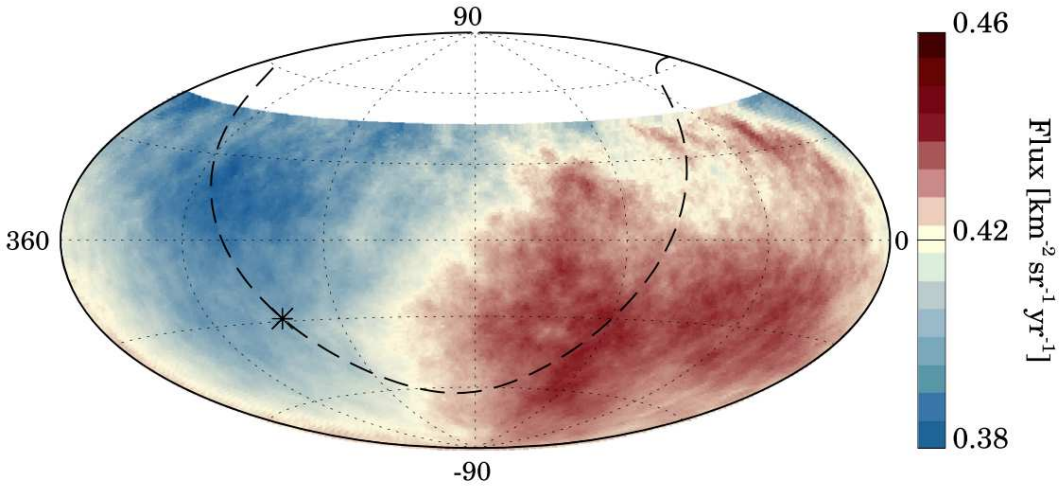

FIGURE 1.9: Large scale anisotropy in the flux of UHECR above $\geq$ 8 GeV, measured by the PAO in Argentina (Aab et al., 2018a). The dashed line shows the Galactic plane, with a star indicating the Galactic center.

turbulent, propagation is thus erratic and small changes in the initial momentum results in completely uncorrelated paths. Hence, for sources at reasonable distance, i. e. beyond multiple l_c, the IGMF accounts for a broadening of the source signal, without a shift in source position. However, sources within distance of l_c, which might be up to several Mpc, or with a cosmic filament along the LoS might show significant source disposition. Yüksel et al. (2012) investigate the angular distribution of the excess in UHECRs observed around Centaurus A and estimate the IGMF to be $\gtrsim$ 20 nG in that direction, assuming that Centaurus A is indeed the source of this excess. Dolag et al. (2005) perform cosmological MHD simulations that resemble the local Universe and simulate the propagation of UHECRs and find significant influence of IGMFs mostly on UHECRs that cross galaxy clusters. They conclude that statistical properties of UHECRs can be used to investigate the large-scale properties of IGMFs.

In this thesis, I investigate how the small amount of dipole anisotropy observed in the UHECR full sky can be used to infer the strength, shape and origin of IGMFs using reasonable assumptions for the sources of UHECRs. To this end, like Dolag et al. (2005), I use CRPROPA - an open-source software code to simulate the propagation of UHECRs - with MHD simulations for the IGMF in the local Universe, provided by Franco Vazza, for the first time assuming different scenarios of magneto-genesis along with several possible source catalogues. I obtain the expected flux at position of the MW, compare to the Auger dipole and examine what can be learned about the sources of UHECRs, the ejected composition of UHECRs as well as the IGMF.

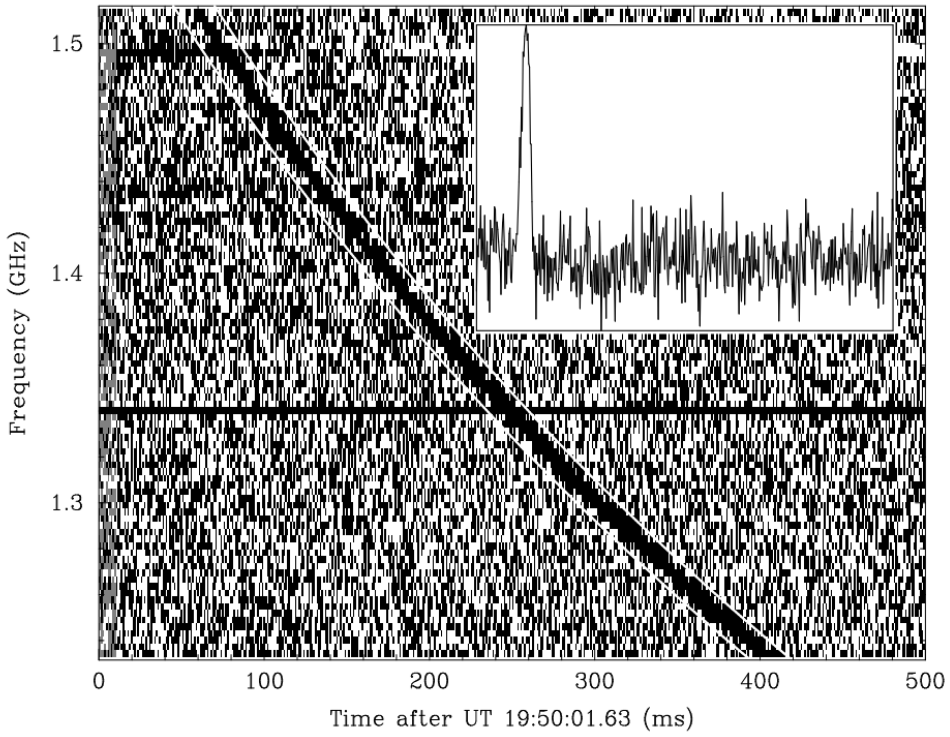

FIGURE 1.10: Frequency evolution and integrated pulse shape (upper right) of the first detected FRB identified by Lorimer et al. (2007). The delay in arrival time at lower frequencies matches with expectation from dispersion in plasma, $t \propto \nu^-2$ (Eq. 1.5).

1.3 Fast Radio Bursts

1.3.1 What are FRBs?

Fast radio bursts (FRBs) are bright (50 mJy - 100 Jy) pulses of millisecond duration in the radio spectrum, ≈ 1 GHz, with a total power of up to 10^{43} erg s^{-1} and inferred brightness temperature of about 10^{35} K. So far, FRBs have been observed to last < 30 μs (Michilli et al., 2018) to about 30 ms (Farah et al., 2017). The first FRB, shown in Fig. 1.10, was discovered by Lorimer et al. (2007) in archival data of a pulsar survey of the Parkes radio telescope in Australia. The arrival time of the short pulse, which was previously disregarded as interference, has a frequency-dependent delay in arrival time. The slope in frequency ν exactly matches expectations from dispersion in plasma along the LoS

$$t = 4.15 \text{ ms } \left(\frac{\text{DM}}{\text{pc cm}^{-3}}\right) \left(\frac{\nu}{\text{GHz}}\right)^{-2}, \tag{1.5}$$

that causes a time-delay t in propagation of light due to electrostatic interactions with charged particles in the plasma. The dispersion measure DM is defined as column density of free electrons

$$\text{DM} = \int_0^d n_e \, \text{d}l \tag{1.6}$$

and represents the number of free electrons per unit area between observer and source at distance d.

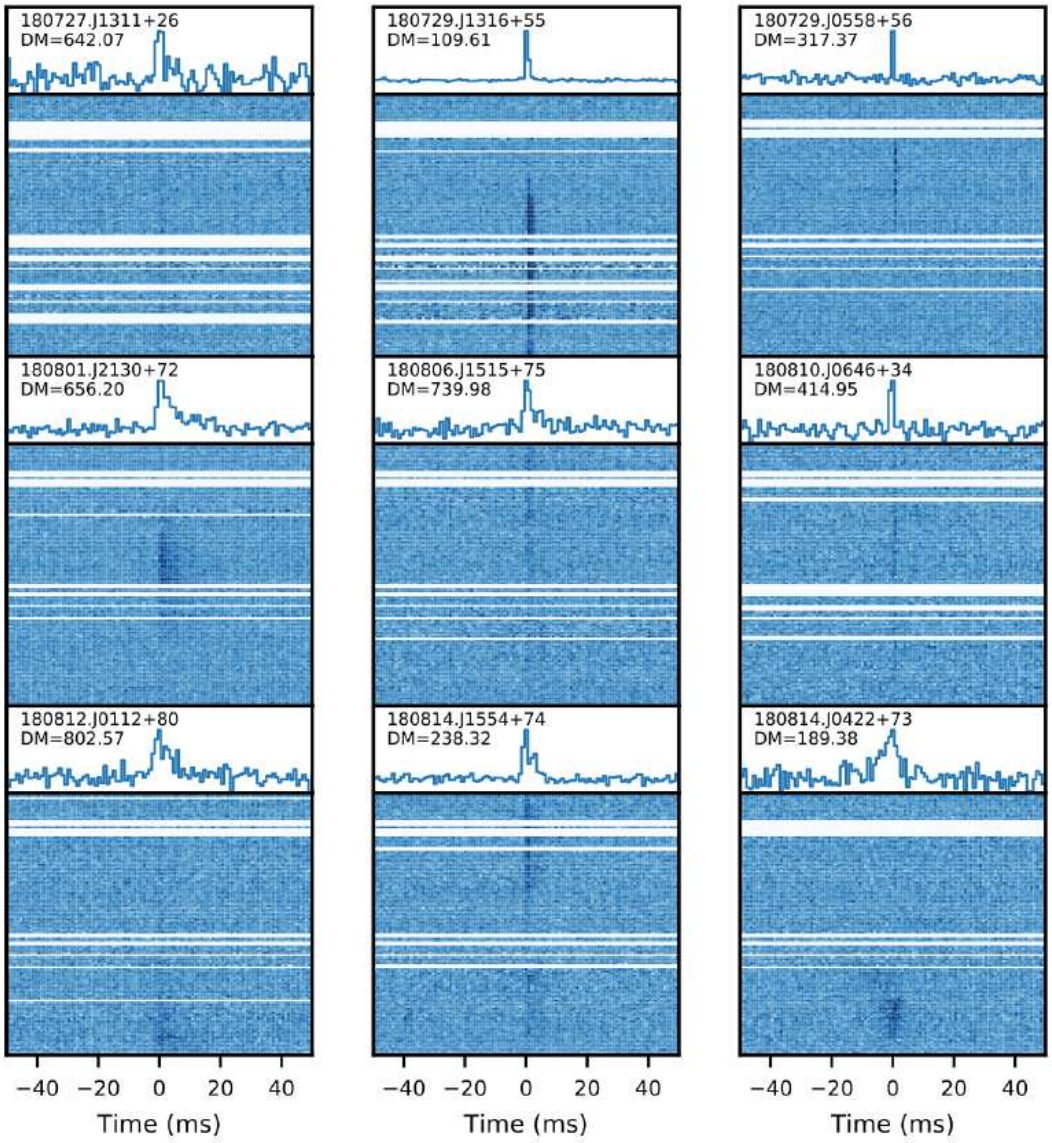

FIGURE 1.11: Dynamic spectrum or "Waterfall" plots for sample of pre-commissioning events observed by CHIME (taken from Amiri et al., 2019), for which arrival times at different frequencies have been dedispersed, i. e. the delay corresponding to the inferred DM (cf. Eq. 1.5) has been removed. The blue line plots above each spectrum show the frequency-summed burst profiles in full time resolution. The colour scale indicates the signal-to-noise ratio. In nearly all cases radio frequencies in the 729–756 MHz band have been removed due to the presence of radio frequency interference from cell phone communication, as have narrower bands corresponding to television and other interfering signals. Most events are broadband, with some spanning the whole bandwidth of 400 MHz, while others span a more limited range.

FRBs have been observed with frequencies down to 300 MHz (Chawla et al., 2020; Pilia et al., 2020) and up to 8 GHz (Gajjar et al., 2018). However, their bandwidths show strong variance between individual bursts and can hardly be described systematically as of yet, see e. g. Fig. 1.11.

FRBs are mostly shorter than the temporal resolution of the receivers. They are hence characterized by the fluence, defined as the time-integral of the flux density. Typically, FRBs are observed with a fluence of $1 - 10$ Jy ms. However, the exact location of the FRB signal in the beam of the instrument is uncertain and, since the amount of received energy is not uniform throughout the beam, reported fluences only serve as a lower limit. Based on results of previous surveys, more than $\gtrsim 10^3$ FRBs above a fluence threshold of $\gtrsim 1$ Jy ms are expected to be detectable over the whole sky every day (Champion et al., 2016).

The inferred brightness temperature of FRBs are as high as 10^{37} K, which implies bunched coherent emission, similar to radio pulsars. In many aspects, FRBs are much alike radio pulsars, which are rapidly rotating neutron stars. At their poles, open field lines of their strong magnetic fields act as long-lived particle accelerators that cause coherent radio emission (Lorimer and Kramer, 2012). Due to the rotation of the neutron star, the sweeping beam is observed as periodic pulses of 0.1 - 1000 ms duration.

For radio bursts observed with DM close to maximum expectations of the contribution of the MW, it is unclear whether it is a FRB, pulsar or rotating radio transient (RRAT). The latter are a subclass of periodic bright pulsars in our galaxy with ms duration. In many aspects, FRBs are very similar to radio pulsars. Both have similar peak flux densities around ~ 1 Jy and show a variety of linear and circular polarization fractions, pulse widths and structure as well as spectra. So far, there is no strict definition of FRBs, albeit ongoing attempts to formalize FRB classification (Foster et al., 2018).

The most prominent difference between FRB and other bright radio transients is the high DM, which far exceeds expectations from the MW, see Fig. 1.12. Further, their distribution in the sky shows no evidence of anisotropy so far (Rane et al., 2016; Bhandari et al., 2017), which would be expected if they originated in the Galaxy. This suggests that FRBs are of extragalactic origin. In fact, some have been localized to galaxies beyond redshift $z > 0.1$. FRBs are thus the first radio transients observed beyond the local galaxy group, rendering them an interesting new probe for astrophysics and cosmology. Katz (2016) and Petroff et al. (2019) provide excellent reviews on FRBs and the interesting history of the discovery of these fast radio transients.

1.3.2 What do we know about FRBs?

Pulsars and FRBs are observed with similar peak flux densities of 1 Jy, while the latter are at $\sim 10^6$ times greater distance. This implies a 10^{12} times greater luminosity. Further, the short duration of FRBs implies a coherent emission mechanism and requires a small ejection region, ≈ 10 km, about the size of a neutron star. However, the magnetospheres of canonical pulsars can hardly provide the required energy. This suggests magnetars, young neutron stars with extreme magnetic fields of $10^{14}-10^{16}$ G, as the sources of FRBs (e. g. Popov and Postnov, 2010; Beloborodov, 2017).

Magnetars have been observed to emit highly erratic radio pulses with an average pulse profile that changes over time (Camilo et al., 2006). The recent detection of a short radio burst consistent with cosmological FRBs from flaring Galactic magnetar

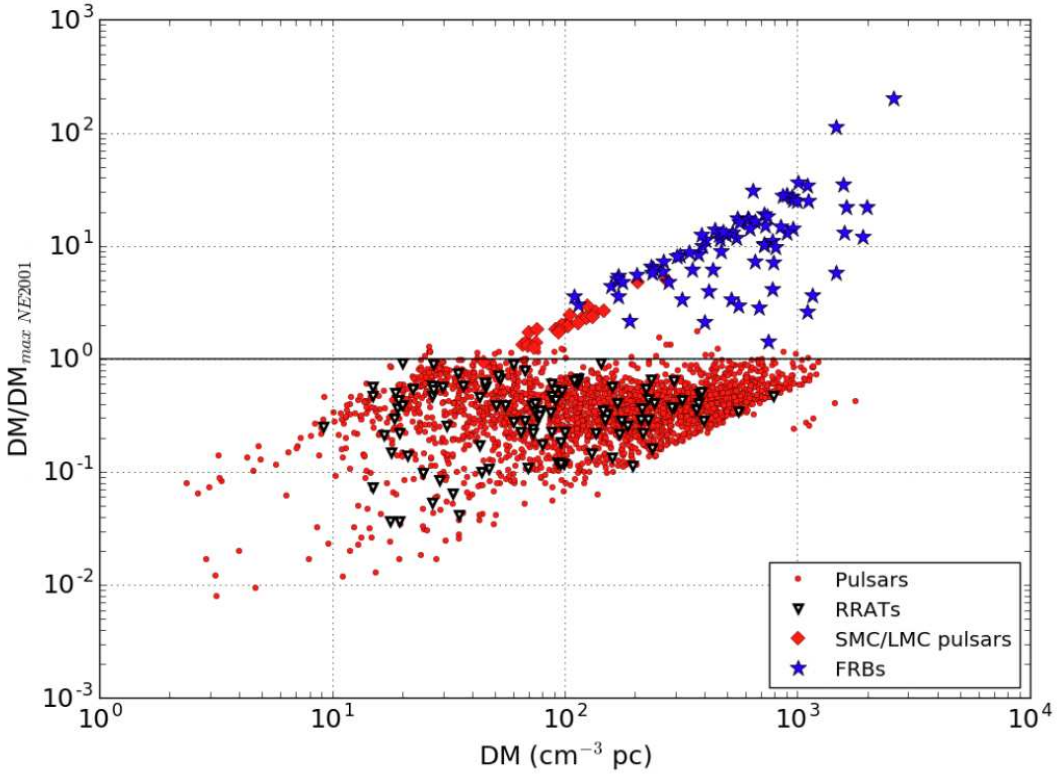

FIGURE 1.12: Dispersion measure DM observed for Galactic radio pulsars, Galactic rotating radio transients (RRATs), radio pulsars in the Small and Large Magellanic Clouds (SMC & LMC) as well as FRBs, normalized to maximum Galactic contribution expected in observed direction according to NE2001 model (Cordes and Lazio, 2002) of the MW free electron density. Figure taken from Petroff et al. (2019), also see Spitler et al. (2014).

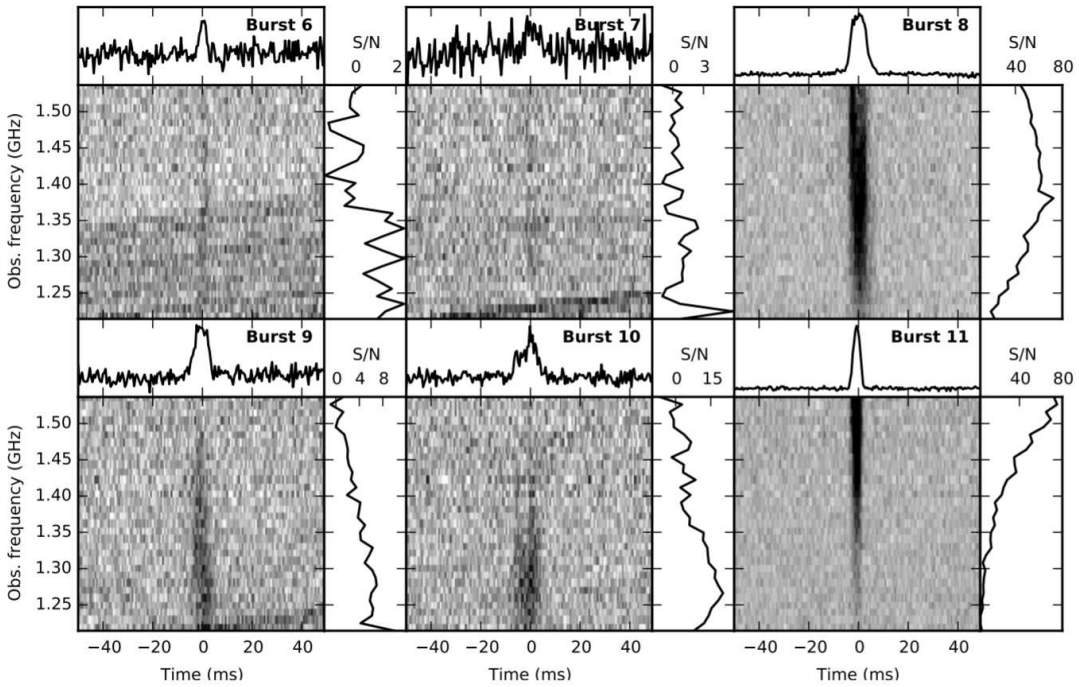

FIGURE 1.13: Dynamic spectrum or "Waterfall" plots similar to Fig. 1.11 for multiple detections from the Spitler Burst FRB121102. The graph to the right of every dynamic spectrum shows the temporally integrated spectrum as signal-to-noise ratio. The spectra vary among bursts.

SGR 1935+2154 hardens this suggestion (Bochenek et al., 2020; Collaboration et al., 2020; Mereghetti et al., 2020).

The polarization properties of FRBs are rather diverse. Some appear to be completely unpolarized, others show only circular or linear polarization, while some show a combination of both. Rarely, frequency dependent polarization properties could be observed (Price et al., 2019). The heterogeneity of polarization properties could arise from time-variable emission, different viewing geometries or local environments and are not necessarily caused by separate source types.

FRBs are observed with frequencies down to 300 MHz and they probably exist at even lower frequencies. However, observations with LOFAR down to 140 MHz so far failed to detect any FRBs (Coenen et al., 2014; Karastergiou et al., 2015). This might hint on an intrinsic cut-off at low frequencies, but might also be explained by absorption in the local environment or during propagation, e. g. by induced Compton scattering or free-free absorption (Rajwade et al., 2020a).

While most FRBs have only been observed to burst once, some of them have repeated multiple times. For a long time the Spitler burst FRB121102 was the only known repeating FRB. The ongoing surveillance of this burst has so far seen several hundred bursts from this source over an active period of more than seven years since 2012. However, the repetitions show epochs of high and low activity and so far do not seem to follow any particular pattern (Oppermann et al., 2018), despite a possible periodic behaviour of the "on" and "off" cycles (Rajwade et al., 2020b), which yet needs to be confirmed. So far, FRB180916 is the only other source to show a pattern in burst emission (Amiri et al., 2020), which is, however, about ten times faster than that of FRB121102.

Further, different spectra are observed for each new burst, see Fig. 1.13. The Spitler burst consistently shows extremely high Faraday rotation measure $RM \simeq 1.46 \times 10^5$ rad m^{-2}, which decreased to 1.33×10^5 rad m^{-2} within 7 months (Michilli et al., 2018). The extreme RM is of the same order as observed from the supermassive black hole in the centre of the MW (Marrone et al., 2006; Macquart et al., 2006) and is likely to be caused by the local environment (Michilli et al., 2018). The decrease over time yields further information about the source. By now, more than 20 repeaters have been observed in total (Amiri et al., 2019; Andersen et al., 2019; Fonseca et al., 2020). Though a total of several hundred FRBs have been observed from different locations, it cannot yet be excluded that all of these are repeaters (Caleb et al., 2019). Still, it suggests that there may be two or even more populations of FRBs from different source classes.

The progenitors of FRBs could not yet be identified. Historically, the number of proposed models has risen in the same pace as the number of reported FRB observations. However, theorists have a hard time to keep abreast now that new instruments observe few FRBs every day. For example, since starting operation in late 2018, the CHIME/FRB project (Amiri et al., 2018) has detected about 1000 FRBs, however, so far published only a small subset, mostly repeating FRBs (e. g. Andersen et al., 2019; Fonseca et al., 2020). The online catalogue FRBcat[1] (Petroff et al., 2016) collects FRBs observed by telescopes around the world. The FRB living theory catalogue[2] (Platts et al., 2018) provides a collection and summary of prominent models.

The source models can be roughly divided into two categories. Cataclysmic events produce a single FRB or a small set of those on short time-scale at the end of the progenitors life. These are typically collapses of neutron stars (e. g. Fuller and Ott, 2015) or merger events (Wang et al., 2016), where interactions of magnetic fields, such as magnetic reconnection, accelerate particles, which emit coherent radio emission.

The progenitor of a non-cataclysmic event survives the emission of a FRB and can hence emit several of those over a longer timespan. Some of the most popular repeating FRB models consider a young neutron star with strong magnetic field (Popov and Postnov, 2010; Lyubarsky, 2014; Murase et al., 2016; Beloborodov, 2017; Metzger et al., 2019). Flares from that star cause a shock when they hit a surrounding nebula caused by stellar winds of the progenitor star. A strong coherent magnetic field builds up at the shock front and gyrating particles emit coherent radio emission. Though these models do well explain observations of some FRB, they could not yet be unambiguously identified as their sources (Beloborodov, 2017; Metzger et al., 2017; Vieyro et al., 2017; Margalit and Metzger, 2018).

Many source models predict afterglows and other counterparts to the FRB outside the radio spectrum. Observations of such counterparts would be a smoking gun for the identification of FRB progenitors. However, despite tests with X-ray, γ-ray, optical and even neutrino telescopes (Scholz et al., 2016; Bhandari et al., 2017; Scholz et al., 2017; Xi et al., 2017; Tavani et al., 2020; Scholz et al., 2020; Marnoch et al., 2020; Bouwhuis et al., 2020) no counter parts could be detected as of yet, except for the possible detection of transient γ-ray counterparts to FRB131104 (DeLaunay et al., 2016) and FRB171209 (Wang et al., 2020).

The localization of short duration transients like FRBs is very challenging, as is the identification of their host galaxies (Eftekhari and Berger, 2017). The accuracy of

[1] frbcat.org
[2] frbtheorycat.org

their angular localization depends on the spatial resolution of the observing telescope and can be enhanced using interferometry. Further, FRBs come without a direct measure of redshift. For FRBs at cosmic distance $z > 0.1$, DM is probably dominated by the IGM, due to the large scales involved. The DM can hence be used to estimate the redshift of FRB hosts, or at least put upper limits on the distance, since high DM of nearby FRBs might also be produced by high density environments along the LoS (Dolag et al., 2015; Walker et al., 2018; Niino, 2018; Luo et al., 2018; Pol et al., 2019). This leaves an enormous volume for the potential position of the FRB progenitor. Repeating FRBs allow for a more precise angular localization. So far, nine FRBs have been localized in several types of galaxies (Macquart et al., 2020), ranging from low-metallicity starburst dwarf galaxies (Tendulkar et al., 2017) to massive galaxies with modest star-formation rates (Bhandari et al., 2020).

1.3.3 What can FRBs tell us about the Universe?

The very short duration of FRBs requires the observing telescope to have a very fine temporal resolution, on the order of ms or even below in order to resolve the variability of the burst signal. The ASKAP interferometer in Australia (Macquart et al., 2010) combines a temporal resolution of few ns, allowing for detailed studies of source mechanisms (Cho et al., 2020), with a very fine angular resolution of $8''$, enabling an unprecedented precision in the localization of FRBs that allows to pinpoint the position of the FRB progenitor within the host galaxy (Bhandari et al., 2020). Together with its large field of view ≈ 30 deg^2, ASKAP promises remarkable results and huge number of localized FRBs in the near future, and especially once the full SKA starts operation around 2027. The CHIME observatory in Canada (Amiri et al., 2018) that started operation in late 2018 has a temporal resolution on the 1 ms level together with a field of view ≈ 200 deg^2, which enables it to observe several FRBs every day. With these new telescopes at operation, a reasonable number of FRB observations will become available in the near future, tearing this new window to the Universe wide open.

FRBs are a new and interesting signal with the potential to answer many long lasting astrophysical and cosmological questions. Studies of FRBs can provide insight on the processes that fuel galaxy evolution (Abbott et al., 2017) and the compact stellar remnants left behind (Hamilton et al., 1985; Lyne et al., 2001). They might be used to constrain the photon mass (Wu et al., 2016) as well as violations of Einstein's equivalence principle (Wei et al., 2015; Tingay and Kaplan, 2016). FRBs that are strongly lensed might probe dark matter (Muñoz et al., 2016) and cosmic curvature (Li et al., 2018). Several publications discuss the use of DM-redshift relation of either FRBs associated with γ-ray bursts or localized FRBs to constrain the equation of state of dark energy as well as other cosmological parameters (Zhou et al., 2014; Gao et al., 2014; Yang and Zhang, 2016; Walters et al., 2018). Instead, Wei et al. (2018) propose to use the luminosity distance of gravitational waves associated to FRBs together with their DM to constraint cosmic parameters. However, Jaroszynski (2019) suggest that cosmological parameters and amount of ionized baryons in the IGM cannot be constrained separately. They conclude that constraints on the distribution of ionized gas is the most promising cosmological application of FRBs.

Statistical combination of observations in the local Universe, $z < 2$, can only account for $60-70\%$ of baryonic matter expected according to the ΛCDM-model and observations by PLANCK. The missing baryons are believed to be in the warm-hot intergalactic medium. This phase of the IGM has a temperature of $T = 10^5 - 10^7$ K

and only couples with radiation through electronic transitions and is thus difficult to detect (for a review, see Nicastro, 2016). Corroboration for this hypothesis is provided e. g. by correlation of Sunyeav-Zeldovich effects in the CMB with the visible galaxy distribution (Tanimura et al., 2018) and detection via thermal absorption lines (Nicastro et al., 2018). FRBs are the first radio transients observed outside the local galaxy group. Hence, their DM delivers an excellent measure of the baryon content in the IGM that can be used to falsify this solution for the missing baryon problem.

1.3.4 What can FRBs tell us about CMFs?

Electrons in the halo of the MW dominate DM of FRBs at low distance (Platts et al., 2019, 2020). Together with UHECRs, that are sensitive to the halo magnetic field, they provide a unique measure of the MW halo. Some FRBs are observed with sufficiently strong linear polarization to allow observation of Faraday rotation. For example, the repeating Spitler Burst FRB121102 was observed with 100% linear polarization and a Faraday rotation measure RM $\gtrsim 10^5$ rad m^{-2} (Michilli et al., 2018). Though this outstanding RM is by far the highest observed for any FRB and likely caused by an extreme magneto-ionic environment, in general, the RM of an ensemble of FRBs together with their dispersion measure DM are a potential probe of the IGMF. Akahori et al. (2016) use ΛCDM universe simulations that assume turbulent flow motions to provide todays magnetic fields from a weak primordial seed field. Excluding FRBs that pass through galaxy clusters, they show that the ratio of RM/DM possibly signals information on magnetic fields in filaments. Vazza et al. (2018) investigate the expected DM and RM due to the IGM using cosmological MHD simulations, comparing two extreme scenarios for the origin of magnetic fields, one with predominantly primordial origin, the other considering a weak PMF and the IGM being magnetized by astrophysical processes, such as magnetic feedback from active galactic nuclei. They find that the ratio of RM/DM is a potential probe for the origin of magnetic fields in our Universe. However, the dominant contribution to DM and RM might stem from different regions along the LoS. Hence, the RM/DM ratio should be considered with caution when inferring the magnetic field (Piro and Gaensler, 2018). Furthermore, these works do only account for RM from the IGM, but do not consider other environments along the LoS.

In my work. I refine these results by probing constrained cosmological MHD simulations that resemble the local Universe, provided by Franco Vazza. Further, I consider sophisticated models for all dominant regions along the LoS, including the IGM, source environment, host and additional galaxies that possibly intersect the LoS, as well as their contribution to DM and RM. The model for the dwarf galaxy IC10 is provided by Volker Heesen. The likelihood functions for the ensemble of host and intervening galaxies is provided by Luiz F. S. Rodrigues. The model for the local environment of the magnetar is provided by Tony Piro. To obtain predictions and compare them to observations, I make use of Bayesian tools, such as Monte-Carlo simulations. I obtain predictions in the form of likelihood functions, that can be used to quantify the posterior likelihood of hypothetical scenarios to reproduce observations. This can be used to systematically identify models that best describe our Universe. For this purpose, I created the open-source python software package PrEFRBLE, "Probability Estimates for Fast Radio Bursts to obtain model Likelihood Estimates" (Hackstein, 2020), designed to enhance communication between theoretical models and observational results. I show how FRB observations expected in the coming few years will allow us to put reasonable constraints on magnetic fields outside of galaxy clusters as well as the cosmic origin of magnetic fields.

Chapter 2

Publications

Monthly Notices of the ROYAL ASTRONOMICAL SOCIETY

MNRAS **475,** 2519–2529 (2018) doi:10.1093/mnras/stx3354
Advance Access publication 2018 January 4

Simulations of ultra-high energy cosmic rays in the local Universe and the origin of cosmic magnetic fields

S. Hackstein,[1]★ F. Vazza,[1,2] M. Brüggen,[1] J. G. Sorce[3,4] and S. Gottlöber[4]

[1]*Hamburger Sternwarte, Gojenbergsweg 112, D-21029 Hamburg, Germany*
[2]*INAF, Istituto di Radioastronomia di Bologna, via Gobetti 101, I-41029 Bologna, Italy*
[3]*Université de Strasbourg, CNRS, Observatoire astronomique de Strasbourg, UMR 7550, F-67000 Strasbourg, France*
[4]*Leibniz Institute for Astrophysics Potsdam, An der Sternwarte 16, D-14482 Potsdam, Germany*

Accepted 2017 December 27. Received 2017 November 28; in original form 2017 August 6

ABSTRACT

We simulate the propagation of cosmic rays at ultra-high energies, $\gtrsim 10^{18}$ eV, in models of extragalactic magnetic fields in constrained simulations of the local Universe. We use constrained initial conditions with the cosmological magnetohydrodynamics code ENZO. The resulting models of the distribution of magnetic fields in the local Universe are used in the CRPROPA code to simulate the propagation of ultra-high energy cosmic rays. We investigate the impact of six different magneto-genesis scenarios, both primordial and astrophysical, on the propagation of cosmic rays over cosmological distances. Moreover, we study the influence of different source distributions around the Milky Way. Our study shows that different scenarios of magneto-genesis do not have a large impact on the anisotropy measurements of ultra-high energy cosmic rays. However, at high energies above the Greisen–Zatsepin–Kuzmin (GZK)-limit, there is anisotropy caused by the distribution of nearby sources, independent of the magnetic field model. This provides a chance to identify cosmic ray sources with future full-sky measurements and high number statistics at the highest energies. Finally, we compare our results to the dipole signal measured by the Pierre Auger Observatory. All our source models and magnetic field models could reproduce the observed dipole amplitude with a pure iron injection composition. Our results indicate that the dipole is observed due to clustering of secondary nuclei in direction of nearby sources of heavy nuclei. A light injection composition is disfavoured, since the increase in dipole angular power from 4 to 8 EeV is too slow compared to observation by the Pierre Auger Observatory.

Key words: MHD – relativistic processes – methods: numerical – cosmic rays – ISM: magnetic fields.

1 INTRODUCTION

Evidence for the existence of magnetic fields have been reported for all types of structures found throughout the Universe. Galaxies host magnetic fields with typical strengths of ∼5–15 μG, which were measured using Faraday rotation and synchrotron emission up to redshift $z \sim 2$–6 (e.g. Vallée 2004; Bernet, Miniati & Lilly 2013; Beck 2016; Kim et al. 2016). The magnetic field in clusters of galaxies was found to be of the order ∼μG (Feretti et al. 2012). Future radio observations will offer the chance to measure the magnetization at the outskirts of clusters and in filaments that connect them (Brown 2011; Araya-Melo et al. 2012; Vazza et al. 2015). A recent study has reported upper limits on the magnetic field strength of ∼0.03 μG from the absence of a correlation between synchrotron emission and the large-scale structure (LSS, Brown et al. 2017; Vernstrom et al. 2017). Limits on the magnetic fields in voids were derived from the angular power spectrum, the bispectrum and the trispectrum of the cosmic microwave background ($B_{\rm void} < 1$ nG, Trivedi, Subramanian & Seshadri 2014;Planck Collaboration XIX 2016), absence of evolution with redshift in Faraday rotation measures ($B_{\rm void} < 1.7$ nG, Pshirkov, Tinyakov & Urban 2016) , and the lack of secondary emission around blazar sources ($B_{\rm void} > 10^{-7}$ nG, Neronov & Vovk 2010; Alves Batista et al. 2017)[1]. Magnetohydrodynamical (MHD) cosmological simulations have been used to evolve magnetic fields of primordial or other origin that are

★ E-mail: stefan.hackstein@hs.uni-hamburg.de

[1] See however discussion in Broderick, Chang & Pfrommer (2012) for a different view of the issue.

amplified during structure formation and by additional dynamo processes (e.g. Dolag 2006; Ryu et al. 2012). These simulations produce models of cosmic magnetic fields (CMFs) that agree to some extent with observations (e.g. Dolag, Bartelmann & Lesch 1999; Brüggen et al. 2005; Donnert et al. 2009). All amplification scenarios have in common that they require a seed field, whose structure, strength, and origin is unknown.

In this paper, we probe the possibility to learn about the origin of CMFs using measurements of cosmic rays at ultra-high energies. Previous studies on similar topics mainly focused on properties of the Galactic magnetic field (Stanev 1997; Takami & Sato 2008) or small-scale anisotropies (Harari, Mollerach & Roulet 2002a; Yoshiguchi et al. 2003). Other works used unconstrained MHD models to study the implications of CMFs on ultra-high energy cosmic rays (UHECRs) astronomy (Sigl, Miniati & Ensslin 2003; Sigl, Miniati & Enßlin 2004; Sigl, Miniati & Ensslin 2004; Das et al. 2008; Kotera & Lemoine 2008; Hackstein et al. 2016). An overview of UHECR studies using MHD simulations can be found in Alves Batista et al. (2017). Analytical studies on the implication of CMFs on UHECR observations are provided in Harari, Mollerach & Roulet (2000), Harari et al. (2002a), Harari et al. (2002b), Tinyakov & Tkachev (2005), and Takami et al. (2012).

In previous work (Hackstein et al. 2016), we found strong variance in the observables of UHECRs induced by the position of, both, observer and sources (also cf. e.g. Sigl et al. 2004). To reduce this cosmic variance, it is necessary to use constrained MHD models that resemble the local Universe, as has been done by Dolag et al. (2004). They conclude that UHECR protons are reasonably deflected only when they cross galaxy clusters, though they assumed a rather weak field in voids of $\lesssim 10^{-11}$ G. Our new work expands the early work by Dolag et al. (2004) in a few ways: (a) we use the most recent set of initial conditions by Sorce et al. (2016), which were derived with more updated algorithms and observational constraints (see Sec. 2.1); (b) we relied on a different numerical method: i.e. the grid-MHD simulations with ENZO instead of smoothed-particle hydrodynamics simulations, which gives us a better sampling of moderate and low resolution regions; (c) we performed a survey of magnetic field models, rather than assuming a single specific scenario.

Data suggest that cosmic rays are fully ionized nuclei that constantly hit the Earth from outer space with energies that range over 11 orders of magnitude. At low energies ($<10^{17}$ eV), the predominant sources were found to be supernova remnants in our own Galaxy, where charged particles experience *Fermi* acceleration in magnetic shocks (e.g. Blasi 2013). UHECRs are less prone to the deflection in CMFs, thus they are not confined within their host galaxy and presumably are of extragalactic origin. The sources of UHECRs are currently unknown. If we assume the same acceleration process as at low energies, the size of the source limits the maximum energy of emitted UHECRs. This is the famous Hillas criterion (Hillas 1984) that limits the candidates for sources of UHECRs at $\gtrsim 10^{20}$ eV to very few objects, namely radio galaxy lobes, clusters of galaxies, active galactic nuclei, and gamma-ray bursts (e.g. Dova 2016). Recent works have reported signs of anisotropy in simulations with pure proton composition and limited source density in correlation with the LSS (di Matteo & Tinyakov 2017; Abreu et al. 2013), which are not observed in nature. They infer lower bounds on the density of sources of $\sim 10^{-4}$ Mpc^{-3}. Also, they conclude that the UHECR flux cannot be dominated by protons. In this work, we investigate the effect of different source distributions of UHECRs on the observed arrival directions.

This article is organized as follows: In Section 2, we present details on the simulation of the MHD models and of the propagation of UHECRs. The results of these simulations are then discussed in Section 3. Our conclusions are finally given in Section 4.

2 SIMULATION

2.1 Constrained initial conditions

Simulations that resemble the local Universe stem from particular initial conditions. Unlike typical initial conditions that abide solely by a cosmological prior, these initial conditions are additionally constrained by local observational data that can be either redshift surveys (Lavaux 2010; Heß, Kitaura & Gottlöber 2013) or radial peculiar velocities of galaxies (Kravtsov, Klypin & Hoffman 2002; Klypin et al. 2003; Sorce et al. 2014). We use the latter with a backward (by opposition to forward, Heß et al. 2013; Jasche & Wandelt 2013; Kitaura 2013; Wang et al. 2014) technique (Bertschinger 1987; Hoffman & Ribak 1991, 1992; Ganon & Hoffman 1993; van de Weygaert & Bertschinger 1996; Bistolas & Hoffman 1998; Lavaux et al. 2008). The catalogue of constraints is fully described in Tully et al. (2013) and the method to produce the constrained initial conditions is summarized in Sorce et al. (2016). The process involves various steps from the minimization of biases (Sorce 2015) in the catalogue of peculiar velocities to the constrained realization technique (Hoffman & Ribak 1991) to get the final product: the initial conditions. We work within the Planck cosmology framework (Ω_m=0.307, Ω_Λ=0.693, $h = 0.677$, $\sigma_8 = 0.829$, Planck Collaboration XVI 2014).

2.2 MHD-simulations

The MHD simulations performed in this paper have been produced with the cosmological grid code ENZO that follows the dynamics of dark matter with a particle-mesh N-body method and uses a variety of shock-capturing Riemann solvers to evolve the gas component (Bryan et al. 2014). The MHD equations were solved with the method by Dedner et al. (2002). To keep $\nabla \cdot \boldsymbol{B}$ as low as possible, it uses hyperbolic divergence cleaning. The fluxes at cell interfaces are reconstructed with the Piecewise Linear Method. They are evolved using the local Lax–Friedrichs Riemann solver (Kurganov & Tadmor 2000), with time integration using the total variation diminishing second-order Runge–Kutta scheme (Shu & Osher 1988). The set of simulations was run on Piz-Daint (CSCS) and made use of the recent implementation of the Dedner algorithm using CUDA (Wang, Abel & Kaehler 2010).

To model the local Universe at $z = 0$, the MHD simulations started at $z = 60$ with initial conditions described in Section 2.1. We sampled a volume of $(500\ \mathrm{Mpc}\, h^{-1})^3$, with 512^3 cells and dark matter particles. We use this large volume in order to remove effects from periodic boundary conditions in the constrained subregion of the MHD simulation. Since the initial perturbation for baryonic matter are not provided in the initial conditions of Section 2.1, we simply initialize baryons to the uniform cosmological density, assuming an initial zero-velocity field for baryons everywhere. Although more accurate ways to couple baryons to dark matter perturbations since the beginning are possible, this choice is irrelevant for the level of details we are concerned here (e.g. Vazza et al. 2011). Full resolution of the whole box is not necessary and costly, therefore only the constrained innermost $(200\ \mathrm{Mpc}\, h^{-1})^3$ volume was further refined by a factor 32 using adaptive-mesh refinement. The refinement here follows the standard local overdensity criterion, doubling the cell resolution whenever the local gas overdensity was three times larger than the surroundings, up to a maximum of five levels of

Table 1. List of magnetic field models investigated in this paper. First column: name of the model; second column: physical module for the gas component; third column: generation of magnetic field. All models were simulated within a volume of $(500\,\mathrm{Mpc}\,h^{-1})^3$. In CRPROPA , we used the innermost $(250\,\mathrm{Mpc}\,h^{-1})^3$ with 1024^3 data cells and a resolution of $245\,\mathrm{kpc}\,h^{-1}$.

Mnemonic	Gas physics	Magnetic field
B=0	non-radiative	$B_0 = 0$
primordial	non-radiative	$B_0 = 0.1$ nG
primordial2R	non-radiative	$(\langle B^2\rangle)^{0.5} = 1$ nG, $n_B = -3$
primordial3R	non-radiative	$(\langle B^2\rangle)^{0.5} = 1$ nG, $n_B = -4$
astrophysical	cooling and AGN feedback	$5 \cdot 10^{58}$ erg, $z < 4$; $B_0 = 10^{-11}$ nG
astrophysicalR	cooling and AGN feedback	10^{60} erg, $z < 4$; $B_0 = 10^{-11}$ nG
astrophysical1R	cooling and AGN feedback	10^{60} erg to $5 \cdot 10^{58}$ erg, $z < 1$; $B_0 = 10^{-11}$ nG

refinement ($\approx$31 kpc h^{-1} per cell). The clusters that form in this volume closely resemble real local structures (e.g. the Centaurus, Virgo, Coma and Perseus clusters), within typical offsets of order $\leq$2–3 Mpc h^{-1} which are however not crucial for the global studies we perform here.

The limited size of computer memory used for the simulation of UHECR propagation did not allow us to use the full volume of the CMF models obtained from MHD simulations. In order to minimize effects from periodic boundaries (see Section 2.3), we restricted the simulations in CRPROPA to the innermost $(250\,\mathrm{Mpc}\,h^{-1})^3$ volume and reduced the number of cells inside that volume to 1024^3. The resulting resolution is then 245 kpc h^{-1}.

The use of constrained simulations of the local Universe is an important step forward compared to our previous work (Hackstein et al. 2016), where we found a large variance in the observed properties of UHECRs from observer to observer. Given the strong impact of $\leq$35 Mpc h^{-1} sources of UHECRs, it is not guaranteed that the average over many observers is representative of what can be observed by the specific observer at Earth's location. However, in these new runs placing our observer within the Local Group allows us to remove these uncertainties. At distances $>100\,\mathrm{Mpc}\,h^{-1}$, deflection and the increasing number of sources provide an UHECR flux almost independent of the exact position of distant sources. It is therefore sufficient to model the source distribution only within that distance.

Following a procedure similar to Hackstein et al. (2016), we ran several MHD simulations with different scenarios for the origin of CMFs. In the *primordial* model, we used a uniform initial magnetic field of strength 0.1 nG (comoving) along each axis at $z = 60$. In the *primordial2R* and *primordial3R* models, similar fields were generated by drawing the magnetic field from an analytically generated power-law distribution of magnetic fields, with two different slopes for the power spectrum, $n_B = -3$ and -4, respectively (with $P_B \propto k^{n_B}$), see Planck Collaboration XIX (2016) for details. We have generated a power-law spectrum distribution of the vector potential in the Fourier space for a 1024^3 grid, randomly drawn from the Rayleigh distribution, and we have computed the magnetic field in real space as $\vec{B} = \nabla \times A$, ensuring $\nabla \cdot \vec{B} = 0$ by construction. We have assumed that the maximum coherence scale of the magnetic field is 500 Mpc h^{-1} and that the minimum scale is the root grid resolution, and that the power-law of fluctuations follows the input P_B power spectrum, similar to Bonafede et al. (2013). In both cases, the normalization of the spectrum of initial fluctuations is chosen such that $(\langle B^2\rangle)^{0.5} = B_0$, i.e. the rms magnetic field is equivalent to the uniform seeding case.

The astrophysical origin of CMFs was modelled as impulsive thermal and magnetic feedback in haloes where the physical gas number density exceeded a critical value of 10^{-2} cm^{-3}. The thermal energy is released as a couple of overpressurized outflows at random opposite directions from the halo centre. The feedback magnetic energy, assumed to be 50 per cent of the injected thermal energy, is released as dipoles around the centre.

In the *astrophysical* model, we assumed a release of 5×10^{58} erg per feedback episode starting from $z = 4$; in the *astrophysicalR* model, we used instead a larger budget of 10^{60} erg per event. Finally, in the *astrophysical1R* model, we considered a mixed scenario, where we changed the energy budget from 10^{60} to 5×10^{58} erg per event from $z = 1$ to 0.

All runs with astrophysical scenarios for the emergence of extragalactic magnetic fields used equilibrium radiative gas cooling, assuming a fixed metallicity of $Z = 0.3\,Z_\odot$. While the cooling is necessary to trigger the onset of cooling flows and start the cooling-feedback cycle in our haloes, the large-scale distribution of gas matter outside simulated haloes is similar across all runs (see Section 3.1).

In all astrophysical runs, we impose a uniform lower magnetic field level of $B_0 = 10^{-20}$G comoving at $z = 60$. This extremely low magnetization prevents the formation of spurious numerical effects at the boundary between magnetized and unmagnetized regions in the simulation (in contrast to the primordial models, where there is a non-zero magnetic field everywhere). An overview of the models is given in Table 1.

2.3 UHECR simulations

The resulting CMF models used in CRPROPA have a volume of $(250\,\mathrm{Mpc}\,h^{-1})^3$, discretized by 1024^3 cells of $(244\,\mathrm{kpc}\,h^{-1})^3$ volume that contain a uniform field. These models are used to simulate the propagation of UHECRs in the local Universe in order to search for different signatures in the UHECR arrival directions. This is done with CRPROPA 3.0[2] (Armengaud et al. 2007; Kampert et al. 2013; Batista et al. 2016), a publicly available code to study the propagation of UHECRs. CRPROPA computes all the relevant processes of propagation, this includes Lorentz deflection, energy loss by production of particles and cosmic expansion, photo disintegration and nuclear decay. The code further allows us to track the trajectories of particles in a 3D volume.

We let CRPROPA inject 10^8 protons with random momentum from random positions. The initial energies range from 1 to 10^3 EeV, following a power spectrum of E^{-1}. This choice does not result in the energy spectrum observed in nature, but was used in order to increase number statistics at the highest energies.[3]

[2] https://crpropa.desy.de

[3] A steeper injection spectrum would result in too low accuracy of the measurement of anisotropy around 100 EeV, as can be seen by Eq. 1.

Table 2. List of the injection models. First column: name of model; second column: set of sources; third column: box length of the simulated volume; fourth column: number of sources in the simulated volume; fifth column: number density of sources.

Mnemonic	Injection scenario	$L_{\rm box}$	$N_{\rm sources}$	$n_{\rm sources}$
		(Mpc h^{-1})		(Mpc$^{-3}h^3$)
homogeneous	random positions	250	10^8	6,4
density	same as *homogeneous* with $p.d.f. = \rho_{\rm gas} / \sum \rho_{\rm gas}$	250	10^8	6,4
mass halo	virial haloes, uniform luminosity	250	2672	$1.71 \cdot 10^{-4}$

After injection, the energy loss and trajectories of the particles are calculated. In case a trajectory leaves the volume, it is continued on the opposite side. An event is recorded when a trajectory intersects with the observer. This observer is represented by a sphere of radius 800 kpc in the centre of the simulation, which is the defined position of the observer in a constrained simulation. For a discussion on the role of the finite observer size in CRPROPA simulations, we refer the reader to Hackstein et al. (2016).

After intersection, trajectories continue so they may reach another replica of the observer. Environments with strong magnetic fields can trap particles so they arrive at the same observer again. If the same particle is recorded multiple times at the same observer, we randomly chose one of these events. This choice excludes overcounting of trapped particles and no further weighting is necessary.

In a different set of runs, we repeat the process with 10^7 iron nuclei, taking care also of nuclear decay and disintegration processes, and follow the trajectories of secondary nuclei.

In order to investigate the influence of the distribution of sources, we tested different source models for UHECRs in all the CMF models listed above. In order to bracket the present uncertainties on the degree of isotropy in the distribution of sources, we analyse the extreme case of a *homogeneous* model, in which we inject each particle at a random position anywhere in the simulated volume. This mimics the absence of structure in the distribution of sources and shows the impact of source distribution in comparison to the other models.

It is generally assumed that sources of UHECRs are powerful sources located in galaxies. Therefore, we assume that the distribution of sources correlates with the LSS. In the *density* model, particles are injected at random positions with a probability density function identical to the gas density, re-normalized by the total gas density in the volume, $p.d.f. = \rho_{\rm gas}/\sum \rho_{\rm gas}$. This model with maximum source density reflects a huge number of transient sources that may be found in all types of galaxies, such as gamma-ray bursts or magnetars.

Finally, the *mass halo* model agrees with the lower bounds on source density ($\sim 10^{-4}$ Mpc^{-3}, Abreu et al. 2013), where we take as sources the centres of 2672 virial haloes identified in our simulation, each with the same luminosity of UHECRs. This model mimics the case of very few stationary sources, e.g. radio galaxies or active galactic nuclei (AGNs). The precision of the MHD-simulations did not allow us to resolve these structures individually. An overview of the source models can be found in Table 2.

3 RESULTS

3.1 Simulated extragalactic magnetic fields

Fig. 1 shows the maps of projected gas density (top) and of mean magnetic field along the line of sight (centre, bottom) for the *primordial2R* run (left-hand panels) and for the *astrophysicalR* run (right-hand panels) at $z = 0$. Although the different implementations for gas physics do not significantly change the distribution of gas matter on large scales, the differences in the assumed magnetogenesis scenarios affect the morphological distribution and strength of extragalactic magnetic fields.

In Fig. 2, we present the volume filling factor of the models listed in Table 1. All models have magnetic fields in cluster regions that agree with observational limits. The different *primordial* models show very similar filling factors with dominant strength at $\sim$0.1 nG, close to the upper limit on magnetic field strength in voids from analysis of the CMB anisotropy (Trivedi et al. 2014; Planck Collaboration XIX 2016).

The strong fields in the *astrophysical* models are concentrated in the dense regions of the simulation, which are predominantly filled with very weak fields, at odds with lower limits inferred from the lack of secondary emission around blazar sources (Neronov & Vovk 2010). The filling factors of the *astrophysicalR* and *astrophysical1R* models are almost identical, only in the *astrophysical* model an even smaller volume contains strong fields. Due to the later seeding of magnetic field in all of the astrophysical models, as compared to the primordial models, more of the original, oriented field components survive until $z = 0$ and thus a greater influence on the propagation of UHECRs is expected.

3.2 Energy spectrum

In Fig. 3, we show the energy spectrum of UHECRs as injected at the sources and measured by the observer. For clarity, the graphs are renormalized by the total number of observed events N and multiplied by the inverted energy spectrum at injection, which was set to be E^{-1}. Below 100 EeV, the energy spectrum is universal, as predicted by the propagation theorem (Aloisio & Berezinsky 2004). In particular, we find no influence of the underlying magnetic field on the observed energy spectrum, as has been shown in Hackstein et al. (2016).

In the proton injection scenarios, the total number of observed events is $N = 50\,000$ with 15 000 events above 10 EeV. In the iron injection scenarios, $N = 100\,000$ with 5 000 events above 10 EeV. The fluctuation of these numbers between scenarios with the same initial composition is about 10 per cent. Therefore, number statistics of the observables presented in Sections 3.3 and 3.4 are comparable.

In the proton injection scenarios, the slope above the Greisen–Zatsepin–Kuzmin (GZK) cut-off is not universal but shows significant variation in different source models. We show, both, the Poisson shot-noise as well as the standard deviation for different magnetic field models. They are almost identical, i.e. the error is dominated by statistical fluctuations. Magnetic fields leave no significant impact, as expected for quasi-rectilinear propagation.

The spectrum at $\sim$100 EeV is significantly harder in the *mass halo* injection model, where there is an above-average amount of sources within a few Mpc of the observer. Furthermore, in the *homogeneous* and *mass halo* injection models, protons with up to 800 EeV arrive at the observer in all magnetic field models. However, in the *density*

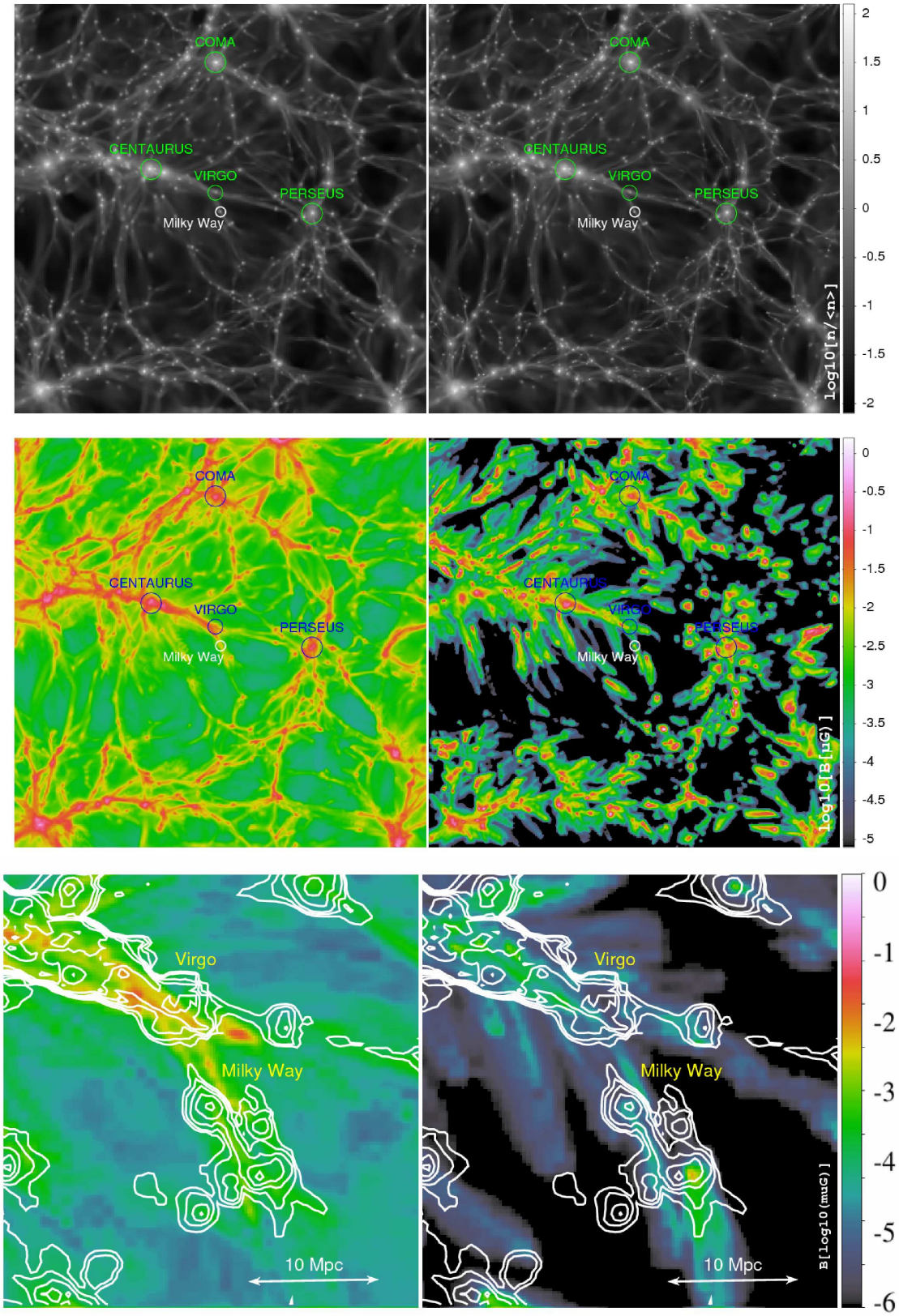

Figure 1. Maps of projected gas number density (top) and mean magnetic field along the line of sight (centre, bottom) for the *primordial2R* model (left-hand panel) and for the *astrophysicalR* model (right-hand panel) at $z = 0$. The gas number density n is normalized to the average density in the whole volume, $n/\langle n \rangle$. The magnetic field is shown in μG. Colours are in logarithmic scale. The top and centre panels have a side-length of 200 Mpc h^{-1}, the projection axes are the X and Y in the supergalactic coordinates. The bottom panels give a more detailed view on the central 40 Mpc h^{-1}. The position of the Milky Way observer considered in this work is exactly at the centre of the box, indicated by a white circle in the top and centre panels. The additional circles show the location of the simulated counterparts of real objects in the local Universe.

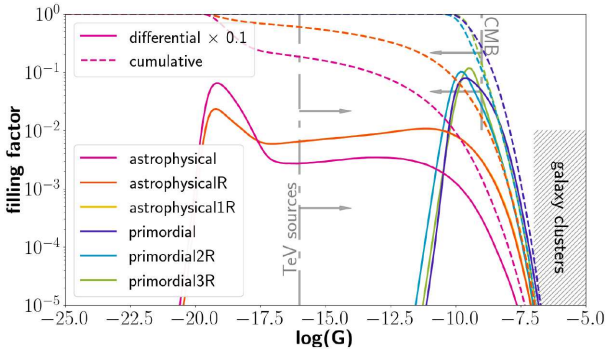

Figure 2. Volume filling factor of the models listed in Table 1. The solid lines show the differential filling factor renormalized by 0.1 for clarity, dashed lines show the cumulative filling factor. The grey arrows and shaded area indicate the limits given from observations as listed in the introduction. The yellow line of the *astrophysical1R* model fits exactly with the *astrophysicalR* model.

injection senario, there are no particles received above 400 EeV. The closer the nearby sources, the higher the number of events that are observed at the most extreme energies and the higher the maximum energy of observed events.

Most particles injected in the simulation never reach the observer and are lost. The injected spectrum plotted in Fig. 3 only shows the injected energies of particles received by the observer. In the proton case, the injected spectrum of observed particles perfectly recreates the injection spectrum used for simulation. In the iron case, multiple secondary nuclei of the same nucleus can reach the observer. In the injected energy spectrum, the primary nucleus is counted once for every secondary nucleus that is observed. This double counting accounts for the sharp increase in the injected spectrum above 40 EeV. At low energies, $\gtrsim$1 EeV, the injected spectrum is slightly decreased in the stronger magnetic field models. Iron nuclei at low energy are deflected more strongly and are more likely to lose their energy before they reach the observer.

The slope of the observed spectrum is much steeper than in the proton case. The low energies are dominated by the secondary protons of iron injected at the highest energies. Only few events are observed with energies >100 EeV. This is because most of heavy nuclei at those energies disintegrate completely within a few Mpc and distribute their energy evenly among their secondary protons (Epele & Roulet 1998; Allard 2012). Thus, too few events are observed in the iron injection case to measure deviation from isotropy. In conclusion, a sharp cut-off, as observed by extensive air shower arrays (Ivanov 2010; Letessier-Selvon 2014), would hint at a low number of nearby sources or a maximum acceleration energy of protons at the sources that is below the cut-off.

3.3 Angular power spectrum

To compute the angular power C_l presented in this section, we first produce full-sky maps of the arrival directions of UHECR events for different minimum energies of considered particles.[4] These maps are then decomposed into spherical harmonics $\Phi(n) = \sum a_{lm} Y_{lm}(n)$ and C_l is calculated from the obtained amplitudes, $C_l = (2l+1)^{-1} \sum |a_{lm}|^2$ (cf. Tinyakov & Urban 2015). Finally, the whole spectrum is normalized by the monopole moment, which is 4π times the square of the average flux.

We present the dipole and quadrupole moment of the angular power spectrum C_l of UHECR arrival directions. These moments were shown to be most promising in the search for anisotropy signals (di Matteo & Tinyakov 2017), but the general trends reported in this section also apply to the octopole moment.

The isotropic prediction is obtained analytically for an isotropic full-sky with N events (Campbell 2015). The mean value of the angular power

$$C_l = 4\pi/N \tag{1}$$

and the general sample deviation

$$\sigma = \sqrt{\frac{2}{2l+1}} C_l \,, \tag{2}$$

which shows the variation for realizations of a Gaussian random process. For an isotropic sky, both, C_l and σ, scale with $1/N$. The logarithmic deviation stays constant. In order to account for fluctuation in C_l, we show σ as error bars for every graph.

Since the value and fluctuation of C_l in an isotropic sky of finite counts are determined by the number of events and our simulations do not reproduce the spectrum observed in nature (cf. Section 3.2), we need to compare to predictions for the simulated spectrum that depends on the injected composition. We indicate with shaded regions the confidence level of anisotropy (C. L. anisotropy). This is obtained from the isotropic prediction and 1, 2, and 3σ sample deviation, equations (1) and (2). The number of particles N used to calculate the isotropic prediction is the average N observed in each energy bin. The fluctuation of N is about 10 per cent for same injection composition, so the C. L. anisotropy is roughly the same for all models.

In addition to the simulations with magnetic field in all plots, we also present a simulation where the magnetic field is globally set to zero, *B=0* (black line).[5] This simulation is shown in order to unambiguously determine the cases where the magnetic field model is important.

We further show the prediction given by a baseline homogeneous model (thick grey line). It shows the average and 1σ standard deviation of a test group of 27 realizations of a scenario with *homogeneous* injection in the absence of magnetic fields, $B = 0$. These fully homogeneous scenarios produce the most isotropic results possible in our simulation. The result is not fully isotropic, since it entails all artefacts intrinsic in the simulation, e.g. finite observer effect, overcount of secondary nuclei, and assumed periodicity of the magnetic field and sources (for a detailed discussion see Armengaud, Sigl & Miniati 2005; Hackstein et al. 2016). This makes the homogeneous baseline model a suitable test to find the qualitative contribution of sources and magnetic fields.

The proton injection scenarios are shown in Fig. 4. The prediction from the homogeneous baseline model obtained by the procedure explained above is almost identical to the isotropic prediction. At energies below the GZK-limit of ~40 EeV, the quadrupole angular power is in good agreement with the isotropic prediction for the *homogeneous* and *density* injection models presented in the top two panels. In the *mass halo* injection model, the angular power is above 95 per cent C. L. anisotropy at all energies in virtually all

[4] Due to the hard injection spectrum used in our simulations, the full-sky maps contain too many events at high energies. However, since the observed spectra, in general, are steeper than E^{-1}, this effect is negligible.

[5] except for the *homogeneous* plot, where it is given by the homogeneous prediction.

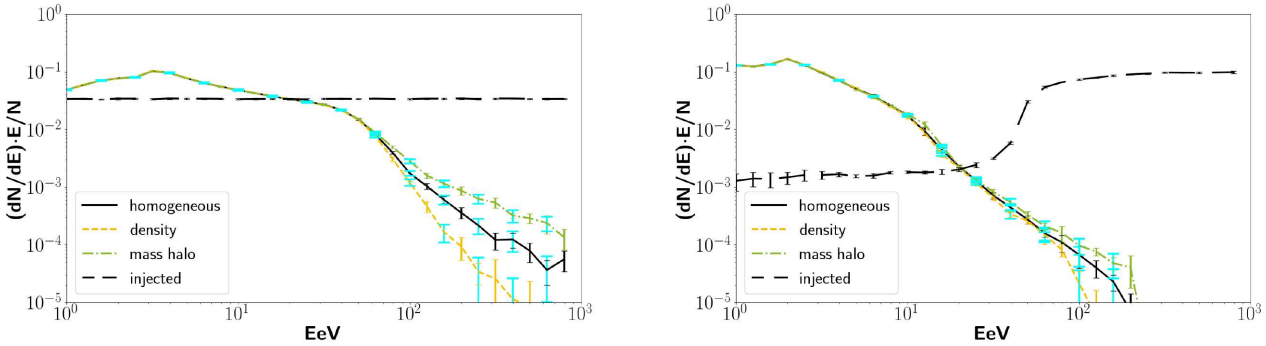

Figure 3. Energy spectrum of UHECRs as injected at the sources (dashed lines) and measured by the observer for a pure proton and a pure iron injected composition (left- and right-hand panels, respectively). The colours and line styles indicate the injection models listed in Table 2. The graphs show the average over all magnetic field models, the standard deviation is indicated by the narrow error bars. The big cyan error bars show the Poisson noise at each second data point. For clarity, the graphs are multiplied by the inverted energy spectrum at injection E, and renormalized with the total number of particles N.

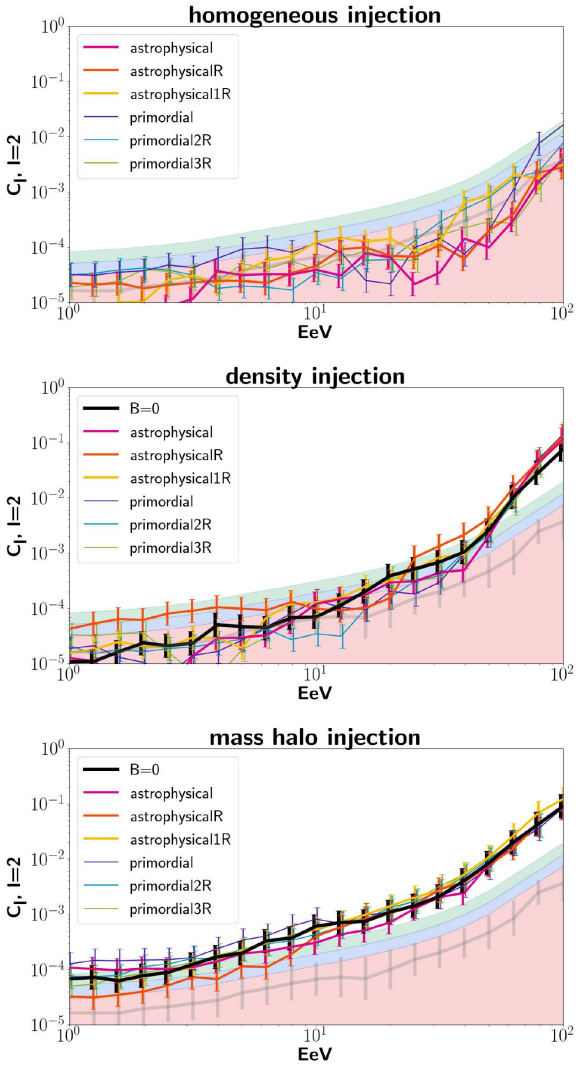

Figure 4. Angular power C_l of the quadrupole $l = 2$ for all models listed in Table 1 in a pure proton injection scenario. The errorbars indicate sample deviation given by equation (2). From the top to bottom, the panels show the cases of *homogeneous* , *density* , and *mass halo* injection listed in Table 2. The thick grey line is the average and 1σ standard deviation of the baseline homogeneous model. The shaded regions indicate the 68 per cent, 95 per cent, and 99 per cent C. L. of anisotropy.

of the models. This is in agreement with results from di Matteo & Tinyakov (2017) and Abreu et al. (2013) that show that UHECRs cannot predominantly be protons from few sources in the LSS and that an anisotropic signal should have already been measured for source densities $\lesssim 10^{-4}$ Mpc^{-3}.

The magnetic field models do not significantly change the angular power spectrum of arrival directions of UHECR protons at all energies. At very high energies, ∼100 EeV, the variation in the coefficients, C_l, between the magnetic field models is the lowest, though the number of protons and thus the accuracy is the lowest. The *density* and *mass halo* injection models show a strong deviation from isotropy, whereas the *homogeneous* injection is in good agreement with the prediction from isotropy. The error bars indicate that this feature is not an effect of sample variance, but is statistically significant. This shows that the distribution of nearby sources imposes on the observer an anisotropic signal of UHECRs right below the energy cut-off, where propagation of UHECRs is believed to be quasi-rectilinear. This anisotropic signal can be used to identify the sources of UHECRs.

In the iron injection scenario shown in Fig. 5, almost all models have significantly higher values of C_l below 20 EeV than expected in an isotropic distribution. This energy coincides with $E_{\rm max}/A_{\rm Fe}$, the maximum energy of injected particles $E_{\rm max} = 1000$ EeV divided by the mass number of iron $A_{\rm Fe} = 56$. The predictions from the homogeneous baseline model and the *B=0* model generally show the highest values. Anisotropy occurs, independent of the source model, due to complete disintegration of heavy nuclei over very short length scales after they have been injected nearby at the highest energies. Due to the high Lorentz-factor, in the absence of deflection, the arrival directions of these secondary nuclei are almost identical, causing an excess of events in direction of the most nearby injection positions (cf. e.g. Lemoine & Waxman 2009). We see that the stronger *primordial* models, in general, show lower C_l values than the weaker *astrophysical* models. The anisotropy produced by the procedure explained above is lowered by CMFs. Since the anisotropy is predominantly produced by nearby sources, only the local field (up to 10 × distance to closest source, Dundović & Sigl 2017) is responsible for this effect. This is in agreement with Sigl et al. (2004), who infer that strong magnetic fields around the observer can suppress large-scale anisotropy.

At the highest energies, ∼ 100 EeV, the number of observed events is too low in the iron injection case to measure the deviation from isotropy.

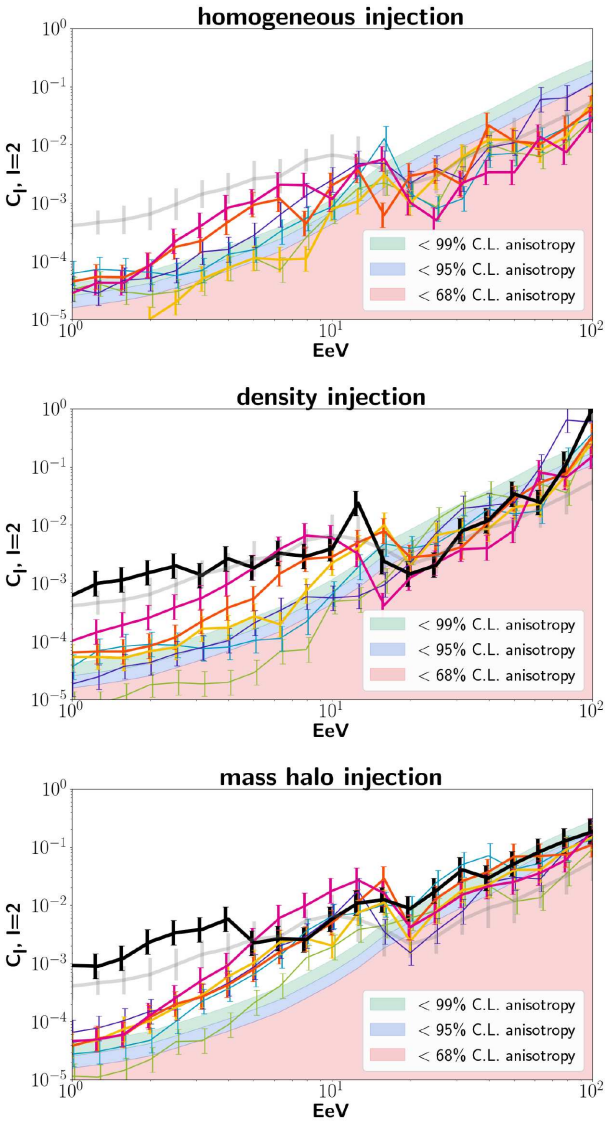

Figure 5. Same as Fig. 4, in a pure iron injection scenario.

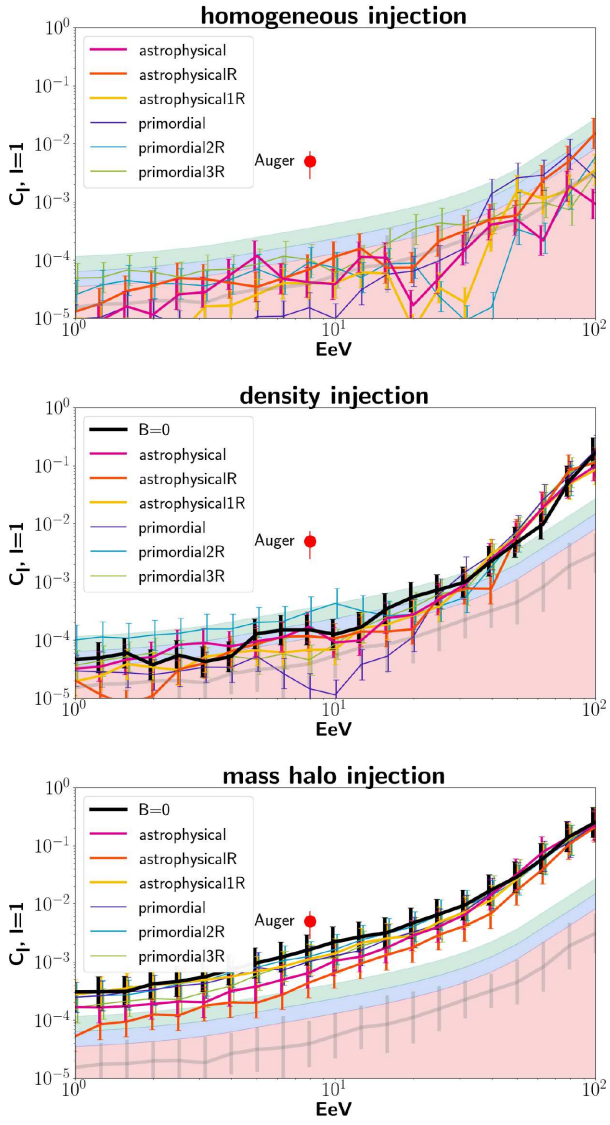

Figure 6. Angular power C_l of the dipole $l = 1$ for all models listed in Table 1 in a pure proton injection scenario. The errorbars indicate sample deviation given by equation (2). From the top to bottom, the panels show the cases of *homogeneous* , *density* , and *mass halo* injection listed in Table 2. The thick grey line is the average and 1σ standard deviation of the baseline homogeneous model. The shaded regions indicate the 68 per cent, 95 per cent, and 99 per cent C. L. of anisotropy. The red point corresponds to the amplitude of the recent dipole signal reported by Auger.

During the review process of this manuscript, the Pierre Auger Collaboration reported a significant dipole in the arrival directions of UHECRs with energies >8 EeV at a 5.2σ level of significance with an amplitude of 6.5 per cent (The Pierre Auger Collaboration et al. 2017) or $C_1 = 0.0050 \pm 0.0025$ in terms of the angular dipole power (Aab et al. 2017). In Figs 6 and 7, we present the dipole moment $l = 1$ of the angular power C_l in our simulations and also indicate the recent observation. The features in these graphs are basically the same as discussed for the quadrupole.

Note that the number of particles above 8 EeV in our simulations is different from the amount of particles considered in The Pierre Auger Collaboration et al. (2017). While result is calculated for $\gtrsim$32.000 events >8 EeV, our simulations have only about ∼17.000 and ∼6.000 events in the proton and iron runs, respectively. Hence, results of our simulations are of lower statistical significance. However, the energy spectra in our simulations are much harder than observed by the Pierre Auger Collaboration, and therefore anisotropic signal from source distribution are expected to be more dominant.

None of the models explored in this paper can reproduce the signal observed in nature with pure proton injection (Fig. 6). Only for the *mass halo* model there is a small overlap of 1σ deviations with the Auger measurement. The level of anisotropy does not decrease strongly from 8 to 4 EeV. This indicates that a strong dipole in the distribution of nearby sources is necessary to reproduce the Auger signal with a light injection composition. In that scenario, the dipole angular power C_1 increases at most linear with energy between 1 and 10 EeV in our simulations. The amplitude is proportional to the square root of C_1 and increases too slow compared to observations by the Pierre Auger Observatory. This makes a light injection composition of UHECRs at the highest energies unlikely in view of the recent observation.

Injection of iron nuclei, Fig. 7, results in a dipole similar to that observed by Auger – in amplitude, not in significance. Further, C_1 increases roughly quadratical for heavy injection composition

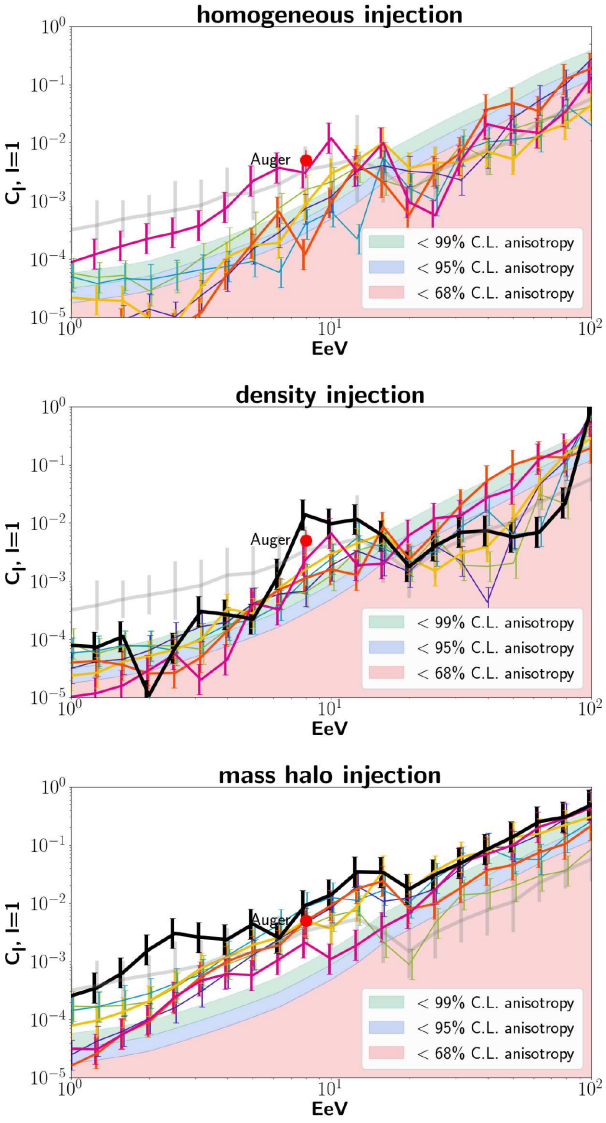

Figure 7. Same as Fig. 6, in a pure iron injection scenario.

and compares better to results of Pierre Auger Collaboration. In the *homogeneous* model, magnetic fields can suppress the signal to agree with the isotropic prediction. In the *density* and *mass halo* model, the anisotropic signal is dominated by the distribution of sources and not suppressed efficiently by magnetic fields.

Our results suggest that the dipole signal in UHECRs observed by the Pierre Auger Observatory may be the product of clustering of secondary nuclei in direction of the nearby sources.

3.4 Composition

In Fig. 8, we show the average mass number $\langle A \rangle$ of observed events as function of energy in the iron injection scenarios. At low energies, the composition is very light since secondary protons of injected iron nuclei dominate observations. At $\lesssim 20$ EeV $\approx E_{\rm max}/Z_{\rm Fe}$, there is a steep increase in $\langle A \rangle$. This coincides with the maximum energy of secondary protons. At higher energies, only the (partly disintegrated) primary nuclei are observed. All magnetic field and injection models show a very similar slope of $\langle A \rangle$. We conclude that CMFs in agreement with observational upper limits, in general, are too weak

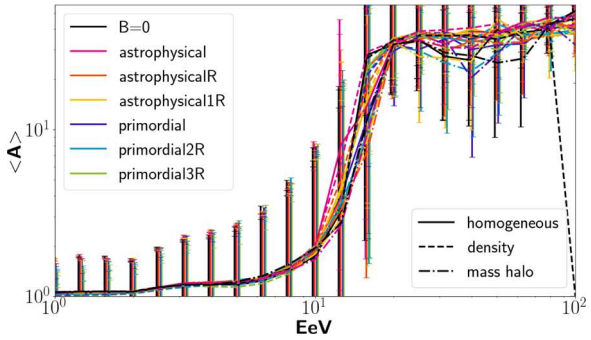

Figure 8. Average mass number $\langle A \rangle$ of UHECRs observed at different energies. The errorbars show the 1σ standard deviation. The colours indicate the magnetic field model listed in Table 1 and the linestyle shows the source model listed in Table 2.

to impose a significant difference in the all-sky average composition of UHECRs.

4 CONCLUSIONS

We have studied the influence of CMFs on the propagation of UHECRs using MHD-simulations with different models for seeding of magnetic fields for both, primordial and astrophysical, processes. We found no evidence that magnetic field seeding scenarios could be distinguished via the use of the angular power spectrum of the spherical harmonics decomposition of the full-sky of arrival directions of UHECRs.

We have studied the influence of different source scenarios on the energy spectrum of UHECRs and on the angular power of anisotropy. We have found that for a pure proton composition, the slope of the energy spectrum at energies >100 EeV depends on the number of, and distance to, the most nearby sources. The closer the sources, the harder the energy spectrum. If only iron is injected, almost no events are observed above that energy. Thus, the sharp energy cut-off observed with extensive air shower arrays (Ivanov 2010; Letessier-Selvon 2014) might suggest a low number of sources in the near vicinity of the observer if the cut-off does not coincide with the maximum energy of proton acceleration.

We have investigated the angular power spectrum of arrival directions. We have found that there is a clear deviation from isotropy, $\lesssim$100 EeV, if the distribution of sources follows the LSS. This offers the chance to identify the sources with future full-sky measurements (Dawson, Fukushima & Sokolsky 2017) and high number statistics at the highest energies.

We were able to reproduce the dipole in the arrival directions of UHECRs >8 EeV recently reported by the Pierre Auger Collaboration (The Pierre Auger Collaboration et al. 2017) with all our source models, but only using pure iron injection composition instead of protons. Our results indicate that the observed dipole is the result of clustering in direction of nearby sources of heavy nuclei (Lemoine & Waxman 2009). Strong magnetic fields might be necessary to explain the absence of anisotropy signal in the higher multipoles. Exploring such possibilities (also joined with a more thorough exploration of the role of UHECRs composition in the production of a dipole excess) will be subject of forthcoming work.

For the injection of protons from the virial haloes with a very low number density, around the limit from Abreu et al. (2013, $\sim 10^{-4}$ Mpc^{-3}), we have found 95 per cent C. L. quadrupolar anisotropy at all energies, in conflict with present observations (Pierre Auger Collaboration 2012; Aab et al. 2014). This confirms

the findings of di Matteo & Tinyakov (2017) that UHECRs cannot primarily be protons from few sources in the LSS.

Finally, we have analysed the observed composition of UHECRs via the average mass number of events. There is no evidence that CMFs significantly influence the all-sky composition of UHECRs at all energies.

In our study, we did not account for the influence of the magnetic field of the Milky Way, but energy losses are negligible on galactic scales. Furthermore, the angular power spectrum at large scales has been shown to have low impact of deflections in the Galactic magnetic field (Tinyakov & Urban 2015; di Matteo & Tinyakov 2017).

In summary, with newer constrained simulations of the local Universe, we confirmed our previous findings (Hackstein et al. 2016), i.e. that the properties of observed UHECRs do not seem to carry much information on the genesis and distribution of extragalactic magnetic fields. This in turn strengthens the possibility of performing 'UHECRs astronomy' (Dolag et al. 2004), thus motivating further investigations on the origin of UHECRs across a wide range of energies where the impact of the Galactic magnetic field should be sub-dominant.

ACKNOWLEDGEMENTS

Computations described in this work were performed using the ENZO code (http://enzo-project.org), which is the product of a collaborative effort of scientists at many universities and national laboratories. The constrained initial conditions have been developed in the context of the Constrained Local UniversE Simulations (CLUES) project (https://www.clues-project.org/). FV acknowledges financial support from the European Union's Horizon 2020 research and innovation programme under the Marie-Sklodowska-Curie grant agreement no. 664931 and the ERC STarting Grant MAGCOW, no. 714196. JGS acknowledges support from the Astronomy ESFRI and Research Infrastructure Cluster ASTERICS project, funded by the European Commission under the Horizon 2020 Programme (GA 653477). We acknowledge the usage of computational resources on the JURECA cluster at the at the Juelich Supercomputing Centre (JSC), under projects no. 10755, 11823, 9016 and 8998, and on the Piz-Daint supercluster at CSCS-ETHZ (Lugano, Switzerland) under project s701. SH, FV, and MB additionally thank G. Sigl and A. Dundovic for fruitful discussion as well as the other developers of CRPROPA for making the code public. We further acknowledge the use of computational resources at the Rechenzentrum of the University of Hamburg. The whole group would also like to thank the referee for fruitful comments and careful reading of the manuscript. We also thank S. Mollerach for adjuvent comments and discussion on the manuscript.

REFERENCES

Aab A. et al., 2014, ApJ, 794, 172
Aab A. et al., 2017, J. Cosmol. Astropart. Phys., 6, 026
Abreu P. et al., 2013, J. Cosmol. Astropart. Phys., 1305, 009
Allard D., 2012, Astropart. Phys., 39, 33
Aloisio R., Berezinsky V., 2004, ApJ, 612, 900
Alves Batista R., Shin M.-S., Devriendt J., Semikoz D., Sigl G., 2017, Phys. Rev. D, 96, 023010
Araya-Melo P. A., Aragón-Calvo M. A., Brüggen M., Hoeft M., 2012, MNRAS, 423, 2325
Armengaud E., Sigl G., Miniati F., 2005, Phys. Rev., D, 72, 043009
Armengaud E., Sigl G., Beau T., Miniati F., 2007, Astropart. Phys., 28, 463
Batista R. A. et al., 2016, J. Cosmol. Astropart. Phys., 2016, 038
Beck R., 2016, A&AR, 24, 4
Bernet M. L., Miniati F., Lilly S. J., 2013, ApJ, 772, L28
Bertschinger E., 1987, ApJ, 323, L103
Bistolas V., Hoffman Y., 1998, ApJ, 492, 439
Blasi P., 2013, A&AR, 21, 70
Bonafede A., Vazza F., Brüggen M., Murgia M., Govoni F., Feretti L., Giovannini G., Ogrean G., 2013, MNRAS, 433, 3208
Broderick A. E., Chang P., Pfrommer C., 2012, ApJ, 752, 22
Brown S. D., 2011, J. Astrophys. Astron., 32, 577
Brown S. et al., 2017, MNRAS, 468, 4246
Brüggen M., Ruszkowski M., Simionescu A., Hoeft M., Dalla Vecchia C., 2005, ApJ, 631, L21
Bryan G. L. et al., 2014, ApJS, 211, 19
Campbell S. S., 2015, MNRAS, 448, 2854
Das S., Kang H., Ryu D., Cho J., 2008, ApJ, 682, 29
Dawson B. R., Fukushima M., Sokolsky P., 2017, preprint (arXiv:1703.07897)
Dedner A., Kemm F., Kröner D., Munz C.-D., Schnitzer T., Wesenberg M., 2002, J. Comput. Phys., 175, 645
di Matteo A., Tinyakov P., 2017, MNRAS, preprint (arXiv:1706.02534)
Dolag K., 2006, Astron. Nachr., 327, 575
Dolag K. M., Bartelmann M., Lesch H., 1999, A&A, 348, 351
Dolag K., Grasso D., Springel V., Tkachev I., 2004, J. Exp. Theor. Phys. Lett., 79, 583
Donnert J., Dolag K., Lesch H., Muller E., 2009, MNRAS, 392, 1008
Dova M. T., 2016, preprint (arXiv:1604.07584)
Dundović A., Sigl G., 2017, preprint (arXiv:1710.05517)
Epele L. N., Roulet E., 1998, J. High Energy Phys., 10, 009
Feretti L., Giovannini G., Govoni F., Murgia M., 2012, A&AR, 20, 54
Ganon G., Hoffman Y., 1993, ApJ, 415, L5
Hackstein S., Vazza F., Brüggen M., Sigl G., Dundovic A., 2016, MNRAS, 462, 3660
Harari D., Mollerach S., Roulet E., 2000, J. High Energy Phys., 02, 035
Harari D., Mollerach S., Roulet E., 2002a, J. High Energy Phys., 7, 006
Harari D., Mollerach S., Roulet E., Sánchez F., 2002b, J. High Energy Phys., 3, 045
Heß S., Kitaura F.-S., Gottlöber S., 2013, MNRAS, 435, 2065
Hillas A. M., 1984, Annu. Rev. Astron. Astrophys., 22, 425
Hoffman Y., Ribak E., 1991, ApJ, 380, L5
Hoffman Y., Ribak E., 1992, ApJ, 384, 448
Ivanov A. A., 2010, ApJ, 712, 746
Jasche J., Wandelt B. D., 2013, MNRAS, 432, 894
Kampert K.-H., Kulbartz J., Maccione L., Nierstenhoefer N., Schiffer P., Sigl G., van Vliet A. R., 2013, Astropart. Phys., 42, 41
Kim K. S., Lilly S. J., Miniati F., Bernet M. L., Beck R., O'Sullivan S. P., Gaensler B. M., 2016, ApJ, 829, 133
Kitaura F.-S., 2013, MNRAS, 429, L84
Klypin A., Hoffman Y., Kravtsov A. V., Gottlöber S., 2003, ApJ, 596, 19
Kotera K., Lemoine M., 2008, Phys. Rev., D, 77, 023005
Kravtsov A. V., Klypin A., Hoffman Y., 2002, ApJ, 571, 563
Kurganov A., Tadmor E., 2000, J. Comput. Phys., 160, 241
Lavaux G., 2010, MNRAS, 406, 1007
Lavaux G., Mohayaee R., Colombi S., Tully R. B., Bernardeau F., Silk J., 2008, MNRAS, 383, 1292
Lemoine M., Waxman E., 2009, J. Cosmol. Astropart. Phys., 11, 009
Letessier-Selvon A., 2014, Braz. J. Phys., 44, 560
Neronov A., Vovk I., 2010, Science, 328, 73
Pierre Auger Collaboration, 2012, ApJS, 203, 34
Pshirkov M. S., Tinyakov P. G., Urban F. R., 2016, Phys. Rev. Lett., 116, 191302
Planck Collaboration XVI, 2014, A&A, 571, A16
Planck Collaboration XIX, 2016, A&A, 594, A19
Ryu D., Schleicher D. R. G., Treumann R. A., Tsagas C. G., Widrow L. M., 2012, Space Sci. Rev., 166, 1
Shu C.-W., Osher S., 1988, J. Comput. Phys., 77, 439
Sigl G., Miniati F., Ensslin T. A., 2003, Phys. Rev., D68, 043002
Sigl G., Miniati F., Ensslin T., 2004, Nucl. Phys. Proc. Suppl., 136, 224
Sigl G., Miniati F., Enßlin T. A., 2004, Phys. Rev. D, 70, 043007

Sorce J. G., 2015, MNRAS, 450, 2644
Sorce J. G., Courtois H. M., Gottlöber S., Hoffman Y., Tully R. B., 2014, MNRAS, 437, 3586
Sorce J. G. et al., 2016, MNRAS, 455, 2078
Stanev T., 1997, AJ, 479, 290
Takami H., Sato K., 2008, Astrophys. J., 681, 1279
Takami H., Inoue S., Yamamoto T., 2012, Astropart. Phys., 35, 767
The Pierre Auger Collaboration et al., 2017, preprint (arXiv:1709.07321)
Tinyakov P. G., Tkachev I. I., 2005, Astropart. Phys., 24, 32
Tinyakov P. G., Urban F. R., 2015, Sov. J.Exp. Theor. Phys., 120, 533
Trivedi P., Subramanian K., Seshadri T. R., 2014, Phys. Rev. D, 89, 043523
Tully R. B. et al., 2013, AJ, 146, 86
Vallée J. P., 2004, New Astron. Rev., 48, 763
van de Weygaert R., Bertschinger E., 1996, MNRAS, 281, 84
van Vliet A. R., 2014, PhD thesis, Hamburg University
Vazza F., Dolag K., Ryu D., Brunetti G., Gheller C., Kang H., Pfrommer C., 2011, MNRAS, 418, 960
Vazza F., Ferrari C., Brüggen M., Bonafede A., Gheller C., Wang P., 2015, A&A, 580, A119
Vernstrom T., Gaensler B. M., Brown S., Lenc E., Norris R. P., 2017, MNRAS, 467, 4914
Wang P., Abel T., Kaehler R., 2010, New Astron., 15, 581
Wang H., Mo H. J., Yang X., Jing Y. P., Lin W. P., 2014, ApJ, 794, 94
Yoshiguchi H., Nagataki S., Tsubaki S., Sato K., 2003, AJ, 586, 1211, (Erratum: Yoshiguchi H., Nagataki S., Tsubaki S., Sato K., 2004, AJ, 601, 592)

APPENDIX A: RE-WEIGHTED ENERGY SPECTRUM

The energy spectra presented in this work do not recreate the spectrum observed in nature. This can be achieved by modifying the injection spectrum, in particular, by using a softer spectral index and introducing an exponential cut-off. The resulting injection spectrum has the form

$$\frac{\mathrm{d}N}{\mathrm{d}E} \propto E_0^{-\gamma} e^{-E_0/(Z_0 R_{\max})} , \tag{A1}$$

with initial energy E_0, initial charge number Z_0, spectral index γ, and maximum rigidity $R_{\max} = E_{0,\max}/Z_0$. The modification can be done in post-processing by multiplying every event with a specific weight factor (Armengaud et al. 2005; van Vliet 2014)

$$w(E_0, Z_0) = E_0^{\gamma_{\mathrm{init}}-\gamma} \mathrm{e}^{-E_0/(Z_0 R_{\max})} , \tag{A2}$$

where γ_{init} is the spectral index used for the simulation.

In order to obtain the correct spectrum at injection, we fit the observed spectral index between the ankle $E_A \approx 5$ EeV and the cut-off $E_C \approx 20$ EeV, which is observed to be $\gamma = 2.63 \pm 0.04$ (Letessier-Selvon 2014). The best fit in the proton injection scenarios is an injection index of $\gamma = 2$, as expected for Fermi acceleration. The best fit for the iron injection scenarios is $\gamma = 2.4$.

The shape of the spectrum beyond the cut-off energy E_C is recreated well by using $E_{0,\max} = 100$ EeV for the exponential cut-off. The maximum rigidity is then $R_{\max,\mathrm{p}} = 100$ EV for the proton injection scenarios and $R_{\max,\mathrm{Fe}} = 100/26$ EV ≈ 3.8 EV for iron injection scenarios. The resulting spectra are shown in Fig. A1.

After re-weight, the effective number of observed particles is $N_{\mathrm{eff,\,p}} \approx 7\,000$ in the proton injection scenarios and $N_{\mathrm{eff,\,Fe}} \approx 600$ in the iron injection scenarios. The isotropic prediction for the angular power spectrum depends on the number of particles (see eq. 1). Therefore, after re-weight the isotropic prediction increases everywhere by about an order of magnitude at least. Accordingly, the colour bands are raised in Figs 4–7. All re-weighted scenarios are below 68 per cent C. L. anisotropy at all energies.

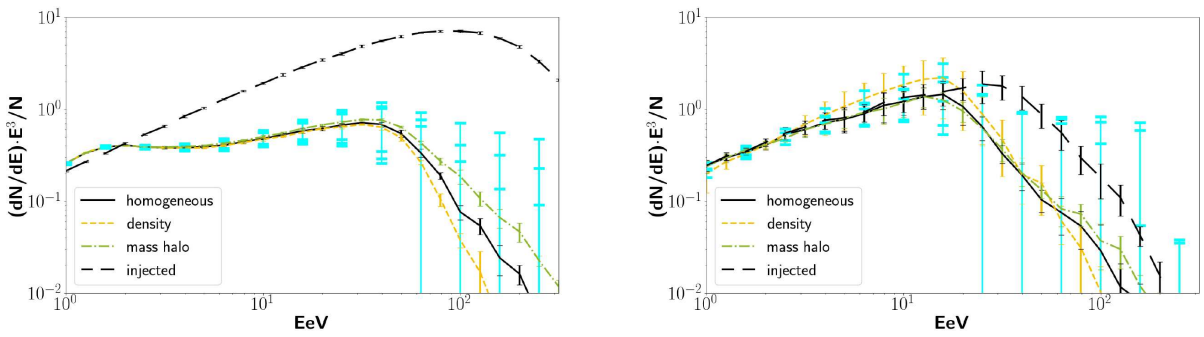

Figure A1. Re-weighted energy spectrum of UHECRs as injected at the sources (dashed lines) and measured by the observer for a pure proton and a pure iron injected composition (left- and right-hand panels, respectively). The colours and line styles indicate the injection models listed in Table 2. The graphs show the average over all magnetic field models, the standard deviation is indicated by the narrow error bars. The big cyan error bars show the Poisson noise at each second data point. The graphs are renormalized with the total number of particles N and multiplied by E^{-3} to enable better comparison to the figures presented in Letessier-Selvon (2014).

This paper has been typeset from a TEX/LATEX file prepared by the author.

Monthly Notices
of the
ROYAL ASTRONOMICAL SOCIETY

MNRAS **488,** 4220–4238 (2019)
Advance Access publication 2019 July 25

doi:10.1093/mnras/stz2033

Fast radio burst dispersion measures and rotation measures and the origin of intergalactic magnetic fields

S. Hackstein,[1★] M. Brüggen,[1] F. Vazza,[1,2,3] B. M. Gaensler[4,5] and V. Heesen[1]

[1]*Hamburger Sternwarte, University of Hamburg, Gojenbergsweg 112, D-21029 Hamburg, Germany*
[2]*Department of Physics and Astronomy, University of Bologna, Via Gobetti 93/2, I-40129 Bologna, Italy*
[3]*Istituto di Radioastronomia, INAF, Via Gobetti 101, I-40129 Bologna, Italy*
[4]*Dunlap Institute for Astronomy and Astrophysics, University of Toronto, Toronto, ON M5S 3H4, Canada*
[5]*Department of Astronomy and Astrophysics, University of Toronto, Toronto, ON M5S 3H4, Canada*

Accepted 2019 July 12. Received 2019 July 10; in original form 2019 April 18

ABSTRACT

We investigate the possibility of measuring intergalactic magnetic fields using the dispersion measures and rotation measures of fast radio bursts. With Bayesian methods, we produce probability density functions for values of these measures. We distinguish between contributions from the intergalactic medium, the host galaxy, and the local environment of the progenitor. To this end, we use constrained, magnetohydrodynamic simulations of the local Universe to compute lines-of-sight integrals from the position of the Milky Way. In particular, we differentiate between predominantly astrophysical and primordial origins of magnetic fields in the intergalactic medium. We test different possible types of host galaxies and probe different distribution functions of fast radio burst progenitor locations inside the host galaxy. Under the assumption that fast radio bursts are produced by magnetars, we use analytic predictions to account for the contribution of the local environment. We find that less than 100 fast radio bursts from magnetars in stellar-wind environments hosted by starburst dwarf galaxies at redshift $z \gtrsim 0.5$ suffice to discriminate between predominantly primordial and astrophysical origins of intergalactic magnetic fields. However, this requires the contribution of the Milky Way to be removed with a precision of $\approx 1\,\mathrm{rad\,m^{-2}}$. We show the potential existence of a subset of fast radio bursts whose rotation measures carry information on the strength of the intergalactic magnetic field and its origins.

Key words: polarization – galaxies: intergalactic medium – galaxies: magnetic fields – cosmology: large-scale structure of universe – cosmology: observations – radio continuum: general.

1 INTRODUCTION

Fast radio bursts (FRBs) are impulsive bursts in the radio sky of very short duration (0.1–10 ms) with frequencies of about 1 GHz, observed down to 400 MHz (Lorimer et al. 2007). Their observed dispersion measure (DM) exceeds the contribution of the Milky Way (MW), implying an extragalactic origin. Their short duration suggests an emitting region of the order of 100 km, suggesting a neutron star origin. Such a small region only allows for small intrinsic variation of, e.g. the polarization angle, used to observe the Faraday rotation measure (RM), which is directly related to the magnetic field strength along the line of sight (LoS). FRBs are hence potential probes for the intergalactic medium (IGM) and interstellar medium (ISM) in the MW and in the host galaxy, especially in the local environment of the FRB progenitor (see e.g. Zheng et al. 2014; Keane et al. 2016; Ravi et al. 2016). In this work, we investigate whether FRBs with observed RMs can be used to derive information on the origin of intergalactic magnetic fields (IGMFs).

Currently, the most widely accepted constraints on the comoving strength of magnetic fields in voids stem from observations of the CMB ($B \lesssim 4.4 \times 10^{-9}$ G, Ade et al. 2016) and of TeV-Blazars ($B \gtrsim 3 \times 10^{-16}$ G, Neronov & Vovk 2010), about seven orders of magnitude apart. For a summary of constraints on the magnetic field strength and coherence lengths, see Taylor, Vovk & Neronov (2011) or Dzhatdoev et al. (2018).

A number of processes have been proposed to generate cosmic magnetic fields. Primordial scenarios consider processes in the early Universe, mostly prior to the recombination epoch, e.g. during phase transitions or inflation (e.g. Campanelli 2009; Kahniashvili et al. 2010; Subramanian 2016). Another possible scenario is the generation of magnetic fields during early galaxy formation, e.g. by feedback of active galactic nuclei (AGNs; e.g. Vazza

★ E-mail: shackste@physnet.uni-hamburg.de

et al. 2017) or winds from compact galaxies (Kronberg, Lesch & Hopp 1999; Donnert et al. 2009; Dubois & Teyssier 2010). For a detailed overview on the different models, see e.g. Widrow (2002). These two scenarios result in severely different predictions for the magnetic field strengths in voids of the large-scale structure. In reality, it is likely that both the scenarios contribute to the origin of cosmic magnetic fields. Measuring their strength would allow us to put reasonable constraints on the origin of those fields (e.g. Vazza et al. 2017).

Since their first discovery (Lorimer et al. 2007), there has been a large number of studies addressing the nature and origin of FRBs (e.g. Zhang 2014; Ravi & Loeb 2018; Marcote & Paragi 2019), see Katz (2016a), Lorimer (2018), and Petroff, Hessels & Lorimer (2019) for reviews. Ravi et al. (2019) have summarized the expected progress in the coming decade.

So far, two repeating sources have been identified (Scholz et al. 2016; Spitler et al. 2016; CHIME/FRB Collaboration 2019) that rule out cataclysmic scenarios, at least for those events. Many more discoveries are expected in the very near future. Repeating signals allow us to test time dependence of their properties, making them the subject of intensive studies (e.g. Lu, Kumar & Narayan 2018; Hessels et al. 2019; Houben et al. 2019; Li et al. 2019; Lyutikov 2019; Yang, Zhang & Zhang 2019).

Still, very little is known about the population and origin of FRBs (e.g. Caleb, Spitler & Stappers 2018; Katz 2018; Palaniswamy, Li & Zhang 2018; Caleb et al. 2019; James 2019). To keep track of all the different models, they are collected in the living theory catalogue of FRBs (Platts et al. 2018). Here, we investigate the application of FRBs as probes of cosmic magnetism, with a few priors on their possible origin. We present a framework that can be used to compare observations to theory to make quantitative inferences.

At this point, only a few FRBs have observed RMs. Once the next generation of telescopes, such as e.g. CHIME/FRB, FAST, MeerKat, and SKA, begin their surveys, this number is expected to increase drastically (Jonas 2009; Nan et al. 2011; Keane, Fender & Hassall 2013; Macquart et al. 2015; The CHIME/FRB Collaboration 2018).

Akahori, Ryu & Gaensler (2016) produced predictions for the intergalactic $\mathrm{DM_{IGM}}$ and $\mathrm{RM_{IGM}}$ of FRBs from the IGM. They use numerical simulations for the large-scale structure and the IGMF to test whether combining both measurements yields information on IGMFs. Their results show that the RM is dominated by the hot gas in clusters while the dominant contributor to DM changes with redshift. Still, they show that the radial component of the density-weighted IGMF strength in filaments can be inferred from combined measurements within a factor of $\sim$2.

Vazza et al. (2018) investigate the variance in $\mathrm{RM_{IGM}}$ due to the assumed magneto-genesis model. They assume astrophysical or primordial origin of cosmic magnetic fields, similar to the models used in this work. For FRBs located at a redshift of $z = 1$, they find differences in $\langle \mathrm{RM_{IGM}} \rangle$ between the models of about one order of magnitude. In principle, this allows us to draw conclusions on the strength of the IGMF. However, it is unclear at which redshift the observed signal reveals most information.

Walker, Ma & Breton (2018) provide a framework similar to the one presented in this paper. They obtain predictions of DM in the form of likelihood functions for the different contributing regions. They use these to derive estimates on the redshift of FRBs, which mostly agree with $z \approx 0$ in the lower bounds. Thus, they conclude that the observed $\mathrm{DM_{obs}}$ can only be used to infer an upper limit on the redshift. This is in agreement with several other studies on that topic (Dolag et al. 2015; Luo et al. 2018; Niino 2018; Pol et al. 2019). We note that the framework presented here easily allows one to infer the redshift of an FRB from its DM, similar to the findings of Walker et al. (2018) and Pol et al. (2019). However, our results are subject to the same uncertainties and cannot improve on previous results.

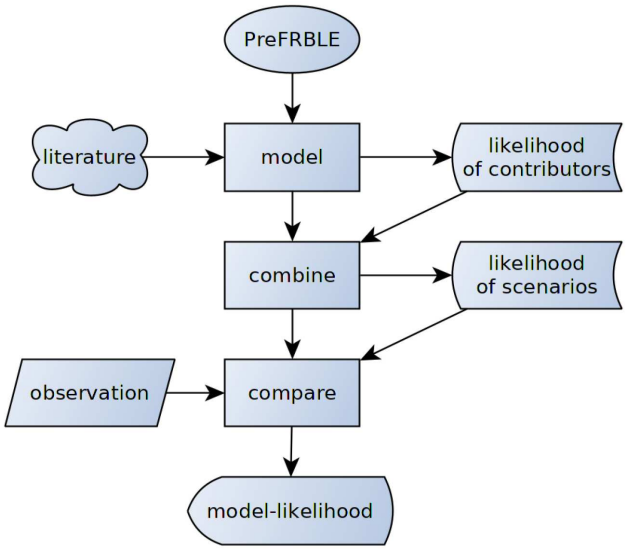

Figure 1. Flowchart to depict the basic structure of the inference presented in this work. We use results in the literature to model the contributions to DM and RM from different regions along the LoS of FRBs. These results are combined to predict the full measures expected at the Earth in different scenarios for the combination of contributor models. Finally, the results are compared to observational data to quantify and compare the posterior likelihood of several scenarios to produce the observed data.

In this work, we show how to combine predictions of DM and RM for different regions along the LoS of FRBs and to compare them to the observed $\mathrm{DM_{obs}}$ and $\mathrm{RM_{obs}}$ in order to study the IGMF. Fig. 1 shows an overview of the basic structure of the inference.

We improve on previous studies by use of constrained simulations of the local Universe that resemble different scenarios of magneto-genesis, and further, by comparing the individual contributions to DM and RM along the LoS, considering redshifts out to $z = 6$.

This paper is organized as follows. In Section 2, we explain how we model the different contributions to DM and RM along the LoS of FRBs and how to compute their likelihood functions. In Section 3, we discuss the results of the individual models of the contributing regions. In Section 4, we combine the predictions of all contributors to predict observed $\mathrm{DM_{obs}}$ and $\mathrm{RM_{obs}}$. We show how these can be used to interpret $\mathrm{DM_{obs}}$ and $\mathrm{RM_{obs}}$ regarding the origin of IGMFs. Finally, in Section 5 we discuss our results and in Section 6 we conclude.

2 MODELS

In this section, we describe the models investigated in this work and how we obtain the likelihood functions. A summary of all models can be found in Table 1.

2.1 Intergalactic medium

2.1.1 Model

We model the IGM using constrained magnetohydrodynamic (MHD) simulations of the local Universe, produced with the ENZO

Table 1. Summary of all models investigated in this work. $n_{\rm FRB}$ is the assumed number density of possible progenitor positions, and $n_\star$ is the number density of stars in the MW. NE2001 stands for the density model of thermal electrons in the MW presented in Cordes & Lazio (2002). JF12 stands for the magnetic field model of the MW developed by Jansson & Farrar (2012).

Mnemonic	Physics
IGM:	
Primordial	3D-MHD model of the local Universe with strong uniform initial magnetic field of $B_0 = 1$ nG comoving
Astrophysical	3D-MHD model of the local Universe with very weak initial magnetic field and magnetic feedback of an AGN
Host galaxy:	
Uniform	MW-like spiral galaxy model (NE2001 and JF12), $n_{\rm FRB} = const.$
Star density	MW-like spiral galaxy model (NE2001 and JF12), $n_{\rm FRB} \propto n_\star$
Dwarf	Starburst dwarf galaxy similar to IC10 or host of FRB121102, $n_{\rm FRB} \propto n_\star$
Local environment of progenitor:	
Uniform	Magnetar in uniform ISM environment
Wind	Magnetar in environment dominated by stellar winds of seed star
Wind+SNR	*Wind* plus contributions of SNR
Milky Way:	
NE2001 + JF12	Best-fitting model for Galactic RM (NE2001 and JF12)

code (Bryan et al. 2014). The simulations start from initial conditions obtained from a procedure summarized by Sorce et al. (2016). The constraints applied in order to reproduce the local Universe at $z = 0$ are fully described by Tully et al. (2013). Simulations have been produced within the Planck cosmology framework ($\Omega_{\rm m} = 0.307$, $\Omega_\Lambda = 0.693$, $h = 0.677$, $\sigma_{\rm s} = 0.829$, Planck Collaboration I 2014). Further information on the models can be found in Hackstein et al. (2018), where they have been investigated in the context of propagation of cosmic rays. The three-dimensional data sets at $z = 0$ are also publicly available at https://crpropa.desy.de/ under 'Additional resources'.

We consider two different scenarios for the predominant genesis of IGMFs, *primordial* versus *astrophysical*. To do so, we make use of the result of a single simulation, which considers the *primordial* origin of IGMFs. From that and from the *astrophysical* model presented in Hackstein et al. (2018), we extract the $|B| \propto \rho$ relation in Fig. 2 (cf. Vazza et al. 2017). The difference in $|B|(\rho)$ between the two models is most prominent at very low density, far away from the central cluster regions, where most AGNs reside. However, the contribution from these regions to the RM is likely far below the ionospheric foreground $\approx$1 rad m^{-2}, hence not observable. The most interesting regions are the vicinity of clusters, filaments, and other regions, where $1 < \rho/\langle\rho\rangle < 200$.

The *primordial* model starts with a uniform magnetic field with comoving magnetic field strength $B_0 = 1$ nG, slightly below upper limits of the PLANCK collaboration, $B_0 \lesssim 4.4$ nG (Ade et al. 2016). Note that Trivedi, Subramanian & Seshadri (2014) derived an upper limit of $B_0 \lesssim 0.6$ nG using the CMB Trispectrum. The *astrophysical* model is initialized with a $B_0 = 10^{-8}$ nG. Though this is below the lower limits obtained for present fields in voids, the final result of the simulation agrees with that limit, $B_{\rm void} \gtrsim 3 \times 10^{-7}$ nG (Neronov & Vovk 2010). In order to obtain magnetic fields that agree with observations of clusters, this model allows for additional seeding of magnetic fields by feedback of AGNs below redshift 4. In order to obtain results for the *astrophysical* model from the data of *primordial*, we apply the ratio of average $|B|(\rho)$ for these two models as correction factor on the magnetic field outside of galaxy clusters, where cosmic gas density $\rho < 200\langle\rho\rangle$. This allows us to test different prescriptions for three-dimensional magnetic fields in our cosmological volume with a limited consumption of computing time. However, in this work we investigate only two models at the extreme ends of possible strengths of the IGMF in order to see whether FRBs carry any information on the IGMF.

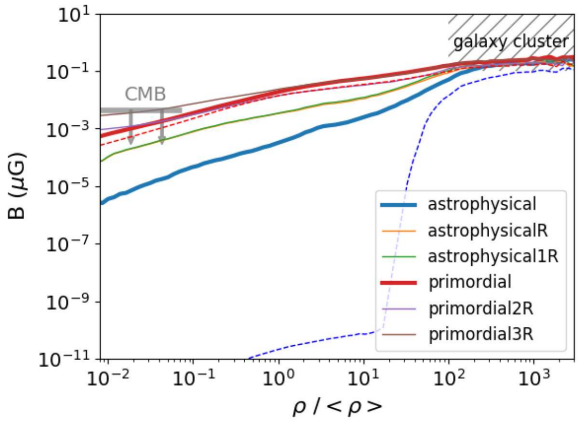

Figure 2. Relation between average magnetic field strength B and gas density ρ in the different IGM models investigated in Hackstein et al. (2018). The two models used in this paper are drawn with thick lines. The dashed lines show results for the median of B, instead of the mean. We indicate the range of magnetic fields in clusters (e.g. Feretti et al. 2012) as well as the upper limit of fields in voids according to CMB observations by PLANCK, $B_0 \lesssim 4.4$ nG (Ade et al. 2016).

Note that the average of $|B|$ is dominated by the high values in a density bin. The median, shown as dashed lines in Fig. 2, reflects much better the huge difference in the magnetic field outside high-density structures. Using the median ignores possible high values of $|B|$ within a density bin, hence underestimates the magnetic field and the RM. The average instead is dominated by these high values and forces the magnetic field to values of similar strength, everywhere within the density bin. In this case, the results for the *astrophysical* model are much closer to the *primordial*, representing the most pessimistic case to tell the two extreme models apart. Hence, the use of the average instead of the median strengthens the conclusion that the observation of FRBs can be used to distinguish between these two models.

We note, however, that the *primordial* model we probe here is initialized with a uniform field, whose topology is preserved in low-density regions. This can affect the distribution of RM from FRBs in the local Universe, making smaller values less probable. This is because the contributions from different parts of the IGM are less likely to cancel out each other. In Appendix A, we investigate how that influences the final results and find a negligible impact on observable $\mathrm{RM_{obs}} \gtrsim 1\,\mathrm{rad\,m^{-2}}$ (see also Vazza et al. 2018).

The use of numerical simulations will improve our results over those of Walker et al. (2018) and Niino (2018) by accounting for the uncertainty that arises due to inhomogeneities in the IGM. Like Akahori et al. (2016), we apply the usual method of cosmological data stacking (e.g. da Silva et al. 2000). We reconstruct the cosmic space from redshift $z = 0$ to 6 with use of simulation outputs at redshifts $z = 0.0$, 0.2, 0.5, 1.5, 2.0, 3.0, and 6.0. The LoS starts at redshift $z = 6$ and traverses the simulated volume in a randomly oriented rectilinear path. When the LoS reaches the corresponding redshift, the trajectory is continued in the next snapshot. The final snapshot at $z = 0$ is used from half the cosmic time towards the previous snapshot at $z = 0.2$. Finally, all values are corrected for a smooth evolution with redshift.

The $\mathrm{DM_{IGM}}$ for a LoS with cosmological distance is

$$\mathrm{DM_{IGM}} = \int_0^{d_{\mathrm{FRB}}} (1+z)^{-1} \left(\frac{n_\mathrm{e}}{\mathrm{cm^{-3}}}\right) \left(\frac{\mathrm{d}l}{\mathrm{pc}}\right) \mathrm{pc\,cm^{-3}}, \quad (1)$$

where d_{FRB} is the comoving distance to the FRB source and n_e is the proper thermal electron density (Xu & Han 2015). DM measures the extra traveltime of radiation at low frequencies due to dispersive effects in plasma. Hence, it scales with redshift as $\mathrm{DM} \propto (1+z)^{-1}$.

The $\mathrm{RM_{IGM}}$ for a LoS with cosmological distance is

$$\mathrm{RM_{IGM}} = \frac{\Delta\Phi}{\Delta\lambda^2} \approx 0.81 \int_{d_{\mathrm{FRB}}}^{0} (1+z)^{-2} \left(\frac{B_\parallel}{\mu\mathrm{G}}\right) \left(\frac{n_\mathrm{e}}{\mathrm{cm^{-3}}}\right) \times \left(\frac{\mathrm{d}l}{\mathrm{pc}}\right) \mathrm{rad\,m^{-2}}, \quad (2)$$

where $B_\parallel$ the proper magnetic field component parallel to the LoS (Xu & Han 2014). RM is the ratio of relative rotation of polarization angles Φ at different frequencies divided by the difference of the squared wavelength λ. The former is not affected by cosmic expansion, therefore RM scales with redshift as $\mathrm{RM} \propto (1+z)^{-2}$.

The free electron density, n_e, is computed assuming full ionization and a mean molecular weight $\mu_\mathrm{e} \approx 1.16$ of an electron for cosmic fractions of hydrogen and helium.

2.1.2 *Likelihood function*

We obtain the likelihood function of the IGM contribution from LoS integrals. These are produced using the LIGHTRAY function of the TRIDENT package (Hummels, Smith & Silvia 2017). This function extracts field values from data cells intersected by a LoS, defined by start and end positions in the three-dimensional volume. It also computes the redshift that reflects the distance to the observer. This way, it allows us to compute the redshift-corrected values along the LoS that contribute to the DM and RM.

These LoSs start from the position of the MW, defined as the centre of the box in our constrained simulation of the local Universe. They progress in evenly distributed directions defined by the HEALPIX (Górski et al. 2005) tessellation of the sphere (similar to Stasyszyn et al. 2010). We use a total of 49 152 LoSs, corresponding to a pixel radius of 1–2°. This allows us to resolve local structures while computation costs are kept at a minimum. The total computation took about 1200 h of CPU time. Differences in the likelihood function are <0.1 per cent compared to the next smaller tessellation of the sky with 12 288 LoSs. Hence, the likelihood function is reasonably converged.

The total path-length of the LoS exceeds the size of the constrained high-resolution portion of our simulation volume, which is the central $(250\ \mathrm{Mpc})^3$. Therefore, direction-dependent results beyond the first crossing of this region would be misleading. Instead, for results at higher redshifts ($z \gtrsim 0.1$) we investigate a statistical sample of LoS with random orientation. These are obtained by stacking segments between random points taken from the constrained regions, until the LoS reaches the redshift of the current snapshot. The process continues with the next snapshot, until the full LoS is built. The final snapshot of the simulation is at $z = 0$ and would not be used in the procedure described above. Hence, it is used until half of the cosmic time towards the next snapshot at $z = 0.2$, where $z \approx 0.9$. The fact that $\nabla \cdot \vec{B}$ is not conserved to 0 at the interfaces where we combine different segments of the LoS does not pose any problem for our analysis, as <1 per cent of cells are affected by this problem.

The likelihood function is proportional to the amount of LoSs that deliver the same value. Assuming an isotropic distribution of FRBs in the sky, the calculation is straightforward:

$$p(\mathrm{DM}'|z) = \frac{\oint \delta(\mathrm{DM}(\theta,\phi;z) = \mathrm{DM}')\mathrm{d}\theta\mathrm{d}\phi}{\oint \mathrm{d}\theta\mathrm{d}\phi} \approx \frac{N_{\mathrm{DM}'}}{N_{\mathrm{tot}}}, \quad (3)$$

where $N_{\mathrm{DM}'}$ is the number of LoSs from a redshift z with $\mathrm{DM} \approx \mathrm{DM}'$, and N_{tot} is the total number of LoSs from that redshift. The same holds for the RM.

2.2 Host galaxy

2.2.1 *Model*

To highlight the influence of host galaxies, we investigate two different types of galaxies, a spiral galaxy similar to the MW and a starburst dwarf galaxy similar to the host of FRB121102. We note that this small number of models does not suffice to reflect the variety of different galaxies that are likely to host FRBs, but gives a rough estimate on the range of possible contributions.

Integrating the galaxy stellar mass function (Baldry et al. 2012) yields that 68 per cent of stars reside in galaxies of 10^{11}–$10^{12}\,\mathrm{M_\odot}$, similar to the MW. Such galaxies are likely hosts, if FRBs are produced by magnetars (e.g. Popov & Postnov 2010; Katz 2016b; Beloborodov 2017; Metzger, Berger & Margalit 2017; Metzger, Margalit & Sironi 2019). We obtain predictions for the spiral host galaxy with use of the NE2001 model (Cordes & Lazio 2002) for the thermal electron density, combined with the JF12 model (Jansson & Farrar 2012) for the magnetic field, where we use the best-fitting parameters for the MW. Luo et al. (2018) compared the results of NE2001 with the model of Yao, Manchester & Wang (2017) and found that the overall statistics are rather similar, NE2001 tending to slightly higher values of DM. Here we exclusively use the NE2001 model, which was also assumed by Jansson & Farrar (2012).

Though it has been argued that the NE2001 model is not good enough to exactly reconstruct the DM foreground of pulsar data (see Xu & Han 2015), it is a reasonable choice to obtain a decent statistical estimate. Calculations have been performed using the HAMMURABI code (Waelkens et al. 2009), which computes the LoS integrals in evenly distributed directions on the whole sky seen from a given position to the edge of the galaxy model.

The likelihood of a given value of DM_{host} and RM_{host} from the host highly depends on the position of the progenitor within the host, which is uncertain. To account for that, a reasonable choice is to sample different possible positions and combine their predictions. The positions are drawn randomly, following a probability density that we assume to be either uniform or proportional to the star density. In particular, for the latter we use the combination of a thick disc and a thin disc of radius R_i and scale height Z_i with exponentially falling star density

$$n_{star}(R, Z) \propto \exp\left(-\frac{R}{R_i} - \frac{|Z|}{Z_i}\right), \quad (4)$$

using the best-fitting parameters obtained for distribution of M dwarfs in the MW, i.e. $R_{thick} = 3.6$ kpc, $Z_{thick} = 0.9$ kpc, $R_{thin} = 2.6$ kpc, and $Z_{thin} = 0.3$ kpc (Jurić et al. 2008).

Dwarf irregular galaxies in a starburst phase, which we will refer to as starburst dwarf galaxies hereafter, have high star formation rates, hence their stellar population is relatively young. Magnetars have short lifespans, $\approx 10^4$ yr (e.g. Beniamini et al. 2019), and are produced by massive stars, 20–45 $M_\odot$ (Chabrier 2003), that have rather short lifetimes, $\sim 10^7$ yr (e.g. Wit et al. 2005). This makes starburst dwarf galaxies a likely host for FRBs produced by magnetars.

The first localized FRB121102 was indeed found to reside in such a starburst dwarf galaxy, having a high star formation rate, low metallicity, and no AGN (Chatterjee et al. 2017; Tendulkar et al. 2017). Low-mass and low-metallicity galaxies with high star formation rates were also found to be overrepresented hosts of gamma-ray bursts and superluminous supernovae at low redshift (e.g. Fruchter et al. 2006; Vergani et al. 2015; Perley et al. 2016).

A well-studied starburst dwarf galaxy in the local Universe is IC 10, which is at 0.8 Mpc distance. It is the only member of the Local Group that is currently in the starburst phase. Its properties are very similar to that of the host of FRB121102 (e.g. Richer et al. 2001; Leroy et al. 2006; Magrini & Gonçalves 2009). We use the magnetic field model of Heesen et al. (2011), who studied IC 10 with radio continuum polarimetry, to estimate the possible RM contribution of a starburst dwarf galaxy. We assume a constant thermal electron density n_e in the galactic mid-plane, which falls off exponentially with height. For the magnetic field, a combination of a spiral plane-parallel field and a poloidal vertical field both with a characteristic strength B_{host} is used. We neglect random components of the magnetic field since they do not significantly affect the distribution of RM. The distribution of stars in dwarf galaxies is centred on the disc. We model their distribution with an exponential with a scale height of 300 pc (similar to Leroy et al. 2006, who studied IC 10).

2.2.2 Likelihood function

Within the MW-like spiral galaxy, we draw a sample of possible positions of the progenitor, according to the assumed distribution function. Tests showed that 1000 positions are enough to ensure converged results. For each of these positions, we compute the full sky of DM_{host} and RM_{host} measurements, similar to the approach used by Walker et al. (2018). The LoS integral is then computed to the edge of the host in all different directions defined by the HEALPIX (Górski et al. 2005) tessellation of the sphere. The probability density of values on the full sky delivers the likelihood functions $P(DM_{host})$ and $P(RM_{host})$. The sum of the likelihood functions at the different positions is then the full likelihood function for the host galaxy.

Note that the results at the position of the Sun can be used to obtain predictions for the contribution from the MW itself. By construction, the results are identical to results in Jansson & Farrar (2012).

For the starburst dwarf galaxy, we compute LoS integrals for different inclination angles and penetration depths, such that the assumed distribution of FRBs in the host is constant throughout the disc. Since the model is rotationally invariant, variations of the azimuthal angle are redundant. LoSs are calculated until they leave the disc, excluding contributions of the galactic halo, which, however, is expected to be at least one order of magnitude below the galactic contribution.

To account for possible variance across the distribution of similar starburst dwarf galaxies, we combine predictions for several choices of n_e and B_{host}, according to prior distributions explained in detail in Appendix B.

The dispersion delay produced at the host increases, due to cosmic expansion. The observed contribution of DM_{host} to the total DM_{obs} scales with the source redshift as $(1 + z)^{-1}$ (e.g. Macquart et al. 2015), so the likelihood function shifts accordingly (Walker et al. 2018) as

$$p(DM_{host}|z_s) = (1 + z_s)p((1 + z_s)DM_{host}|z_0). \quad (5)$$

For $RM = \frac{\Delta\Phi}{\Delta\lambda^2}$, the contribution of the host scales with $(1 + z)^{-2}$ instead. Therefore, the corresponding likelihood function shifts as

$$p(RM_{host}|z_s) = (1 + z_s)^2 p((1 + z_s)^2 RM_{host}|z_0). \quad (6)$$

2.3 Local environment

2.3.1 Model

We assume FRBs to be produced by magnetars (e.g. Popov & Postnov 2010; Pen & Connor 2015; Katz 2016b; Beloborodov 2017; Metzger et al. 2017; Metzger et al. 2019). Neutron stars are generally considered one of the most likely sources for FRBs. Beniamini et al. (2019) concluded that 12–100 per cent of neutron stars are born as magnetars. Hence, it is expected that they are numerous around star-forming regions. Their number density scales with the star formation rate. Results of Niino (2018) and Locatelli et al. (2019) suggest that the number density of FRBs does also scale with the star formation rate. This makes magnetars a likely candidate for the source of FRBs. Many other objects have been proposed as sources of FRBs (see Platts et al. 2018, who provide a living catalogue of theories). We restrict this study to exemplary compare two models of the local environment of the FRB progenitor.

To account for the local environment of a magnetar FRB progenitor, we make use of the models and results of Piro & Gaensler (2018). They give theoretical predictions for the DM_{prog} and RM_{prog} from the local environment of the FRB, assuming they are produced by a young neutron star. They consider two models. One model assumes a uniform local ISM, while the other accounts for changes in the ISM due to stellar winds of the seed star.

In this work, we consider the two models for the *uniform* and *wind* cases, plus we consider the additional contribution of the SNR environment for the latter model in the *wind+SNR* case. We use this low number of models to show how multiple progenitor models can be compared and combined to be tested against observations.

Stellar winds cause the magnetic field of the local environment to align and form a significant large-scale component. The RM predictions for that environment in the *wind* model are thus much more robust than for the supernova remnants. The latter model

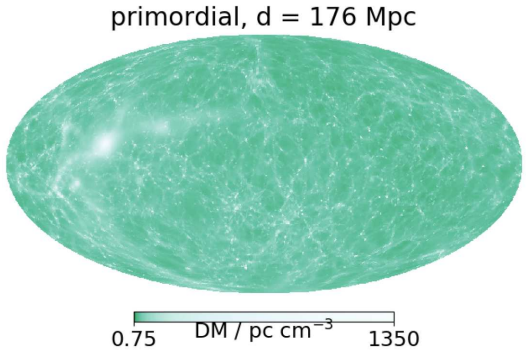

Figure 3. Full-sky map of DM_{IGM} predictions for sources at 176 Mpc distance in the local Universe. Results are shown in supergalactic coordinates for the *primordial* model. The distribution of free electrons, hence DM, is identical to the *astrophysical* case.

assumes the shock-generated magnetic field to be coherent, while the topology is very likely random. Hence, results for the *uniform* and the *wind+SNR* model should be considered as upper limits.

2.3.2 *Likelihood function*

Under the assumption that FRBs are produced at young neutron stars, Piro & Gaensler (2018) have derived expectation values for the DM_{prog} and RM_{prog} of the local FRB environment. These are given as functions of the ISM number density n_{ISM}, the time since the SN t, the energy of the explosion E, the mass of SN ejecta M, the wind mass-loading parameter K, the stellar radius $R_\star$, and the stellar magnetic field $B_\star$.

The likelihood function is obtained with a Monte Carlo method, where we sample these parameters with reasonable prior distributions, calculate the corresponding DM_{prog} and RM_{prog}, and compute their probability density. The priors chosen to obtain those are summarized in Appendix B.

The contribution from the progenitor undergoes the same evolution with redshift as the contribution from the host, see equations (5) and (6).

3 MODEL RESULTS

3.1 IGM, constrained results for the local Universe

3.1.1 *Dispersion measure*

In Fig. 3, we show the full-sky projection of the expected DM_{IGM} of FRBs at a distance of 176 Mpc. This nicely shows the distribution of structure in the local Universe (see Hackstein et al. 2018). The Virgo cluster is the most dominant local contributor with up to $DM_{IGM} \gtrsim 10^3$ pc cm^{-3}.

The DM_{IGM} prediction is the same in both IGM models, as they result in almost identical distribution of gas.

Taken from such full-sky maps at different redshifts, in Fig. 4 we present the evolution of the likelihood function of DM_{IGM}. These results agree reasonably well with results in Dolag et al. (2015) and Walker et al. (2018). At short distances, the tail at high values is more pronounced, caused by nearby, high-density regions. With increasing distance, the distribution moves towards a log-normal distribution, the mean of which increases steadily due to the cumulative growth of DM_{IGM}. Also, an increasing number of LoS crosses high-density structures, which add to the tail at high values.

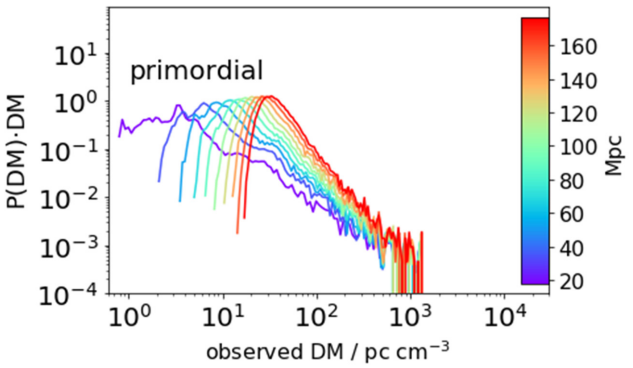

Figure 4. Likelihood function $P(DM_{IGM}|d)$ for FRB sources at distance d in the local Universe, $d \lesssim 176$ Mpc, for the *primordial* model. The distribution of free electrons, hence DM, is identical to the *astrophysical* case.

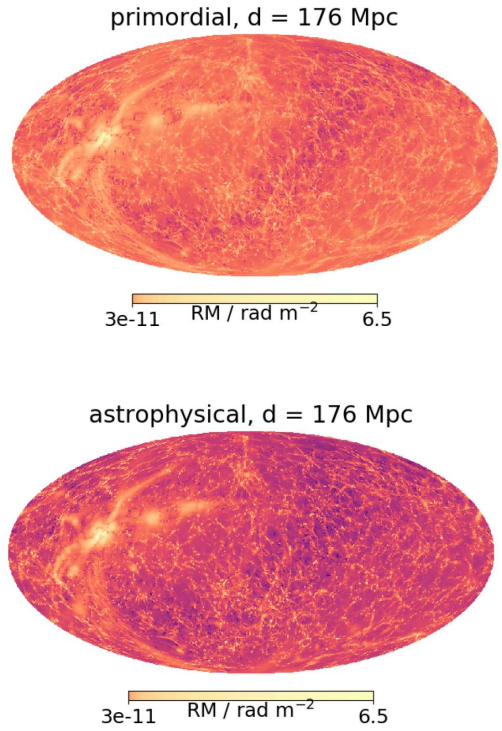

Figure 5. Full-sky map of $|RM_{IGM}|$ predictions for sources at 176 Mpc distance in the local Universe, for the *primordial* (top) and *astrophysical* models (bottom). Results are shown in supergalactic coordinates.

3.1.2 *Rotation measure*

In Fig. 5, we show the full-sky projection of expected RM_{IGM} of FRBs at a distance of 176 Mpc for both the *primordial* and *astrophysical* models. The structure of the local Universe is nicely reproduced. Again, the Virgo cluster appears as the most dominant contributor with up to $RM_{IGM} \gtrsim 6$ rad m^{-2}, which roughly agrees with the observations of Vallée (1990).

Both IGM models result in almost identical maximum values of RM_{IGM}. These are found in LoSs that pass through regions of high density, like the Virgo cluster, that contribute very high values of RM_{IGM}. The models were built to reproduce the conditions observed in these regions in the local Universe. However, the two

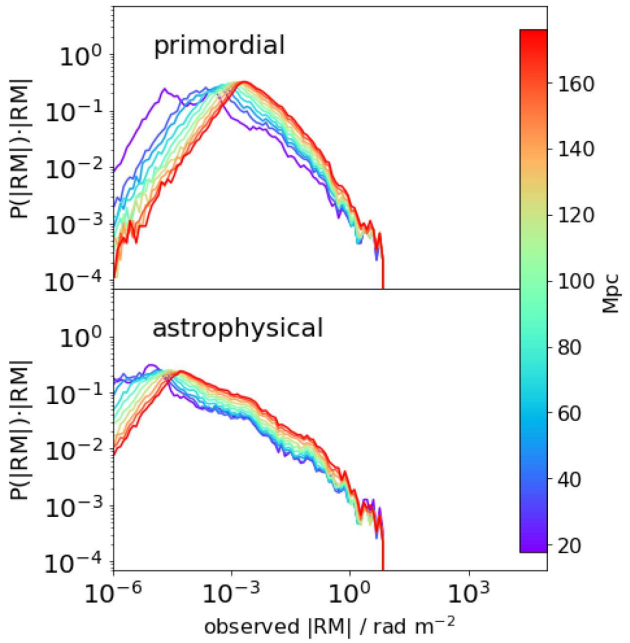

Figure 6. Likelihood function $P(|\mathrm{RM_{IGM}}||d)$ for FRB sources at distance d in the local Universe, $d \lesssim 176$ Mpc for the *primordial* (top) and *astrophysical* models (bottom).

magneto-genesis scenarios result in severely different magnetic fields in voids. Fig. 5 shows that LoSs that do not pass through regions of high density have $\mathrm{RM_{IGM}}$ lower by up to two orders of magnitude.

Taken from such full-sky maps at different redshifts, in Fig. 6 we present the evolution of the likelihood function of $\mathrm{RM_{IGM}}$. Since the distribution of positive and negative values is very similar, we make use of log (|RM|) in all our likelihood functions to compare contributions of different orders in more detail.

The highest values, $\mathrm{RM_{IGM}} \approx 1$–$10\,\mathrm{rad\,m^{-2}}$, agree in both models. These are LoSs that intersect high-density regions, associated with the $\rho/\langle\rho\rangle \geq 10^2$ overdensity of galaxy clusters, contributing high values of $\mathrm{RM_{IGM}}$. However, the fraction of such LoSs is limited, and they do not affect much the overall distribution of $\mathrm{RM_{IGM}}$ (Vazza et al. 2018).

As the peak increases with distance, the *astrophysical* case peaks about two orders of magnitude below the *primordial* case. However, the overall contribution of $\mathrm{RM_{IGM}}$ is much too low to have significant influence on the total $\mathrm{RM_{obs}}$ within maximum distance in the constrained volume, 176 Mpc. This also holds for possibly different results for positive and negative $\mathrm{RM_{IGM}}$ caused by dense structure outside of cores of clusters.

Note that the *primordial* model started from a magnetic field that was coherent over the whole simulation volume. Outside of dense structures, this topology of the initial field is conserved and results in very optimistic estimates of $\mathrm{RM_{IGM}}$, as contributions from separate parts of the LoS cannot cancel each other. A more detailed study of this effect can be found in Appendix A. Note that for the constrained distance, this feature is of the order of $10^{-2}\,\mathrm{rad\,m^{-2}}$ in the *primordial* case, subdominant to other contributions along the LoS and hence not observable. At greater distances, we combine separate trajectories with random orientations, thus enabling the contributions from separate sections of the LOS to cancel each other.

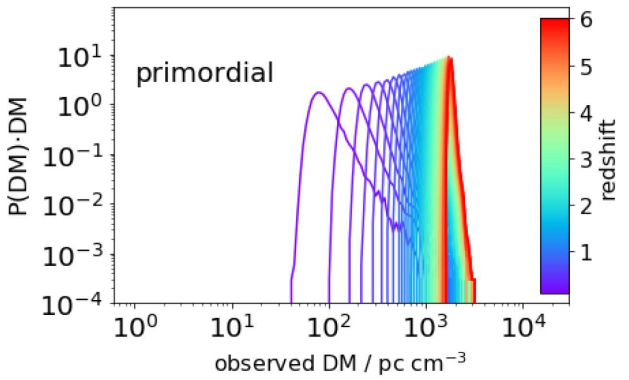

Figure 7. Likelihood function $P(\mathrm{DM_{IGM}}|z)$ for FRB sources at redshift z in the distant Universe for the *primordial* model. The distribution of free electrons, hence DM, is identical to the *astrophysical* case. From blue to red, the graphs show results at redshifts $z = 0.1$–6.0 in steps of 0.1.

3.2 IGM, high-redshift results

3.2.1 Dispersion measure

In Fig. 7, we present the resulting likelihood function of $\mathrm{DM_{IGM}}$ contribution from the IGM for FRB at different redshifts in the distant Universe for the *primordial* model. The distribution of free electrons, hence DM, is identical to the *astrophysical* case. The distribution of $\mathrm{DM_{IGM}}$ ($z = 1$) is very peaked around $1000\,\mathrm{pc\,cm^{-3}}$, in good agreement with results of previous studies, where this value is reported to be 855–$1200\,\mathrm{pc\,cm^{-3}}$ (Ioka 2003; Inoue 2004; McQuinn 2013; Deng & Zhang 2014; Dolag et al. 2015; Walker et al. 2018; Pol et al. 2019). The shape is similar to the results in Fig. 4 at the highest distance and compares well with the results of Dolag et al. (2015) and Walker et al. (2018).

With increasing redshift, the proper density of free electrons increases, as does the average $\mathrm{DM_{IGM}}$ contribution of the IGM. This makes the whole likelihood function $P(\mathrm{DM_{IGM}})$ shift to higher values with increasing redshift. As the cumulative growth of $\mathrm{DM_{IGM}}$ from low-density regions approaches the scale of dense structure contributions, $P(\mathrm{DM_{IGM}})$ becomes much narrower. However, the overall change is slower at higher redshift z (Zheng et al. 2014). Therefore, the likelihood function for high $\mathrm{DM_{IGM}}$ is much broader in z. This shows that, although the DM delivers good upper limits on z, the uncertainties in the estimate will always remain rather large, and other ways to infer z, e.g. by identification of the host, are preferred (cf. Dolag et al. 2015; Walker et al. 2018; Kumar & Linder 2019; Pol et al. 2019).

3.2.2 Rotation measure

In Fig. 8, we present the likelihood function of $\mathrm{RM_{IGM}}$ contribution from the IGM for FRB at redshift z in the *primordial* and *astrophysical* models of the distant Universe. As the models used here were produced with the same tools and physics as the ones used by Vazza et al. (2018), the results we find are quite similar. However, the average value of these distributions is significantly lower than the results of Akahori et al. (2016), which is due to the lower magnetic field strength outside of clusters. Here we use $B \sim 0.1$ nG instead of the 10–100 nG of Akahori et al. (2016), due to the more efficient dynamo amplification assumed in the latter model.

At lower redshifts, $z \sim 0.1$, $\mathrm{RM_{IGM}}$ tends to low values close to zero. Only a few LoSs show high values of up to $\mathrm{RM_{IGM}} \sim 100$ rad

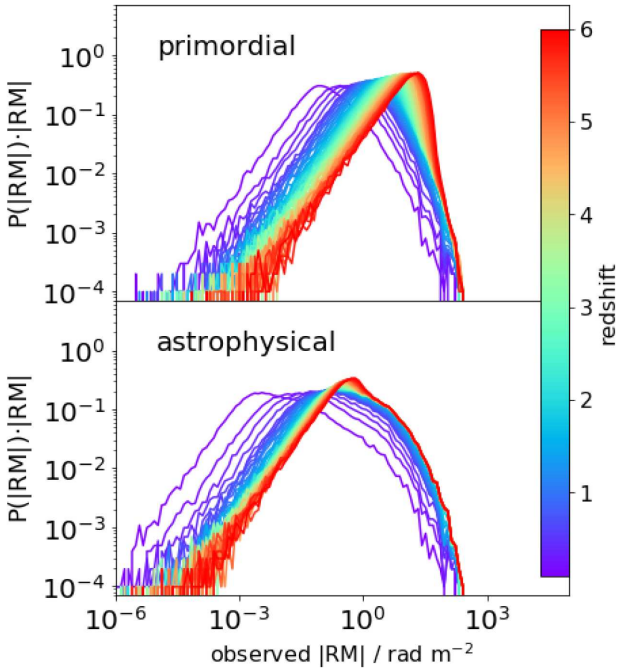

Figure 8. Likelihood function $P(\mathrm{RM_{IGM}}|z)$ for FRB sources at redshift z in the distant Universe in *primordial* (top) and *astrophysical* (down) models. From blue to red, the graphs show results at redshifts $z = 0.1$–6.0 in steps of 0.1.

m^{-2}. These are LoSs that traverse high-density regions, associated with the $\rho/\langle\rho\rangle \geq 10^2$ overdensity of galaxy clusters, which contain amplified magnetic fields. With higher redshift, more and more LoS traverse clusters, some even twice, and their $\mathrm{RM_{IGM}}$ reach values above 100 rad m^{-2} in both the *primordial* and *astrophysical* cases.

Many of the LoSs traverse the low-density IGM only and contribute most of $\mathrm{RM_{IGM}}$. The cumulative growth shifts $\mathrm{RM_{IGM}}$ to higher values, but slower than $\mathrm{DM_{IGM}}$, as $\mathrm{RM_{IGM}}$ from different regions of the IGM can cancel each other.

The IGM model we used considers an initial magnetic field that is coherent over 250 Mpc h^{-1}, i.e. the full simulation volume. This is well conserved in low-density regions and results in a uniform sign of $\mathrm{RM_{IGM}}$ contributions along a continuous LoS segment. However, since several of these segments with random orientation are combined to obtain the full LoS, they can cancel each other and we obtain results that are statistically equivalent to a stochastic field with lower coherence length.

There is a significant difference in $P(\mathrm{RM_{IGM}}|z)$ between the *primordial* and *astrophysical* cases. The peak of $\mathrm{RM_{IGM}}$ is two orders of magnitude lower in the latter case, similar to results at low redshift, shown in Fig. 6. Further, the shape looks increasingly different at higher redshift z. Though the peak value is rather low, $\lesssim$10 rad m^{-2} still at $z = 6$, the different shapes will likely reflect in the distribution of extragalactic $\mathrm{RM_{EG}}$, given that there is no dominant contribution from the other regions.

3.3 Progenitor environment, host galaxy, and MW

3.3.1 Dispersion measure

The likelihood functions of DM for all models investigated in this work are presented at redshift $z = 1$ in Fig. 9.

The two models for the IGM, *primordial* and *astrophysical*, have identical $\mathrm{DM_{IGM}}$ by construction. The two behaviours overlap each other. The dominant peak is at around 10^3 pc cm^{-3}.

The model that assumes a spiral host galaxy similar to the MW is modelled with two distribution functions of the position of the FRB progenitor, one is *Uniform* and the other follows the *star density* in the MW. The bulk of both of these distributions is similar to the MW. There is less $\mathrm{DM_{host}}$ around 10^3 pc cm^{-3}, since there are less LoSs that traverse big parts of the galaxy. For the *Uniform* distribution, a lot of progenitors are located close to the border of their host. A huge number of LoSs traverse only small parts of the galaxy. Therefore, the tail towards lower values is much more pronounced.

Xu & Han (2015) also investigate a spiral galaxy. The maximum, $\approx$1500 pc cm^{-3}, and most probable values, $\approx$ few pc cm^{-3}, are similar to our results.

The likelihood function for starburst *dwarf* galaxies as FRB hosts shows a flat plateau at $\mathrm{DM_{host}} = 1$–10^3 pc cm^{-3} due to the assumed flat prior. In most cases, the contribution will be significantly lower than the IGM. However, there is a small probability of a few per cent that it contributes more to the $\mathrm{DM_{EG}}$.

The *uniform* model described by Piro & Gaensler (2018) strongly depends on the ISM density n_{ISM}. The shape of the likelihood function is almost identical to the chosen prior distribution $\pi(n_{\mathrm{ISM}})$. Of course, this depends on the host galaxy and we will show below the result for both host galaxy models investigated in this work.

For the case of MW-like spiral galaxies, we see in Fig. 9 that the supernova remnants can provide an observed $\mathrm{DM_{prog}}$ up to several 10^3 pc cm^{-3}, even at a distance of $z = 1$, if the magnetar is located in an H II region. Only the *dwarf* host model has very small chance to contribute similarly high values of $\mathrm{DM_{host}}$. None of the other models is able to produce such high values of DM. This shows how likelihood functions can be used to rule out contributor models for single events and, subsequently, for whole populations.

Fig. 9 also shows that a high $\mathrm{DM_{obs}}$ does not necessarily imply a high redshift, but can also be produced in the local environment of the FRB, even if the probability is rather low, $\lesssim$1 per cent. However, if future observations reveal a significantly higher number of large $\mathrm{DM_{obs}} \gtrsim 10^3$ pc cm^{-3}, this would argue in favour of a population at reasonable cosmic distance, $z \gtrsim 1$.

The *wind* model in Piro & Gaensler (2018) results in a rather flat distribution of $\mathrm{DM_{prog}}$ around (10^{-2})–(10^{-1}) pc cm^{-3} that decreases rapidly at both ends. Adding the SNR contribution in *wind+SNR*, the plateau expands to substantially higher values of 10^1 pc cm^{-3} and the tail includes $\mathrm{DM_{prog}} \gtrsim 10^2$ pc cm^{-3} with a probability of $\approx$0.1 per cent. At redshift $z = 1$, this is far below the IGM contribution.

3.3.2 Rotation measure

Fig. 10 shows the likelihood functions of RM for all models at redshift $z = 1$.

The model for the MW is in agreement with the data provided by Oppermann et al. (2015). The likelihood function is of similar shape as for the IGM, about an order of magnitude above the *primordial* model. It stays above both models of the IGM for all redshifts probed in this work, $z \leq 6$.

The host model that resembles an MW-like spiral galaxy shows a likelihood function for $\mathrm{RM_{host}}$ that is very peaked around 10^1–10^2 rad m^{-2} – about a magnitude above the peak of the *primordial* model – in case the positions of FRB progenitors scale with the *star*

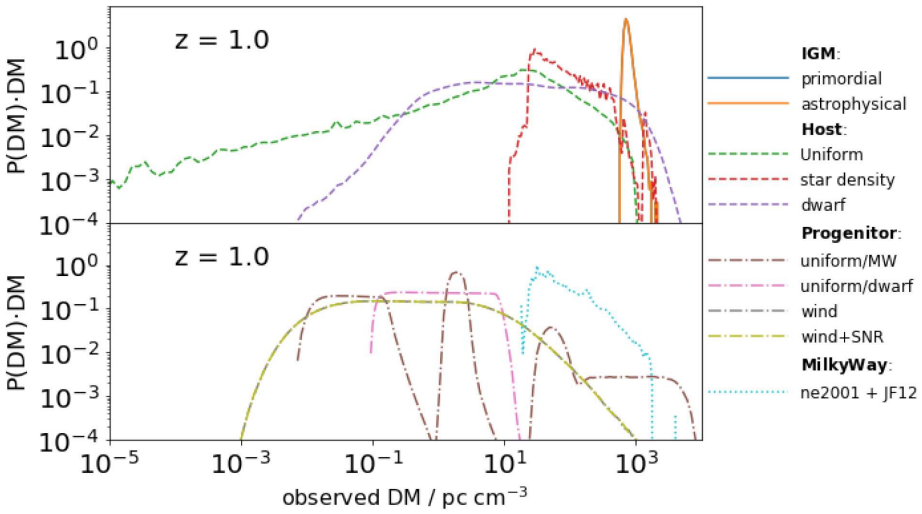

Figure 9. Likelihood functions $P(\mathrm{DM}|z = 1)$ for all contributor models investigated in this work. The linestyle indicates the contributing region described by the model.

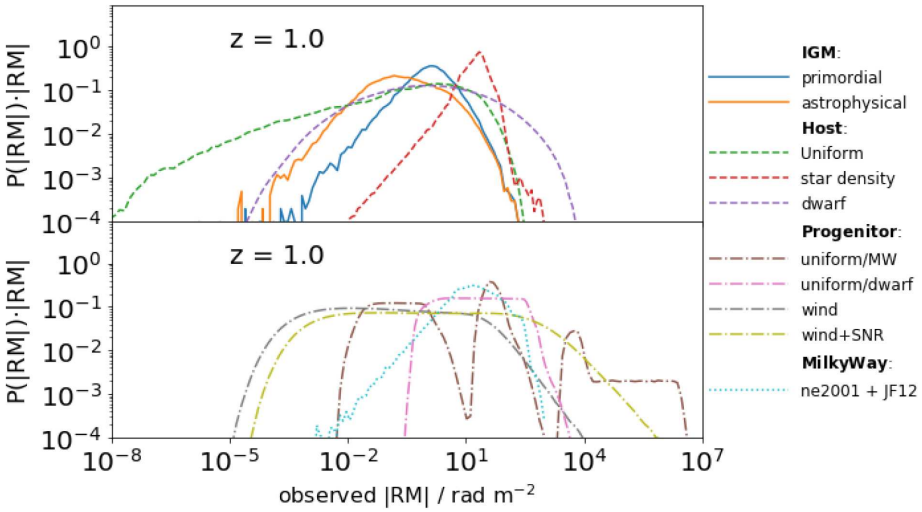

Figure 10. Likelihood functions $P(\mathrm{RM}|z = 1)$ for all contributor models investigated in this work. The linestyle indicates the contributing region described by the model.

density. This falls off exponentially with distance from the centre of the galaxy, which hosts most candidate locations and gives the strongest contribution to $\mathrm{RM_{host}}$.

For a *Uniform* distribution of progenitors, there is a wide and pronounced tail towards lower values of $\mathrm{RM_{host}}$, due to the numerous short LoSs of progenitors located at the border of the galaxy. In this case, the bulk of $\mathrm{RM_{host}}$ is comparable to the IGM contribution. These models are in best agreement with the results by Basu et al. (2018), who investigated the RM contribution of a randomly orientated galaxy in the LoS of a quasar. The range up to $\lesssim$ few 100 rad m^{-2} and median $\approx$10 rad m^{-2} of their distribution is comparable to our results.

The starburst *dwarf* galaxy model assumes the distribution of progenitor positions to be concentrated close to the galactic centre. Overall, the contribution is stronger than for a *Uniform* distribution of sources in a spiral galaxy, since most LoSs traverse considerable portions of high-density regions in the galactic disc. Due to the small size of a dwarf galaxy, the majority of LoSs show $\mathrm{RM_{host}}$ below the most probable value found for *star density* distribution in spiral galaxies.

The *uniform* model of the local environment of neutron stars described in Piro & Gaensler (2018) strongly depends on the local ISM density n_{ISM}. Hence, the shape of the likelihood function is determined by the prior distribution chosen for n_{ISM} and allows us to easily associate $\mathrm{RM_{prog}}$ with the medium around the progenitor. This depends on the galaxy that hosts the FRB and we present results for both models of the host galaxy investigated in this work. In case of a spiral galaxy like the MW, we see that for magnetars located in H II regions, the contribution of the remnants of the recent supernova can reach extremely high $\mathrm{RM_{prog}}$ up to several 10^6 rad m^{-2}, exceeding RMs in that region observed with background sources by several orders of magnitude (e.g. Harvey-Smith, Madsen & Gaensler 2011).

There is a reasonable probability of about 1 per cent to see $\mathrm{RM_{prog}} \gtrsim 10^4$–$10^5$ rad m^{-2} from magnetars in these regions. This suggests that the high $\mathrm{RM_{obs}}$ of FRB121102 (Michilli et al. 2018) might be the signal of an FRB located in an H II region. However, the bulk of

RM_{prog} expected in both models is of the order of the contribution of the IGM or the MW.

If the local environment of the magnetar was instead dominated by the stellar *wind* of the seed star, the likelihood function of RM_{prog} is rather flat (10^{-4})–(10^{1}) rad m^{-2} with rapidly falling tails on both sides. Adding the SNR contribution in *wind+SNR*, the plateau expands to 10^{3} rad m^{-2} with a high-end tail reaching out to 10^{5} rad m^{-2}. However, it barely reaches values high enough to explain the high RM_{obs} of FRB121102. Since this model is more of an upper limit than a prediction, this scenario is highly unlikely. Therefore, the best-fitting scenario for FRB121102 from the models of this paper is a magnetar localized in an H II region. This is in close agreement with previous works, which concluded that FRB121102 is likely produced by a magnetar in high-density regions (Masui et al. 2015; Spitler et al. 2016; Beloborodov 2017). Note, however, that a wide range of sizes and densities of H II regions is excluded by constraints from DM and the absence of free–free absorption (Michilli et al. 2018).

3.4 Dependence on redshift

From the likelihood functions derived above, we compute the expectation value and deviation of the contributor models in order to compare their contribution at different redshifts more easily. The results are shown in Fig. 11.

The MHD simulations probed by Vazza et al. (2018) are produced in the same framework. We use similar starting parameters, adding the constrained initial conditions. The resulting LoSs are, statistically speaking, almost identical. The redshift dependence of the average $\langle DM \rangle$ contribution of the IGM compares well to the results of Akahori et al. (2016). Since the other extragalactic contributions decrease with redshift, the IGM strongly dominates the total DM_{obs} at redshifts $z \gtrsim 1$. However, there is little change in DM_{IGM} with redshift $z > 1$–2. This introduces huge uncertainties in estimating the corresponding redshift for high DMs.

At low redshifts, $z < 0.1$, the IGM contribution is substantially subdominant to the contributions of the MW and the host galaxy. Hence, the DM_{obs} can only provide an upper limit on z (cf. Dolag et al. 2015; Niino 2018; Walker et al. 2018; Pol et al. 2019). The different models for progenitor environment and host galaxy do not show significant differences.

For the $\langle RM \rangle$, the different models of progenitor environment and host galaxy result in rather different contributions. For example, a spiral galaxy similar to the MW on average contributes two orders of magnitude higher RM_{host} than a dwarf galaxy similar to IC 10.

Regardless of the model, the contribution from the host galaxy and/or the progenitor environment dominates the RM_{obs} of FRBs in the local Universe $z < 0.1$. The choice of models determines at which point the IGM will take over. Although the contribution of the MW is dominant at all redshifts up to $z = 6$, we argue that this contribution can be removed by subtracting the MW component with sophisticated modelling of the Galaxy (Boulanger et al. 2018). At high latitudes, $RM_{MW} \approx 10$ rad m^{-2} are still very likely. Hence, it does not suffice to restrict the sample to FRBs observed outside the Galactic plane.

The difference in average $\langle RM_{IGM} \rangle$ between the primordial and astrophysical models is about one order of magnitude at $z = 1$. That difference increases with redshift to almost two orders of magnitude at $z = 6$, where the *primordial* model is dominant over all other extragalactic contributions. This shows that RM_{EG} of FRBs delivers information on and can be used to constrain the strength and origin of the IGMF. However, the minimum redshift of FRBs required to allow us to derive conclusions strongly differs for different host galaxies and progenitor environments.

4 COMBINED RESULTS

4.1 Extragalactic likelihood function

In the previous sections, we derived likelihood functions for all extragalactic contributors of DM_{obs} and RM_{obs} measured for FRBs. In this section, we combine these results into a likelihood function for the total extragalactic contribution. The combined likelihood function of the sum of independent variables is the convolution of their individual likelihood functions,

$$P_{EG} = P_{IGM} * P_{host} * P_{prog}. \quad (7)$$

We stress that the results presented in this section cannot yet be compared to observations directly, without assumptions on the FRB population and observational selection effects. If, for example, the number of FRBs increases with redshift, higher values of DM and RM are expected than for a constant number of FRBs. In the future, population assumptions and selection effects will be implemented using results of FRBPOPPY[1] in order to provide detailed predictions, tailored to the individual telescope, to be compared to observations.

We compute the likelihood of the extragalactic component DM_{EG}, assuming that FRBs are produced in a *wind* progenitor environment hosted by a starburst *dwarf* galaxy. This set of models was chosen in order to obtain the most optimistic results on obtaining info about the IGMF. Since the density distribution is the same in the *primordial* and *astrophysical* IGM models, we only show results for the former. These are shown in Fig. 12 for FRBs at different redshifts.

As explained in the previous section, the DM_{EG} is strongly dominated by the IGM at high redshifts $z > 1$. Therefore, the combined likelihood function is almost identical to that of the IGM alone. The distribution in Fig. 12 becomes much narrower. The range reduces from over two orders of magnitude, $\sim 10^{2}$–10^{4} pc cm^{-3}, at redshift $z = 0.1$ to a range of less than factor 2 at redshift $z = 6$, peaked at around 2×10^{3} pc cm^{-3}. The peak value is determined by the IGM and increases with redshift. The tail to high RM_{EG}, provided by strong progenitor contribution, decreases and is completely overshadowed by the IGM distribution by redshift $z \approx 1$. However, the increase of the peak value is rather slow at high redshift. This introduces a high uncertainty in determination of the exact redshift using DM_{obs}.

The contribution of the host galaxy can cause huge values of observed DM_{host}. which exceed the contribution of the IGM even at very high redshifts, $z \gtrsim 6$. Therefore, high DMs do not necessarily imply a high redshift of the source, but could also be produced in a nearby host galaxy. Note, though, that the likelihood of high DM_{host} at low $z < 1$ is rather low, $\lesssim$few per cent, as the bulk of DM_{host} is about an order of magnitude below results of the IGM at $z > 1$. If the observed amount of FRBs with high DMs is found to be $\gtrsim 5$ per cent, this would allow us to conclude on a cosmic population $z > 1$.

We further compute the likelihood of the extragalactic component RM_{EG}, assuming that FRBs are produced in a *wind* progenitor environment hosted by a starburst dwarf galaxy. To see the difference for the scenarios of magneto-genesis of IGMFs, we compute results for

[1] https://github.com/davidgardenier/frbpoppy

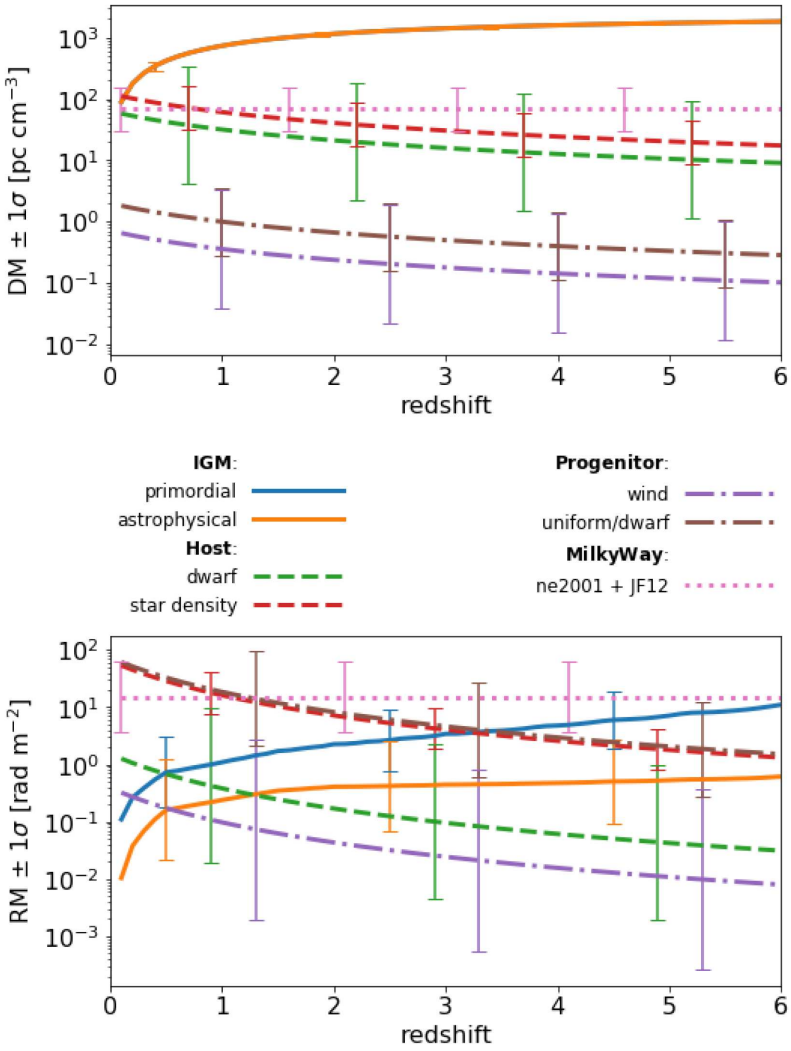

Figure 11. Redshift dependence in the distant Universe of the different average contributions ⟨DM⟩ (top) and ⟨RM⟩ (bottom).

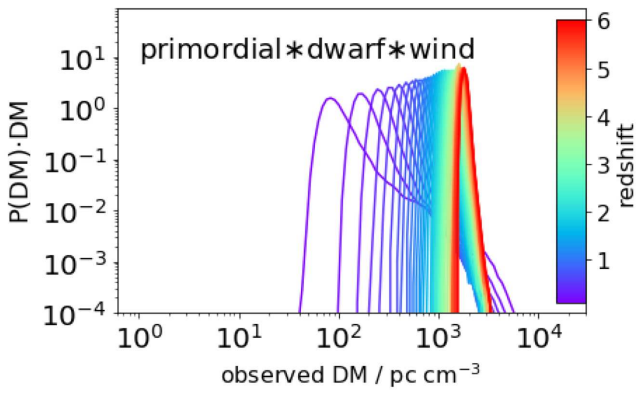

Figure 12. Combined likelihood function $P_{\rm EG}$ of all extragalactic contributors to DM, assuming that FRBs are produced at redshift z in a *wind* progenitor environment and hosted by a starburst *dwarf* galaxy embedded in an IGMF of *primordial* origin. From blue to red, the graphs show results for increasing redshift in the distant Universe, $0.1 \leq z \leq 6.0$ in steps of 0.1.

both the *primordial* and *astrophysical* cases. The results for FRBs at different redshifts are shown in Figs 13 and 14.

At low redshift, the shape of $P(\mathrm{RM_{EG}}|z)$ is determined by the host contribution. However, there is a significant difference between the two models, already at $z = 0.5$, that grows with redshift, though the average of both distributions is comparable. A quantification of that difference can be found in Section 4.2.

For the *primordial* model, contributions from the IGM become comparable to the host contribution at $z \approx 0.5$. This allows us to lower the chance of the highest $\mathrm{RM_{EG}}$ due to cancellation of RM from different regions, while intermediate results $\gtrsim$1 rad m^{-2} become more likely.

At higher redshift, $z \gtrsim 4$, the shape is completely determined by the IGM contribution, as it exceeds the observed contribution of the host galaxy at such high redshifts. This shows the capability of $\mathrm{RM_{obs}}$ of FRBs to shed light on the origin of IGMFs.

Note that, although the values of $\mathrm{RM_{IGM}}$ in the *astrophysical* case are equal or smaller than in the *primordial* case, there can be a slightly higher chance of a high $\mathrm{RM_{EG}}$ in the former case. This is because RMs from different regions of the LoS, e.g. IGM and host, can cancel each other. Hence, two comparably strong contributors

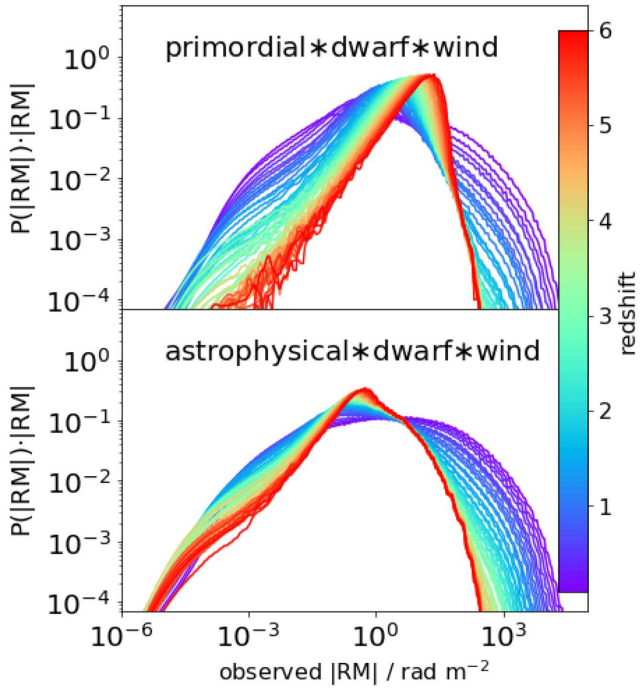

Figure 13. Combined likelihood $P_{\rm EG}$ of all extragalactic contributors to RM, assuming that FRBs are produced at redshift z in a *wind* progenitor environment and hosted by a starburst *dwarf* galaxy embedded in an intragalactic magnetic field of *primordial* (top) or *astrophysical* (bottom) origin. From blue to red, the graphs show results for increasing redshift in the distant Universe, $0.1 \leq z \leq 6.0$ in steps of 0.1.

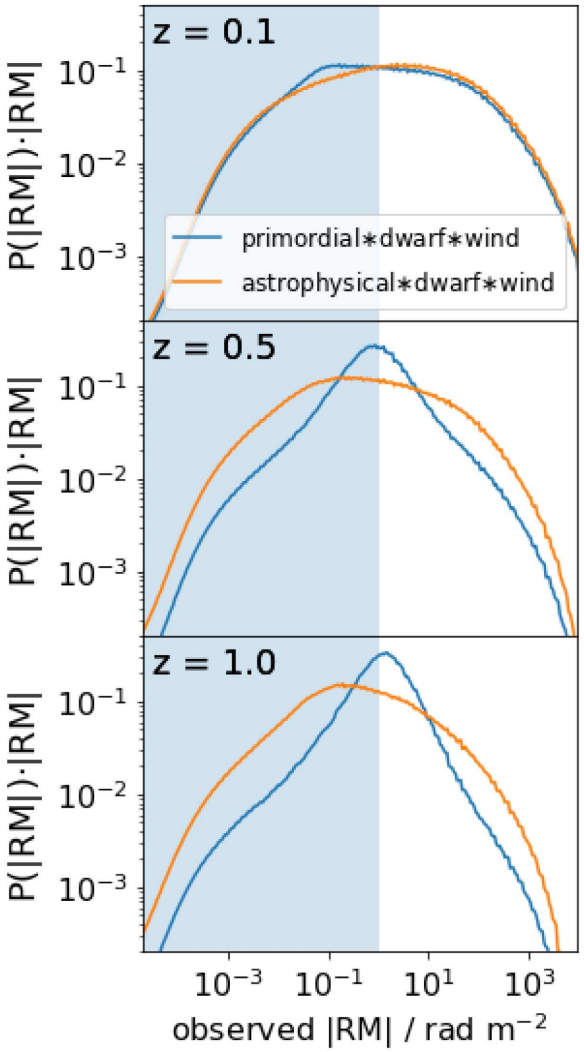

Figure 14. Same as Fig. 13 with both models in a single plot for a small set of redshifts to allow better comparison. The grey area indicates $\mathrm{RM_{EG}} < 1\,\mathrm{rad\,m^{-2}}$ that we consider as not observable due to uncertainties in removing the foreground of the MW and ionosphere.

can weaken the likelihood for high $\mathrm{RM_{obs}}$, as compared to only one dominant contributor. Use of the likelihood function can account for that, which is an advantage as compared to considering only the average value.

We stress that results in this section highly depend on the choice of contributor models. Here, we made use of those host galaxy and progenitor environment models, which showed the least contribution to $\mathrm{RM_{EG}}$. We did this in order to derive the most optimistic results on obtaining info on the IGM. The results in Figs 9–11 show that the other host and progenitor models investigated here provide much higher values of RM that overshadow the IGM contribution up to redshift $z = 3$–4. Ways to restrict the inference to those FRBs that fit the presented choice of models will be discussed in Section 5 and will be the subject of upcoming works.

4.2 Application to observations

At this point, there are few observations of FRBs with $\mathrm{RM_{obs}}$. This will change soon, after new telescopes dedicated to observe FRBs, e.g. CHIME/FRB, FAST, SKA, and MeerKat, begin producing RM data (Jonas 2009; Nan et al. 2011; Keane et al. 2013; Macquart et al. 2015; The CHIME/FRB Collaboration 2018). We therefore investigate samples of random tuples of DM and RM that resemble the expected distribution at redshift $z = 0.5$ shown in Figs 7 and 14. Note that contributions from the ionosphere to the RM are expected to be a few $\mathrm{rad\,m^{-2}}$ (Weisberg et al. 2003), therefore hampers investigation of the distribution of $\mathrm{RM_{obs}} < 1\,\mathrm{rad\,m^{-2}}$. To account for that, we only sample RM above that value.

For each of the (DM, RM) tuples, we compute the Bayes factor

$$b(\mathrm{DM, RM|primordial, astrophysical}) = \frac{P(\mathrm{DM, RM|primordial})}{P(\mathrm{DM, RM|astrophysical})}, \quad (8)$$

which quantifies how much more likely it is that the given tuple of $\mathrm{DM_{EG}}$ and $\mathrm{RM_{EG}}$ is produced in the *primordial* rather than in the *astrophysical* case. A Bayes factor $b(O, M_1, M_2) > 10$ shows that observation O is more than 10 times more likely in model M_1 than in model M_2. This signals strong evidence in favour of M_1 as compared to M_2. For values $b > 100$, the evidence is considered to be decisive (Jeffreys & Jeffreys 1961).

The likelihood of two events is the product of their individual likelihoods. The same holds for the Bayes factor, which applies a number to our corroboration towards one model over the other.

In particular, we use the $\mathrm{DM_{EG}}$ to derive a likelihood function $P(z|\mathrm{DM_{EG}})$ for the redshift of the FRB. This is then used as a prior

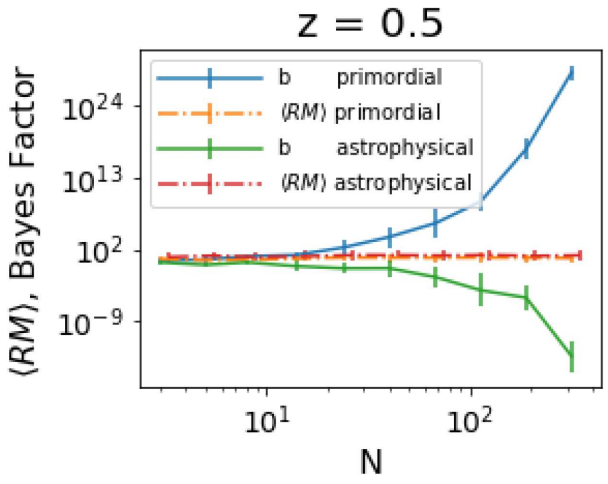

Figure 15. Bayes factor b and average $\langle \mathrm{RM_{EG}} \rangle$ for two fake populations at the indicated redshift that resemble the *primordial* and *astrophysical* cases. The errorbars of $\langle \mathrm{RM_{EG}} \rangle$ show the 1σ standard deviation of RM in the population. For b, they show the standard deviation of six random samples of the population.

to derive the likelihood of the $\mathrm{RM_{EG}}$

$$P(\mathrm{DM_{EG}}, \mathrm{RM_{EG}}|BO) \propto \int P(\mathrm{RM_{EG}}|BO, z) P(z|\mathrm{DM_{EG}}) \mathrm{d}z \,. \quad (9)$$

Note that this inference does not require knowledge on the redshift of the FRB, but only uses the $\mathrm{DM_{EG}}$ and $\mathrm{RM_{EG}}$. If the redshift is known, $P(z|\mathrm{DM_{EG}})$ can be replaced by a narrower function in order to decrease the range of possible $\mathrm{RM_{EG}}$ in the different models and allow for more precise results.

Note that RMs from AGNs are much easier to be associated with a redshift. Hence, including AGNs in our analysis in future work will significantly improve the results of this section, despite the missing DM.

We compute the Bayes factor for different sizes of the sample to see how many FRBs are required at a given redshift in order to allow conclusions on the IGM. We also compute the average $\langle \mathrm{RM_{EG}} \rangle$ of these samples to compare the efficiency of the Bayesian inference to the frequentists' approach. The results are shown in Fig. 15.

The $\langle \mathrm{RM_{EG}} \rangle$ agree within 1σ standard deviation for both populations, whereas the Bayes factor shows a difference $\gtrsim$10 orders of magnitude for a number of 100 FRBs at redshift $z = 0.5$, in case they are produced by magnetars in wind environments hosted by dwarf galaxies. This huge difference clearly sets apart the scenarios for the generation of the IGMF.

We stress that this result is largely dependent on the assumed model for the host galaxy and progenitor environment since Fig. 11 shows that other choices lead to very different results. This can shift the required redshift of FRBs, e.g. hosted by spiral galaxies, to much higher redshifts, $z \gtrsim 3$ or even above. Hence, an identification of the host galaxy as well as the local environment of the progenitor is crucial for their use to probe IGMFs. This can be a difficult task, especially for the case of dwarf galaxies (e.g. Eftekhari & Berger 2017).

We compare several possible combinations of models to investigate the redshift of FRB sources required to obtain information on the IGMF in those scenarios. We sample $\mathrm{DM_{EG}}$ and $\mathrm{RM_{EG}}$ of 100 FRBs, all at the same redshift and compute the corresponding Bayes factor b(DM, RM|primordial, astrophysical) (equation 8). This procedure is then repeated with increasing redshift. We compute six random samples at each of these redshifts and plot the average and standard deviation of the Bayes factor. The results are shown in Fig. 16.

For three of the seven combinations of models, at redshifts $z \gtrsim 0.5$, the resulting Bayes factor is $b \gg 10^2$ and hence clearly speaks for a *primordial* origin of IGMFs (in case of a *primordial* fake population. The same holds for the *astrophysical* scenario.). These are the combinations that assume the *wind* or *wind+SNR* model for the progenitor together with a *dwarf* host galaxy. The *wind* model delivers a distribution of $\mathrm{RM_{prog}}$ that is more concentrated on lower values as compared to the *uniform* model. Though the former delivers much higher values of $\mathrm{RM_{prog}}$, this is mostly for times $t \lesssim 25$ yr, below which the radio bursts are weakened by the supernova ejecta (Margalit et al. 2018). At later times, the predicted $\mathrm{RM_{prog}}$ decreases much faster in the *wind* than in the *uniform* case, accounting for the higher amount of low $\mathrm{RM_{prog}}$ in the former case.

The third combination considers both galaxy models, the *dwarf* as well as the MW-like spiral galaxy, *star density*, as equally likely hosts. This is done by using the renormalized sum of both likelihood functions, shown in Figs 9 and 10. The resulting distribution is much less peaked than the *star density* case and tends to lower values, therefore enabling those FRBs to deliver information on the IGM. This means that, even if not all of the FRBs taken into account are hosted by *dwarf* galaxies, their overall statistics at redshift $z \gtrsim 0.5$ may still allow us to draw conclusions on the magneto-genesis of IGMFs.

We note that the equal weighting of the two host models is an arbitrary choice, not based on any realistic population synthesis of galaxies. In reality, the weighting for different types of galaxies changes with redshift, as does the galactic stellar mass function (e.g. Lilly et al. 2009) as well as the major star population and their age in different types of galaxies (e.g. Hopkins 2004). An increase of the weight of spiral galaxies, *star density*, would increase probability of strong host contributions and hence push the redshift required to probe the IGM to higher values. Future work should account for that by assuming several possible populations of FRBs, their possible host galaxies and redshift distribution.

Four of the seven combinations result in indecisive Bayes factors, $b \lesssim 10^2$, at redshifts below $z \lesssim 3$. These are scenarios that assume either an MW-like galaxy, *star density*, as the host of FRBs with any model for the progenitor investigated in this work, or a magnetar embedded in a *uniform* environment hosted by a *dwarf* galaxy. In these cases, the local contribution is too strong to allow us to infer information on the IGM. For the spiral galaxy model, the distribution of $\mathrm{RM_{host}}$ peaks at about $\gtrsim 10^1$ rad m^{-2} in the host rest frame. This strong contribution can overshadow the contribution from the IGM at high redshift. However, even for these unfavourable models, beyond redshifts of $z \gtrsim 3.5$–4, the contribution of the IGM becomes strong enough to allow to distinguish between different scenarios of magneto-genesis of IGMFs. FRBs at such high redshift probably will not even require us to select a special subset of the population, e.g. hosted by dwarf galaxies, in order to obtain reasonable results. However, using only FRBs beyond redshift $z \sim 4$ might be even harder to accomplish, as it is a tough task, in case they exist, to find the exact redshift of FRBs at this distance. On the one hand, the DM can only be used to derive an upper limit on z, as we show in Section 4. On the other hand, identification of the a dwarf host galaxy becomes increasingly harder with growing redshift (e.g. Eftekhari & Berger 2017).

Note that the *dwarf∗uniform* case shows vastly lower values of the Bayes factor at redshifts $z > 4$ than all of the *star density* combinations. The latter are dominated by the host contribution

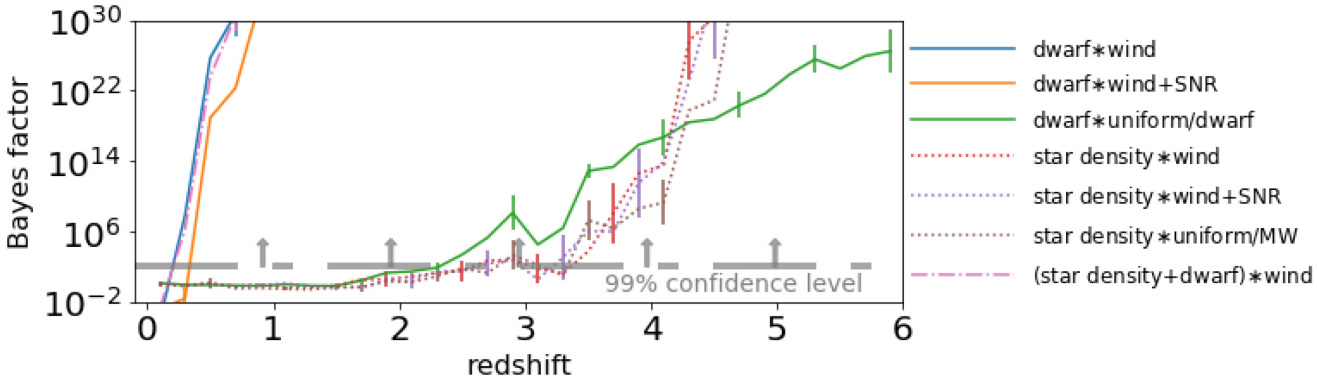

Figure 16. Bayes factor for fake samples of 100 FRBs at different redshifts, resembling the population in the *primordial* magneto-genesis scenario, combined with several sets of models indicated by colours and linestyles. The solid lines consider a *dwarf* galaxy as the host of FRBs, the dotted lines assume the MW-like spiral galaxy, *star density*, while the dash–dotted line allows for both of these galaxy types to host similar numbers of FRBs. The grey line marks a Bayes factor of 10^2, which indicates a 100 times higher chance for the fake population to be produced in the *primordial* rather than in the *astrophysical* scenario, assuming the same models for the other contributors. This indicates the 99 per cent confidence level to rule out the latter scenario in favour of the former.

for all models of the progenitor environment. The very narrow distribution $P(\mathrm{RM_{host}}|\textit{star density})$ peaks between the *primordial* and *astrophysical* $P(\mathrm{RM_{IGM}})$. Their convolution, $P_{\mathrm{Host}}{*}P_{\mathrm{IGM}}$, is rather different for the two cases.

In contrast, the *dwarf∗uniform* case is dominated by the local environment of the progenitor, which shows a very flat distribution, $P(\mathrm{RM_{prog}})$, due to the assumed flat prior. The *primordial* $P(\mathrm{RM_{IGM}})$ peaks within the range of $P(\mathrm{RM_{prog}})$; their convolution, $P(\mathrm{RM_{EG}})$, has similar shape to $P(\mathrm{RM_{prog}})$, altered only by a subtle peak at high values. The primarily low contributions of the *astrophysical* $\mathrm{RM_{IGM}}$ do not alter the shape of $P(\mathrm{RM_{prog}})$ significantly. Hence, the full likelihood functions $P(\mathrm{RM_{EG}})$ have similar shape for both models of the IGM. Single events have less weight as evidence because the Bayes factor is generally closer to unity. In mathematical terms, the integral over the absolute difference of the likelihood functions of the two cases is higher for the *star density* galaxy combinations than for the *dwarf∗uniform* case, which is hence less informative. Note that this is another measure that might be used to infer the likelihood of different combinations of models.

Note further that for all four of these models, the Bayes factor b drops significantly at around $z \approx 3$. This is because the shapes of $P(\mathrm{RM_{host}}|\textit{star density})$ and $P(\mathrm{RM_{IGM}}|\textit{primordial})$ are almost identical, as their peaks move through the same value at this redshift. This causes the two contributions to greatly match each other, resulting in an identical shape of the full $P(\mathrm{RM_{EG}})$. In contrast to that, $\mathrm{RM_{IGM}}$ values in the *astrophysical* scenario are too weak to significantly alter the shape of $P(\mathrm{RM_{host}})$. Hence, the two IGM scenarios appear very similar at that redshift. This cosmic conspiracy might be used to infer the strength of the primordial magnetic field B, as the position of the dip highly depends on B. However, it also strongly depends on the shape of the contribution of the host galaxy and might not be visible for other sets of models.

We have shown that there likely exists at least a subset of FRBs – produced by magnetars in wind environments hosted by starburst dwarf galaxies – that carries information on the IGMF. However, other host galaxies and progenitor classes completely overshadow that signal of the IGM. This shows how important it is to carefully consider the numerous possible models for regions along the LoS and to identify the host galaxies and source objects in order to measure the IGMF using FRBs.

According to the Bayes' theorem, in order to arrive at the ratio of posterior likelihoods L for the different models, the Bayes factor B has to be multiplied by the prior corroboration $\pi(M)$ towards a model M, based on information other than the investigated observation O (e.g. Boulanger et al. 2018; Fraix-Burnet et al. 2018):

$$\frac{L(M_1|O)}{L(M_2|P)} = b(O|M_1, M_2) \times \frac{\pi(M_1)}{\pi(M_2)}\,. \tag{10}$$

Note that we assume the two IGM models to be equally likely, i.e. $\pi = const$. It therefore suffices to investigate the Bayes factor b to infer the posterior likelihood of different models.

5 DISCUSSION

We investigate whether observations of FRBs can deliver information about the IGMF and its origins. To this end, we consider two extreme scenarios of magneto-genesis: a scenario where the IGMF is seeded at very high redshift (termed *primordial* scenario) and a second scenario where the magnetic field is mainly supplied by galactic outflows and other astrophysical processes (termed *astrophysical* scenario).

The initial magnetic field is very different in the two scenarios. Hence, the two scenarios account for a strong difference in the strength of magnetic fields far outside the overdense regions in the Universe. This implies significantly different results for the RM and makes these two suitable models to investigate the potential of FRBs to probe the IGMF. We compute likelihood functions of these measures that allow a comparison of the assumed models to observational data.

To account for the contribution towards the rotation and dispersion measures of the host, we investigated two models for the host galaxy, i.e. an MW-like spiral galaxy and a starburst dwarf galaxy similar to IC 10 or the host of FRB121102. This only serves as an illustration of our framework to compare theory and observations and this framework can easily be expanded to include a large variety of models for the host galaxy. Results agree with previous works (Xu & Han 2015; Basu et al. 2018).

Likewise, we model in Section 2.3 the contribution of the local environment of the progenitor with Monte Carlo simulations using the results of Piro & Gaensler (2018). The source of FRBs is assumed to be a magnetar embedded either in a uniform ISM or an environment disturbed by stellar winds of the seed star. For the *uniform* case, the distribution of possible ISM number densities n_{ISM} is determined by the host galaxy.

In accordance with previous work (Dolag et al. 2015; Niino 2018; Walker et al. 2018; Pol et al. 2019), we find that the DM is an imprecise measure of the source redshift and only delivers reasonable upper limits. Only few of the investigated models had low probability to supply DM in excess of DM_{IGM}. Hence, a significant fraction $\gtrsim$5 per cent of high $DM_{obs} \gtrsim 10^3$ pc cm^{-3} would point to a population of FRBs at cosmic distance, $z \gtrsim 1$. However, this requires a more detailed investigation that takes into account the uncertain evolution of the number of FRB sources with redshift, as well as the selection effects of the telescopes. We note that this is the scope of FRBPOPPY!,[2] the results of which will be implemented in this framework in the future.

Bhandari et al. (2017) report three FRBs with very high $DM_{obs} >$ 1500 pc cm^{-3} detected by the Parkes telescope. Although the DMs are highly debated to be produced locally, they raise hope that there is indeed an FRB population at large distance that will be detected in the years to come. For example, the MeerKat and Parkes telescopes can detect FRBs out to redshift $z \approx 4$ (Keane 2018). ARECIBO may detect bursts at $z \approx 5$ (Lorimer 2018), while FAST will be able to detect FRBs even out to $z \approx 15$ (Zhang 2018), with DM_{obs} exceeding 10^4 pc cm^{-3}. Our study shows that these FRBs are an interesting source of information on the IGMF and its origins.

For the limited set of models investigated in this paper, only a few progenitor models are capable to produce the high RM observed for FRB121102 (Michilli et al. 2018). For other FRBs with less extreme RMs, conclusions on their source are less obvious and require careful investigation of the convolved likelihood functions of the different contributors. The time evolution of repeating FRBs can be used to put much better constraints on the source model. This is, however, beyond the scope of this study and will be considered in upcoming work.

The models applied for the host galaxy use analytic functions and do not account for local overdensities, which can add significantly to RM_{host}. Also, our models of the host do not yet account for cosmic evolution of the galaxy. Results of Pillepich et al. (2019) suggest that low-mass star-forming galaxies do not change their size significantly out to redshift $z = 4$–5. Hence, the values of DM_{host} are not expected to change much for the dwarf-type of galaxies considered here. They further find that massive galaxies similar to the MW tend to be smaller at higher redshift. The density can be higher by a factor of few tens, while the path-length is reduced by a factor of a few, accounting for a DM higher by about one order of magnitude than predicted in our model, still mostly below the contribution of the IGM.

For magnetic fields in galaxies, the amplification time is of the order of 10^7–10^8 yr (e.g. Schober, Schleicher & Klessen 2013). Observations and simulations of galaxies at high redshift suggest magnetic fields of similar strength as in present-day galaxies (Bernet et al. 2008; Kronberg et al. 2008; Pakmor, Marinacci & Springel 2014; Mao et al. 2017). Hence, the expected change to the RM_{host} is of the same order as for the DM_{host}, insignificant for dwarf-type and about one order of magnitude higher for galaxies similar to the MW. This implies that the latter type of host dominates the extragalactic contribution and does not allow for conclusions on the IGMF, even out to redshift $z = 6$. However, Rodrigues et al. (2018) conclude that a significant fraction of massive spiral galaxies contain negligible large-scale magnetic fields at redshifts $z > 3$, suggesting a significantly weaker host contribution. A more physical modelling of the host galaxies will be the subject of future work.

[2]https://github.com/davidgardenier/frbpoppy

We account for effects from the possible progenitor positions by testing different distributions within the host galaxy. We find that assuming a uniform distribution in the host disc affects the distribution of expected DM_{host} only at values $\lesssim$ few pc cm^{-3}, as compared to a distribution that concentrates on the centre of the galaxy.

The distribution of expected RM_{host} is very different, even $\gtrsim 10^1$ rad m^{-2}, close to the maximum possible value, with a much higher probability in the centred case because the highest RM_{host} come from the centre of the galaxy. We note, however, that our model does not include the high RM $\approx -5.6 \times 10^5$ rad m^{-2} found for Sagittarius A* (Marrone et al. 2006). Such contributions from a LoS through the galactic centre of the host galaxy might explain the high RM observed for FRB121102 (Michilli et al. 2018). We argue that such LoSs are very unlikely for progenitors that are not themselves located in the centres of their host galaxy.

By assuming only magnetars as progenitors, we restrict the parameter space for equations in Piro & Gaensler (2018), as compared to neutron stars with weaker magnetic fields, e.g. pulsars. By that, we mostly exclude lower values of RM_{prog}, hence arrive at rather optimistic predictions for the contribution from the local environment of the progenitor. Further, their model assumes that shocks in supernova remnants produce coherent magnetic fields, while it most likely has a random topology. Hence, the results for the *uniform* and the *wind+SNR* model should be considered as upper limits. In case the real contribution of RM from such magnetars is significantly lower, these sources might also deliver information on the IGMF.

We do not account for the contributions of the MW halo. For the DM, they are comparable to the contribution from the Galactic disc, ≈30–80 pc cm^{-3} (Dolag et al. 2015; Prochaska & Zheng 2019). The RM from the halo is probably lower than from the disc, due to the weaker magnetic fields. However, the likelihood function of the two models for the IGM show reasonable difference at redshift $z = 0.5$ even for $RM_{EG} > 1$ rad m^{-2}. We only used RM_{EG} above this value in estimates of the model likelihood in Section 4.2.

We do not account for the distribution of galaxies that host FRBs. By applying a constant weight to each LoS, we implicitly assume a uniform distribution of host galaxies. Reducing the weight of LoS through low-density regions mostly reduces the likelihood of low values of RM that cannot be probed by telescopes. Estimating the effect on likelihood of RM $\gtrsim 1$ rad m^{-2} is not trivial and will be studied in upcoming works. However, for FRBs beyond redshift $z \gtrsim 0.1$, the overall statistics are not expected to change, since the Universe is homogeneous on large scales.

We do not account for the contribution of intervening galaxies (e.g. Basu et al. 2018). If the intervening galaxy is of the same type as the host, the contribution is comparable to the host contribution at the redshift of intersection and therefore hampers the investigation of the IGM component (Zheng et al. 2014). If the pulse broadening of FRB radiation is found to be dominated by scattering in intervening galaxies, this can help to exclude LoS with a significant contribution of intervening galaxies (Lorimer et al. 2013; Spitler et al. 2014). This will be a subject of future studies.

Our results are provided in the form of likelihood functions for the different contributions to RM and DM. We show how these likelihood functions can be used for parameter inference. This framework can help to infer the origin of FRBs as well as the origin of extragalactic magnetic fields (Caleb et al. 2018; Katz 2018; Palaniswamy et al. 2018).

6 CONCLUSIONS

In this paper, we have studied the different contributions to the DMs and RMs along the lines of sight of FRBs. We have built a Bayesian framework to interpret observable information of FRBs. We show how this can be used to constrain the amplitude of magnetic fields in the IGM along the line of sight. Our key findings are as follows:

(i) The strengths of the different contributions to the observed RM_{obs} highly depend on the assumed model for FRBs and their host galaxies. Magnetars embedded in wind environments hosted by starburst dwarf galaxies provide the lowest average local contribution to RM of the investigated models. For this generous set of models, RM_{EG} from redshifts $z \gtrsim 0.5$ can potentially provide information on the magnetic field in the IGM and its origin. At this redshift, the contribution of the IGM is still subdominant to that of the host. Still, there is a significant change in the distribution of extragalactic RM_{EG}. This allows one to draw conclusions on the magnetic field using Bayesian inference.
Conversely, for other models of the host galaxy and progenitor, the expected local contribution can be significantly stronger. These models require FRBs beyond $z \gtrsim 3$ in order to probe IGMFs. We conclude that there are good reasons to believe that at least a subset of FRBs observed with RMs delivers information on the IGMF and its origin. How to identify this subset will be subject of future studies.

(ii) The MW provides the dominant contribution of RM, even for FRBs out to redshift $z \gtrsim 6$. A prerequisite for the above result is the removal of the contribution of the MW to a precision of $\sim$1 rad m^{-2}. This is non-trivial, as argued by Han (2017), who suggested that up to $\sim 10^4$–10^5 values of RM may be necessary to tell apart Galactic from extragalactic contributions. However, the fast growing level of complexity in modelling magnetic fields in the MW is expected to improve at the same pace as RM statistics, making the removal of the MW foreground more viable (for a recent review, see e.g. Boulanger et al. 2018).

(iii) Using likelihood functions allows one to infer information on the host galaxy and progenitor. They allow us to systematically rule out models for a single FRB or groups of those.

(iv) From the present set of models, only some progenitor models are capable of producing the very high RM_{obs} of FRB121102. Our results suggest that, if the progenitor is a magnetar, then it is most likely located in a dense environment, such as an H II region, which we found to be capable of producing RMs that exceed those of FRB121102 by two orders of magnitude. Note, however, that the strong magnetic fields generated by shocks in the supernova remnants are likely random. This can result in much lower RM than predicted by the model of Piro & Gaensler (2018), who assumed a coherent magnetic field.
We find a much smaller chance that stellar winds of the seed star in other environments can account for the high RM_{obs} as well. The shape of magnetic fields induced by stellar winds is very coherent and can account for very high values of RM. However, the expected RM_{prog} falls rapidly with age of the magnetar. This implies a much lower chance to observe high RM_{prog} from such a source.

We provide a framework for the comparison between observations and theories of FRBs. So far, we consider a very limited set of models in order to present our framework. Still, we could show the likely existence of a subset of FRBs that delivers information on the IGMF and its origins. Future work will include more models, such as elliptical or disc host galaxies, and take into account their evolution with redshift. We will vary the strength of a primordial magnetic field in realistic combination with astrophysical processes. This will allow us to precisely probe the average strength of IGMFs today as well as the strength of the primordial seed field, thus allow us to constrain processes of magneto-genesis with FRBs.

At this point, we only consider the DM and RM. In future work, more observables will be considered, such as temporal scattering, flux density, and fluence. Further contributing regions will be considered, such as intervening galaxies and the halo of the MW. Combining this with knowledge on the selection effect of telescopes and assumptions on the underlying population of FRBs, we can produce individual predictions for the distribution of observables as measured at different telescopes.[3]

ACKNOWLEDGEMENTS

We thank Tony Piro for his help in understanding and reproducing results from his paper. We also thank Ryan Mckinven for interesting comments. Further, we thank the anonymous referee for a detailed review and constructive comments. SH would like to thank all participants of 'A Bayesian View on the Galactic Magnetic Field' as well as the Lorentz Center for an inspiring meeting. SH would also like to thank the organizers, speakers, and participants of the 'Stat4Astro School of Statistics for Astrophysics 2017: Bayesian Methodology' and the 'FRB2019' conference in Amsterdam for interesting discussions.

Our cosmological simulations were performed with the ENZO code (http://enzo-project.org), under project HHH38 and HHH42 at the Jülich Supercomputing Centre (P.I. F. Vazza). FV acknowledges financial support from the ERC Starting Grant 'MAGCOW', no. 714196. We thank Jenny Source and Stefan Gottlöber for providing us with the CLUES initial conditions and for their help in implementation.

The Dunlap Institute is funded through an endowment established by the David Dunlap family and the University of Toronto. BMG acknowledges the support of the Natural Sciences and Engineering Research Council of Canada (NSERC) through grant RGPIN-2015-05948, and of the Canada Research Chairs programme.

REFERENCES

Ade P. et al., 2016, A&A, 594, A19
Akahori T., Ryu D., Gaensler B. M., 2016, ApJ, 824, 105
Baldry I. et al., 2012, MNRAS, 421, 621
Basu A., Mao S. A., Fletcher A., Kanekar N., Shukurov A., Schnitzeler D., Vacca V., Junklewitz H., 2018, MNRAS, 477, 2528
Beloborodov A. M., 2017, ApJ, 843, L26
Beloborodov A. M., Li X., 2016, ApJ, 833, 261
Beniamini P., Hotokezaka K., van der Horst A., Kouveliotou C., 2019, MNRAS, 487, 1426
Bernet M. L., Miniati F., Lilly S. J., Kronberg P. P., Dessauges-Zavadsky M., 2008, Nature, 454, 302
Bhandari S. et al., 2017, MNRAS, 475, 1427
Boulanger F. et al., 2018, J. Cosmol. Astropart. Phys., 2018, 049
Bryan G. L. et al., 2014, ApJS, 211, 19
Caleb M., Spitler L. G., Stappers B. W., 2018, Nat. Astron., 2, 839
Caleb M., Stappers B. W., Rajwade K., Flynn C., 2019, MNRAS, 484, 5500
Campanelli L., 2009, Int. J. Mod. Phys. D, 18, 1395
Chabrier G., 2003, PASP, 115, 763

[3]This is the aim of the PREFRBLE ('Predictions of FRB models and their Likelihood Estimates') python package that comes with the presented results for a fast application to observational data. This package is currently under construction and will be publicly available soon.

Chabrier G., 2005, in Corbelli E., Palle F., eds, The Initial Mass Function 50 Years Later. Springer, Dordrecht, p. 41
Chatterjee S. et al., 2017, Nature, 541, 58
CHIME/FRB Collaboration, 2019, Nature, 566, 235
Chyży K. T., Drzazga R. T., Beck R., Urbanik M., Heesen V., Bomans D. J., 2016, ApJ, 819, 39
Cordes J. M., Lazio T. J. W., 2002, astro-ph/0207156
da Silva A. C., Barbosa D., Liddle A. R., Thomas P. A., 2000, MNRAS, 317, 37
de Avillez M. A., Breitschwerdt D., 2005, A&A, 436, 585
Deng W., Zhang B., 2014, ApJ, 783, L35
Derman E., Demircan O., Kahraman G., 1990, A&AS, 86, 421
Dolag K., Gaensler B. M., Beck A. M., Beck M. C., 2015, MNRAS, 451, 4277
Donnert J., Dolag K., Lesch H., Müller E., 2009, MNRAS, 392, 1008
Dubois Y., Teyssier R., 2010, A&A, 523, A72
Dzhatdoev T., Khalikov E., Kircheva A., Podlesnyi E., Telegina A., 2018, in Volkova V.E., Zhezher Y. V., Levkov D. G., Rubakov V. A., Matveev V. A., eds, EPJ Web Conf., Vol. 191, Intergalactic Electromagnetic Cascades in the Magnetized Universe as a Tool of Astroparticle Physics. EDP Sci. - Web Conf., Les Ulis Cedex A, France, p. 08009
Eftekhari T., Berger E., 2017, ApJ, 849, 162
Feretti L., Giovannini G., Govoni F., Murgia M., 2012, A&AR, 20, 54
Ferrière K. M., 2001, Rev. Mod. Phys., 73, 1031
Fraix-Burnet D., Girard S., Arbel J., Marquette J.-B., 2018, Statistics for Astrophysics: Bayesian Methodology. EDP Sci., Les Ulis Cedex A, France, https://hal.archives-ouvertes.fr/hal-01952759
Fruchter A. et al., 2006, Nature, 441, 463
Górski K. M., Hivon E., Banday A. J., Wandelt B. D., Hansen F. K., Reinecke M., Bartelmann M., 2005, ApJ, 622, 759
Hackstein S., Vazza F., Brüggen M., Sorce J. G., Gottlöber S., 2018, MNRAS, 475, 2519
Han J. L., 2017, ARA&A, 55, 111
Harvey-Smith L., Madsen G. J., Gaensler B. M., 2011, ApJ, 736, 83
Heesen V., Rau U., Rupen M., Brinks E., Hunter D. A., 2011, ApJ, 739, L23
Hessels J. et al., 2019, ApJ, 876, L23
Hopkins A. M., 2004, ApJ, 615, 209
Houben L. J. M., Spitler L. G., ter Veen S., Rachen J. P., Falcke H., Kramer M., 2019, A&A, 623, A42
Hummels C. B., Smith B. D., Silvia D. W., 2017, ApJ, 847, 59
Inoue S., 2004, MNRAS, 348, 999
Ioka K., 2003, ApJ, 598, L79
James C. W., 2019, MNRAS, 486, 5934
Jansson R., Farrar G. R., 2012, ApJ, 757, 14
Jeffreys H., Jeffreys H., 1961, Theory of Probability, 3rd edn. Clarendon, OUP Oxford, 1998
Jonas J. L., 2009, Proc. IEEE, 97, 1522
Jurić M. et al., 2008, ApJ, 673, 864
Kahniashvili T., Tevzadze A. G., Sethi S. K., Pandey K., Ratra B., 2010, Phys. Rev. D, 82, 083005
Katz J. I., 2016a, Mod. Phys. Lett. A, 31, 1630013
Katz J. I., 2016b, ApJ, 826, 226
Katz J. I., 2018, Prog. Part. Nucl. Phys., 103, 1
Keane E. et al., 2016, Nature, 530, 453
Keane E., 2018, Nat. Astron., 2, 1811
Keane E. F., Fender R. P., Hassall T. E., 2013, MNRAS, 436, 371
Kronberg P., Bernet M., Miniati F., Lilly S., Short M., Higdon D., 2008, ApJ, 676, 70
Kronberg P. P., Lesch H., Hopp U., 1999, ApJ, 511, 56
Kumar P., Linder E. V., 2019, preprint (arXiv:1903.08175)
Leroy A., Bolatto A., Walter F., Blitz L., 2006, ApJ, 643, 825
Li B., Li L.-B., Zhang Z.-B., Geng J.-J., Song L.-M., Huang Y.-F., Yang Y.-P., 2019, preprint (arXiv:1901.03484)
Lilly S. J. et al., 2009, ApJS, 184, 218
Locatelli N., Ronchi M., Ghirlanda G., Ghisellini G., 2019, A&A, 625, A109
Lorimer D., Bailes M., McLaughlin M., Narkevic D., Crawford F., 2007, Science, 318, 777
Lorimer D. R., 2018, Nat. Astron., 2, 860
Lorimer D. R., McLaughlin M. A., Karastergiou A., Johnston S., 2013, MNRAS, 436, L5
Lu W., Kumar P., Narayan R., 2018, MNRAS, 483, 359
Luo R., Lee K., Lorimer D. R., Zhang B., 2018, MNRAS, 481, 2320
Lyutikov M., 2019, preprint (arXiv:1901.03260)
Macquart J. P. et al., 2015, Proc. Sci., Fast Transients at Cosmological Distances with the SKA. SISSA, Trieste, PoS#55
Magrini L., Gonçalves D. R., 2009, MNRAS, 398, 280
Mao S. et al., 2017, Nat. Astron., 1, 621
Marcote B., Paragi Z., 2019, preprint (arXiv:1901.08541)
Margalit B., Metzger B. D., Berger E., Nicholl M., Eftekhari T., Margutti R., 2018, MNRAS, 481, 2407
Marrone D. P., Moran J. M., Zhao J.-H., Rao R., 2006, ApJ, 654, L57
Masui K. et al., 2015, Nature, 528, 523
McQuinn M., 2013, ApJ, 780, L33
Metzger B. D., Berger E., Margalit B., 2017, ApJ, 841, 14
Metzger B. D., Margalit B., Sironi L., 2019, MNRAS, 485, 4091
Michilli D. et al., 2018, Nature, 553, 182
Nan R. et al., 2011, Int. J. Mod. Phys. D, 20, 989
Neronov A., Vovk I., 2010, Science, 328, 73
Niino Y., 2018, ApJ, 858, 4
Oppermann N. et al., 2015, A&A, 575, A118
Pakmor R., Marinacci F., Springel V., 2014, ApJ, 783, L20
Palaniswamy D., Li Y., Zhang B., 2018, ApJ, 854, L12
Pen U.-L., Connor L., 2015, ApJ, 807, 179
Perley D. A. et al., 2016, ApJ, 830, 13
Petroff E., Hessels J. W. T., Lorimer D. R., 2019, A&AR, 27, 4
Pillepich A. et al., 2019, preprint (arXiv:1902.05553)
Piro A. L., Gaensler B. M., 2018, ApJ, 861, 150
Planck Collaboration I, 2014, A&A, 571, A1
Platts E., Weltman A., Walters A., Tendulkar S., Gordin J., Kandhai S., *Physics Reports* (2019)
Pol N., Lam M. T., McLaughlin M. A., Lazio T. J. W., Cordes J. M., 2019, preprint (arXiv:1903.07630)
Popov S. B., Postnov K. A., 2010, Evolution of Cosmic Objects through their Physical Activity. Proceedings of the Conference dedicated to Viktor Ambartsumian's 100th Anniversary ed HA Harutyunian, AM Mickaelian, Y. Terzian (Yerevan: NAS RA). Vol. 129. 2010. p. 129
Prochaska J. X., Zheng Y., 2019, MNRAS, 485, 648
Ravi V. et al., 2016, Science, 354, 1249
Ravi V. et al., 2019, Bull. Am. Astron. Soc., 51, 420
Ravi V., Loeb A., 2018, ApJ, 874, 72
Richer M. et al., 2001, A&A, 370, 34
Rodrigues L. F. S., Chamandy L., Shukurov A., Baugh C. M., Taylor A. R., 2018, MNRAS, 483, 2424
Salpeter E. E., 1955, ApJ, 121, 161
Schober J., Schleicher D. R., Klessen R. S., 2013, A&A, 560, A87
Scholz P. et al., 2016, ApJ, 833, 177
Siegel M., Majewski S., Reid I., Thompson I., 2002, ApJ, 578, 151
Sorce J. G. et al., 2016, MNRAS, 455, 2078
Spitler L. et al., 2014, ApJ, 790, 101
Spitler L. et al., 2016, Nature, 531, 202
Stasyszyn F., Nuza S. E., Dolag K., Beck R., Donnert J., 2010, MNRAS, 408, 684
Subramanian K., 2016, Rep. Prog. Phys., 79, 076901
Taylor A., Vovk I., Neronov A., 2011, A&A, 529, A144
Tendulkar S. P. et al., 2017, ApJ, 834, L7
The CHIME/FRB Collaboration, 2018, ApJ, 863, 48
Trivedi P., Subramanian K., Seshadri T. R., 2014, Phys. Rev. D, 89, 043523
Tully R. B. et al., 2013, AJ, 146, 86
Vallée J., 1990, AJ, 99, 459
Vazza F., Brüggen M., Gheller C., Hackstein S., Wittor D., Hinz P. M., 2017, Class. Quantum Gravity, 34, 234001
Vazza F., Brüggen M., Hinz P. M., Wittor D., Locatelli N., Gheller C., 2018, MNRAS, 480, 3907
Vergani S. et al., 2015, A&A, 581, A102

Waelkens A., Jaffe T., Reinecke M., Kitaura F., Enßlin T., 2009, A&A, 495, 697
Walker C. R. H., Ma Y.-Z., Breton R. P., 2018, preprint (arXiv:1804.01548)
Weisberg J. M., Cordes J. M., Kuan B., Devine K. E., Green J. T., Backer D. C., 2004, *ApJS*, 150(1), 317
Wickramasinghe D., Ferrario L., 2008, MNRAS, 389, L66
Widrow L. M., 2002, Rev. Mod. Phys., 74, 775
Wit W. d., Testi L., Palla F., Zinnecker H., 2005, Astron. Astrophys.-Les Ulis, 437, 247
Woosley S., Weaver T., 1995, No. UCRL-ID-122106, Lawrence Livermore National Lab., CA (United States)
Xu J., Han J., 2014, MNRAS, 442, 3329
Xu J., Han J. L., 2015, Res. Astron. Astrophys., 15, 1629
Yang Y.-H., Zhang B.-B., Zhang B., 2019, ApJ, 875, L19
Yao J., Manchester R., Wang N., 2017, ApJ, 835, 29
Zhang B., 2014, ApJ, 780, L21
Zhang B., 2018, ApJ, 867, L21
Zheng Z., Ofek E., Kulkarni S., Neill J., Juric M., 2014, ApJ, 797, 71

APPENDIX A: UNIFORM PRIMORDIAL MAGNETIC FIELD

In this section, we briefly investigate the effects of choosing a uniform primordial magnetic field on the resulting RM likelihood functions. To this end, we compare the six models presented by Hackstein et al. (2018). In this paper, we used their *primordial* model, which starts with a uniform magnetic field. The other *primordial* models start from a purely turbulent field using different power-law indices, while the *astrophysical* models use a very faint seed field and instead allow for magnetic feedback from an AGN.

Using the uniform resolution grid at $z = 0$, we calculate RM for LoS parallel to two axes, positive and negative directions, to obtain both signs for RM values. From that, we obtain likelihood function of RM for the different configuration of initial magnetic field.

The result in Fig. A1 shows that for the *primordial* model, which starts from a completely uniform magnetic field, there is a pronounced peak at around 10^{-3} rad m^{-2}. The other *primordial2R* and *primordial3R* models start from a stochastic field, so contributions along the LoS can cancel out each other, and the likelihood reduces at the peak value and increases at lower values. Higher values, contributed by denser structures, are not affected by the shape of the primordial field. However, this feature is visible in the IGM component at order $\mathrm{RM_{IGM}} \approx 10^{-4}$ rad m^{-2}, and hence not accessible. This implies that RMs of FRBs do not carry information on the coherence length of primordial fields.

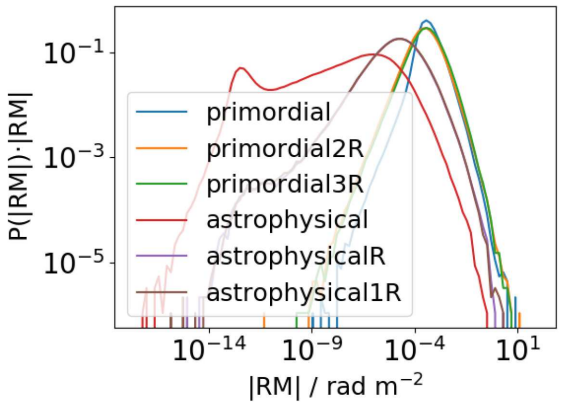

Figure A1. Likelihood function P(RM) for the different models of the local Universe from Hackstein et al. (2018).

The *astrophysical* models show similar highest values of $\mathrm{RM_{IGM}}$ to the *primordial* ones. The bulk of values is a few orders of magnitude below the *primordial* peak and the low tail reaches to substantially smaller values. The shape at low values is rather different from the results in Fig. 8 at redshift $z = 1$, as it reaches to smaller values and peaks again at around 10^{-13} rad m^{-2}. The difference is because predictions in this work have been reconstructed from the *primordial* model. However, since the difference in results is for values of RM that are far too low to be measurable, we consider the data sufficient for the argument of this work.

APPENDIX B: PRIORS

We perform Monte Carlo simulations in order to obtain likelihood functions for the contribution of the progenitor and the host galaxy. This requires a choice of reasonable prior probability distribution of the parameters that enter the equations. All parameters and their priors are summarized in Table B1.

We assume the source of FRBs to be magnetars, which stem from B- and O-type stars with masses of $m = 20$–$45\,\mathrm{M}_\odot$ and $B_\star = 800$–1500 G dipole magnetic fields. This assumption is reasonable, according to the results of Wickramasinghe & Ferrario (2008). The DM and RM contribution for this case of the local environment is given by Piro & Gaensler (2018).

Woosley & Weaver (1995) showed that such supernovae explode with a typical energy of $E = 1.2 \times 10^{51}$ erg, which we adopt as a constant value.

The mass of neutron stars is about $M_{\mathrm{NS}} \approx 1.5\,\mathrm{M}_\odot$, regardless of the progenitor stars mass. Hence, the mass of supernova ejecta is the mass of the progenitor star m minus the mass of the neutron star. The prior of the mass of the progenitor star is given by the initial mass function, well approximated by the Salpeter function $\pi(M) \propto M^{-2.35}$ (Salpeter 1955; Chabrier 2003, 2005), and has a support in the mass range stated above, reduced by the mass of the neutron star.

We obtain the stellar radius from the radius–mass relation of heavy stars given in Derman, Demircan & Kahraman (1990).

[t]

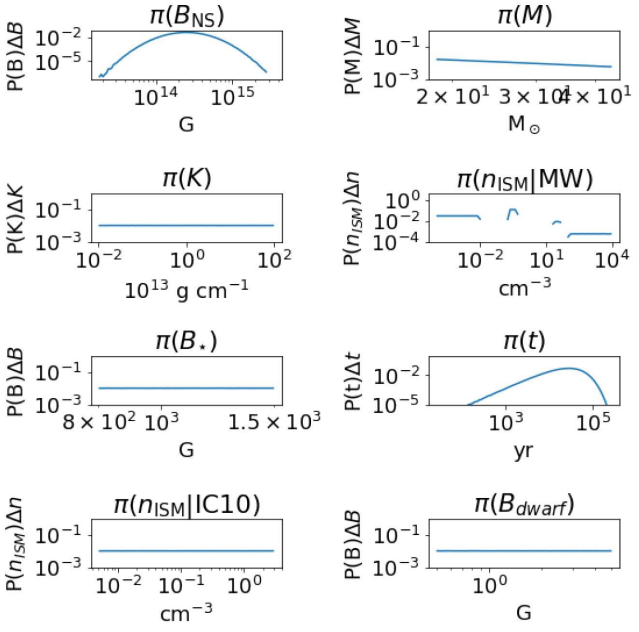

Figure B1. Graphical depiction of the priors in the Table B1.

Table B1. Parameters for Monte Carlo simulations, and their prior distributions together with a reference.

Priors:		
Host galaxy		
Position of progenitor *pos*	MW: $\prod_{i\in[\text{thin,thick}]} e^{-\frac{z}{Z_i}} e^{-\frac{r}{R_i}}$	Siegel et al. (2002); Jurić et al. (2008)
–	IC10: $e^{-\frac{z}{Z}} e^{-\frac{r}{R}}$	Leroy et al. (2006)
Magnetic field of host B_{host}	IC10: log-flat, $B_{\text{host}} \in [0.5, 5]$ μG	Chyży et al. (2016)
Progenitor		
Magnetic field of magnetar B_{NS}	LogNorm (log(2.5×10^{14} G), 0.5)	Wickramasinghe & Ferrario (2008)
Mass of SN ejecta M	$M = m^{-2.35} - M_{\text{NS}}$, $m \in \{20, 45\}$ M$_\odot$	Chabrier (2003)
ISM number density n_{ISM}	$MW : \sum \frac{p_i}{\Delta n} (\Theta(n - n_i) - \Theta(n_{i+1} - n))$	Ferrière (2001)
–	IC10: log-flat, $n_{\text{ISM}} \in [5 \times 10^{-3}, 3]$	de Avillez & Breitschwerdt (2005)
Time since SN t	Flat, $t \in \{25\,\text{yr}, t_{\text{diss}}\}$	Margalit et al. (2018); Beloborodov & Li (2016)
Wind mass-loading parameter K	Log-flat, $K \in \{10^{11}, 10^{15}\}$ g cm^{-1}	–
Magnetic field of seed star $B_\star$	Log-flat, $B_\star \in \{800, 1500\}$ G	Wickramasinghe & Ferrario (2008)

The number density of the ISM, n_{ISM}, in an MW-like galaxy is highly varied across the different media found throughout the galaxy. We use the ranges of n_{ISM} given by Ferrière (2001) together with the well-known volume filling factors of the different media. Within each of these ranges, we choose a log-flat distribution, renormalized, such that the integral over the range gives the volume filling factor of the corresponding medium.

For IC10, we assume a constant n_{ISM} throughout the disc of the dwarf galaxy that falls exponentially with scale height. Since FRBs are mostly located in the disc, we use identical priors for the progenitor and the host galaxy.

In general, the production of FRBs is not related to the supernova that gives birth to the magnetar. Hence, no age of the magnetar is preferred over another, which is reflected by a flat prior. Free–free absorption by supernova ejecta can weaken FRB radiation. This implies a lower limit of $t \gtrsim 25$ yr on the age of magnetars to emit visible FRBs (Margalit et al. 2018). We adopt this value as a strict lower limit. The activity period of magnetars is limited by the dissipation of their strong magnetic field, 10^{14}–10^{16} G. The dissipation time-scale was derived by Beloborodov & Li (2016):

$$t_{\text{diss}} = 600 \left(\frac{L}{1\,\text{km}}\right)^{1.6} \left(\frac{\delta B_{\text{NS}}}{10^{16}\,\text{G}}\right)^{0.4} \left(\frac{B_{\text{NS}}}{10^{16}\,\text{G}}\right)^{-1.6} \left(\frac{\rho}{\rho_{\text{nuc}}}\right)^{1.2} \text{yr}, \tag{B1}$$

where L is the typical scale of variation, δB_{NS}, of the magnetar's magnetic field strength, B_{NS}. ρ is the density of the magnetar and $\rho_{\text{nuc}} = 2.8 \times 10^{14}$ g cm^{-3} is the nuclear saturation density. While the magnetic field dissipates, FRBs become less likely. We account for that by sampling possible values of t_{diss} and use the shape above the maximum of the resulting probability density function.

The dissipation time, t_{diss}, depends on parameters that are independent of all other parameters of interest. To sample t_{diss}, we assume typical values of $L = 10^5$ cm and $\rho = 10^{14}$ g cm^{-3} (Beloborodov & Li 2016). For the magnetic field of the magnetar, B_{NS}, we roughly fit the results of Wickramasinghe & Ferrario (2008) with a LogNorm function centred at 2.5×10^{14} G.

The wind mass-loading parameter, K (Piro & Gaensler 2018), is not well constrained so far. Hence, we choose a log-flat prior in the expected range $K = 10^{11}$–10^{15} g cm^{-1}.

The distribution of strong magnetic fields in B- and O-type stars, $B_\star$, is rather uncertain, as is the relation between the magnetic field of the progenitor star and that of the magnetar. This is because the strong field of the magnetar could stem from either a fossil field or a shear-driven dynamo. As a conservative choice, we use a log-flat prior for $B_\star$ and consider $B_\star$ and the magnetic field of the magnetar, B_{NS}, as independent.

By definition, $B_{\text{NS}} = 10^{14}$–10^{16} G. Wickramasinghe & Ferrario (2008) give the distribution of B_{NS} for observed magnetars and their best-fitting model. In order to minimize selection effects from observations, we adopt their best-fitting model as a LogNorm with a mean $\mu = 2.5 \times 10^{14}$ G and a logarithmic deviation $\sigma = 0.5$.

For simplicity, we assume that $\delta B_{\text{NS}} \sim B_{\text{NS}}$, which is generally the case for magnetic fields of such strength (see e.g. Beloborodov & Li 2016).

For the host galaxy, we investigate two different models: an MW-like spiral galaxy and a dwarf galaxy similar to IC10.

We assume that the probability for the position of an FRB scales with the number density of stars. In the MW-like galaxy, the best-fitting model is the combination of two discs, thin and thick, with exponential decay from centre towards the borders. We use the best-fitting parameters for the MW, given in Jurić et al. (2008), $Z_{\text{thin}} = 0.3$ kpc, $R_{\text{thin}} = 2.6$ kpc, $Z_{\text{thick}} = 0.9$ kpc, and $R_{\text{thick}} = 3.6$ kpc.

The distribution of stars in dwarf galaxies like IC10 is irregular. We hence use a simple disc model with a scale height $Z = 300$ kpc (Leroy et al. 2006) and a radius $R = 900$ kpc.

de Avillez & Breitschwerdt (2005) provide a distribution of ISM density, n_{ISM}, in star-forming galaxies that is well described by a log-flat distribution and can be used as prior distribution of n_{ISM} in dwarf galaxies like IC10.

Chyży et al. (2016) give a range of possible strengths for the ordered magnetic field of the dwarf galaxy IC10. We do not assume a particular shape, as the number of values is too low to derive a reasonable distribution. Hence, we use a log-flat distribution that covers the range of these values.

At this point, we take all our models as candidates with equal prior likelihood. The ratio of their inferred posteriors is hence equal to the ratio of their measure likelihoods, i.e. the Bayes factor.

This paper has been typeset from a TEX/LATEX file prepared by the author.

MNRAS **000**, 1–22 (2020) Preprint 20 August 2020 Compiled using MNRAS LATEX style file v3.0

Redshift estimates for fast radio bursts and implications on intergalactic magnetic fields

S. Hackstein[1⋆], M. Brüggen[1], F. Vazza[1,2], L. F. S. Rodrigues[3]
[1] *Hamburger Sternwarte, University of Hamburg, Gojenbergsweg 112, 21029, Germany*
[2] *University of Bologna, Department of Physics and Astronomy, Via Gobetti 93/2, I-40129, Bologna, Italy; Istituto di Radioastronomia, INAF, Via Gobetti 101,40129 Bologna, Italy*
[3] *Department of Astrophysics/IMAPP, Radboud University, Postbus 9010, 6500 GL, Nijmegen, Netherlands*

20 August 2020

ABSTRACT

Context: Fast Radio Bursts are transient radio pulses from presumably compact stellar sources of extragalactic origin. With new telescopes detecting multiple events per day, statistical methods are required in order to interpret observations and make inferences regarding astrophysical and cosmological questions.

Purpose: We present a method that uses probability estimates of fast radio burst observables to obtain likelihood estimates for the underlying models.

Method: Considering models for all regions along the line-of-sight, including intervening galaxies, we perform Monte-Carlo simulations to estimate the distribution of the dispersion measure, rotation measure and temporal broadening. Using Bayesian statistics, we compare these predictions to observations of Fast Radio Bursts.

Results: By applying Bayes theorem, we obtain lower limits on the redshift of Fast Radio Bursts with extragalactic DM $\gtrsim 400$ pc cm^{-3}. We find that intervening galaxies cannot account for all highly scattered Fast Radio Bursts in FRBcat, thus requiring a denser and more turbulent environment than a SGR 1935+2154-like magnetar. We show that a sample of $\gtrsim 10^3$ unlocalized Fast Radio Bursts with associated extragalactic RM ≥ 1 rad m^{-2} can improve current upper limits on the strength of intergalactic magnetic fields.

Key words: cosmology: observations – cosmology: large-scale structure of universe – galaxies: intergalactic medium – galaxies: magnetic fields – polarization – radio continuum: general

1 INTRODUCTION

Fast Radio Bursts Fast radio bursts (FRBs) are millisecond transient sources at ≈ 1 GHz with very high luminosities, first discovered by Lorimer et al. (2007). Their observed dispersion measure (DM) often exceeds the contribution of the Milky Way (MW), suggesting an extragalactic origin. FRBs have the potential to help answer many long-lasting astrophysical and cosmological questions (e.g. Katz 2016; Ravi et al. 2019; Petroff et al. 2019, for reviews), provided theoretical predictions can be tested against observations. For this purpose, we present a Bayesian framework to constrain models of FRB sources as well as the different regions along their lines-of-sight (LoS): the intergalactic medium (IGM), the host and intevening galaxies as well as the local environment of the progenitor.

FRB progenitor Numerous models have been put forward that explain the origin of FRBs. These models are collected in the living theory catalog[1] (Platts et al. 2018). Many models assume that flares of young neutron stars cause shock waves in the surrounding medium, where gyrating particles emit coherent emission (Popov & Postnov 2010; Lyubarsky 2014; Murase et al. 2016; Beloborodov 2017; Metzger et al. 2019). Cataclysmic events usually consider interactions of magnetic fields during the merger of two compact objects, e. g. two neutron stars (Wang et al. 2016), or during the collapse of a single object, e. g. neutron star to black hole (Fuller & Ott 2015). The search for an FRB counter-part proves elusive (Scholz et al. 2016; Bhandari et al. 2017; Scholz et al. 2017; Xi et al. 2017), except for the possible detection of a transient γ-ray counterpart to FRB131104

⋆ E-mail: stefan.hackstein@hs.uni-hamburg.de

[1] frbtheorycat.org

(DeLaunay et al. 2016) and a γ-ray burst with spatial coincidence to FRB171209 (Wang et al. 2020), which both point to magnetars (see also Metzger et al. 2017; Zanazzi & Lai 2020; Li & Zhang 2020). Furthermore, the recent detection of a X-ray flare from Galactic magnetar SGR 1935+2154, accompanied by a radio burst of millisecond duration consistent with cosmological FRBs (Collaboration et al. 2020; Bochenek et al. 2020; Lyutikov & Popov 2020; Mereghetti et al. 2020), provides strong evidence for magnetars as sources of FRBs, though these are required to be different from Galactic magnetars (Margalit et al. 2020).

FRBs as cosmological probes The use of FRBs as cosmological probes has been discussed in several papers. FRBs might be used to constrain the photon mass (Wu et al. 2016), violations of Einstein's equivalence principle (Wei et al. 2015; Tingay & Kaplan 2016), Dark Matter (Muñoz et al. 2016; Sammons et al. 2020; Liao et al. 2020) and cosmic curvature (Li et al. 2018). Several publications discuss the use of DM-redshift relation of either FRBs associated with γ-ray bursts or localized FRBs to constrain the equation of state of dark energy as well as other cosmological parameters (Zhou et al. 2014; Gao et al. 2014; Yang & Zhang 2016; Walters et al. 2018; Wu et al. 2020). Wucknitz et al. (2020) show how to use gravitationally lensed repeating FRBs to constrain cosmological parameters (see also Wei et al. (2018); Jaroszynski (2019)).

FRB localization Most methods to use FRBs as cosmological probes requires the localisation of a large number of FRBs. However, the localization of sources of short-duration signals without known redshift is difficult (Eftekhari & Berger 2017; Mahony et al. 2018; Marcote & Paragi 2019; Prochaska et al. 2019a). The current sample of known host galaxies of five localized FRBs includes massive as well as dwarf galaxies, with some showing high, others low rates of star formation (Tendulkar et al. 2017; Ravi et al. 2019; Bannister et al. 2019; Prochaska et al. 2019b; Marcote et al. 2020).

Here, we show how to use unlocalized FRBs with reasonable assumptions on their intrinsic redshift distribution to test models of FRBs and the intervening matter.

FRB redshift distribution Several researchers have tried to infer the intrinsic redshift distribution of FRBs either by modelling the distribution of DM and other FRB properties with analytical or Monte-Carlo methods (Bera et al. 2016; Caleb et al. 2016; Gardenier et al. 2019), or by performing a luminosity-volume test (Locatelli et al. 2018). They conclude that data sets from different telescopes disagree on the redshift distribution.

There has been previous work to estimate the redshift of individual FRB sources based on their DM (Dolag et al. 2015; Niino 2018; Luo et al. 2018; Walker et al. 2018; Pol et al. 2019). The observed DM is dominated by the long scales of the IGM already at low redshift, $z \lesssim 0.1$. However, possible contributions by high-density regions (e.g. halos of galaxies) or the local environment of the source can bias the use of DM to infer the redshift of the source $z_{\rm FRB}$. Thus earlier work has concluded that only upper limits on $z_{\rm FRB}$ can be derived based on DM.

FRBs as probe for intergalactic magnetic fields Some FRBs show high levels of linear polarization, up to 100 per cent (Michilli et al. 2018; Day et al. 2020). Their associated Faraday rotation measure (RM) contains information on the traversed magnetic field. Akahori et al. (2016) and Vazza et al. (2018) show that DM and RM of FRBs potentially signal information about the intergalactic magnetic field (IGMF). However, so far a detailed investigation of the combined contribution of all other regions along the line of sight is missing.

Magnetic fields in galaxies (e. g. Beck 2016) have been investigated mainly using synchrotron emission via Faraday rotation of background radio sources or RM Synthesis. However, due to limited sensitivity and angular resolution, observing galaxies and their properties becomes increasingly difficult at high redshifts (Bernet et al. 2008; Mao et al. 2017).

Magnetic fields in clusters are of the order of $0.1-10\ \mu$G (e. g. van Weeren et al. 2019). However, the strength and shape of IGMFs in the low-density Universe is still poorly constrained (e. g. Taylor et al. 2011; Dzhatdoev et al. 2018). Current limits range from $B \lesssim 4.4 \times 10^{-9}$ G comoving (Planck Collaboration et al. 2016) to $B \gtrsim 3 \times 10^{-16}$ G (Neronov & Vovk 2010).

In Hackstein et al. (2019), we developed a framework to investigate the combined contribution to RM from all regions along the LoS. We could show that this allows us to tell apart extreme models for the origin of IGMFs. Here, we refine the modelling of IGMFs and investigate how many unlocalized FRBs observed with RM are required to improve current constraints on IGMFs.

Intervening galaxies The LoS to a source at cosmological distances has significant chances to traverse an additional galaxy between host galaxy and the MW (e. g. Macquart & Koay 2013). Due to the lower redshift, contributions to the RM are probably even higher than for the host galaxy, limiting our ability to probe IGMFs. However, intervening galaxies are expected to dominate temporal smearing τ due to the ideal position of the high-density plasma lense (Macquart & Koay 2013). Here we investigate the use of τ to identify LoS with intervening galaxies.

For this purpose, we have created the open-source python software package PREFRBLE(Hackstein 2020), using a framework of Bayesian inference, similar to Luo et al. (2020) and Macquart et al. (2020). The observational measures investigated in this paper are shortly discussed in Sec. 2. In Sec. 3, we summarize the statistical methods used in PREFRBLE. The different models are explained in Sec. 4. A few possible applications of PREFRBLE using FRBs in FRBcat are presented in Sec. 5: Identification of intervening galaxies is discussed in Sec. 5.1. We estimate the host redshift of unlocalized FRBs in Sec. 5.2. In Sec. 5.3 we show how to infer the IGMF from DM and RM of unlocalized FRBs. Finally, we conclude in Sec. 6. A list of all symbols used throughout the paper is shown in Tab. 2. Explanations of subscripts can be found in Tab. 3.

2 OBSERVABLES

2.1 Dispersion measure

When propagating through plasma, radio waves are dispersed, causing a delay in arrival time that scales with the squared wavelength (e. g. McQuinn 2013). This delay is quantified by the frequency-independent DM, defined as the free electron column density

$$\mathrm{DM} = \int_0^d \left(\frac{n_e}{\mathrm{cm}^{-3}}\right) \left(\frac{\mathrm{d}l}{\mathrm{pc}}\right) \mathrm{pc\ cm}^{-3}, \tag{1}$$

i. e. the number of free electrons per unit volume n_e along the LoS to distance d. Due to their large volume filling factor in the cosmic web, filaments, walls and voids contribute most of the DM by the IGM, while galaxy clusters account for only ~ 20 per cent of $\mathrm{DM_{IGM}}$ (Zhu et al. 2018). Thus, DM can be used to infer the distance to the FRB (Dolag et al. 2015; Niino 2018; Luo et al. 2018; Walker et al. 2018; Pol et al. 2019).

2.2 Faraday rotation measure

Linearly polarised radio waves that travel through a magnetised plasma experience a rotation in their polarization angle. This is quantified by the frequency-independent RM, defined as the column density of free electrons times magnetic field along the LoS $B_\parallel$,

$$\mathrm{RM} \approx 0.81 \int_d^0 \left(\frac{n_e}{\mathrm{cm}^{-3}}\right) \left(\frac{B_\parallel}{\mu\mathrm{G}}\right) \left(\frac{\mathrm{d}l}{\mathrm{pc}}\right) \mathrm{rad\ m}^{-2}. \tag{2}$$

However, significant contributions to the RM are expected from all regions along the LoS (e. g. Hackstein et al. 2019), which complicates their interpretation.

RM can be positive and negative, thus contributions from separate regions may cancel each other out. This is considered in the numerical computation of results for the full LoS (Eq. (9)).

2.3 Temporal smearing

Inhomogeneities in a turbulent plasma can partly scatter radio waves off and back onto the LoS. Multipath propagation creates a partial delay of the signal, causing temporal smearing τ of short pulses, as well as angular scattering θ_{scat} of the observed signal. However, τ strongly depends on the wavelength of the scattered wave. It can be calculated by the frequency-independent scattering measure (SM), which is defined as the path integral over the amplitude of the turbulence per unit length, C_N^2, (Macquart & Koay 2013)

$$\mathrm{SM} = \int_l^{l+\Delta l} \left(\frac{C_N^2}{1\ \mathrm{m}^{-20/3}}\right) \left(\frac{\mathrm{d}l}{1\ \mathrm{kpc}}\right) \mathrm{kpc\ m}^{-20/3}. \tag{3}$$

For objects that are part of the Hubble flow, it is convenient to define the effective scattering measure

$$\mathrm{SM_{eff}} = \int_l^{l+\Delta l} C_N^2 (1+z)^{-2} \mathrm{d}l, \tag{4}$$

that refers all quantities back to the observers frame. Macquart & Koay (2013) give an estimate for the amplitude of Kolmogorov turbulence inside of galaxies

$$C_{N,gal}^2 = 1.8{\times}10^{-3} \left(\frac{n_e}{10^{-2}\ \mathrm{cm}^{-3}}\right)^2 \left(\frac{L_0}{0.001\ \mathrm{pc}}\right)^{-2/3} \mathrm{m}^{-20/3}. \tag{5}$$

We follow the argument of Macquart & Koay (2013) and assume a fully modulated electron density, $\delta n_e \approx n_e$, and that the power spectrum of turbulence follows a power law with index β, hence $C_N^2 \propto \langle \delta n_e^2 \rangle L_0^{\beta-3} = \langle n_e \rangle^2 L_0^{\beta-3}$. For a power law with sufficient range, i. e. inner scale $l_0 \ll L_0$, SM is determined by the outer scale of turbulence L_0.

Future observations of FRBs may provide observed SM by comparing θ_{scat} and τ at different frequencies. However, FRBs available in the FRBcat catalog (Petroff et al. 2016) provide only observed τ for the dominant frequency of the burst. Extracting SM from τ requires assumptions on the redshift of source and scattering medium. Hence, by directly predicting τ instead of SM, comparison to observations relies on fewer assumptions.

According to Macquart (2004), the temporal smearing can be approximated by a thin screen approximation, even for media extended along the LoS. For radio signals with wavelength λ_0, scattered by a medium at redshift z_L, Macquart & Koay (2013) provide a numerical expression for the scattering time

$$\tau = 1.8{\times}10^{8}\ \mathrm{ms} \left(\frac{\lambda_0}{1\ \mathrm{m}}\right)^{\frac{22}{5}} (1{+}z_L)^{-1} \left(\frac{D_{\mathrm{eff}}}{1\ \mathrm{Gpc}}\right) \left(\frac{\mathrm{SM_{eff}}}{\mathrm{kpc\ m}^{-20/3}}\right)^{\frac{6}{5}} \tag{6}$$

with effective lensing distance $D_{\mathrm{eff}} = \frac{D_L D_{LS}}{D_S}$, i. e. the ratio of angular diameter distances observer to source D_S, observer to scattering medium D_L and medium to source $D_{LS} \neq D_S - D_L$. This result requires that l_0 is smaller than the length scale of plasma phase fluctuations r_{diff}. Numerical tests show, that for the frequencies of FRBs considered in this paper, $r_{\mathrm{diff}} > l_0 \approx 1$ AU always (See App. A).

We compute results for $\lambda_0 = 0.23$ m, corresponding to a frequency $\nu \approx 1300$ MHz. Temporal scattering at other wavelengths, λ, can simply be computed in post-processing, by applying a global factor of $(\lambda/\lambda_0)^{\frac{22}{5}}$. Considering that $\mathrm{SM_{eff}} \propto (1+z)^{-2}$, Eq. (6) implies temporal scattering occurring within the host galaxy, computed once assuming $z_{\mathrm{FRB}} = 0$, e. g. for the redshift independent model of the local environment, scales with source redshift as $\tau(z_{\mathrm{FRB}}) \propto (1+z_{\mathrm{FRB}})^{-\frac{17}{5}}$.

3 PrEFRBLE

PrEFRBLE[2], "Probability Estimates for Fast Radio Bursts to model Likelihood Estimates", is an open-source Python software package designed to quantify predictions for the RM, DM and SM of FRBs and compare them to observations (Hackstein 2020). The results can be used to obtain estimates of the likelihood of models of progenitors of FRBs as well as the different regions along their LoS.

[2] github.com/FRBs/PreFRBLE

Model likelihood We model the contribution of individual models using Monte-Carlo simulations. The distribution of predicted measures $v(\theta)$, sampled randomly according to a prior distribution $\pi(\theta)$ of model parameters θ, reflects the expected likelihood to observe a given measure, $L(v|\mathcal{M})$, to which we refer as model likelihood. $L(v|\mathcal{M})$ is also known as model evidence or marginal likelihood function, as it is marginalised over any model parameters, i.e.

$$L(v|\mathcal{M}) = \int L'(v|\mathcal{M},\theta)\pi(\theta)\ \mathrm{d}\theta. \tag{7}$$

A detailed description of the Monte-Carlo simulations for the individual models are presented in Sec. 4.

We often use a logarithmic range for the values described by L, resulting in an uneven binning of results. When visualising the model likelihood, we either plot the complementary cumulative likelihood, $L(>x) = \int_x^\infty L(x)\ \mathrm{d}x$, or the product, $L(x)\cdot x$, which is a physical value and not affected by binning.

Combine models of separate regions We consider the contribution from the following regions along the LoS of FRBs: the local environment of the progenitor, the host and intervening galaxies, the IGM. However, we neglect the foregrounds of the MW and the Earth's ionosphere. All of these regions are described by separate models. When provided in the form of likelihoods $L(\mathrm{measure}|\mathrm{model})$ – normalized to $1 = \int L(v|\mathcal{M})\mathrm{d}v$ – the prediction of separate regions can be combined to realistic scenarios via convolution

$$v_{\mathrm{EG}} = v_{\mathrm{Local}} + v_{\mathrm{Host}} + v_{\mathrm{IGM}}, \tag{8}$$
$$L_{\mathrm{EG}} = L_{\mathrm{Local}} * L_{\mathrm{Host}} * L_{\mathrm{IGM}}. \tag{9}$$

This way, we predict the distribution $L(v_{\mathrm{EG}}|z)$ of the extragalactic component of the observed measures $v_{\mathrm{obs}} = v_{\mathrm{MW}} + v_{\mathrm{EG}}$ from FRBs at some redshift z, which can be compared to observations of localized FRBs with carefully subtracted Galactic foregrounds v_{MW}.

In practice, the convolution of likelihoods is obtained by adding samples of identical size for each L and computing the likelihood of the resulting sample. The size of this sample is chosen to be the smallest size of samples used to compute individual L, usually $N \approx 5\cdot 10^4$ (see Sec. 4.1). The error of the convolution is given by the shot-noise of this sample. This is a more conservative estimate than following Gaussian error propagation of individual deviations.

For some regions, e.g. intervening galaxies (Sec. 4.3), the norm of L is < 1, representing the likelihood of no contribution. For computation of the convolution, we consider an amount of $1-\mathrm{norm}$ of events in the corresponding sample to be equal to zero.

Some measures (e.g. RM) can have a positive or negative sign, allowing for contributions from different regions to cancel each other. To account for that, each value in the sample of the logarithmic distribution is attributed a random algebraic sign.

Likelihood of observation The majority of FRBs is not localised and the source redshift, z, is unknown. However, by assuming a distribution of host redshifts, a prior $\pi(z)$, described in Sec. 4.5, we obtain the distribution of some measure, v, expected to be observed,

$$L(v) = \int \pi(z)\ L(v|z)\ \mathrm{d}z. \tag{10}$$

These predictions can be directly compared to observations. In App. B we show the expected contribution of individual models to the signal observed by several instruments.

Multiple measures For the observation of an event with a single measure, v, the likelihood for this to occur in a model $\mathcal{M}$ is the corresponding value of the likelihood $L(v|\mathcal{M})$, obtained in Eq. (10). However, when considering multiple measures v_i, e.g. DM and RM, from the same event, we have to account for their common redshift. Instead of multiplying their individual likelihoods $L_0(v_0)\times L_1(v_1)$, as would be done for separate events, the likelihood of the second measure is thus factored into the integral in Eq. (10),

$$L(\vec{v}) = \int \pi(z)\ L_0(v_0|z)\ L_1(v_1|z)\ \mathrm{d}z = \int \pi(z)\ \prod_i L_i(v_i|z)\ \mathrm{d}z. \tag{11}$$

This way we use the full information provided by an observation with measures v_i instead of reducing it to a ratio of measures (cf. e.g. Akahori et al. 2016; Vazza et al. 2018; Piro & Gaensler 2018).

Bayes factor The model likelihood computed for a single model does not hold any information on its own. Instead, comparing the likelihoods of competing models allows to identify the best-fit candidates and to rule out less likely models. The Bayes factor $\mathcal{B}$ is defined as the ratio of the marginal likelihoods of two competing models (e.g. Boulanger et al. 2018),

$$\mathcal{B}(v|\mathcal{M}_1,\mathcal{M}_0) = \frac{L(v|\mathcal{M}_1)}{L(v|\mathcal{M}_0)}. \tag{12}$$

It quantifies how the observation of v changes our corroboration from model $\mathcal{M}_0$ relative to $\mathcal{M}_1$. By comparing all models to the same baseline model $\mathcal{M}_0$, comparison of $\mathcal{B}$ is straight forward. $\mathcal{B} < 10^{-2}$, i. e. 100 times less likely, is usually considered decisive to rule out $\mathcal{M}_1$ in favour of $\mathcal{M}_0$ (Jeffreys & Jeffreys 1961).

According to Bayes theorem,

$$P(\mathcal{M}|v) \propto L(v|\mathcal{M})\pi(\mathcal{M}), \tag{13}$$

in order to arrive at the ratio of posteriors P, $\mathcal{B}$ has to be multiplied by the ratio of priors π of the models, which quantifies our knowledge due to other observational and theoretical constraints. However, the results of our approximate Bayesian computation should only be used for identification of trends rather than model choices, which need to be confirmed by further analysis (cf. Robert et al. 2011).

4 MODELS

In this section, we explain how to quantify the contributions from the different regions along the LoS. In our benchmark scenario, we assume FRBs to be produced around magnetars, hosted by a representative ensemble of host galaxies. We consider contributions of the IGM as well as a representative ensemble of intervening galaxies and their intersection

probabilities. Finally, we consider the expected distribution of host redshifts for FRBs observed by different telescopes.

4.1 Intergalactic medium

We estimate the contributions of the IGM using a constrained cosmological simulation that reproduces known structures of the local Universe, such as the Virgo, Centaurus and Coma clusters. This simulation was produced using the cosmological magnetohydrodynamical code ENZO (Bryan et al. 2014) together with initial conditions obtained following Sorce et al. (2016). The simulation starts at redshift $z = 60$ with an initial magnetic field, uniform in norm and direction, of one tenth of the maximal strength allowed by CMB observations of PLANCK (Planck Collaboration et al. 2014), i. e. $B_0 \approx 0.1$ nG comoving. Hence, this simulations is called *primordial*. Structure formation and dynamo amplification processes are computed up until redshift $z = 0$, providing us with a realistic estimate of the structure of IGM and residual magnetic fields at high redshift as well as for the local Universe. The constrained volume of $(250\ \mathrm{Mpc}/h)^3$ that resembles the local Universe is embedded in a full simulated volume of $(500\ \mathrm{Mpc}/h)^3$, in order to minimize artifacts from boundary conditions. The adaptive mesh refinement applied in the central region allows to increase resolution in high-density regions by 5 levels to a minimum scale of ≈ 30 kpc. Further information on this model can be found in Hackstein et al. (2018) and Hackstein et al. (2019). A reduced version of this model can be found on crpropa.desy.de under "additional resources", together with the other models probed in Hackstein et al. (2018).

Probability estimate We extract the simulation data along different LoS, using the LightRay function of the Trident package (Hummels et al. 2017). This returns the raw simulation output of all physical fields within each cell of the LoS. The distribution of results from all LoS to the same redshift z is used to assess the likelihood of measures for FRBs hosted at this redshift, e.g. $L(\mathrm{DM_{IGM}}|z_{\mathrm{FRB}})$. With ≈ 50000 LoS, likelihoods above 1 per cent have a shot noise below 0.05 per cent.

Cosmological data stacking The cosmological simulation provides snapshots at several redshifts, namely $z_{\mathrm{snaps}} \in [0.0, 0.2, 0.5, 1.5, 2.0, 3.0, 6.0]$. To extract LoS, we stack the data (e.g. Da Silva et al. 2000; Akahori et al. 2016). As the path lengths of LoS within a redshift interval exceeds the constrained comoving volume of $(250\ \mathrm{Mpc}/h)^3$, we combine randomly oriented segments until the redshift interval is completed. The segments in a snapshot are computed for redshifts above z_{snaps}. This implies that the increased clumping of matter, expected at the end of a redshift interval, is also assumed for higher redshifts within the same interval, which may slightly over-estimate (within a factor $\lesssim 2$) the local matter clustering there, as well as the predictions for RM, SM and τ. However, given that the DM is mostly due to IGM in voids, walls and filaments (e.g. Zhu et al. 2018), effects from over-estimation of matter clustering are negligible.

Intergalactic DM We obtain the proper free electron number density $n_e = \rho/(m_p\ \mu_e)$ from the gas density ρ with

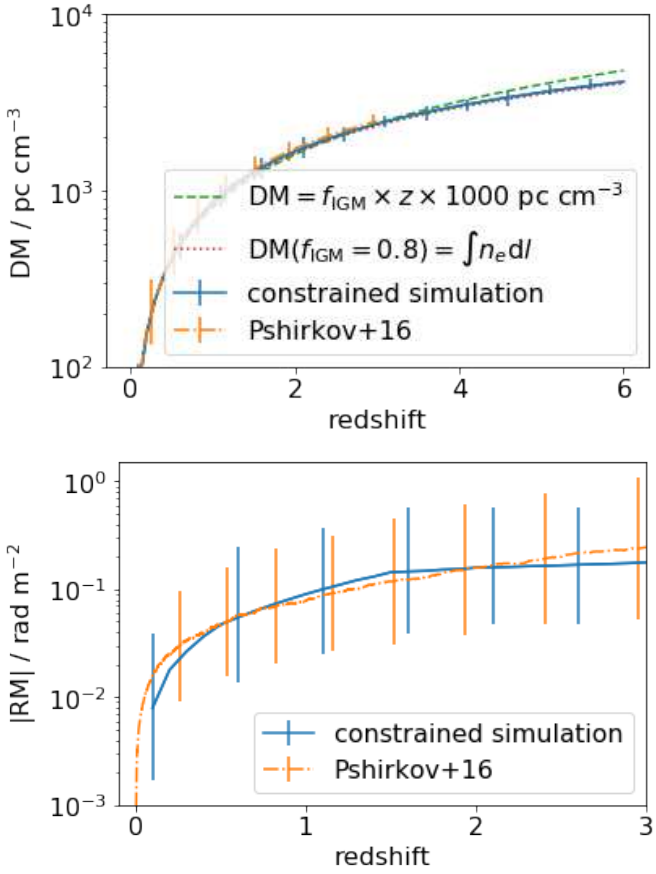

Figure 1. $\langle \mathrm{DM_{IGM}} \rangle$ (top) and $\langle \mathrm{RM_{IGM}} \rangle$ (bottom) as function of source redshift z as obtained from IGM simulation (solid-blue) compared to parametrization (dashed-green & dotted-red) and theoretical prediction obtained via Monte-Carlo simulation (dash-dot-orange). For consistent comparison to estimates following Pshirkov et al. (2016), we use $f_{\mathrm{IGM}} \approx 0.83$, $l_c = 1$ Mpc and $B_0 = 0.1$ nG.

proton mass m_p and molecular weight of electrons $\mu_e = 1.16$, assuming that hydrogen and helium in the IGM are completely ionized, a common assumption after the epoch of reionization. With this, we compute the DM along the LoS using

$$\mathrm{DM}(z_{\mathrm{FRB}}) = \int_0^{d(z_{\mathrm{FRB}})} n_e(z)\ (1+z)^{-1}\ \mathrm{d}l(z). \tag{14}$$

The distribution of results along several LoS provides the expected likelihood of DM from sources at redshift z_{FRB}, $L(\mathrm{DM_{IGM}}|z_{\mathrm{FRB}})$. From this we can compute the estimated mean value

$$\langle \mathrm{DM} \rangle(z) = \int \mathrm{DM} \times L(\mathrm{DM}|z)\ \mathrm{dDM}. \tag{15}$$

The $\langle \mathrm{DM} \rangle$-redshift-relation obtained from the IGM simulation is in good agreement with (cf. Niino 2018; Connor 2019)

$$\langle \mathrm{DM} \rangle = z \times 1000\ \mathrm{pc\ cm^{-3}}, \tag{16}$$

as well as with the predictions obtained following Pshirkov et al. (2016). For the latter, we perform a Monte-Carlo simu-

lation, where we divide the LoS in segments of Jeans-length size and pick random n_e from a log-normal distribution according to Eq. 2 in Pshirkov et al. (2016). In Fig. 1 we compare these numerical expectations with theoretical expectations of DM for FRBs at cosmological distance with uniform IGM

$$\langle \mathrm{DM}(z) \rangle = \frac{c \rho_{\mathrm{crit}} \Omega_b f_{\mathrm{IGM}}}{m_p \mu_e H_0} \int \frac{(1+z)}{H(z)} \, \mathrm{d}z, \tag{17}$$

with Hubble parameter $H(z)$ and $H_0 = H(z=0)$. We use the critical density ρ_{crit} and baryon content of the Universe Ω_b from Planck Collaboration et al. (2014).

IGM baryon content The results of our constrained simulation agree well with Eqs. (16) and (17) if we assume that a fraction $f_{\mathrm{IGM}} = 1$ of baryons resides in the IGM. This is expected as the limited resolution of the simulation does not allow us to properly resolve galaxy formation and the condensation of cold gas out of the IGM. However, it is estimated that in the local Universe about 18 ± 4 per cent of baryonic matter is in collapsed structures (Shull et al. 2012). The 7 ± 2 per cent of baryons found in galaxies are accounted for in the other models in Sec. 4.4 - 4.3. In order to conserve the amount of baryons in our consideration, we have to subtract this part from f_{IGM} and adjust results of our constrained simulation accordingly,

$$L(\mathrm{DM}|f_{\mathrm{IGM}}) = f_{\mathrm{IGM}} \times L(f_{\mathrm{IGM}} \times \mathrm{DM}). \tag{18}$$

Pshirkov et al. (2016) assume $n_e = 1.8 \times 10^{-7}$ cm^{-3} at $z = 0$, which implicitly assumes $f_{\mathrm{IGM}} \approx 0.83$. We choose this value to compute the other graphs in Fig. 1.

Intergalactic RM The contribution to RM scales with the electron density times the magnetic field strength. Accounting for cosmic expansion,

$$\mathrm{RM}(z_{\mathrm{FRB}}) = \int_0^{d(z_{\mathrm{FRB}})} B_{\parallel} \, n_e(z) \, (1+z)^{-2} \, \mathrm{d}z. \tag{19}$$

In Fig. 1 we compare results to theoretical predictions obtained following Pshirkov et al. (2016). The LoS magnetic field is obtained assuming that $B \propto n_e^{2/3}$, with a random change in direction after several Jeans lengths, which is assumed to be the coherence length. We use a correlation length of $l_c = 1$ Mpc and $B_0 = 0.1$ nG, in order to match the settings of the constrained simulation *primordial*. The results agree sufficiently well. The estimates following Pshirkov et al. (2016) assume a steeper $B \sim n_e$ relation than the constrained simulation, thus show slightly lower $\langle \mathrm{RM} \rangle$ for $0.5 \lesssim z \lesssim 2.0$, while the more realistic history of magnetic fields at higher redshift account for the decreased slope $z \gtrsim 1.5$.

Regardless of the magnetic field strength, low-density regions contribute very little to the observed signal, i.e. $\ll 1$ per cent of $\mathrm{RM}_{\mathrm{IGM}}$, making them hard to be detected and easily overshadowed by other regions along the LoS. Hence, $\langle RM \rangle$ is not a direct measure of IGMFs in voids. A more detailed discussion on this matter can be found in App. C.

Given the present lack of available observational detections of extragalactic magnetic fields beyond the scale of clusters of galaxies, there is a large uncertainty in the strength of magnetic fields at higher over-densities, even up to $\rho/\langle\rho\rangle \approx 200$ (Vazza et al. 2017). While within galaxies and galaxy clusters magnetic fields are known to be $0.1 - 10$ μG (van Weeren et al. 2019), models for the origin and amplification of IGMFs differ in their predictions at intermediate density scales, $10 < \rho/\langle\rho\rangle < 200$ (e.g. Vazza et al. 2017), associated with filaments and sheets, capable to imprint a detectable signal on $\langle RM \rangle$. Still, investigation of $L(\mathrm{RM})$ is much more promising than $\langle \mathrm{RM} \rangle$, as it allows for a more detailed investigation of LoS crossing different regions of over-density.

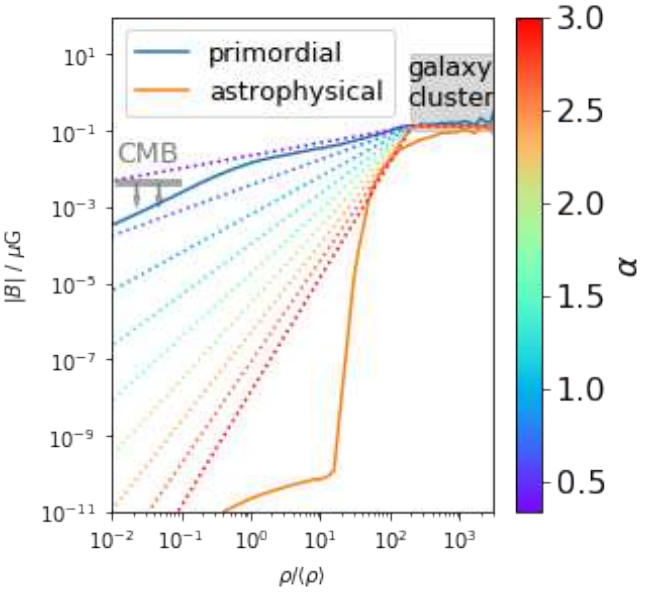

Figure 2. Median magnetic field strength B as function of gas density ρ. The solid lines represent MHD simulations of extreme scenarios, i. e. primordial magnetic field of maximum allowed strength (*primordial*, blue) or minimum strength (*astrophysical*) together with astrophysical dynamo processes and magnetic feedback of AGN. We parametrize this shape with Eq. (20). The dotted lines represent different values of index α, indicated by the colorbar. Constraints by Planck Collaboration et al. (2016) and van Weeren et al. (2019) are indicated by the gray line and shade, respectively.

Model IGMFs By parametrizing the slope of the B-ρ-relation at lower densities, based on different simulations, we can evaluate different shapes and provide general constraints for models of the IGMF. This allows us to quantify the likelihood for a variety of models based on a limited set of parameters without having to perform new simulations.

A simple parametrization is

$$|B| = \beta \rho^{\alpha}, \tag{20}$$

where we vary α and choose β accordingly to match the simulated value at $\rho/\langle\rho\rangle = 200$. The magnetic field-density relation for different α is shown in Fig. 2.

In order to estimate the LoS magnetic field $B_{\parallel}$ according to α, we use the ratio of relations in Fig. 2 as renormalization factor for $B_{\parallel}$ extracted from *primordial*, dependent on the local over-density $\rho/\langle\rho\rangle < 200$. This procedure does reasonably well in reproducing the statistics of other IGM

simulations and allows for rapid investigation of an extensive set of magnetic models. However, we do not explore different magnetic field topologies this way.

Due to their overall similarity in the interesting $1 \leq \rho/\langle\rho\rangle \leq 200$ range of density, as well as to minimise numerical artifacts, we identify the *primordial* model with $\alpha = \frac{1}{3}$, which we use as the baseline to compute the renormalization factor for other choices of α. $\alpha = \frac{1}{3}$ is thus representative for the upper limit on IGMF strength provided by Planck Collaboration et al. (2016), while $\alpha = \frac{9}{3}$ is representative for the lower limit on IGMF strength provided by Neronov & Vovk (2010). The range of α thus roughly brackets all possible cases for the IGMF.

Intergalactic scattering To compute the effective SM, as in Zhu et al. (2018), we assume that turbulence in the IGM follows a Kolmogorov spectrum

$$\mathrm{SM_{IGM}} \approx 1.42 \cdot 10^{-13}\ \mathrm{kpc\ m^{-20/3}} \left(\frac{\Omega_b}{0.049}\right)^2 \left(\frac{L_0}{\mathrm{pc}}\right)^{-2/3} \times \int_0^d \left(\frac{\rho(z)}{\langle\rho\rangle(z)}\right)^2 (1+z)^4 \left(\frac{\mathrm{d}l}{\mathrm{kpc}}\right). \tag{21}$$

Macquart & Koay (2013) state that L_0 can lie between 0.001 pc and 0.1 Mpc. Zhu et al. (2018) require $L_0 \approx 5$ pc in order to explain the $\tau_{\mathrm{IGM}} = 1 - 10$ ms scattering time at 1 GHz to be produced by the IGM alone. However, according to Lazio et al. (2008), the large scales available in IGM would even allow for $L_0 \approx 1$ Mpc. Ryu et al. (2008) investigate the IGM with hydrodynamical simulations and find that typical cosmological shocks during structure formation have curvature radii of the order of $\sim$ few Mpc and represent the characteristic scale of dominant eddies. We adopt the latter as a reference here, and assume a constant $L_0 = 1$ Mpc out to redshift 6. L_0 can be varied in post-processing, by applying a global factor, even if this is beyond the scope of this paper. Still, for $L_0 = 1$ Mpc, contributions of the IGM to temporal smearing τ are much lower than assumed in other work (e.g. Zhu et al. 2018).

The IGM is distributed along the entire LoS, barring negligible parts within host galaxy and MW. Thus, to estimate τ (Eq. (6)), D_{eff} should be of the order of half the distance to the source, which would be the ideal position for a hypothetical lens (Macquart 2004). For a possible source redshift z_{FRB}, we find the redshift z_L of a hypothetical lens that maximizes

$$D_{\mathrm{eff}}(z_{\mathrm{FRB}}, z_L) = \frac{D_A(0, z_L) D_A(z_L, z_{\mathrm{FRB}})}{D_A(0, z_{\mathrm{FRB}})}. \tag{22}$$

We use the resulting values of z_L and D_{eff} in Eq. (6) to calculate τ_{IGM} from $\mathrm{SM_{eff}}$ obtained for FRBs at redshift z_{FRB}.

In practice, it is not necessary to calculate τ_{IGM} for each LoS individually. Instead, Eq. (6) implies identical shape of the likelihood for $\mathrm{SM_{IGM}}$ and τ_{IGM} for sources at redshift z_{FRB},

$$L(\tau_{\mathrm{IGM}}(\mathrm{SM_{IGM}}, z_{\mathrm{FRB}})|z_{\mathrm{FRB}}) \propto L(\mathrm{SM_{IGM}}|z_{\mathrm{FRB}}), \tag{23}$$

where the integral over τ_{IGM} normalizes to 1.

4.2 Host galaxies

In this section, we describe the model for density and magnetic fields in galaxies.

4.2.1 Model description

Lacey et al. (2016) studied the evolution of galaxies with the semi-analytic galaxy formation model Galform. Dark matter halos in an N-body simulation provide a halo merger tree. Furthermore, these halos provide a seed for individual galaxies, whose formation is modelled using differential equations for gas cooling, angular momentum and star formation. Using the evolution of halo properties, including their merger history, they study the evolution of galaxies with a set of coupled differential equations of global galaxy parameters that correspond to well-defined astrophysical processes in galaxies, including AGN as well as stellar feedback. Lacey et al. (2016) provide a set of best-fit initial parameters for galaxy formation theory that reproduces the observed galaxy stellar mass function $\Phi(M_\star, z)$, morphological fractions, stellar metallicity, the Tully-Fisher relation as well as several luminosity functions. The final output of the model is a large sample of galaxies that represents the expected ensemble of galaxies. For brevity, we will refer to set of time evolving properties of an galaxy in Galform's output as a 'galaxy model'.

The sample includes, both, central and satellite galaxies, where the latter corresponds to the most massive galaxy after a halo merger. Since most stellar mass is concentrated in the more massive central galaxies, there is small likelihood for satellites to host FRBs. For simplicity, we thus consider only central galaxies.

Model galactic magnetic field Rodrigues et al. (2019) use the results presented by Lacey et al. (2016) with an optimised size-mass relation. They investigate the evolution of magnetic fields for galaxies using the Magnetizer code (Rodrigues & Chamandy 2020), which numerically solves nonlinear turbulent mean-field dynamo theory (e.g. Beck et al. 1994; Arshakian et al. 2009; Chamandy et al. 2014), assuming thin galactic discs and axial symmetry. For the small-scale magnetic field, they assume that the energy density is half of the interstellar turbulence energy density. This small-scale field serves as a seed field for the large-scale magnetic field and does not enter the computation of RM, for which we only use the coherent field component produced by the turbulent mean-field dynamo. These equations deliver radial profiles of the strength of radial and toroidal components, while the axial component is obtained via $\nabla \cdot \vec{B} = 0$. For the dependence on the axial coordinate, the magnetic field strength is assumed to be proportional to density, which declines exponentially. This description of the coherent magnetic field allows to reconstruct the magnetic field along a LoS of arbitrary orientation and, together with the radial profile of free electron density, can be used to compute LoS integrals through the galaxy.

Galaxy sample Rodrigues et al. (2019) provide a sample of a few million galaxies, in agreement with current observations (see Lacey et al. 2016). This sample represents the ensemble of galaxies in the Universe, thus prior expectations

$\pi(\epsilon)$ for distribution of galaxy properties ϵ, e.g. star formation rate, stellar population, metallicity, luminosity and circular velocity. The total stellar mass $M_\star$ of these galaxies ranges from 10^7 $M_\odot$ to 10^{12} $M_\odot$. By different combinations of disc and bulge properties, all morphologies of axisymmetric galaxies can be reproduced. The sample thus includes spiral, lenticular and elliptical galaxies, represented by spherical galaxy models, but does not include irregular or peculiar galaxies, which account for only ≈ 5 per cent of galaxies.

Magnetic fields in Rodrigues19 sample A prediction of Rodrigues et al. (2019) is that a significant number of galaxies at $z = 0$, especially with low $M_\star$, have very weak large-scale magnetic fields $< 0.05\,\mu$G, because the conditions for a large-scale galactic dynamo are not satisfied. They find evidence for their claim in a sample of 89 galaxies compiled by Beck & Wielebinski (2013).

Furthermore, Rodrigues et al. (2019) assume the large-scale field to be destroyed completely by disc instabilities or during a merger of galaxies of comparable mass. Hence, elliptical galaxies, that result from these processes, have weak regular magnetic fields. Though, these fields can be amplified to μG strength in a time scale of $2-3$ Gyr (Arshakian et al. 2009), estimates of RM for elliptical galaxies with vanishing coherent fields are mostly determined by numerical noise, since only the large-scale magnetic field enters computation. They are, thus, too low to provide a significant contribution to observed RM. However, observations showed fluctuation of mainly low RM with amplitude of order $\lesssim 10$ rad m^{-2} throughout elliptical galaxies (e.g. Owen et al. 1990; Clarke et al. 1992). Thus, ellipticals are expected to not contribute significantly to the observed RM. We hence argue that for the purpose of statistical investigation of measurable RM, the *Rodrigues19* sample is well-suited to represent the entire ensemble of galaxies.

4.2.2 Probability estimate

We obtain the likelihood $L(\mathrm{DM_{host}}|z_\mathrm{FRB})$ for the contribution of an unknown host at redshift z_FRB by a prior weighed integral, e.g.

$$L(\mathrm{DM_{host}}|z) = \int L'(\mathrm{DM_{host}}|\epsilon, z)\ \pi(\epsilon|z)\ \mathrm{d}\epsilon, \tag{24}$$

where $L(\mathrm{DM_{host}}|\epsilon, z)$ is the likelihood of the expected contribution for an individual galaxy with properties ϵ at redshift z. The prior of ϵ at z is denoted by $\pi(\epsilon|z)$.

$$L'(\mathrm{DM}|\epsilon, z) = (1+z)L((1+z)DM|\epsilon) \tag{25}$$

is the likelihood of the signal as seen by the observer, computed from the modeled expectation of residual DM. Similar relations hold for SM and RM, that evolve as $(1+z)^{-2}$ (cf. e.g. Hackstein et al. 2019).

Monte-Carlo simulation In practice, it is not necessary to compute the full likelihood $L(\mathrm{DM}|\epsilon)$ for each galaxy model. Instead, we do a Monte-Carlo experiment and repeatedly pick a random axisymmetric model, inclination angle and impact parameter. By choosing the sample according to priors π, the distribution of those results provides us with the required likelihood.

For the impact parameter, we naturally assume uniform π, while the inclination is sampled from a cosine distribution, expecting more galaxies face on, according to the orientation of galaxies in the local supercluster (e.g. Hu et al. 1995; Yuan et al. 1997). We assume FRBs to be produced by magnetars, which are most likely found in the vicinity of star-forming regions. Molecular gas, which allows for effective cooling, is a good tracer of star-forming regions (e.g. Arce et al. 2007). Along the LoS, defined by inclination and impact parameter, we compute the integral to position of the source. The path integral is computed only within an ellipsoid whose major axis and disc size, respectively, are 3.5 times scale height and 2.7 times half-mass radius of a given galaxy model, which marks the distance where surface mass density reaches 1 per cent of the central value. The position of the source is picked randomly according to the profile of molecular gas density. The LoS is excluded, if it does not enter the galactic ellipsoid or in case that the molecular gas density along the LoS does not surpass a minimum value of $\rho_\mathrm{mol} \gtrsim 10^{-37}$ g cm^{-3}, chosen for numerical reasons, which is too low to indicate the possible habitat of magnetar FRB progenitors. For this choice, the models are representative for the contribution of stellar disks of galaxies. However, a physically motivated certainly higher limit on ρ_mol would even more concentrate the assumed distribution of source positions on the dense part of their host galaxies and thus account for increased contributions to the observed measures.

Furthermore, the likelihood for LoS to contain a possible FRB progenitor is proportional to the column density of molecular gas. However we argue that this is dominated by path length and the resulting likelihood function is well reproduced by disregarding LoS with probability given by the path length through the ellipsoid (see App. D) divided by maximum path length, i. e. disk diameter.

The galaxy population modelled by Rodrigues et al. (2019) represents theoretical prior expectations $\pi(\epsilon|z_\mathrm{FRB})$ of the distribution of galaxy properties ϵ at different source redshifts z_FRB. Sampling the entirety of this population naturally accounts for this prior assuming that all types of axisymmetric galaxies host FRBs. However, more massive galaxies contain a greater number of stars, thus are more likely to host FRB progenitors. To account for this, we multiply the prior of galaxies by their total stellar mass $M_\star$. We pick a sample of $\approx 10^6$ galaxy models and compute for each a number of 10 LoS. The results for this sample of $\approx 10^7$ LoS provides a converged estimate of the likelihood for the host contribution, without knowledge of the inclination angle, source position or galaxy type. With this sample, likelihoods above 1 per cent are accurate to less than 0.003 per cent.

4.2.3 Host scattering

To estimate the SM contributed by the host galaxy, we use Eqs. (3) & (5). We set $L_0 = 0.1$ kpc to the maximum size of supernova remnants, before they drop below the sound speed.

Finally, we calculate τ from Eq. (6). Obviously, z_L is identified with the redshift of the host galaxy z_FRB. Inside the host galaxy, the angular diameter distance to source and plasma along the LoS are almost identical, $D_S \approx D_L$. hence $D_\mathrm{eff} \approx D_{LS}$. To estimate scattering in the host galaxy, D_eff

should be characteristic for the distance to the bulk of material (Macquart 2004). A reasonable choice is half the path length of LoS inside the host galaxy, obtained for the individual LoS. The same choice is a fair approximation for scattering in the MW. Here, we approximate the path length by the redshift-dependent average size of galaxies of the probed sample. This assumption yields a reasonable estimate on the magnitude of τ, which is below < 10 ns, hence not observable by current instruments.

4.3 Intervening galaxies

Model description The results of Rodrigues et al. (2019), used to model the host galaxy in Sec. 4.2, can also be used to model the contribution of intervening galaxies. The expectation for a variety of galaxies can be computed in the same manner, i.e. for a random inclination angle and impact parameter we can compute LoS integrals through the entire galaxy. By sampling the galaxy population of Rodrigues et al. (2019) at redshift $z_{\rm Inter}$, we obtain the model likelihood for contributions from intervening galaxies at this redshift, $L(\mathrm{RM}_{\rm Inter}|z_{\rm Inter})$. Of course, the impact parameter and the inclination angle have a prior with uniform and cosine shape, respectively (cf. Sec. 4.2). However, we only consider LoS within the ellipsoid representing the galaxy model, which is considered to where it falls below 1 per cent of the central surface mass density (cf. Sec. 4.2). Smaller galaxies have less chance to intersect a LoS and in order to account for this, we multiply the prior of galaxies by their squared half-mass radius.

Intersection probability The mean number of intersecting galaxies along a LoS to source at redshift $z_{\rm FRB}$ can be estimated by (Macquart & Koay 2013)

$$N_{\rm Inter}(z_{\rm FRB}) = \int_0^{z_{\rm FRB}} \pi r_{\rm gal}^2 \, n_{\rm gal} \frac{d_H(z)}{(1+z)} \, \mathrm{d}z = \int_0^{z_{\rm FRB}} \pi_{\rm Inter}(z) \, \mathrm{d}z, \tag{26}$$

with galaxy radius r_{gal}, galaxy number density n_{gal} and Hubble radius $d_H(z)$. By definition, the complementary cumulative galaxy stellar mass function yields the number density of galaxies as function of minimum mass M_0

$$n_{\rm gal}(> M_0, z) = \int_{M_0}^{\infty} \Phi(M_\star, z) \, \mathrm{d}M_\star. \tag{27}$$

By accounting for $\Phi(M_\star, z)$) in the *Rodrigues19* sample (see Lacey et al. 2016), we obtain realistic contribution from intervening galaxies of all $M_\star > M_0$, independent on the choice of M_0.

We obtain $n_{\rm gal}$ from the number of galaxies and considered volume of the *Rodrigues19* sample and $\langle r_{\rm gal} \rangle$ as 2.7 times the average half-mass radius of galaxy models used to sample L (cf. Sec. 4.2). Thus, $\langle r_{\rm gal} \rangle$ considers the galaxies weighted by their intersection probability $\propto r_{\rm gal}^2$. In Fig. 3, top, we show both, $n_{\rm gal}$ and $\langle r_{\rm gal} \rangle$, as function of redshift. Galaxies increase their mass and volume over time, thus $\langle r_{\rm gal} \rangle$ decreases with redshift. Mergers also reduce the number of galaxies within a fixed volume, thus $\frac{\mathrm{d}n_{\rm gal}}{\mathrm{d}z} > 0$. However, we only consider galaxies with $M_\star > 10^7 M_\odot$, which have to grow from smaller galaxies at higher redshift that we do not account for. Thus, $n_{\rm gal}$ decreases at high redshift. However, since we consider all galaxies $> 10^7 M_\odot$, independent of a brightness limit, $n_{\rm gal} \approx 0.03$ Mpc^{-3} at $z = 0$, significantly higher than assumed elsewhere (e.g. $n_{\rm gal} \approx 0.007$ Mpc^{-3} in Macquart & Koay 2013).

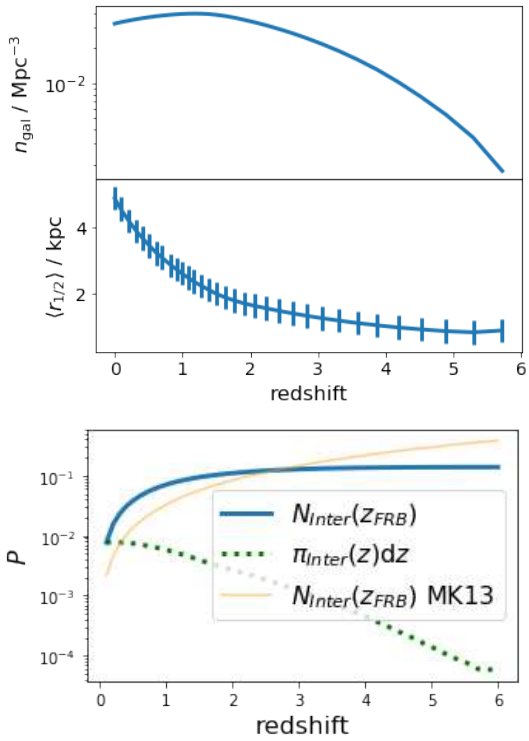

Figure 3. Top: comoving number density $n_{\rm gal}$ and average half-mass radius $r_{1/2}$ of the considered galaxy sample as function of redshift. Galaxies grow in average size ($\mathrm{d}r_{1/2}/\mathrm{d}z < 0$), mostly due to expansion and mergers, which also reduces their number in a fixed volume ($\mathrm{d}n_{\rm gal}/\mathrm{d}z < 0$), together determining the shape of $\pi_{\rm Inter}(z)$. Note that we do not consider galaxies with stellar mass $M_\star < 10^7 M_\odot$, causing $n_{\rm gal}$ to go down at high redshift. The implicit number density assumed for galaxies with different mass threshold are considered according to galaxy stellar mass function and redshift evolution (see Lacey et al. 2016). Bottom: average number of intervening galaxies (solid blue) in LoS to source at redshift $z_{\rm FRB}$ and prior (dotted green) for intervening galaxy at z (Eq. (26)) per redshift interval $\mathrm{d}z = 0.1$. The thin orange line shows the expectation of Macquart & Koay (2013).

Probability estimate The integrand of Eq. (26) defines a prior $\pi_{\rm Inter}(z)$ for the LoS to intersect a galaxy at redshift z, which can be used to obtain the likelihood, e.g. of RM, from intervening galaxies along a LoS to source redshift $z_{\rm FRB}$,

$$L(\mathrm{RM}_{\rm Inter}|z_{\rm FRB}) = \int_0^{z_{\rm FRB}} L(\mathrm{RM}_{\rm Inter}|z) \; \pi_{\rm Inter}(z) \; \mathrm{d}z. \tag{28}$$

By sampling the entire ensemble of models provided by Rodrigues et al. (2019), all types of axisymmetric galaxies could intervene the LoS. We pick a sample of $\approx 10^6$ galaxy models and compute for each a number of 10 LoS. The results for this sample of $\approx 10^7$ LoS provides a converged estimate of the likelihood for the contribution of intevening galaxies,

without knowledge of the inclination angle, galaxy type or position along the LoS. Again, likelihoods above 1 per cent are accurate to less than 0.003 per cent.

Probability of intervening galaxies We assume that all progenitors of FRBs are located within a galaxy. Thus, for a FRB hosted at redshift $z_{\rm FRB}$, the normalization, e. g. of $\int L(\mathrm{RM_{host}}|z_{\rm FRB})\ \mathrm{dRM_{host}} = 1$, indicates that the host contributes $\mathrm{RM_{host}}$ within the range of $L(\mathrm{RM_{host}}|z_{\rm FRB})$ to each LoS. In order to represent the probability of intersecting another galaxy, $L(\mathrm{RM_{Inter}}|z_{\rm FRB})$ must be normalized to the expected average number of intervening galaxies per LoS, (Eq. (26))

$$N_{\rm Inter}(z_{\rm FRB}) = \int L(\mathrm{RM_{Inter}}|z_{\rm FRB})\ \mathrm{dRM_{Inter}}, \tag{29}$$

indicating that $\mathrm{RM_{Inter}}$ are only contributed to $N_{\rm Inter} < 100$ per cent of LoS. The correct normalization $N_{\rm Inter}$ highly depends on the choice of $r_{\rm gal}$, which should thus represent the size of galaxy model considered for computation. The results for $N_{\rm Inter}(z)$ and $\pi_{\rm Inter}(z)$ are shown in Fig. 3. Compared to results of Macquart & Koay (2013), we expect more galaxies to intersect the LoS to low redshifts $z < 3$, e.g. they expect less than 5 per cent of LoS to $z = 1.5$ compared to < 10 per cent for the *Rodrigues19* sample, which is due to the ≈ 4 times higher $n_{\rm gal}$ at $z = 0$. However, we expect less LoS to high redshift $z > 3$ to be intervened, e.g. they expect < 40 per cent for $z = 4$, while only < 30 per cent in *Rodrigues19*. Though the decreasing size of galaxies is partly responsible, this feature is dominated by the artificial choice to not account for galaxies with $M_\star < 10^7\ M_\odot$.

Intervening galaxy scattering For the temporal smearing τ by an intervening galaxy, $D_{\rm eff}$ depends on redshift of both, the source $z_{\rm FRB}$ and the intervening galaxy $z_{\rm Inter}$, requiring explicit computation of $D_{\rm eff}$ in Eq. (6), Since only global factors are applied to $\mathrm{SM_{eff}}$, the expected contribution of intervening galaxies at redshift $z_{\rm Inter}$ to SM, $L(\mathrm{SM_{Inter}}|z_{\rm Inter})$, and to τ, $L(\tau_{\rm Inter}|z_{\rm FRB}, z_{\rm Inter})$, observed for FRBs hosted at redshift $z_{\rm FRB}$, are of identical shape (cf. Eq. (23)). The likelihood $L(\tau_{\rm Inter}|z_{\rm FRB})$ for contribution of an intervening galaxy at unknown redshift to the signal from source at $z_{\rm FRB}$ is obtained by the prior-weighed integral over $z_{\rm Inter}$,

$$L(\tau_{\rm Inter}|z_{\rm FRB}) = \int L(\tau_{\rm Inter}|z_{\rm FRB}, z)\ \pi_{\rm Inter}(z)\,\mathrm{d}z\,, \tag{30}$$

with $\pi_{\rm Inter}(z)$ from Eq. (26).

4.4 Local environment

Model description and probability estimate Here, we assume that all FRBs are produced by magnetars (Metzger et al. 2017; Zanazzi & Lai 2020). The contribution to the DM and RM from the local environment of a young neutron star are described in Piro & Gaensler (2018). More details on this model, the Monte-Carlo simulation to obtain probability estimates as well as the considered priors can be found in Hackstein et al. (2019), where we quantify predictions of the DM and RM. We consider a sample of 10^7 events, thus likelihoods above 1 per cent are accurate to less than 0.003 per cent. Note that the majority of magnetars in this model are of decent age $> 10^2$ yr and thus contribute rather low amounts of DM and RM (cf. Figs. 7 & 8 in Piro & Gaensler 2018).

Local scattering To estimate the SM contributed by the local environment of a magnetar, we use Eqs. (3) & (5). Calculation of the SM is hence almost identical to DM,

$$\mathrm{SM} = \alpha_c L_0^{-2/3} \int n_e^2\ \mathrm{d}l, \tag{31}$$

where α_c is a factor and L_0 the outer scale. Assuming that n_e is constant within the different regions of the supernova remnant, their contribution can be computed as (cf. to Eqs. 10 & 13 in Piro & Gaensler 2018)

$$\mathrm{SM_{SNR}} = \alpha_c L_0^{-2/3} n_r^2 (R_c - R_r), \tag{32}$$

$$\mathrm{SM_{ISM}} = 16\alpha_c L_0^{-2/3} n^2 (R_b - R_c), \tag{33}$$

for the *uniform* case and (cf. to Eqs. 38 & 39 in Piro & Gaensler 2018)

$$\mathrm{SM_{SNR}} = \alpha_c L_0^{-2/3} n_r^2 (R_c - R_r), \tag{34}$$

$$\mathrm{SM_{w,sh}} = 16\alpha_c L_0^{-2/3} n^2 (R_b - R_c), \tag{35}$$

$$\mathrm{SM_{w,unsh}} = \alpha_c L_0^{-2/3} n^2 R_b, \tag{36}$$

for the *wind* case, where $\alpha_c = 0.18$ kpc $\mathrm{m}^{-20/3}$, L_0 is in pc, n and n_r are in cm^{-3}. Equations for n_r as well as radii R_b and R_c are given in Piro & Gaensler (2018). For L_0 we assume the size of the supernova remnant R_b. To obtain the observed $SM_{\rm eff}$ caused by the local environment at cosmological distance, these results are shifted to the redshift, $z_{\rm FRB}$, by applying factor $(1+z_{\rm FRB})^{-2}$, according to Eq. (4). For our benchmark model, we consider magnetars in the *wind* case, embedded in an environment dominated by stellar winds from the heavy progenitor star.

Inside the host galaxy, the angular diameter distance to source and lensing material are almost identical, $D_S \approx D_L$ (cf. Eq. (6)), hence $D_{\rm eff} \approx D_{LS}$. To estimate scattering in the host galaxy, $D_{\rm eff}$ should be characteristic for the distance to the bulk of material (Macquart 2004). A reasonable choice is half the path length of LoS inside the host galaxy, obtained for the individual LoS. For the local environment of the FRB progenitor, $D_{\rm eff}$ is well approximated by half the size of the environment. In case of the magnetar model, this is half the size of the supernova remnant, $D_{\rm eff} = R_b/2$. Obviously, z_L is identified with the redshift of the host galaxy $z_{\rm FRB}$, allowing us to calulate τ from Eq. (6).

4.5 Redshift distribution

Reasonable choices for the redshift prior of FRBs $\pi(z)$ should assume a physically motivated intrinsic distribution of z and consider instrument responses that determine the detectable subset of the population. FRBPOPPY[3] (Gardenier et al. 2019) is a python-package built to investigate the population of FRBs. It allows to assume reasonable intrinsic redshift distributions and to apply the selection effects of individual instruments due to sensitivity, wavelength range, or time resolution.

[3] github.com/davidgardenier/frbpoppy

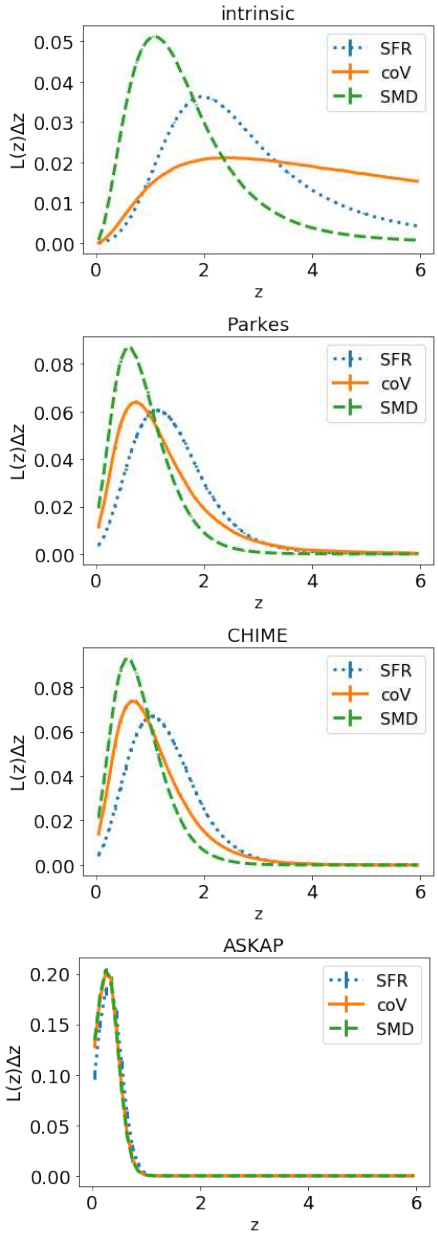

Figure 4. Top: Intrinsic distribution of host redshift for FRBs in case of FRB redshift distribution following stellar mass density (SMD, dashed), comoving volume (coV, solid) or star formation rate (SFR, dotted) (Eqs. (37) - (39)). Others: distribution of redshifts, expected to be observed by Parkes, CHIME or ASKAP (top to bottom). These estimates serve as a prior for redshift $\pi(z)$ in the interpretation of z-dependent measures of unlocalized FRBs. The barely visible error bars show the shot noise of the Monte-Carlo sample. The redshift bins are scaled linearily, thus each bin has the same $\Delta z = 0.1$.

Assumed intrinsic redshift distribution We consider three different intrinsic redshift distributions for FRBs, presented by Gardenier et al. (2019). The simplest assumption is a constant number density of FRBs,

$$n_{\rm FRB} = \text{const.} \tag{37}$$

This suggests the redshift distribution of FRBs to have a constant comoving density across epochs (coV).

Many models consider stellar objects or the merger of those as sources of FRBs. These are more likely to occur in regions with a high number density of stars, thus suggesting the redshift distribution of FRBs to follow the evolution of the stellar mass density (SMD, Madau & Dickinson 2014),

$$n_{\rm FRB} = \int_z^\infty \frac{(1+z')^{1.7}}{1+[1+z')/2.9]^{5.6}} \frac{{\rm d}z'}{H(z')}. \tag{38}$$

Young neutron stars and magnetars are widely considered to be the most likely sources of FRBs. Such stars are more likely to be found in the vicinity of star-forming regions, implying the FRB redshift distribution to follow the evolution of the cosmic star formation rate (SFR, Madau & Dickinson 2014),

$$n_{\rm FRB} = \frac{(1+z')^{2.7}}{1+[1+z')/2.9]^{5.6}}. \tag{39}$$

All other parameters are set to the values of the *complex* population presented in Gardenier et al. (2019). In Fig. 4 we show the intrinsic distribution of host redshifts, assuming the FRB population to follow SMD, coV or SFR, as well as corresponding $\pi(z)$ expected to be observed with ASKAP (in coherent mode), CHIME or Parkes.

Probability estimate Using FRBPOPPY, we generate a random sample of 10^7 FRBs and their intrinsic properties, such as luminosity and pulse width, following one of the assumed redshift distributions. Subsequently, we apply the selection effects of ASKAP, CHIME and Parkes to filter out FRBs that can actually be measured by those instruments. The initial parameters are optimized in order to reproduce the observed distribution of DM and fluence (for more details, see Gardenier et al. 2019). The redshift distribution of the intrinsic and selected samples is shown in Fig. 4. The latter serve as prior $\pi(z)$ on the host redshift of unlocalized FRBs observed by the corresponding telescope. With a remaining sample size of at least 3×10^4, likelihoods above 1 per cent are accurate to less than $\lesssim 0.05$ per cent.

Discussion The main parameter responsible for the difference in source selection is the gain of the telescope. The values of gain used in FRBPOPPY ranges from 0.1 K Jy^{-1} (ASKAP) over 0.69 K Jy^{-1} (Parkes) to 1.4 K Jy^{-1} (CHIME). Since FRBs at large redshifts are too faint to be observed, our results suggest that the cosmic volume probed by ASKAP is not expected to go beyond $z \approx 1.0$. In this range, the populations can hardly be distinguished since they are all dominated by the increasing volume. However, Parkes and CHIME have rather similar $\pi(z)$ and the chance to observe FRBs at higher redshift $z > 1.0$ differs reasonably between the assumed intrinsic redshift distributions. The generally low distance of FRBs observed by ASKAP makes them more vulnerable to the unknown local contributions.

Note that FRBPOPPY uses estimates, e.g. of DM(z), in order to decide how many FRBs will be observed at a given redshift. Theses estimates have been produced using slightly different assumptions on the contributing regions. However, the DM is dominated by the IGM and the analytical description used in FRBPOPPY provides a good match to our estimates. Hence, we argue that this does not alter

the general conclusions of this work. In the future, we plan to converge the assumptions used in FRBPOPPY and PRE-FRBLE in order to provide consistent results. However, this is not trivial, as the change in one parameter can influence the best-fitting choice for other parameters, thus requires a repetition of the inference presented in Gardenier et al. (2019).

5 APPLICATIONS

5.1 Identification of intervening galaxies

5.1.1 Method

In Fig. 5 we show the complementary cumulative likelihood $L(>\tau)$ of extragalactic τ expected to be observed by different instruments in three similar versions of our benchmark scenario. Each considers contributions from the local environment of the source, assumed to be a magnetar, the host galaxies and the IGM (see Sec. 4). The three versions are

i. *no intervening* only LoS without intervening galaxies.
ii. *only intervening* LoS with a single galaxy along the LoS, at random redshift according to $\pi_{\rm Inter}(z)$ (Fig. 3).
iii. *realistic* LoS with and without intervening galaxies. The ratio of their number for sources at redshift $z_{\rm FRB}$ is given by $N_{\rm Inter}(z_{\rm FRB})$ (Fig. 3).

We quantify the likelihood of FRBs observed with τ to have an intervening galaxy along the LoS by computing the Bayes-factor $\mathcal{B}$ (Eq. (12)) as the ratio of $L(\tau)$ in the two extreme scenarios. $\mathcal{B}(\tau) > 100$ signals that τ is 100 times more likely to be observed in case of an intervening galaxy. However, according to Bayes theorem (Eq. (13)), in order to factor in our previous knowledge, $\mathcal{B}$ has to be multiplied by the ratio of priors, which can be identified as the expected number of LoS which contain at least one intervening galaxy $\pi_{\rm I}$. In our model, this can be obtained by integrating the expected number of LoS with intervening galaxies $N_{\rm Inter}(z_{\rm FRB})$ (Eq. (26)) as function of source redshift $z_{\rm FRB}$, multiplied by prior of source redshift $\pi(z_{\rm FRB})$, obtained in Sec. 4.5,

$$\pi_{\rm I} = \int N_{\rm Inter}(z_{\rm FRB})\ \pi(z_{\rm FRB})\ {\rm d}z_{\rm FRB}. \tag{40}$$

Assuming the intrinsic distribution of $z_{\rm FRB}$ to follow SMD, we predict intervening galaxies along LoS for $\pi_{\rm I} = 2.5$ per cent, 5.9 per cent and 6.2 per cent of FRBs observed by ASKAP, CHIME and Parkes, respectively.

Multiplying the corresponding ratio of priors $\pi_{\rm I}/(1-\pi_{\rm I})$ to $\mathcal{B}$ yields the ratio of posteriors P (Eq. (13)). However, the ratio of posteriors does not exceed 100, marking 99 per cent certainty of an intervening galaxy along the LoS. This is because the scenario without intervening galaxies cannot provide $\tau > 0.06$ ms, according to our models, while the ratio of P for slightly lower values of τ does not yet reach 100.

5.1.2 Results

For FRBs observed by ASKAP and Parkes at $\nu = 1300$ MHz, $\tau_{\rm dist} = 0.06$ ms marks the minimum temporal broadening that is certainly associated to an intervening galaxy. Also, for FRBs observed by CHIME at lower characteristic frequency, $\nu = 600$ MHz, where scattering effects are more severe (see Sec. 2.3), $\tau_{\rm dist} = 1.8$ ms. We find that 26.8 per cent, 30.8 per cent and 30.6 per cent of the sightlines with intervening galaxies will show $\tau > \tau_{\rm dist}$, for ASKAP, Parkes and CHIME, respectively. Thus, we predict that these telescopes observe 0.7 per cent, 1.9 per cent, and 1.8 per cent of FRBs with $\tau \geq \tau_{\rm dist}$. However, for the FRBs listed in FRBcat, we find 3.6 per cent, 48 per cent and 20 per cent above the corresponding $\tau_{\rm dist}$.

5.1.3 Discussion

The expected number of LoS with intervening galaxies is smaller for ASKAP since a narrower redshift range is probed than by CHIME and Parkes (cf. Fig. 4). $D_{\rm eff}$ is significantly smaller at $z < 1$ and galaxies are denser and more turbulent at higher z, thus providing smaller τ at lower redshift. The majority of LoS with $\tau < \tau_{\rm dist}$ either cross smaller galaxies with a low contribution to all measures, intersect only small parts of an intervening galaxy, or the additional galaxy is located close to source or observer, resulting in a sub-optimal $D_{\rm eff}$. Even though most of significant contribution to the other measures, i.e. DM and RM, will arise from the latter subset, consideration of intervening galaxies is still necessary for reasonable interpretation of those measures.

For all telescopes, the observed number of $\tau > \tau_{\rm dist}$ in FRBcat is 5 to 25 times more than expected. Moreover, the total number of LoS with intervening galaxies is reasonably smaller than this number. Thus, the high number of $\tau > \tau_{\rm dist}$ observed by Parkes can hardly be attributed to intervening galaxies alone, which might only account for $\lesssim 13$ per cent of these events. This is despite the fact, that we expect a higher number of intervening galaxies than earlier works (e.g. Macquart & Koay 2013). Note that we do not consider the circumgalactic medium, which would certainly increase this estimate.

For the contribution of the IGM, we assume a physically motivated $L_0 = 1$ Mpc, hence low contribution to τ. Still, in order for the IGM to account for the remaining events, $L_0 \lesssim 1$ pc would be required.

Our magnetar model for the environment local to the source is the only region that provides $\tau \lesssim \tau_{\rm dist}$ (see App. B). However, from the recent observation of an FRB-like radio burst from a Galactic magnetar, Margalit et al. (2020) conclude that magnetars responsible for cosmological FRBs result from other origins than normal core-collapse supernovae, such as superluminous supernovae, accretion-induced collapses or neutron star mergers. Such sources can produce visible FRBs somewhat earlier (Metzger et al. 2017; Margalit et al. 2019), in a much denser and more turbulent state of the remnant. These models might thus account for a stronger scattering than our model.
Considering a higher mass threshold for galaxies than $M_\star \geq 10^7\ M_\odot$ will likely not affect the number of LoS observed with $\tau > \tau_{\rm dist}$ in the realistic sample of FRBs, with and without intervening galaxies. This is because massive galaxies dominate τ and our model realistically considers the galaxy stellar mass function, thus the amount of galaxies with high mass, independent of the chosen minimum mass of small galaxies. Still, other versions of galaxy formation

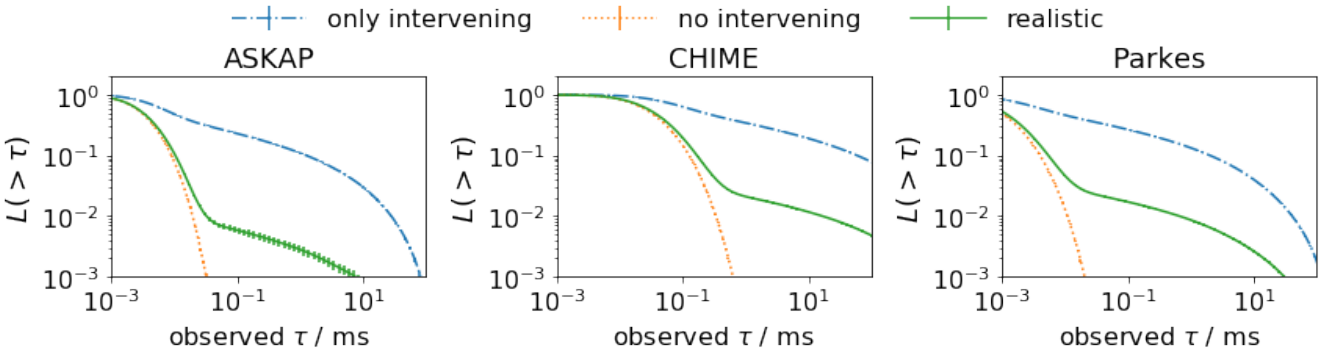

Figure 5. Complementary cumulative distribution of τ expected to be observed with ASKAP (left), CHIME (center) and Parkes (right) in our benchmark scenario, considering LoS with exactly one intervening galaxy (dotted-orange) or without any (dash-dotted-blue). The excess of the former at τ_0 shows how many more FRBs are expected with $\tau > \tau_0$ for LoS with intervening galaxies. The solid green line shows expectations for a realistic mix of LoS with and without intevening galaxies.

theory might differ in their predictions, e.g. of turbulence in galaxies at large distance, thus potentially provide higher amounts of $\tau > \tau_{\rm dist}$, which will be visible in $L(\tau)$.

Here we assume that the number density of galaxies $n_{\rm gal}$ is uniform in space. However, $n_{\rm gal}$ increases with the gas density, as more galaxies reside in the dense environment of galaxy clusters. Hence, a more sophisticated approach should consider clustering, e.g. via density profile of LoS, providing each with an individual prior for redshift of galaxy intersection, $\pi_{\rm Inter}(z)$. This way, LoS with high contribution from IGM, associated with high-density regions, would have a higher chance of additional signal by intervening galaxies with an increased chance for multiple intersections. In turn, for LoS that mainly traverse low-density regions, the chance for intervening galaxies would be lower. Accounting for clustering of galaxies would increase the significance of results from RM of FRBs regarding IGMFs and their cosmic origin (Sec. 5.3). However, in this work we are mostly interested in FRBs from high redshift, $z \gtrsim 0.5$, which are most indicative of the IGMF. On this scale, the structure of the Universe can reasonably be considered as fairly homogeneous. We argue that for FRBs from high redshift the statistical results are almost identical to the more sophisticated approach, which is necessary only for the correct interpretation of FRBs from lower redshift.

Note that it is possible to obtain an estimate on the redshift of an intervening galaxy, $z_{\rm Inter}$, by comparing scenarios with $\pi_{\rm Inter}(z) = \delta(z - z_{\rm Inter})$ for different possible $z_{\rm Inter}$. This is, however, beyond the scope of this paper and will be investigated in the future.

5.2 Redshift estimate

5.2.1 Method

Earlier work has estimated the redshift of FRBs, $z_{\rm FRB}$, based on their DM (Dolag et al. 2015; Niino 2018; Luo et al. 2018; Pol et al. 2019). By comparing the likelihood $L({\rm DM}|z_{\rm FRB})$ at different redshifts, upper limits on $z_{\rm FRB}$ are obtained. However, according to Bayes theorem (Eq. 13)

$$P(z_{\rm FRB}|{\rm DM}) \propto L({\rm DM}|z_{\rm FRB})\ \pi(z_{\rm FRB}), \tag{41}$$

these estimates can be improved by using the posterior $P(z_{\rm FRB}|{\rm DM})$ that considers a reasonable prior of source redshifts, $\pi(z_{\rm FRB})$. Not accounting for this prior is equivalent to assuming the same number of FRBs from any redshift, thus ignoring distribution and evolution of FRBs, the telescopes selection effects as well as the fact, that the probed volume increases with distance. The latter drastically lowers the amount of FRBs expected from low redshift $z \lesssim 0.2$, independent of the history of sources. Walker et al. (2018) used a $\pi(z_{\rm FRB})$ deduced from the observed population of gamma-ray bursts and showed that this allows to obtain lower limits on $z_{\rm FRB}$. In Sec. 4.5, we derive a better motivated $\pi(z_{\rm FRB})$, considering intrinsic redshift distributions of FRBs as well as telescope selection effects. By evaluating the contribution of each region along the LoS (see Secs. 4.1 - 4.4), assuming FRBs from magnetars, we can estimate the distribution of extragalactic ${\rm DM_{EG}}$. We calculate the source redshift of FRBs by extracting the expectation value and 3σ-deviation from the posterior P obtained by Eq. (41). In Fig. 6 we show, as an example, the derivation of $z_{\rm FRB}$ for the localized Spitler burst. We obtain redshift estimates based on ${\rm DM_{EG}} = {\rm DM_{obs}} - {\rm DM_{MW}}$ for all FRBs listed in the FRBcat (Petroff et al. 2016). These values of ${\rm DM_{EG}}$ were shown to be correct to $\approxeq 30$ pc cm^{-3} (Manchester et al. 2005). Results are shown in Table 1.

5.2.2 Results

We estimate the redshift of the Spitler burst to be $z \approx 0.31$ Our over-estimate may be attributed to a strong local DM accompanying the high RM $\gtrsim 10^5$ of FRB121102.

We obtain 3σ lower limits on the redshift of FRBs in FRBcat observed with ${\rm DM_{EG}} \geq 400$ pc cm^{-3}, thus providing the first reasonable estimates on the host redshifts of a large set of unlocalized FRBs. For comparison, Pol et al. (2019) derive lower limits for only a single FRB160102, observed with DM ≈ 2596 pc cm^{-3}.

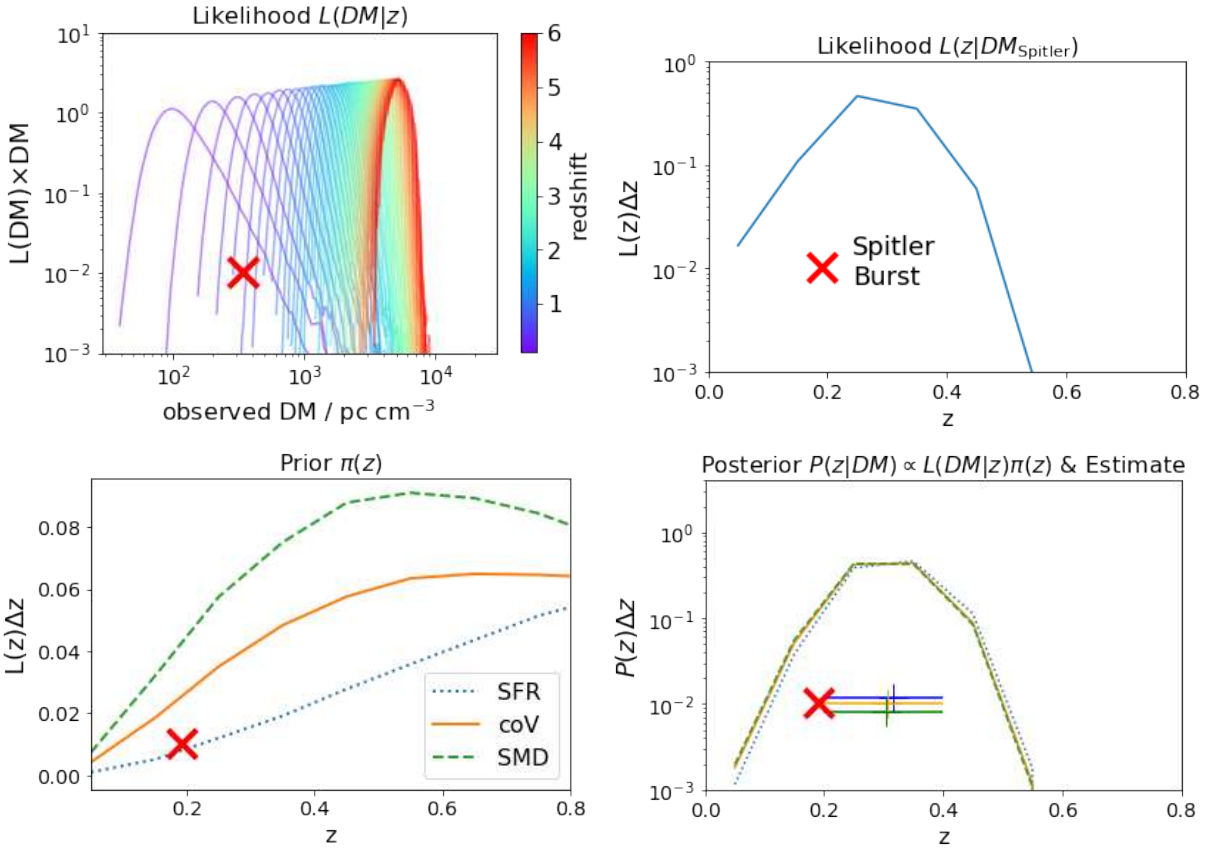

Figure 6. Example of the inference of host redshift for the localized Spitler-burst FRB121102, indicated by a red cross (Tendulkar et al. 2017). Top left: Expected likelihood $L(\mathrm{DM_{EG}}|z)$ assuming FRBs from magnetars in our benchmark scenario (Sec. 4) for increasing redshift, indicated by the colorbar, together with the extragalactic $\mathrm{DM_{Spitler}} \approx 340$ pc cm^{-3} inferred for the Spitler-burst. Top right: Values of $L(\mathrm{DM_{EG}}|z)$ at $\mathrm{DM_{Spitler}}$ for increasing z, renormalized to $1 = \int L(z|\mathrm{DM_{Spitler}})\mathrm{d}z$. Estimating the host redshift from this function implicitly assumes all redshifts to host FRBs with same probability. Bottom left: Prior $\pi(z)$ for host redshift (Sec. 4.5) according to three assumed distributions and selection effects of Parkes (cf. Fig. 4), that measured the displayed value of $\mathrm{DM_{Spitler}}$. These are more realistic assumptions than uniform $\pi(z)$. Bottom right: Posterior $P(z|\mathrm{DM_{Spitler}})$, Eq. (41), for host redshift of the Spitler-burst for three assumed populations together with the expected host redshift and 1σ standard deviation. The $z \approx 0.19$ of the localized Spitler-burst is on the edge of the 1σ deviation. The high estimate on z is probably due to an unlikely strong local contribution of DM, expected to accompany the observed $|RM| > 10^5$ rad m^{-2} signal. Mainly due to vast increase of the probed volume with redshift, the likelihood for the host to reside at $z < 0.1$ is lower by about a magnitude.

5.2.3 Discussion

In order to derive the most conservative lower limits, we overestimate the intergalactic $\mathrm{DM_{IGM}}$, by assuming all baryons to be localized in the ionized IGM, $f_{\rm IGM} = 1$, thus associating the same value of DM with lower redshifts than for smaller choices of $f_{\rm IGM}$. However, more realistic estimates should account for the conservation of baryons, which partly reside in collapsed regions along the LoS, thus $f_{\rm IGM} \leq 0.9$ (cf. Sec. 4.1).

Since at low z the redshift distribution of FRBs is dominated by the increase of the probed volume, rather than the history of the sources, the lower limits are consistent among the different assumed scenarios. Lower values of $\mathrm{DM_{EG}} \lesssim 400$ pc cm^{-3} are more likely to be caused by the local environment or the host galaxy and can be explained by an FRB in the local Universe, thus do not allow for a lower limit on their redshift. However, the local environment of magnetars in the local Universe have a very small chance ($\lesssim 0.02$ per cent in our model) to contribute DM $> 10^3$ pc cm^{-3}, up to several 10^4 pc cm^{-3}. Thus $z = 0$, can never be entirely excluded. Still, the results obtained in this section can be used to estimate the distribution of FRB host redshifts from unlocalized events.

5.3 Inference of intergalactic magnetic field

5.3.1 Method

In this Section we discuss the use of the DM and RM of unlocalized FRBs to put constraints on the index α of B-ρ-relation in the IGM (cf. Eq. 20 and Fig. 2). However, since the RM has the same dependency on the free electron density n_e as DM, it is likewise affected by $f_{\rm IGM}$ – see Eqs. (16) - (19). We assume $f_{\rm IGM} = 0.9$ in order to maximize the contribution of the IGM.

Combined inference of DM and RM According to Eq. (11), the full information from, both, DM and RM of

ID	$\mathrm{DM_{obs}}$ / pc cm^{-3}	$\mathrm{DM_{MW}}$ / pc cm^{-3}	$z_{\mathrm{SFR}}(\mathrm{DM})$	$z_{\mathrm{coV}}(\mathrm{DM})$	$z_{\mathrm{SMD}}(\mathrm{DM})$
FRB190604	552.7	32.0	$0.54^{+0.36}_{-0.44}$	$0.52^{+0.38}_{-0.42}$	$0.51^{+0.39}_{-0.41}$
FRB190417	1378.1	78.0	$1.28^{+0.72}_{-0.78}$	$1.24^{+0.76}_{-0.84}$	$1.19^{+0.81}_{-0.79}$
FRB190222	460.6	87.0	$0.39^{+0.31}_{-0.29}$	$0.37^{+0.33}_{-0.27}$	$0.37^{+0.33}_{-0.27}$
FRB190212	651.1	43.0	$0.62^{+0.38}_{-0.42}$	$0.60^{+0.40}_{-0.40}$	$0.59^{+0.41}_{-0.49}$
FRB190209	424.6	46.0	$0.39^{+0.31}_{-0.29}$	$0.37^{+0.33}_{-0.27}$	$0.37^{+0.33}_{-0.27}$
FRB190208	579.9	72.0	$0.52^{+0.38}_{-0.42}$	$0.50^{+0.40}_{-0.40}$	$0.50^{+0.30}_{-0.40}$
FRB190117	393.3	48.0	$0.36^{+0.24}_{-0.26}$	$0.34^{+0.26}_{-0.24}$	$0.34^{+0.26}_{-0.24}$
FRB190116	444.0	20.0	$0.44^{+0.26}_{-0.34}$	$0.42^{+0.28}_{-0.32}$	$0.42^{+0.28}_{-0.32}$
FRB181017	1281.9	43.0	$1.22^{+0.68}_{-0.72}$	$1.18^{+0.72}_{-0.78}$	$1.14^{+0.76}_{-0.74}$
FRB180817	1006.8	28.0	$0.98^{+0.62}_{-0.58}$	$0.94^{+0.66}_{-0.64}$	$0.92^{+0.58}_{-0.62}$
FRB180812	802.6	83.0	$0.73^{+0.47}_{-0.43}$	$0.70^{+0.50}_{-0.50}$	$0.69^{+0.41}_{-0.49}$
FRB180806	740.0	41.0	$0.71^{+0.49}_{-0.51}$	$0.68^{+0.42}_{-0.48}$	$0.67^{+0.43}_{-0.47}$
FRB180801	656.2	90.0	$0.58^{+0.42}_{-0.38}$	$0.56^{+0.34}_{-0.46}$	$0.55^{+0.35}_{-0.45}$
FRB180730	849.0	57.0	$0.80^{+0.50}_{-0.50}$	$0.77^{+0.53}_{-0.57}$	$0.76^{+0.54}_{-0.56}$
FRB180727	642.1	21.0	$0.63^{+0.37}_{-0.43}$	$0.61^{+0.39}_{-0.41}$	$0.60^{+0.40}_{-0.50}$
FRB180725	716.0	71.0	$0.66^{+0.44}_{-0.46}$	$0.63^{+0.47}_{-0.43}$	$0.62^{+0.48}_{-0.42}$
FRB180714	1467.9	257.0	$1.21^{+0.69}_{-0.71}$	$1.17^{+0.73}_{-0.77}$	$1.13^{+0.77}_{-0.73}$
FRB180311	1570.9	45.2	$1.50^{+0.90}_{-0.90}$	$1.47^{+0.93}_{-0.87}$	$1.41^{+0.89}_{-0.91}$
FRB171209	1457.4	13.0	$1.43^{+0.87}_{-0.83}$	$1.39^{+0.91}_{-0.89}$	$1.34^{+0.86}_{-0.84}$
FRB160102	2596.1	13.0	$2.45^{+1.65}_{-1.25}$	$2.53^{+1.77}_{-1.43}$	$2.31^{+1.69}_{-1.51}$
FRB151230	960.4	38.0	$0.93^{+0.57}_{-0.53}$	$0.90^{+0.60}_{-0.60}$	$0.88^{+0.62}_{-0.58}$
FRB151206	1909.8	160.0	$1.70^{+1.00}_{-0.90}$	$1.68^{+1.12}_{-1.08}$	$1.59^{+1.11}_{-0.99}$
FRB150610	1593.9	122.0	$1.45^{+0.85}_{-0.85}$	$1.42^{+0.88}_{-0.92}$	$1.36^{+0.84}_{-0.86}$
FRB150418	776.2	188.5	$0.60^{+0.40}_{-0.40}$	$0.58^{+0.42}_{-0.48}$	$0.57^{+0.43}_{-0.47}$
FRB150215	1105.6	427.2	$0.69^{+0.41}_{-0.49}$	$0.66^{+0.44}_{-0.46}$	$0.65^{+0.45}_{-0.45}$
FRB140514	562.7	34.9	$0.54^{+0.36}_{-0.44}$	$0.52^{+0.38}_{-0.42}$	$0.51^{+0.39}_{-0.41}$
FRB131104	779.0	71.1	$0.72^{+0.48}_{-0.52}$	$0.69^{+0.41}_{-0.49}$	$0.68^{+0.42}_{-0.48}$
FRB130729	861.0	31.0	$0.85^{+0.45}_{-0.55}$	$0.81^{+0.49}_{-0.61}$	$0.80^{+0.50}_{-0.60}$
FRB130628	469.9	52.6	$0.42^{+0.28}_{-0.32}$	$0.41^{+0.29}_{-0.31}$	$0.41^{+0.29}_{-0.31}$
FRB130626	952.4	66.9	$0.90^{+0.50}_{-0.60}$	$0.86^{+0.54}_{-0.56}$	$0.84^{+0.56}_{-0.54}$
FRB121002	1629.2	74.3	$1.53^{+0.87}_{-0.83}$	$1.50^{+1.00}_{-0.90}$	$1.44^{+0.96}_{-0.94}$
FRB120127	553.3	31.8	$0.54^{+0.36}_{-0.44}$	$0.52^{+0.38}_{-0.42}$	$0.51^{+0.39}_{-0.41}$
FRB110703	1103.6	32.3	$1.08^{+0.62}_{-0.68}$	$1.04^{+0.66}_{-0.74}$	$1.01^{+0.69}_{-0.71}$
FRB110626	723.0	47.5	$0.69^{+0.41}_{-0.49}$	$0.66^{+0.44}_{-0.46}$	$0.65^{+0.45}_{-0.45}$
FRB110220	944.4	34.8	$0.93^{+0.57}_{-0.53}$	$0.89^{+0.61}_{-0.59}$	$0.87^{+0.53}_{-0.57}$
FRB090625	899.5	31.7	$0.88^{+0.52}_{-0.58}$	$0.84^{+0.56}_{-0.54}$	$0.83^{+0.57}_{-0.63}$
FRB010312	1187.0	51.0	$1.14^{+0.66}_{-0.64}$	$1.10^{+0.70}_{-0.70}$	$1.07^{+0.73}_{-0.77}$
FRB010125	790.0	110.0	$0.70^{+0.40}_{-0.50}$	$0.67^{+0.43}_{-0.47}$	$0.66^{+0.44}_{-0.46}$

Table 1. Redshift estimates for 38 FRBs catalogued in FRBcat (Petroff et al. 2016) with observed $\mathrm{DM_{obs}}$ and estimated Galactic foreground $\mathrm{DM_{MW}}$ with $\mathrm{DM_{obs}} - \mathrm{DM_{MW}} \gtrsim 400$ pc cm^{-3} (exact number depends on observing telescope), for which we can estimate 3σ lower limits (cf. Fig. 6). 3σ ranges are computed numerically and show the outer edges of the range that contains > 99.7 per cent of probability, which yields conservative estimates, as an exact computation would result in a more narrow range. We obtain estimates assuming all baryons to be localized in the ionized IGM, $f_{\mathrm{IGM}} = 1$, in order to arrive at the most conservative lower limits, since for lower f_{IGM}, the same value of $\mathrm{DM_{EG}}$ is associated with further distance. We are able to obtain lower limits on the host redshift by applying Bayes theorem (Eq. (12)), combining the full likelihood $L(\mathrm{DM}|z)$, assuming FRBs from magnetars in our benchmark scenario (Sec. 4), with a prior $\pi(z)$ on host redshift derived in Sec. 4.5. Assuming different redshift distributions of FRBs, see Fig. 4, does not affect the lower limits, since they all share the increase of the probed volume that dominates their shape at low redshift.

the same unlocalized event can be obtained as

$$L(\mathrm{DM},\ \mathrm{RM}|,\ \alpha) = \int \pi(z)\ L(\mathrm{DM}|z)\ L(\mathrm{RM}|z,\alpha)\ \mathrm{d}z, \quad (42)$$

thus delivering us the combined likelihood of f_{IGM} and α. The likelihoods $L(\mathrm{DM}|z)$ and $L(\mathrm{RM}|z)$ represent our expectations for the extragalactic contribution to DM and RM, respectively, for FRBs produced at magnetars in our benchmark scenario that considers all regions along the LoS (see Sec. 4), including intervening galaxies. Eq. (42) can be interpreted by identifying the RM-free part of the integrand with the posterior (Eq. (41)) shown in lower-right plot of Fig. 6 , which quantifies our expectation for the host redshift based on DM of the individual unlocalized FRB. This posterior, in turn, acts as the prior for host redshift when interpreting RM regarding the IGMF. This detailed combined analysis of expected distribution of DM and RM for FRBs from different possible host redshift allows to obtain the full information entailed in the observables of FRBs. By renormalizing $L(\mathrm{DM}, \mathrm{RM})$ to the same choice of α for all events, we obtain the Bayes factor $\mathcal{B}$ (Eq. 12). Since we assume that all α have identical priors, $\pi(\alpha) = \mathrm{const.}$, $\mathcal{B}$ is identical to the ratio of posteriors.

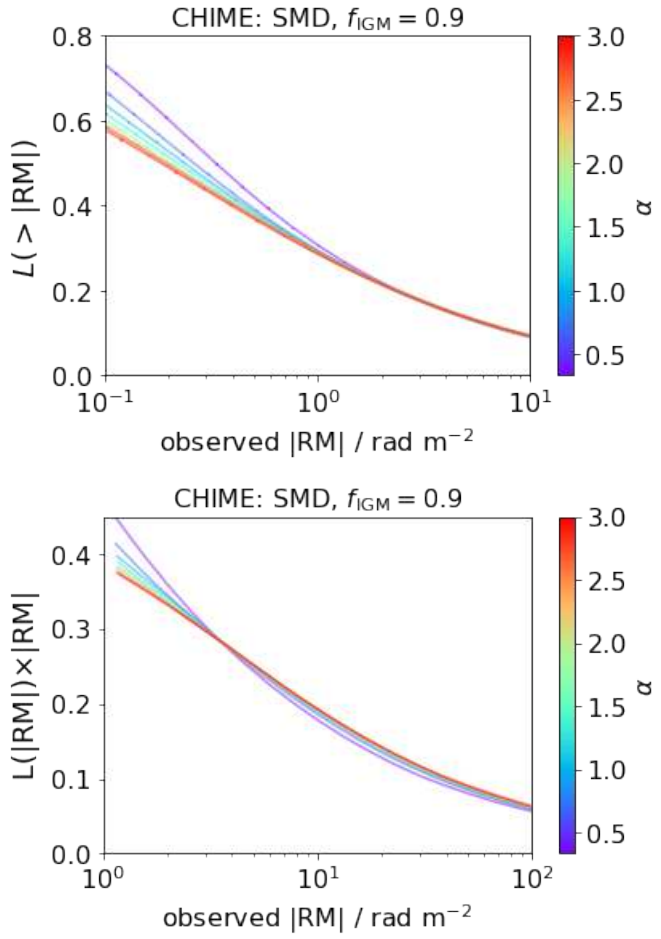

Figure 7. Complementary cumulative (top) and differential (bottom) distribution of $\mathrm{RM_{EG}}$ expected to be observed by CHIME, assuming FRBs from magnetars in our benchmark scenario (Sec. 4), their redshift distribution to follow SMD and an amount of baryons in the IGM, $f_{\rm IGM} = 0.9$. Colors indicate different choices for exponent α of the B-ρ-relation (Eq. (20)). The error bars that represent sampling shot-noise are barely visible, rendering the small difference significant. The amount of observable FRBs with $\mathrm{RM_{EG}} \geq 10^{-1}$ rad m^{-2} (top) as well as the renormalized distribution of reasonable $\mathrm{RM_{EG}} > 1$ rad m^{-2} (bottom) is influenced by the strength of IGMFs. This is true, independent of models chosen for the other regions along the LoS. $\mathrm{RM_{EG}} > 10^2$ are almost completely determined by the local environment and thus not shown here. Our results show that the Spitler burst observed with $|\mathrm{RM}| > 10^5$ rad m^{-2} is a one-in-a-million source $L(> 10^5 \text{ rad m}^{-2}) \lesssim 10^{-6}$. However, due to its high rate of repetition, likelihood of detection is certainly much higher.

Mock sample Here we estimate how many unlocalized CHIME[4] FRBs are required in order to measure α. To this end, we produce mock samples of FRBs, sampling DM and RM according to estimates in our benchmark scenario (Fig. 7, Sec. 4), assuming the weakest of IGMFs, i.e. $\alpha = 9/3$. Investigation of the IGMF with unlocalized FRBs is degenerate to the host redshift distribution and $f_{\rm IGM}$, preventing reasonable conclusions in a joint analysis. We choose the SMD distribution which peaks at lowest redshift of the three compared distributions, thus provides the smallest IGM contribution to RM. The required number of FRBs will hence be lower for the other distributions that peak at more distant redshift. We further assume the maximum possible amount of baryons in the IGM, $f_{\rm IGM} = 0.9$, as suggested by the Macquart relation (Macquart et al. 2020). By increasing the sample size $N_{\rm FRB}$, we investigate how many FRBs are required in order to rule out choices of α, i.e. $\mathcal{B}(\alpha) < 10^{-2}$. For each value of $N_{\rm FRB}$, we take 10 samples, for which we compute the total value for $\mathcal{B}$ and show the logarithmic mean and standard deviation in Fig. 8.

[4] Note that we are mostly interested in RM $\ll 10^3$ rad m^{-2}, which can be probed at low frequencies (Fonseca et al. 2020)

5.3.2 Results

In Fig. 7 we show the likelihood of $\mathrm{RM_{EG}}$ to be observed by CHIME, assuming the redshift distribution of FRBs to follow SMD. The top plot shows the likelihood of FRBs observed with $|\mathrm{RM_{EG}}| > 0.1$ rad m^{-2} which decreases from 70.6 per cent for $\alpha = \frac{1}{3}$ to 59.2 per cent for $\alpha = \frac{9}{3}$. However, the number of observed FRBs expected to have $|\mathrm{RM_{EG}}| > 1$ rad m^{-2} for $\alpha = \frac{1}{3}$ is 30.7 per cent and 29.5 per cent for $\alpha = \frac{9}{3}$, thus hard to distinguish.

Still, the lower α, i.e. the stronger the IGMF, the more FRBs with 0.1 rad m$^{-2} \lesssim |\mathrm{RM_{EG}}| < 10$ rad m^{-2} will be observed. This qualitative result is independent on the exact model of IGMF or assumptions regarding the other regions. Thus, the number of FRBs observed with significant $\mathrm{RM_{EG}}$ in a survey with systematically extracted RM is a good indicator for the IGMF. However, the expected likelihood of $|\mathrm{RM_{EG}}| > 0.1$ rad m^{-2} will change when other models are considered and perhaps hamper the inference of the IGMF. Note that the assumed models for local environment and host galaxy have a decent chance to provide $|\mathrm{RM_{EG}}| < 0.1$ rad m^{-2}, due to old magnetar ages or bimodal distribution of galactic magnetic fields with many virtually unmagnetized galaxies, thus allow for the inference of IGMFs. The contribution of assumed models for the individual regions to the total observed signal can be seen in App. B. This stresses how important it is to exactly estimate all contributions in order to correctly interpret the observed number and distribution of RM.

The bottom plot of Fig. 7 shows that the differential change in the amount of $\mathrm{RM_{EG}}$ significantly changes the distribution of $|\mathrm{RM_{EG}}| > \mathrm{RM_{min}} = 1$ rad m^{-2}, which can be used to infer α from this sub-sample only. Hence, data with carefully subtracted galactic foregrounds can be used to constrain the IGMF. Note that we assume $|\mathrm{RM_{EG}}| > \mathrm{RM_{min}} = 1$ rad m^{-2} can be inferred with precision of 1 rad m^{-2}, determined by the minimal range of bins, by removing the Galactic foreground, e.g. using a Wiener filter Oppermann et al. (2015); Hutschenreuter & Enßlin (2020).

However, the results in Fig. 7 show differences beyond the statistical noise even if we choose higher minimum accessible values of $\mathrm{RM_{EG}}$, 1 rad m$^{-2} \lesssim \mathrm{RM_{min}} < 10$ rad m^{-2}. Thus, constraints on α might also be possible if the MW foreground can be removed with slightly worse precision than 1 rad m^{-2}. This stresses the importance of reliable estimates of the Galactic contribution to the RM as well as confirming the results of Galactic foreground filters with

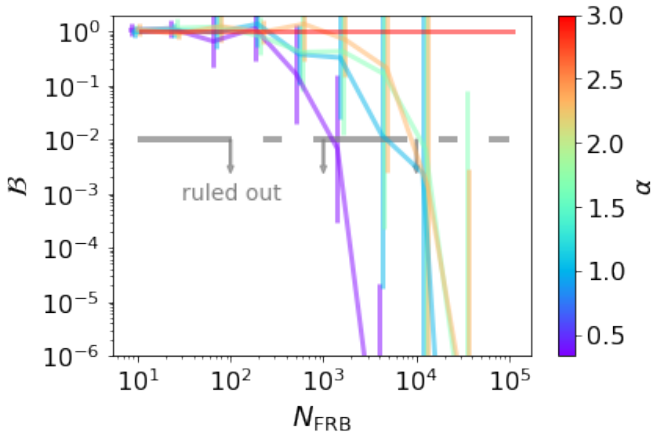

Figure 8. Bayes factor $\mathcal{B}$ for different values of α for mock samples of FRBs with increasing size $N_{\rm FRB}$ assumed to be observed by CHIME in our benchmark scenario assuming FRBs from magnetars, the weakest IGMF model ($\alpha = \frac{9}{3}$), a redshift distribution following SMD, as well as $f_{\rm IGM} = 0.9$. The error bars show the standard deviation for the results of 10 samples of similar size. $\mathcal{B}$ factors for all α compare to the case of $\alpha = \frac{9}{3}$, thus $\mathcal{B}(\alpha_0) < 1e-2$, marked by the gray line, are considered decisive to rule out α_0. The transition of $\mathcal{B}(N_{\rm FRB}|\alpha_0)$ through that line marks the minimum required number of FRBs observed with $\rm RM_{EG} > 1$ rad m^{-2} to constrain $\alpha > \alpha_0$.

robust models for the density and magnetic field of the MW (Boulanger et al. 2018).

Fig. 8 shows that at least $N_{\rm FRB} = 10^3$ FRBs observed with $\rm RM_{EG} \geq 1$ rad m^{-2}, which is $\lesssim 1/3$ of all events, are required in order to constrain $\alpha < \frac{1}{3}$, i.e. constraints comparable to the current upper limit ($B < 4.4$ nG Planck Collaboration et al. 2016). Moreover, for $N_{\rm FRB} \gtrsim 5 \times 10^4$, most $\alpha \leq 8/3$ are ruled out, allowing to probe the IGMF down to the current lower limit ($B > 3 \times 10^{-7}$ nG, Neronov & Vovk 2010).

However, in order to infer the IGMF down to the limit by Neronov & Vovk (2010), a much greater sample is required than these telescopes can acquire in a life-time. Instead, this requires large arrays of telescopes that systematically observe several thousand FRBs each year – such as the SKA (Macquart et al. 2015). Furthermore, the presented estimates on $N_{\rm FRB}$ are optimistic and depend on the exact modelling of all regions along the LoS, which need to be verified by other observables.

5.3.3 Discussion

By using the high value of $f_{\rm IGM} = 0.9$, we obtain the most optimistic estimate for $N_{\rm FRB}$. For lower values of $f_{\rm IGM}$, $\rm RM_{IGM}$ is reduced and a lower number of LoS will be able to significantly contribute to detectable RM. This in turn might increase the number of FRBs $N_{\rm FRB}$, necessary to constrain α, and this will also decrease the range of α detectable using the RM.

Moreover, the ensemble used to model the host and the intervening galaxies contains a significant number of galaxies that do not meet conditions for large-scale dynamos, and thus can only carry weak coherent magnetic fields (cf. Sec. 4.2). This results in a rather low RM contribution from these regions, compared to other works (e.g. Basu et al. 2018). The galaxy models are considered to a distance, at which the surface mass density falls to 1 per cent of the central value, and thus do not account for the halo of galaxies, However, the sources of FRBs might be located at the edge of their host galaxies, if there is sufficient molecular gas to indicate star formation. Such short LoS, especially within the numerous low-mass $M_\star \gtrsim 10^7 M_\odot$ galaxies, only contribute little to the DM and RM. However, we implicitly assume that most FRBs reside in MW-like galaxies, which contain most stellar mass. Still, by considering the numerous low-mass central galaxies of any possible brightness in the low density Universe, the model accounts for even weaker, though arguably more realistic estimates of the galaxy contributions as compared to other works.

Moreover, the elliptical galaxies in the *Rodrigues19* sample only account for negligible contributions to RM as only the vanishing large-scale magnetic field is considered for computation. However, Moss & Shukurov (1996) suggest that high values of RM, up to 100 rad m^{-2}, might possibly be observed from ellipticals with sufficient resolution, which prevents the beam width to contain many correlation lengths whose Faraday rotation interfere destructively. The small angular extent of FRBs renders their RM independent of the instruments angular resolution and hence might carry even higher values of RM from their elliptical host. Future works should thus consider a more realistic estimate of the contribution from turbulent magnetic field in elliptical galaxies. Overall, the low strength of coherent magnetic fields predicted by Rodrigues et al. (2019) implies that our conclusions on the IGMF are optimistic (see Sec. 5.3).

Furthermore, the contribution of the local environment is not well constrained and can significantly affect the shape of $L(\rm RM_{EG})$, which might be misinterpreted as signal of the IGMF. In App. B we provide a comparison of the contributions of different regions to the observed distribution of measures. This shows that basically all regions along the LoS provide significant amounts of RM. Though we could show that RM of FRBs carry detailed information on IGMFs, we might not be able to extract this information, owing to the imprecise knowledge of foregrounds. This stresses the importance to investigate FRBs with identified hosts, whose contribution can be estimated more precisely, as well as to identify the source of FRBs to more exactly quantify the contribution of the local environment. However, even under these circumstances, the contributions of regions different than the IGM may hardly be known with required precision. In future works we will consider further models for the other regions along the LoS in order to identify model-independent signals of the IGMF .

Unambiguous identification of IGMFs solely via $L(\rm RM_{EG})$ of FRBs requires realistic modelling of all contributions and an exact fit to the observed distribution. However, there might be several fitting scenarios that consider different models. Distinguishing between those solutions requires their verification using other measures of FRBs or different astrophysical signals. In future works we aim to include more measures in PrEFRBLE, especially propagation-independent measures that carry information

about the source.

Note that the results in this section exclude Galactic contributions to the RM. In order to constrain IGMFs, we need to be sensitive for $\mathrm{RM_{EG}} \lesssim$ few rad m^{-2}. Hence, future work should account for RM foregrounds due to the MW as well as the ionosphere.

However, the estimate of N_{FRB} are not affected by the Galactic foregrounds that we assume can be removed with precision of 1 rad m^{-2} to identify extragalactic components $\mathrm{RM_{EG}} \geq 1$ rad m^{-2}.

6 CONCLUSION

We model the extragalactic contribution to propagation dependent measures of FRBs from all regions along the line-of-sight, including intervening galaxies, as well as the distribution of host redshift. Using approximate Bayesian computation, we estimate the expected distribution of disperion measure, rotation measure and temporal smearing τ and compare to observations. Our code is provided as an open-source Python software package PREFRBLE[5] (Hackstein 2020).

We use PREFRBLE to identify intervening galaxies, estimate the host redshift of unlocalized FRBs and infer the strength of the intergalactic magnetic field.

The main conclusions of our work can be summarized as follows:

- We find that intervening galaxies are unlikely to account for the entirety of high values of temporal smearing $\tau > 0.06$ ms observed by the Parkes Telescope. The most likely explanation is the presence of a denser and more turbulent environment of the magnetar progenitor than expected from Galactic magnetars. This is in line with earlier findings by Margalit et al. (2020).
- By applying Bayes theorem and making physically motivated assumptions on the redshift distribution of FRBs, we obtain realistic 3σ lower limits on the estimated redshift, from a big sample of 38 unlocalized FRBs with $\mathrm{DM_{EG}} \gtrsim 400$ pc cm^{-3} (see Tab. 1), independent on the exact shape of assumed distribution of host redshift, and thus also independent of source model and history.
- The stronger the IGMF, the more FRBs with 0.1 rad m^{-2} $\lesssim |\mathrm{RM_{EG}}| <$ 10 rad m^{-2} will be observed. This is independent of assumptions regarding the other regions and on the exact model of IGMF. However, the exact number of FRBs with such $\mathrm{RM_{EG}}$ is also influenced by the details of other regions along the LoS, which all contribute significant amounts of RM and maybe hamper the inference of IGMFs. In order to arrive at reasonable conclusions, more competing models have to be considered for each of these regions.
- In order to put constraints on the strength of IGMFs of the order of the current upper limit ($B \lesssim 4.4 \times 10^{-9}$ G, Planck Collaboration et al. 2016), we predict that a number of at least 10^3 unlocalized FRBs with associated $\mathrm{RM_{EG}} >$ 1 rad m^{-2} (i.e. $\lesssim 1/3$ of all events) is required to be observed with CHIME. For this estimate we assumed $f_{\mathrm{IGM}} = 0.9$, and that Galactic foregrounds can be removed with a precision of ≤ 1 rad m^{-2}. Furthermore, it will be possible to derive constraints of the order of the current lower limits from entirely different proxies ($B \gtrsim 3 \times 10^{-16}$ G, Neronov & Vovk 2010), once a higher number of events, $\gtrsim 5 \times 10^4$ FRBs, have been observed with $\mathrm{RM_{EG}} > 1$ rad m^{-2}.

Our estimates of the extragalactic DM, RM and τ make use of models for the local environment of the source, the ensemble of host galaxies, the IGM as well as the ensemble of intervening galaxies. However, we ignore the clustering or haloes of host and intervening galaxies (e. g. Prochaska et al. 2019b; Connor et al. 2020) and do not account for foregrounds from the MW, the Galactic Halo or Earth's ionosphere, which we assume can be removed with sufficient precision to infer the extragalactic component. This will be the subject of future work.

[5] github.com/FRBs/PreFRBLE

ACKNOWLEDGEMENTS

This work was funded by the Deutsche Forschungsgemeinschaft (DFG) under grant BR2026/25. LFSR acknowledges funding from the European Research Council (ERC) under the European Union's Horizon 2020 research and innovation programme (grant agreement No 772663). SH thanks David Gardenier for helpful remarks and for making publicly available the software package FRBPOPPY. Furthermore, SH thanks Rainer Beck, Laura Spitler, Sui Ann Mao, Maja Kierdorf, Charles Walker, Hsiu-Hsien Lin and Pranjal Trivedi for interesting and fruitful discussions on many aspects of this work. LFSR thanks Luke Chamandy for useful discussions. The whole group thanks the referee, Maxim Pshirkov, for interesting remarks.

Our cosmological simulations were performed with the ENZO code (http://enzo-project.org), under project HHH38 and HHH42 at the Jülich Supercomputing Centre (P.I. F. Vazza). FV acknowledges financial support from the ERC Starting Grant "MAGCOW", no. 714196. We thank Jenny Source and Stefan Gottlöber for providing us with the initial conditions and for their help in implementation.

We also acknowledge the use of computational resources at the Rechenzentrum of the University of Hamburg

DATA AVAILABILITY

The data underlying this article are available in the PrEFRBLE repository, at http://doi.org/10.5281/zenodo.3862636

REFERENCES

Akahori T., Ryu D., Gaensler B. M., 2016, ApJ, 824, 105
Arce H. G., Shepherd D., Gueth F., Lee C. F., Bachiller R., Rosen A., Beuther H., 2007, in Reipurth B., Jewitt D., Keil K., eds, Protostars and Planets V. p. 245 (arXiv:astro-ph/0603071)
Arshakian T. G., Beck R., Krause M., Sokoloff D., 2009, A&A, 494, 21
Bannister K. W., et al., 2019, Science, 365, 565
Basu A., Mao S. A., Fletcher A., Kanekar N., Shukurov A., Schnitzeler D., Vacca V., Junklewitz H., 2018, MNRAS, 477, 2528

Beck R., 2016, A&ARv, 24, 4
Beck R., Wielebinski R., 2013, Magnetic Fields in Galaxies. Springer Netherlands, Dordrecht, pp 641–723, doi:10.1007/978-94-007-5612-0_13, https://doi.org/10.1007/978-94-007-5612-0_13
Beck R., Poezd A., Shukurov A., Sokoloff D., 1994, Astronomy and Astrophysics, 289, 94
Beloborodov A. M., 2017, ApJ, 843, L26
Bera A., Bhattacharyya S., Bharadwaj S., Bhat N. R., Chengalur J. N., 2016, Monthly Notices of the Royal Astronomical Society, 457, 2530
Bernet M. L., Miniati F., Lilly S. J., Kronberg P. P., Dessauges-Zavadsky M., 2008, Nature, 454, 302
Bhandari S., et al., 2017, MNRAS, 475, 1427
Bochenek C. D., Ravi V., Belov K. V., Hallinan G., Kocz J., Kulkarni S. R., McKenna D. L., 2020, A fast radio burst associated with a Galactic magnetar (arXiv:2005.10828)
Boulanger F., et al., 2018, Journal of Cosmology and Astro-Particle Physics, 2018, 049
Bryan G. L., et al., 2014, ApJS, 211, 19
Caleb M., Flynn C., Bailes M., Barr E., Hunstead R., Keane E., Ravi V., van Straten W., 2016, Monthly Notices of the Royal Astronomical Society, 458, 708
Chamandy L., Subramanian K., Quillen A., 2014, Monthly Notices of the Royal Astronomical Society, 437, 562
Clarke D. A., Burns J. O., Norman M. L., 1992, The Astrophysical Journal, 395, 444
Collaboration T. C., et al., 2020, A bright millisecond-duration radio burst from a Galactic magnetar (arXiv:2005.10324)
Connor L., 2019, Monthly Notices of the Royal Astronomical Society, 487, 5753
Connor L., et al., 2020, arXiv preprint arXiv:2002.01399
Da Silva A. C., Barbosa D., Liddle A. R., Thomas P. A., 2000, Monthly Notices of the Royal Astronomical Society, 317, 37
Day C. K., et al., 2020, High time resolution and polarisation properties of ASKAP-localised fast radio bursts (arXiv:2005.13162)
DeLaunay J., et al., 2016, The Astrophysical Journal Letters, 832, L1
Dolag K., Gaensler B. M., Beck A. M., Beck M. C., 2015, MNRAS, 451, 4277
Dzhatdoev T., Khalikov E., Kircheva A., Podlesnyi E., Telegina A., 2018, in EPJ Web of Conferences. p. 08009
Eftekhari T., Berger E., 2017, ApJ, 849, 162
Fonseca E., et al., 2020, The Astrophysical Journal, 891, L6
Fuller J., Ott C. D., 2015, MNRAS, 450, L71
Gao H., Li Z., Zhang B., 2014, The Astrophysical Journal, 788, 189
Gardenier D., van Leeuwen J., Connor L., Petroff E., 2019, arXiv preprint arXiv:1910.08365
Hackstein S., 2020, PrEFRBLE, doi:10.5281/zenodo.3862636
Hackstein S., Vazza F., Brüggen M., Sorce J. G., Gottlöber S., 2018, MNRAS, 475, 2519
Hackstein S., Brüggen M., Vazza F., Gaensler B. M., Heesen V., 2019, MNRAS, 488, 4220
Hu F. X., Wu G. X., Su H. J., Liu Y. Z., 1995, A&A, 302, 45
Hummels C. B., Smith B. D., Silvia D. W., 2017, The Astrophysical Journal, 847, 59
Hutschenreuter S., Enßlin T. A., 2020, Astronomy & Astrophysics, 633, A150
Jaroszynski M., 2019, Monthly Notices of the Royal Astronomical Society, 484, 1637
Jeffreys H., Jeffreys H., 1961, Theory of Probability (3rd edn). Clarendon
Katz J., 2016, Modern Physics Letters A, 31, 1630013
Lacey C. G., et al., 2016, Monthly Notices of the Royal Astronomical Society, 462, 3854
Lazio T. J. W., Ojha R., Fey A. L., Kedziora-Chudczer L., Cordes J. M., Jauncey D. L., Lovell J. E., 2008, The Astrophysical Journal, 672, 115
Li Y., Zhang B., 2020, A comparative study of host galaxy properties between Fast Radio Bursts and stellar transients (arXiv:2005.02371)
Li Z.-X., Gao H., Ding X.-H., Wang G.-J., Zhang B., 2018, Nature communications, 9, 1
Liao K., Li Z., Gao H., Zhang S. B., 2020, Constraints on compact dark matter with fast radio burst observations (arXiv:2003.13349)
Locatelli N., Ronchi M., Ghirlanda G., Ghisellini G., 2018, arXiv e-prints, p. arXiv:1811.10641
Lorimer D., Bailes M., McLaughlin M., Narkevic D., Crawford F., 2007, Science, 318, 777
Luo R., Lee K., Lorimer D. R., Zhang B., 2018, MNRAS, 481, 2320
Luo R., Men Y., Lee K., Wang W., Lorimer D. R., Zhang B., 2020, Monthly Notices of the Royal Astronomical Society, 494, 665–679
Lyubarsky Y., 2014, MNRAS, 442, L9
Lyutikov M., Popov S., 2020, Fast Radio Bursts from reconnection events in magnetar magnetospheres (arXiv:2005.05093)
Macquart J. P., 2004, A&A, 422, 761
Macquart J.-P., Koay J. Y., 2013, The Astrophysical Journal, 776, 125
Macquart J.-P., et al., 2015, arXiv preprint arXiv:1501.07535
Macquart J.-P., et al., 2020, Nature, 581, 391–395
Madau P., Dickinson M., 2014, ARA&A, 52, 415
Mahony E. K., et al., 2018, The Astrophysical Journal Letters, 867, L10
Manchester R. N., Hobbs G. B., Teoh A., Hobbs M., 2005, The Astronomical Journal, 129, 1993
Mao S., et al., 2017, Nature Astronomy, 1, 621
Marcote B., Paragi Z., 2019, arXiv preprint arXiv:1901.08541
Marcote B., et al., 2020, Nature, 577, 190
Margalit B., Berger E., Metzger B. D., 2019, The Astrophysical Journal, 886, 110
Margalit B., Beniamini P., Sridhar N., Metzger B. D., 2020, Implications of a "Fast Radio Burst" from a Galactic Magnetar (arXiv:2005.05283)
McQuinn M., 2013, The Astrophysical Journal Letters, 780, L33
Mereghetti S., et al., 2020, INTEGRAL discovery of a burst with associated radio emission from the magnetar SGR 1935+2154 (arXiv:2005.06335)
Metzger B. D., Berger E., Margalit B., 2017, The Astrophysical Journal, 841, 14
Metzger B. D., Margalit B., Sironi L., 2019, MNRAS, 485, 4091
Michilli D., et al., 2018, Nature, 553, 182
Moss D., Shukurov A., 1996, Monthly Notices of the Royal Astronomical Society, 279, 229
Muñoz J. B., Kovetz E. D., Dai L., Kamionkowski M., 2016, Physical Review Letters, 117, 091301
Murase K., Kashiyama K., Mészáros P., 2016, Monthly Notices of the Royal Astronomical Society, 461, 1498
Neronov A., Vovk I., 2010, Science, 328, 73
Niino Y., 2018, ApJ, 858, 4
Oppermann N., et al., 2015, A&A, 575, A118
Owen F. N., Eilek J. A., Keel W. C., 1990, The Astrophysical Journal, 362, 449
Petroff E., et al., 2016, Publ. Astron. Soc. Australia, 33, e045
Petroff E., Hessels J. W. T., Lorimer D. R., 2019, A&ARv, 27, 4
Piro A. L., Gaensler B. M., 2018, ApJ, 861, 150
Planck Collaboration et al., 2014, A&A, 571
Planck Collaboration et al., 2016, A&A, 594, A19
Platts E., Weltman A., Walters A., Tendulkar S., Gordin J., Kandhai S., 2018, arXiv preprint arXiv:1810.05836
Pol N., Lam M. T., McLaughlin M. A., Lazio T. J. W., Cordes J. M., 2019, arXiv e-prints, p. arXiv:1903.07630

Popov S. B., Postnov K. A., 2010, Evolution of Cosmic Objects through their Physical Activity, pp 129–132
Prochaska J. X., et al., 2019a, HST Proposal
Prochaska J. X., et al., 2019b, Science, 366, 231
Pshirkov M. S., Tinyakov P. G., Urban F. R., 2016, Physical review letters, 116, 191302
Ravi V., et al., 2019, Nature, 572, 352
Robert C. P., Cornuet J.-M., Marin J.-M., Pillai N. S., 2011, Proceedings of the National Academy of Science, 108, 15112
Rodrigues L. F. S., Chamandy L., 2020, Magnetizer, doi:10.5281/zenodo.3817091
Rodrigues L. F. S., Chamandy L., Shukurov A., Baugh C. M., Taylor A. R., 2019, MNRAS, 483, 2424
Ryu D., Kang H., Cho J., Das S., 2008, Science, 320, 909–912
Sammons M. W., Macquart J.-P., Ekers R. D., Shannon R. M., Cho H., Prochaska J. X., Deller A. T., Day C. K., 2020, First Constraints on Compact Dark Matter from Fast Radio Burst Microstructure (arXiv:2002.12533)
Scholz P., et al., 2016, ApJ, 833, 177
Scholz P., et al., 2017, The Astrophysical Journal, 846, 80
Shull J. M., Smith B. D., Danforth C. W., 2012, The Astrophysical Journal, 759, 23
Sorce J. G., et al., 2016, MNRAS, 455, 2078
Taylor A., Vovk I., Neronov A., 2011, A&A, 529, A144
Tendulkar S. P., et al., 2017, The Astrophysical Journal Letters, 834, L7
Tingay S. J., Kaplan D. L., 2016, The Astrophysical Journal Letters, 820, L31
Vazza F., Brüggen M., Gheller C., Hackstein S., Wittor D., Hinz P., 2017, Classical and Quantum Gravity, 34, 234001
Vazza F., Brüggen M., Hinz P., Wittor D., Locatelli N., Gheller C., 2018, Monthly Notices of the Royal Astronomical Society, 480, 3907
Walker C. R. H., Ma Y.-Z., Breton R. P., 2018, preprint, (arXiv:1804.01548)
Walters A., Weltman A., Gaensler B. M., Ma Y.-Z., Witzemann A., 2018, The Astrophysical Journal, 856, 65
Wang J.-S., Yang Y.-P., Wu X.-F., Dai Z.-G., Wang F.-Y., 2016, ApJ, 822, L7
Wang X.-G., Li L., Yang Y.-P., Luo J.-W., Zhang B., Lin D.-B., Liang E.-W., Qin S.-M., 2020, The Astrophysical Journal Letters, 894, L22
Wei J.-J., Gao H., Wu X.-F., Mészáros P., 2015, Physical review letters, 115, 261101
Wei J.-J., Wu X.-F., Gao H., 2018, The Astrophysical Journal Letters, 860, L7
Wu X.-F., et al., 2016, The Astrophysical Journal Letters, 822, L15
Wu Q., Yu H., Wang F. Y., 2020, A New Method to Measure Hubble Parameter $H(z)$ using Fast Radio Bursts (arXiv:2004.12649)
Wucknitz O., Spitler L. G., Pen U. L., 2020, Cosmology with gravitationally lensed repeating Fast Radio Bursts (arXiv:2004.11643)
Xi S.-Q., Tam P.-H. T., Peng F.-K., Wang X.-Y., 2017, The Astrophysical Journal Letters, 842, L8
Yang Y.-P., Zhang B., 2016, The Astrophysical Journal Letters, 830, L31
Yuan Q. R., Hu F. X., Su H. J., Huang K. L., 1997, AJ, 114, 1308
Zanazzi J. J., Lai D., 2020, arXiv e-prints, p. arXiv:2002.05752
Zhou B., Li X., Wang T., Fan Y.-Z., Wei D.-M., 2014, Physical Review D, 89, 107303
Zhu W., Feng L.-L., Zhang F., 2018, The Astrophysical Journal, 865, 147
van Weeren R., de Gasperin F., Akamatsu H., Brüggen M., Feretti L., Kang H., Stroe A., Zandanel F., 2019, Space Science Reviews, 215, 16

Symbol	units	description
$L(v\|\mathcal{M})$	-	model likelihood of measure v in case of model $\mathcal{M}$
$\pi(\mathcal{M})$	-	prior of model $\mathcal{M}$
$P(\mathcal{M}\|v)$	-	posterior of model $\mathcal{M}$ in face of observed measure v
$\mathcal{B}(v\|\mathcal{M}_1, \mathcal{M}_2)$	-	Bayes factor, Eq. (12)
RM	rad m^{-2}	Faraday rotation measure
DM	pc cm^{-3}	dispersion measure
SM	kpc m$^{-20/3}$	scattering measure
τ	ms	temporal smearing
B	μG	magnetic field strength
B_0	nG	comoving primordial magnetic field strength
ρ	g cm^{-3}	baryonic gas density
α	-	exponent of $\|B\| \propto \rho^\alpha$ relation
$M_\star$	$M_\odot$	total stellar mass of galaxy
Φ	Mpc^{-3}	galaxy stellar mass function
ϵ	-	properties of galaxy
z	-	redshift
$n_{\rm gal}$	Mpc^{-3}	number density of galaxies
$r_{\rm gal}$	kpc	disk size of galaxy model
$r_{1/2}$	kpc	galaxy half mass radius
d_H	Gpc	hubble radius
C_N^2	m$^{-20/3}$	turbulence per unit length
L_0	pc	outer scale of turbulence
l_0	pc	inner scale of turbulence
n_e	cm^{-3}	electron number density
ν	Hz	frequency
λ	cm	wavelength
D	Gpc	angular diameter distance
$D_{\rm eff}$	Gpc	effective lense distance

Table 2. List of symbols used in the paper.

Subscript	description
IGM	intergalactic medium
FRB	source of FRB
Host	host galaxy
Inter	intervening galaxy
Local	local source environment
MW	Milky Way
gal	galactic
obs	observed
res	residual
eff	effectively observed
L	lensing medium

Table 3. List of subscripts used in the paper.

APPENDIX A: COMPARE INNER SCALE TO PLASMA PHASE FLUCTUATIONS

Macquart & Koay (2013) provide numerical expressions for the temporal scatter τ for plasma phase fluctuations $r_{\rm diff}$ larger or shorter than the inner scale of turbulence l_0. In order to distinguish between these cases, we use their Eq. 10 to compute $r_{\rm diff}$ and compare to $l_0 = 1$ AU, as commonly assumed for the ISM. Results are shown in Fig. A1. Clearly, for all values of SM$_{\rm eff}$ we find that $r_{\rm diff} > l_0$ is a very good assumption. This way, the wavelength of FRB signal λ_0 is a global factor to the different contributions and other choices of λ_0 can easily be investigated in post-processing.

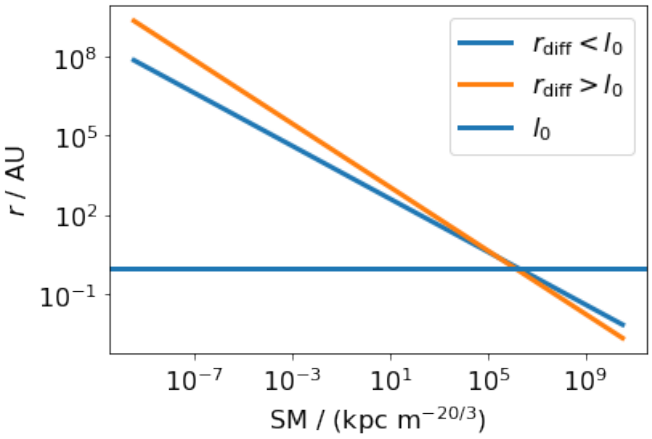

Figure A1. $r_{\rm diff}$ as function of contributed $\rm SM_{eff}$ for wavelength $\lambda_0 = 0.23$ m, prodived by Macquart & Koay (2013). This is used to distinguish between cases of phase structures with different solutions for τ. The blue function shows results valid below l_0, orange is valid above l_0. $l_0 = 1$ AU is marked by the horizontal line. For the models used in this work, all values of $\rm SM_{eff} < 10^5$ kpc m$^{-20/3}$. We thus only need to consider results for the case, where $l_0 > r_{\rm diff}$.

APPENDIX B: TELESCOPE PREDICTIONS

Considering an intrinsic distribution of FRB host redshifts and selection effects (Sec. 4.5) allows to predict the distribution of measures expected for individual telescopes. In Fig. B1 we show the contribution of separate regions to the observed DM, RM and τ for different telescopes and intrinsic redshift distributions. These are obtained from Eq. (10), using for $L(v|z)$ the predictions of individual models explained in Secs. 4.1 - 4.4. These plots allow to easily identify the regions that dominate a given measure.

APPENDIX C: EFFECTIVELY CONTRIBUTING OVER-DENSITY ENVIRONMENTS

We want to use the RM data to distinguish between different models for the origin of IGMFs. Ideally, one would hope to obtain constraints on the strength of the primordial magnetic field B_0, produced at $z \gg 10$, by measuring the magnetic fields in voids. Hence, we produced a number of MHD simulations that consider identical dynamo physics, but start with different strengths of the primordial magnetic field. In Fig. C1, upper left, we show the $|B| \sim \rho$ relation obtained for the present day. To compare the average contribution to $\langle \rm RM \rangle$ from regions with different densities, we estimate the contribution per unit length by $\langle \frac{\rm dRM}{\rm dl} \rangle \propto \rho |B|$, shown in the upper right plot. We multiply this result by the average relative path length, approximated by the model independent density volume filling factor, shown in the lower left, in order to approximate the average contribution to $\langle \rm RM \rangle$ from these regions, shown in the lower right of Fig. C1.

This plot clearly shows that even for the strongest primordial magnetic fields allowed by present constraints (Planck Collaboration et al. 2016), contributions to $\langle \rm RM \rangle$ are negligible from regions with over-densities below 0.1, where the comoving primordial magnetic field strength might be conserved. Hence, $\langle \rm RM \rangle$ is not a direct probe of the magnetic field in voids or of the primordial magnetic field.

However, for over-densities associated with filaments and sheets, $10 < \rho/\langle\rho\rangle < 200$, different shapes of $|B|(\rho)$ can have a significant impact on $\langle \rm RM \rangle$. Moreover, the statistical distribution of RM, expressed by the likelihood function $L(\rm RM)$, allows for a more precise investigation of RM along different LoS, especially of paths that do not enter high-density regions, which dominate $\langle \rm RM \rangle$. This way, $L(\rm RM)$ can be used to constrain parts of $|B|(\rho)$ to lower values of $\rho/\langle\rho\rangle < 10$ than by using $\langle \rm RM \rangle$, allowing to obtain general conclusions on models for the IGMF, independent of the individual formation processes.

APPENDIX D: PATH LENGTH OF LOS THROUGH ELLIPSOID

We want to calculate the path length of a LoS within an axisymmetric galaxy model, represented by a three-dimensional ellipsoid with two identical axes b_G, thus

$$1 = \frac{x^2}{a_G^2} + \frac{y^2}{b_G^2} + \frac{z^2}{b_G^2}, \tag{D1}$$

where x coordinate points along the major axis a_G while y and z are rotationally invariant. Viewed face on with inclination angle $\theta = 0$, impact parameters Δy and Δz both correspond to offset of the LoS from the center of the disc along axes y and z, respectively. However, for $\theta \neq 0$, Δz also entails an offset from the mid-plane at the center of the disc, while only Δy still corresponds to the y-axis of the ellipsoid. Since the y-coordinate is completely determined by Δy, it suffices to consider a LoS passing an ellipse. Eq. (D1) can be rewritten, such that

$$1 = \frac{x^2}{a_G^2\left(1 - \frac{y^2}{b_G^2}\right)} + \frac{z^2}{b_G^2\left(1 - \frac{y^2}{b_G^2}\right)}, \tag{D2}$$

which defines an ellipse with axes

$$a = a_G\sqrt{\left(1 - \frac{y^2}{b_G^2}\right)} \tag{D3}$$

$$b = b_G\sqrt{\left(1 - \frac{y^2}{b_G^2}\right)}. \tag{D4}$$

To obtain the path length L_E of LoS L through ellipse r viewed at angle θ with offset Δz from the center (see Fig. D1), we parametrize

$$L(t|\theta) = t\begin{pmatrix}\sin\theta\\ \cos\theta\end{pmatrix} + \Delta\begin{pmatrix}\cos\theta\\ -\sin\theta\end{pmatrix} \tag{D5}$$

and solve for intersections with ellipse

$$r(\tau) = \begin{pmatrix}b\sin\tau\\ a\cos\tau\end{pmatrix}, \tag{D6}$$

found at

$$\tau_{1/2} = -2\,\mathrm{atan}\left(\frac{b\cos(\theta) \pm \sqrt{a^2\sin^2(\theta) + b^2\cos^2(\theta) - z^2}}{a\sin(\theta) - z}\right). \tag{D7}$$

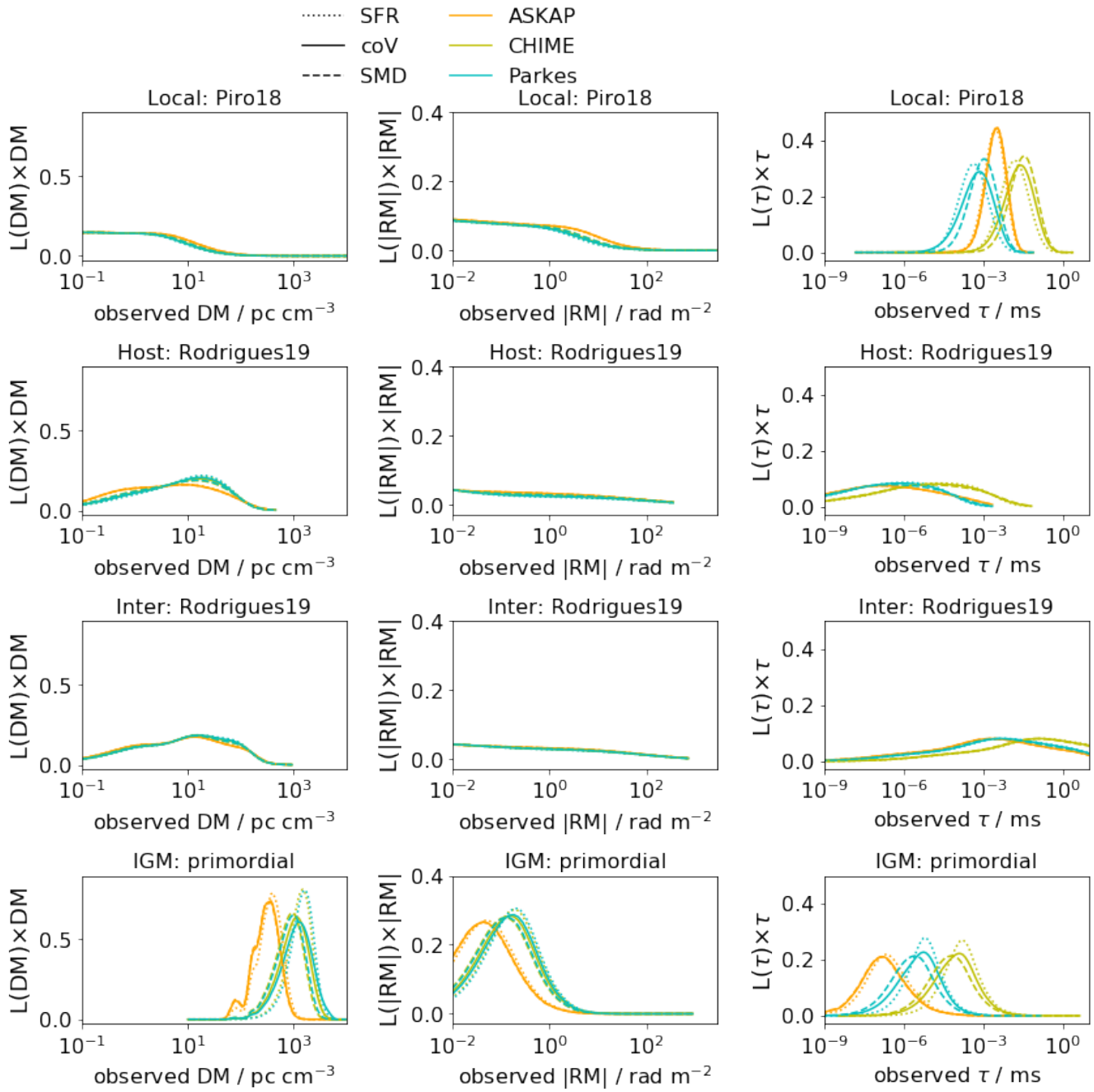

Figure B1. Likelihood of contribution to DM (left), RM (center) and τ (right) to FRBs by individual regions along LoS, indicated in the title, considering models in our benchmark scenario (Secs. 4.1 - 4.4). Assuming the redshift distribution of FRBs to follow coV (solid), SMD (dashed) or SFR (dotted), distributions show the likely contribution of the model according to Eq. (10) in surveys conducted by individual telescopes, i. e. CHIME (blue), ASKAP (orange) and Parkes (green, see Sec. 4.5). The x-axis is cut for values not accessible by terrestrial telescopes, while the shown distributions are normalized to 1 over the whole range of x. Comparing these plots allows to easily identify the dominant / significant / negligible regions and their contribution to observed values.

This delivers the path length of the LoS within the ellipsoid

$$L_E = \sqrt{a^2 \left(\cos\left(\tau_1\right) - \cos\left(\tau_2\right)\right)^2 + b^2 \left(\sin\left(\tau_1\right) - \sin\left(\tau_2\right)\right)^2}. \tag{D8}$$

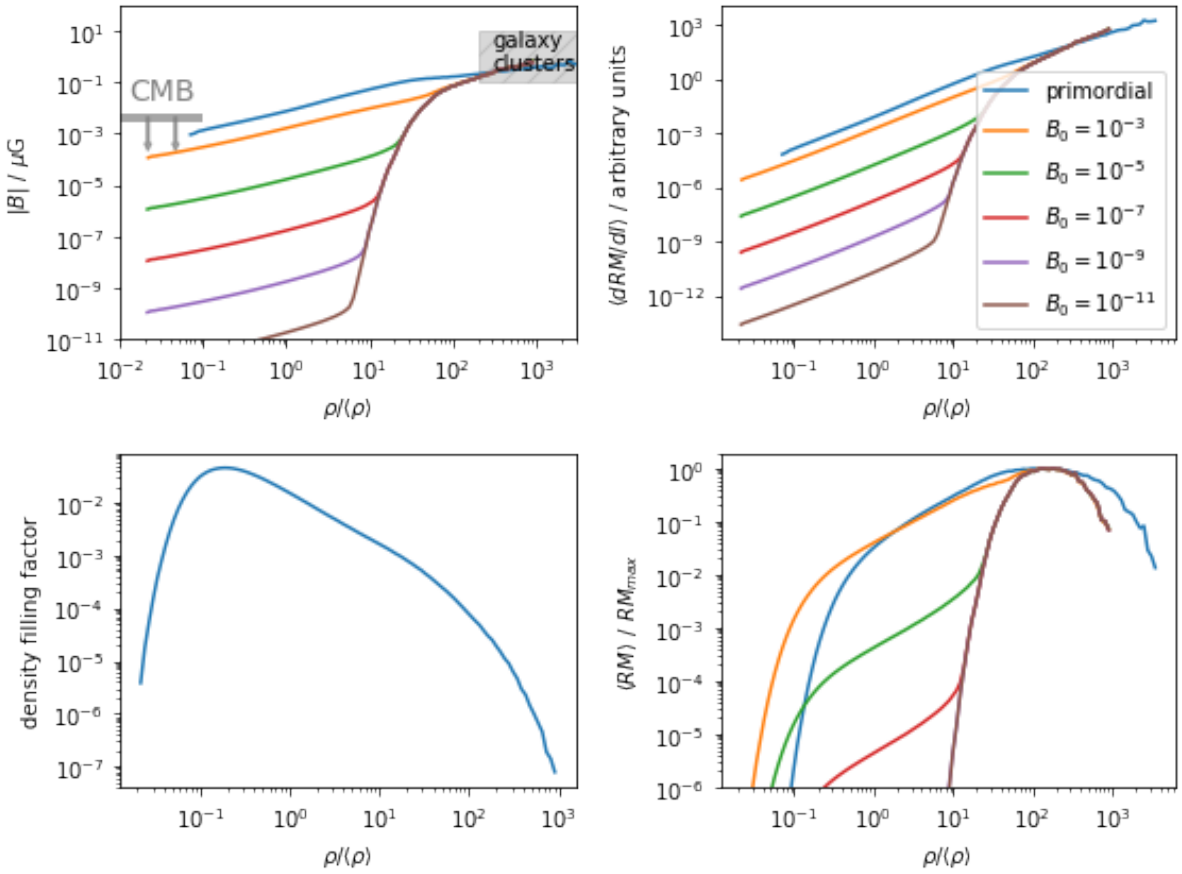

Figure C1. Upper left: Median magnetic field strength $|B|$ as function of over-density $\rho/\langle\rho\rangle$ for a number of MHD models with identical dynamo physics, starting with different strengths of the primordial magnetic field B_0, indicated by the label in μG. Upper right: average contribution to $\langle$RM$\rangle$ per unit length as function of over-density. Obtained by multiplying $|B|(\rho) \times \rho/\langle\rho\rangle$ in the upper-left panel. Lower left: model independent density volume filling factor $f(\rho)$. Lower right: average contribution of $\langle$RM$\rangle$ from regions in the IGM with different over-density, which is obtained by multiplying $\langle$dRM$\rangle \times f(\rho)$ (upper right times lower left). Some of the models are not visible in that plot as they are identical to the case of $B_0 = 10^{-11}$ μG and the y-axis is set to only show the relevant contribution to $\langle$RM$\rangle$. Models that are identical in this plot cannot be distinguished by investigation of $\langle$RM$\rangle$.

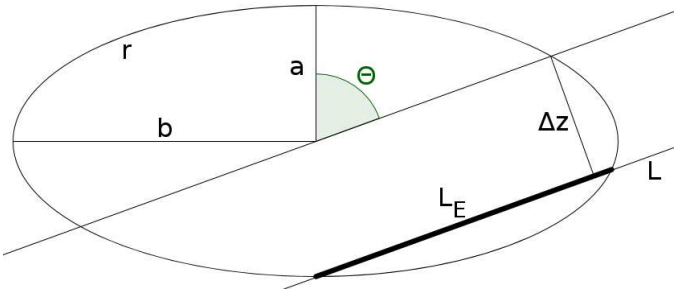

Figure D1. Path length L_E of LoS L through ellipse r viewed at angle θ with offset Δz from the center.

MNRAS **000**, 1–7 (0000) Preprint 1 July 2020 Compiled using MNRAS LATEX style file v3.0

Fast radio burst redshift distribution and the missing baryons

S. Hackstein[1⋆], M. Brüggen[1], F. Vazza[1,2],
[1] *Hamburger Sternwarte, University of Hamburg, Gojenbergsweg 112, 21029, Germany*
[2] *University of Bologna, Department of Physics and Astronomy, Via Gobetti 93/2, I-40129, Bologna, Italy; Istituto di Radioastronomia, INAF, Via Gobetti 101,40129 Bologna, Italy*

1 July 2020

ABSTRACT

Context: Fast radio bursts are transient radio pulses of extragalactic origin. Their dispersion measure is indicative of the baryon content in the ionized intergalactic medium between the source and the observer. However, inference using unlocalized fast radio bursts is degenerate to the distribution of redshifts of host galaxies.

Method: We perform a joint inference of the intergalactic baryon content and the fast radio burst redshift distribution with the use of Bayesian statistics by comparing the likelihood of different models to reproduce the observed statistics in order to infer the most likely models. In addition to the intergalactic medium, we consider contributions from the local environment of the source, assumed to be a magnetar, as well as a representative ensemble of host and intervening galaxies.

Results: We derive an estimate of the extragalactic baryon content $f_{\rm IGM} = 0.84^{+0.06}_{-0.24}$ from the extragalactic dispersion measure of six localized fast radio bursts. Assuming that the missing baryons reside in the ionized intergalactic medium, our results suggest that the redshift distribution of observed fast radio bursts peaks at $z \lesssim 0.6$.

Key words: cosmology: observations – cosmology: large-scale structure of universe – galaxies: intergalactic medium – galaxies: magnetic fields – polarization – radio continuum: general

1 INTRODUCTION

Observations of the cosmic microwave background (CMB) show that $\approx 5\%$ of energy density in the Universe exists as ordinary matter (Planck Collaboration et al. 2014). However, in the $z \leq 2$ range, observations of stars and gas in galaxies, of the hot intracluster medium and of the Lyα-forest can only account for about half of that amount (e. g. Nicastro et al. 2008). The "missing" baryons are believed to be hidden in the warm-hot intergalactic medium (WHIM) (Cen & Ostriker 1999; Dave et al. 2001), with temperatures of $10^5 - 10^7$ K and low baryon densities of $10^{-6} - 10^{-5}$ cm^{-3}. This medium is difficult to observe directly as it only couples with radiation through electronic transitions. However, correlation of the distribution of galaxies with CMB distortions due to Sunyaev-Zel'dovich effect has revealed the likely presence of filaments of warm-hot gas between galaxies, possibly consistent with the missing baryons (e. g. Tanimura et al. 2018; de Graaff et al. 2019).

Several studies have suggested that fast radio bursts (FRBs) can be used to detect the missing baryons. Their signals propagate across cosmological distances and get dispersed by diffuse ionized gas, quantified by the dispersion measure (DM), defined as the column density of free electrons

$$\mathrm{DM} = \int n_e \mathrm{d}l. \quad (1)$$

Wei et al. (2019) proposed to compare the redshift evolution of the DMs using ≈ 3000 FRBs with known redshifts to that of the Hubble parameter to measure the IGM baryon content $f_{\rm IGM}$, i. e. the amount of all baryons that reside in the ionized IGM. Deng & Zhang (2014) argued that the redshift observed for γ-ray bursts associated to FRBs can be used to infer $f_{\rm IGM}$. McQuinn (2013) modelled the distribution of DM expected for FRBs from different redshift and found that ~ 100 DM of FRBs from redshift

⋆ E-mail: stefan.hackstein@hs.uni-hamburg.de

$z > 0.5$, localized with sub-arcminute precision around identified galaxies, can be used to infer the baryon profile of galaxies in order to constrain the localization of cosmic baryons. Muñoz & Loeb (2018) proposed to cross-correlate the DM of arcminute-localized FRBs with the thermal Sunyaev-Zeldovich effect in the CMB. The latter depends on the temperature of the WHIM and the amount of baryons localized in the WHIM, which can be constrained using $\sim$ 1000 FRBs with arcminute localization. Qiang & Wei (2020) suggest to use model-independent Gaussian processes to investigate the evolution of $f_{\rm IGM}$ with DM of FRBs with identified redshift.

All of the aforementioned papers require a large number of well-localized FRBs or cross-correlation with associated observations. However, Yang et al. (2020) argue that the majority of FRBs are not supposed to have strong associated persistent sources. Furthermore, the exact localization of sources of short-duration signals without known redshift is not trivial to constrain, and neither is the identification of the host galaxies of FRBs (Eftekhari & Berger 2017; Mahony et al. 2018; Marcote & Paragi 2019; Prochaska et al. 2019a). The host can be identified using interferometry or by observing persistent counter parts to the FRB. So far, FRBs have been located to a multitude of galaxy types, from star-forming dwarf galaxies (Tendulkar et al. 2017) to very massive galaxies with old stellar population (Ravi et al. 2019; Bannister et al. 2019). Unluckily, the small sample of localized FRBs cannot provide enough information to arrive at reasonable conclusions regarding cosmological questions. However, in this work, we show how it is possible to use DM of a large sample of unlocalized FRBs, in order to infer their host redshift distribution in a statistical way, which also allows us to constrain the amount of ionized baryons located in the cosmic web.

Because of the unknown distance to unlocalized FRBs, the assumed distribution of source redshifts can help interpret the distribution of observed DM. Several papers have tried to infer the intrinsic redshift distribution of FRBs, either by modelling the distribution of DM and other FRB properties with analytical or Monte-Carlo methods (Bera et al. 2016; Caleb et al. 2016; Gardenier et al. 2019), or by performing a luminosity-volume test (Locatelli et al. 2018). So far there are inconsistencies in implications of data from different instruments, e. g. ASKAP requiring faster change in FRB density with redshift than Parkes.

Macquart & Ekers (2018) use the flux density and fluence of FRBs to infer the luminosity distance and evolutionary history, as well as the redshift distribution, and show how the history of the ionized IGM affects the distribution of observed DM, thus influences our inference of the host redshift distribution.

Here we propose to use unlocalized FRBs to perform a joint analysis of the FRB redshift distribution and the IGM baryon content, $f_{\rm IGM}$, by comparing the expected distribution of DM to the available observed values reported by Parkes, CHIME and ASKAP observatories (Staveley-Smith et al. 1996; Macquart et al. 2010; The CHIME/FRB Collaboration et al. 2018), using the PREFRBLE[1] software (Hackstein 2020), presented in Hackstein et al. (2020). In Sec. 2 we explain how we model different values of $f_{\rm IGM}$. The resulting predictions are presented and compared in Sec. 3. We discuss our results in Sec. 4 and conclude in Sec. 5.

2 METHOD

Investigation of the fraction of baryons in the ionized IGM, $f_{\rm IGM} = \Omega_{\rm IGM}/\Omega_{\rm baryons}$, with DM requires comparison of the observed DM with expectations of $\mathrm{DM}(z|f_{\rm IGM})$, according to source redshift z, (Keane et al. 2016)

$$\langle \mathrm{DM}(z) \rangle = \frac{c\rho_{\rm crit}\Omega_b}{m_p \mu_e H_0} \int f_{\rm IGM}(z) \frac{(1+z)}{H(z)} \, \mathrm{d}z. \tag{2}$$

However, FRBs do not come with a direct measure of redshift and for the majority of FRBs, that could not be localized by other means, the DM is the best indicator for the source distance (Dolag et al. 2015; Niino 2018; Luo et al. 2018; Walker et al. 2018; Pol et al. 2019). Still, by assuming different plausible redshift distributions of FRBs, $\pi(z)$, we can estimate the distribution of DM to be observed by instruments, which is determined by $f_{\rm IGM}$.

By comparing the expected distribution to observations, we can quantify the likelihood of different combinations of $\pi(z)$ and $f_{\rm IGM}$. Consequently, this allows us to put constraints on the WHIM density without the need to localize FRBs. Furthermore, by accounting for the redshift-evolution of $f_{\rm IGM}$ in cosmological simulations, the inference presented here can be used to investigate the helium-reionization history (e. g. Linder 2020; Dai & Xia 2020).

In Hackstein et al. (2020), we obtained likelihood estimates, $L(\mathrm{DM}|z)$, to observe extragalactic DM from source at redshift z. These expectations consider contributions from all regions along the LoS in our benchmark scenario, considering magnetars as the source of FRBs as well as a realistic ensemble of different host and intervening galaxies. Predictions for the IGM were obtained using a constrained cosmological simulation of the local Universe, produced using the cosmological magneto-hydrodynamic code ENZO (Bryan et al. 2014) together with initial conditions obtained following Sorce et al. (2016) and cosmological parameters of PLANCK (Ade et al. 2016). The constrained volume of 250 $(\mathrm{Mpc/h})^3$ was embedded in a 500 $(\mathrm{Mpc/h})^3$ grid of 1024^3 cells. The use of five adaptive mesh refinement levels allowed for a maximum resolution of 30 kpc in the most-dense environments. The simulation starts at redshift $z = 60$, where all baryons are in the IGM. However, the limited resolution does not allow us to properly resolve galaxy formation and the condensation of cold gas out of the IGM, thus implies $f_{\rm IGM} = 1$, always. Further information on this model can be found in Hackstein et al. (2018) and Hackstein et al. (2019). A reduced version of this model can be found on crpropa.desy.de under "additional resources", together with the other models presented in Hackstein et al. (2018).

[1] github.com/shackste/PreFRBLE

We further use FRBPOPPY[2] (Gardenier et al. 2019) to model the distribution of host redshift of observed FRBs, $\pi(z)$, assuming physically motivated intrinsic redshift distributions, i. e. following the comoving volume (coV), stellar mass density (SMD) or star formation rate (SFR), as well as the selection effects of ASKAP, CHIME and Parkes instruments.

Together, these observables can be used to quantify the distribution of expected DMs,

$$L(\mathrm{DM}) = \int L(\mathrm{DM}, z) \times \pi(z)\ \mathrm{d}z. \tag{3}$$

For more details on the derivation of likelihood $L(\mathrm{DM}|z)$ and prior $\pi(z)$, see Hackstein et al. (2020).

Numerical simulations suggest that up to 28 ± 11 per cent of baryons are located in neutral hydrogen clouds in the IGM, observable in the photoionized Lyα forest, as well as 25 ± 8 per cent in the WHIM, leaving a baryon shortfall of 29 ± 12 per cent (Shull et al. 2012). This leaves a plausible range of $0.3 \lesssim f_\mathrm{IGM} \lesssim 0.9$ (cf. Li et al. 2019).

As explained above, f_IGM is assumed to be constant with redshift, thus to be a global factor to $\langle \mathrm{DM}(z) \rangle$ (Eq. 2). This allows to obtain estimates for different values of f_IGM in post-processing, allowing us to test how many missing baryons can be located in the WHIM (Deng & Zhang 2014; Keane et al. 2016). To this end, we modify the likelihood of intergalactic contribution, $L(\mathrm{DM_{IGM}}|z)$, obtained from the constrained simulation of the IGM, such that the result returns the required average value according to Eq. 2, while shape and norm are conserved:

$$L(\mathrm{DM_{IGM}}|f_\mathrm{IGM}) = f_\mathrm{IGM} \times L(f_\mathrm{IGM} \times \mathrm{DM_{IGM}}). \tag{4}$$

In order to quantify the likelihood of a scenario of f_IGM and FRB redshift distribution $\pi(z)$ to account for the observation of an individual FRB with $\mathrm{DM_{obs}} = \mathrm{DM_{EG}} + \mathrm{DM_{MW}}$, we take the value of $L(\mathrm{DM_{EG}}|f_\mathrm{IGM})$ for the benchmark scenario, using the estimates for $\mathrm{DM_{MW}}$ according to NE2001 model (Cordes & Lazio 2002) as listed in FRBcat (Petroff et al. 2016). These estimated values of $\mathrm{DM_{EG}}$ were shown to be correct to $\approxeq 30$ pc cm^{-3} (Manchester et al. 2005).

In order to compare different choices of f_IGM and host redshift distribution, we compute the Bayes factor

$$\mathcal{B}(\mathrm{DM_{EG}}|f_{\mathrm{IGM},0}, f_{\mathrm{IGM},1}) = \frac{L(\mathrm{DM_{EG}}|f_{\mathrm{IGM},0})}{L(\mathrm{DM_{EG}}|f_{\mathrm{IGM},1})} \tag{5}$$

by renormalizing all likelihoods of individual FRBs to the same choice of $f_{\mathrm{IGM},1}$. $\mathcal{B}$ quantifies how much the observation of $\mathrm{DM_{EG}}$ changes our corroboration in favour of $f_{\mathrm{IGM},0}$ compared to $f_{\mathrm{IGM},1}$. By renormalizing all $\mathcal{B}$ to the best-fit scenario $\mathcal{B}_\mathrm{max}$, the presented values quantify how much the observations change our corroboration in disfavour of the corresponding scenario.

For FRBs with localized hosts, the information on f_IGM and $\pi(z)$ can be distinguished, thus allowing for separate likelihoods. For the events listed with host redshift z_FRB in FRBcat, instead of the procedure explained above, we obtain the likelihood of f_IGM by comparing values of $L(\mathrm{DM_{EG}}|z_\mathrm{FRB}, f_\mathrm{IGM})$ and compute the Bayes factor $\mathcal{B}$ by renormalizing the likelihood to a particular choice of $f_{\mathrm{IGM},0}$. Likewise, we compare values of $\pi(z_\mathrm{FRB})$ for their implication on the redshift distribution.

$\mathcal{B}$ obtained for individual events and different instruments can simply be multiplied in order to interpret the combined results. Note that $\mathcal{B}$ quantifies how much the current observations change our corroboration between the considered scenarios. However, according to Bayes theorem

$$P(f_\mathrm{IGM}|\mathrm{DM_{EG}}) \propto L(\mathrm{DM_{EG}}|f_\mathrm{IGM})\pi(f_\mathrm{IGM}), \tag{6}$$

the ratio of likelihoods L, $\mathcal{B}$, has to be multiplied by the ratio of priors π in order to arrive at the ratio of posteriors P. $\pi(f_\mathrm{IGM})$ quantifies how likely different values of f_IGM are prior to investigation of $\mathrm{DM_{EG}}$, while P expresses our conclusion on the likelihood of values of f_IGM after consideration of the data. However, we consider no preference for any value of f_IGM, $\pi(f_\mathrm{IGM}) = \mathrm{const.}$, thus $\mathcal{B}$ is identical to the ratio of P.

3 RESULTS

3.1 Expected distribution vs. observation

In Fig. 1 we show the results for all combinations of instruments and redshift distributions for two extreme values of $f_\mathrm{IGM} = 0.3$ and $f_\mathrm{IGM} = 0.9$. These can be compared directly to observations by the corresponding instrument, which are indicated by the dash-dotted line.

The majority of FRBs observed by ASKAP have $\mathrm{DM_{EG}} \approx 500$ pc cm^{-3}. The expected peak values of $\mathrm{DM_{EG}}$ for f_IGM between 0.3 and 0.9 range from 100 pc cm^{-3} to 440 pc cm^{-3}. ASKAP results are thus in favour of high values of $f_\mathrm{IGM} \approx 0.9$. However, for the values of DM observed with ASKAP that are generally higher than expectations, other foregrounds such as the local contributions need to be considered more carefully in order to arrive at reasonable conclusions. The assumed intrinsic redshift distributions do not differ much in their predictions at low z (cf. Hackstein et al. 2020), thus rendering ASKAP results incapable of distinguishing FRB populations with a small sample of FRBs.

While the distribution of DM observed by CHIME peaks at roughly the same value as for ASKAP $\mathrm{DM_{EG}} \approx 500$ pc cm^{-3}, the peak is less pronounced and the upper 1σ-deviation is more than 1.5 times higher than for ASKAP, reaching values beyond 1000 pc cm^{-3}. However, for CHIME, the expected peak values of $\mathrm{DM_{EG}}$ range from 300 pc cm^{-3} to 1500 pc cm^{-3} for $f_\mathrm{IGM} = 0.3$ and $f_\mathrm{IGM} = 0.9$, respectively, far above the observed value, hence expecting many more high values of DM. Thus, the CHIME results favour low $f_\mathrm{IGM} \gtrsim 0.3$, depending on the assumed distribution of the host redshifts. Also, CHIME observes more FRBs with $50 < DM_\mathrm{EG}\ /\ \mathrm{pc\ cm^{-3}} < 200$ than ASKAP, which is not expected according to results in Fig. 1. This hints on an imprecise assumption on the redshift distribution of FRB sources visible to CHIME, that observes at different wavelengths than the other two instruments.

For Parkes, the expected peak value of $\mathrm{DM_{EG}}$ ranges from 300 pc cm^{-3} to 1800 pc cm^{-3} between $f_\mathrm{IGM} = 0.3$ and $f_\mathrm{IGM} = 0.9$, similar as expected for CHIME. However, the observed sample peaks at $\mathrm{DM_{EG}} \approx 1000$ pc cm^{-3} - about

[2] github.com/davidgardenier/frbpoppy

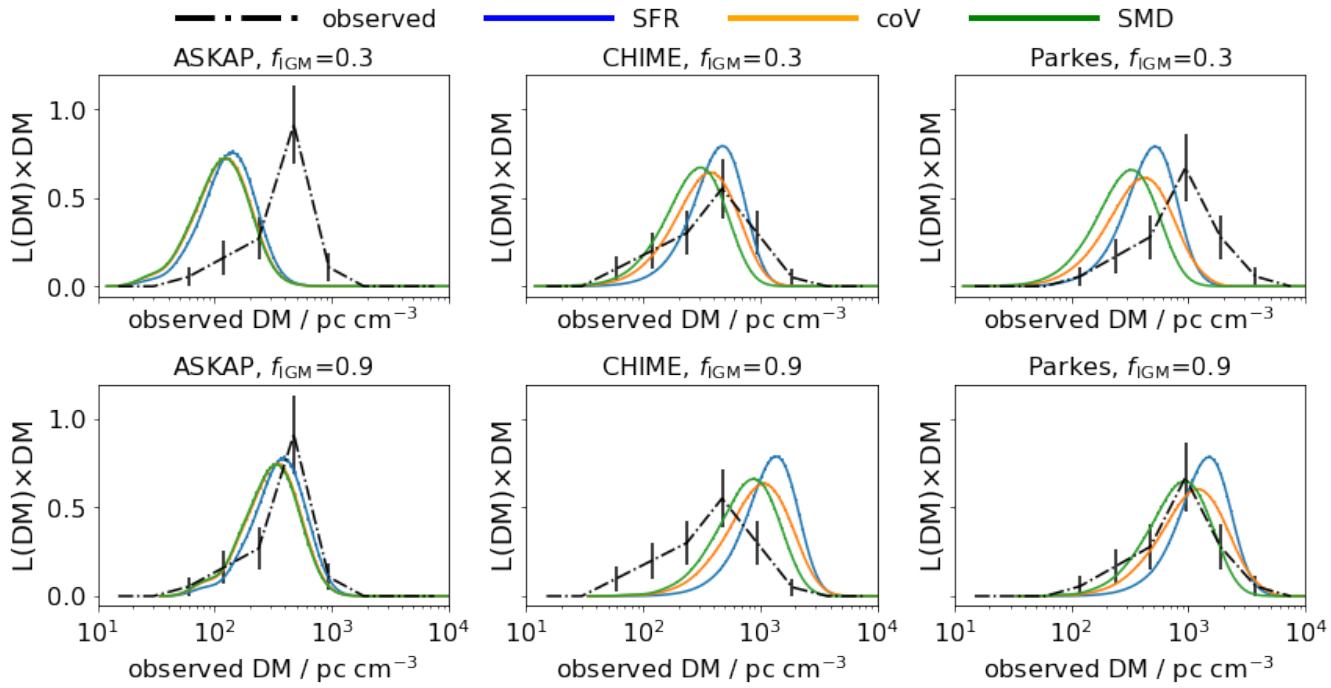

Figure 1. Distribution of extragalactic $\mathrm{DM_{EG}} = \mathrm{DM_{obs}} - \mathrm{DM_{MW}}$ as observed (dash-dot) by ASKAP (left), CHIME (center) and Parkes (right) minus estimate of MW contribution based on NE2001 model, as listed in FRBcat. The solid lines show the expected distribution to be observed by the corresponding instrument according to Eq. 3, assuming FRBs from magnetars in our benchmark scenario and extreme values for baryon content of IGM, $f_{\rm IGM} = 0.3$ (top) or $f_{\rm IGM} = 0.9$ (bottom), as well as FRB redshift distribution to follow star formation rate (SFR, blue), comoving volume (coV, orange) or stellar mass density (SMD, green). The error bars show the shot noise of the observed data. For the expected distribution, the barely visible error bars are the shot noise of the Monte-Carlo samples used to obtain the likelihood function. The product of Bayes factors (Eq. 5) for individual FRBs, shown in Fig. 2, quantifies how well different scenarios recreate the observed distribution.

twice the value observed with CHIME - which is well within the expected range. Hence, different assumed redshift distributions will favour other values of $f_{\rm IGM}$, e. g. a population concentrated at low redshifts, such as SMD, will need a high value of $f_{\rm IGM} \lesssim 0.9$ to explain the observed DMs, while populations with greater redshifts, such as SFR, will require lower values of $f_{\rm IGM}$. The Parkes sample is dominated by high values of DMs, with ≈ 30 per cent of FRBs observed with DM > 1000 pc cm^{-3}. The majority of these is thus likely located at $z \gtrsim 1$, such that local contributions to the DMs are less significant. This makes the Parkes results overall the most reliable for investigation of $f_{\rm IGM}$ and other cosmological properties.

3.2 Inference of $f_{\rm IGM}$ and $\pi(z)$

3.2.1 $f_{\rm IGM}$ from localized FRBs

Recently, Li et al. (2020) estimated $f_{\rm IGM} = 0.84^{+0.16}_{-0.22}$ using DM of the five localized FRBs together with the corresponding luminosity distance of Ia supernovae. Shortly after that, Bhandari et al. (2020) report the localization of two additional FRBs. Using their reported values of $\mathrm{DM_{EG}} = \mathrm{DM_{obs}} - \mathrm{DM_{MW}}$ for all six FRBs localized at decent redshift, $z \geq 0.1$, we estimate $f_{\rm IGM} = 0.84^{+0.06}_{-0.24}$ within 3σ using our more sophisticated approach. Though our inference depends on the chosen cosmology (Ade et al. 2016), as the models for IGM as well as host and intervening galaxies in our benchmark scenario are obtained from a specific cosmological simulation, we derive a similar estimated value, with a slightly more conservative lower limit. Still, the conclusion that this confirms the location of missing baryons in the WHIM should be taken with caution, at least because $f_{\rm IGM}$ is considered to be constant with redshift. Note that the likelihood function used in this estimate for $f_{\rm IGM}$, i. e. $\prod_i L(f_{\rm IGM}|\mathrm{DM}_i, z_i)$, can be used as prior to infer the host redshift distribution using unlocalized FRBs, replacing assumptions on $f_{\rm IGM}$.

3.2.2 $f_{\rm IGM}$ from individual instruments

In Fig. 2 we show the Bayes factors $\mathcal{B}$ resulting from the joint analysis of the FRB redshift distribution and of the IGM baryon content $f_{\rm IGM}$. For the 28 FRBs observed by ASKAP, high values of $0.8 \leq f_{\rm IGM}$ are strongly favoured, regardless of the assumed redshift distribution. Hence, ASKAP values seem to confirm the location of missing baryons in the ionized IGM, most probably the WHIM. Due to the generally low distance of ASKAP events, $\mathcal{B}$ shows the lowest variability between the assumed host redshift distributions. However, estimates using ASKAP results are more vulnerable to the unknown contribution of the host galaxy and local environment of the source and should be taken with great

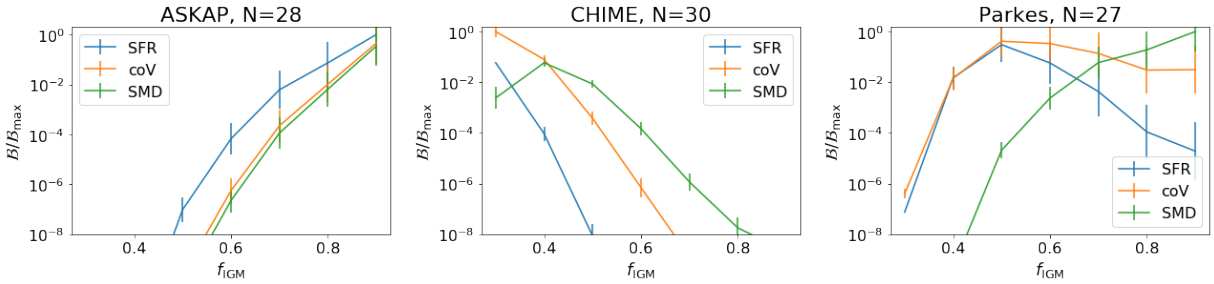

Figure 2. Bayes factor $\mathcal{B}$ of FRBs found in FRBcat comparing scenarios for different baryon content in IGM $f_{\rm IGM}$ and redshift distributions of FRBs, following either star formation rate (SFR), comoving volume (coV) or stellar mass density (SMD), assuming that FRBs are produced by magnetars in our benchmark scenario. The title indicates the instrument that observed the considered number of N FRBs. The estimated value and deviation are obtained via Jackknife resampling. All $\mathcal{B}$ are renormalized to the best-fit $\mathcal{B}_{\rm max}$ to indicate how much less likely a given scenario reproduces the observed data (cf. Fig. 1).

caution. This is further stressed by the fact that ASKAP likely prefers too high $f_{\rm IGM} \gtrsim 0.9$.

The 30 FRBs observed by CHIME, of which 18 have been found to repeat (Amiri et al. 2019; Andersen et al. 2019; Fonseca et al. 2020), clearly favour low values of $f_{\rm IGM} < 0.5$ as the observed distribution of DM concentrates on lower values than expected. Since SFR redshift distribution peaks at a higher redshift, $z \approx 1$, it is disfavoured by CHIME results, except for the case of $f_{\rm IGM} \approx 0.3$. Instead, the SMD distribution, which peaks at lowest redshift, $z \approx 0.5$ is preferred for all probed values of $f_{\rm IGM} > 0.4$ and favours $f_{\rm IGM} = 0.4$. Only for $f_{\rm IGM} \lesssim 0.4$, coV and SFR show higher values of $\mathcal{B}$. However, the parameters for CHIME selection effects available in FRBPOPPY are an early version (see Gardenier et al. 2019), hence results for this instrument should be considered with caution. Still, if the current parameters are proven to be at least roughly correct, the present results either indicate a wrong assumption entering the expected distribution of FRB redshifts, which is likely as CHIME observes a different frequency band than ASKAP and Parkes, or suggest a very low baryon content in the IGM, which we deem as unplausible, as it would contradict the result of any cosmological simulation. However, CHIME results so far seem to disfavour the "WHIM solution" to the missing baryons problem.

The 27 FRBs observed by Parkes show a high variation among the assumed host redshift distributions. The SFR redshift distribution peaks at a higher $z \approx 1.1$ and thus favours $0.4 \lesssim f_{\rm IGM} < 0.7$, while the SMD distribution, peaking at $z \approx 0.6$ prefers a higher $f_{\rm IGM} \geq 0.7$ value. The coV distribution peaks at $z \approx 0.7$ and favours $f_{\rm IGM} \approx 0.6$, however, with relativley low significance.

Not only do the inference of the different data sets differ dramatically, but also the assumed redshift distribution of FRBs affect our interpretation of the data. Thus, the degenerate problem of inferring $f_{\rm IGM}$ with unlocalized FRBs is unlikely to be solved simply by increasing the sample. This stresses the importance of careful investigation of all assumptions entering the interpretation of measures of FRBs in order to arrive at reasonable conclusions. As for now, we cannot derive reasonable conclusions on $f_{\rm IGM}$ and the intrinsic redshift distribution from unlocalized FRBs. Only for the CHIME results we can conclude that the redshift distribution has to peak at $z \lesssim 0.6$, in order to explain the high number of sources with low DMs. This conclusion is independent of the details of the assumed intrinsic redshift distributions and selection effects.

4 DISCUSSION

Our work highlights the fact that the distributions of FRBs obtained by different radio telescopes lead to very different inferences about the cosmological distribution of such events. The disagreement between ASKAP and CHIME is likely to be explained by a strong local contribution of DM to the bright low-distance FRBs observed by ASKAP. These would account for systematically increased values of the observed DM. By not accounting for such a strong local contribution in probability estimates, the increase in DM would be misinterpreted as IGM contribution, calling for a high $f_{\rm IGM}$. If the high DMs observed with ASKAP can be attributed to a stronger local contribution, lower values of $f_{\rm IGM}$ would be favoured by FRB observations. This would reduce the fraction of missing baryons found in the WHIM.

However, the fact that CHIME sees a higher amount of FRBs with $50 < {\rm DM} \ / \ {\rm pc\ cm^{-3}} < 200$ than ASKAP cannot be explained by low baryon content in the IGM or the general FRB population to be concentrated at low redshifts, which would affect CHIME and ASKAP in the same way. If this feature persists in larger samples, it provides a strong hint towards CHIME observing a different subset of FRB sources than ASKAP. The more than 10 times higher gain of CHIME allows it to potentially measure a different set of fainter sources (Amiri et al. 2018), e. g. magnetars of older age (cf. Metzger et al. 2017; Marcote et al. 2020). Since these fainter sources are only visible at low redshift, this would increase the likelihood for CHIME to observe FRBs with low DM. Furthermore, the local environment of older magnetars contributes much less to observed DM (Piro & Gaensler 2018). Thus, old magnetars could account for the increased number of FRBs observed with low DM compared to our expectations that consider the same population of magnetars to be observed by CHIME and ASKAP. Such an increase in the likelihood to observe FRBs from low redshift would also make the CHIME results favour higher values of $f_{\rm IGM}$. However, since CHIME is also able to observe FRBs visible with Parkes (e. g. FRB121102, see Josephy et al.

2019), we require CHIME to detect more events with DM $>$ 800 pc cm^{-3} and any above $>$ 2000 pc cm^{-3} in the future. If there is an extended set of sources available, this should reflect in a higher rate of FRBs observed by CHIME than extrapolated from other surveys (e. g. Chawla et al. 2017).

Note that 18 of the 30 FRBs observed by CHIME we considered here are repeaters (Amiri et al. 2019; Andersen et al. 2019; Fonseca et al. 2020). The high number of repeaters already observed by CHIME would suggest an increased chance to observe fainter bursts from repeating sources, e. g. from old magnetars. For these young neutron stars, this implies a more advanced dissipation of supernova remnants, thus a lower local contribution to DM. If ASKAP can only observe magnetars in an early stage, say $<$ 1000 yr, this could account for the high local contribution to DM, required above, but would also lower the inferred value of $f_{\rm IGM}$. Older magnetars potentially observed by CHIME would also cause a lower contribution to RM, which could be identified by statistical investigation of the distribution of RM observed by the different instruments. However, the current sample of reported RM is too small to allow for any firm conclusions. It might also be possible that separate frequency bands are dominated by completely different sources of FRBs.

Still, even with negligible local contributions, the CHIME results suggest a low IGM baryon content $f_{\rm IGM} \lesssim 0.5$. If this cannot be explained by false assumptions about the FRB redshift distribution and selection effects, the CHIME results would constitute strong evidence against missing baryons in the WHIM or, in fact, anywhere in the ionized IGM.

Caveats Our conclusions are based on a number of different assumptions regarding the IGM baryon content, the FRB redshift distribution as well as local contributions and foregrounds. Furthermore, in our benchmark scenario we assumed all FRBs to be caused by magnetars in axisymmetric galaxies. Alternative progenitor models beyond our assumptions might lead to different conclusions. For example, magnetars that only produce FRBs at an early stage, say less than 10^3 yr after their birth, would produce much stronger dispersion than older ones up to more than 10^5 yr, as assumed in our benchmark scenario, which would make lower values of $f_{\rm IGM}$ more plausible, especially for the low-distance ASKAP sample. In future work, we will consider a wider range of assumptions in order to provide more significant results.

Our estimates of $f_{\rm IGM}$ must rely on the assumption that $f_{\rm IGM}$ is constant. However, as $f_{\rm IGM}$ increases with redshift, we may underestimate the DM from large distances. From te localized FRBs, we can hence only provide a 3σ lower limit on $f_{\rm IGM} \gtrsim 0.6$, which would still leave a baryon deficit of order $\gtrsim$ 20%. The current sample of localized FRBs is thus not yet sufficient to unambiguously solve the missing baryons problem (Macquart et al. 2020). A more sophisticated approach should consider competing scenarios by comparing several IGM simulations of similar setup, including different evolutions of $f_{\rm IGM}$ and compare their predictions regarding DM$_{\rm IGM}$.

Note that FRBPOPPY uses estimates, e.g. of DM(z), in order to decide how many FRBs will be observed at a given redshift. Theses estimates have been produced using slightly different assumptions on the contributing regions. However, the DM is dominated by the IGM and the analytical description used in FRBPOPPY provides a good match to our estimates. Hence, we argue that this does not alter the general conclusions of this work.

Finally, in our benchmark scenario, we do not account for clustering or haloes of host and intervening galaxies (e. g. Prochaska et al. 2019b; Connor et al. 2020). These are especially important for the interpretation of FRBs from low redshifts. However, FRBs from higher redshift, for which these contributions are less important, are much more informative regarding $\pi(z)$ as well as $f_{\rm IGM}$. Thus, the presented results are unlikely to change when haloes are taken into account.

5 CONCLUSIONS

Fast Radio Bursts are an important probe of Baryons in the Universe, as their dispersion measure is sensitive to all phases of the intergalactic medium, including the WHIM. However, inference of the location of missing baryons with unlocalized FRBs is degenerate to the distribution of their host redshifts. In this work we use the estimated extragalactic component of the dispersion measure to jointly infer the redshift distribution of unlocalized FRBs and of the IGM baryon content with a Bayesian statistical approach. We use an analytical model for the local environment of the source, assumed to be a magnetar, semi-analytic models for the ensemble of host and intervening galaxies, as well as models for the IGM from cosmological simulations. Comparing expectations to observations of unlocalized FRBs, we investigate the implications of events observed by ASKAP, CHIME and Parkes, listed in the FRBcat, using the open-source python software package PREFRBLE[3] (Hackstein 2020). Our main conclusions can be so summarised:

- From six localized FRBs beyond redshift $z \geq 0.1$, as listed in Bhandari et al. (2020), we infer the intergalactic baryon content with 3σ limits $f_{\rm IGM} = 0.84^{+0.06}_{-0.24}$. FRBs thus potentially confirm the location of missing baryons in the WHIM. This value agrees well with results of Li et al. (2020).
- In order to unambiguously infer $f_{\rm IGM}$ from unlocalized FRBs, the discrepancy between different instruments need to be resolved, e. g. by identifying different subsets of the FRB population. A mere increase in the number of events will likely not solve this discrepancy.
- Limited to the CHIME sample, we find that the distribution which tracks the star formation rate is the least likely to explain observations. A better agreement is achieved for a distribution that peaks at rather low redshift $z \lesssim 0.6$, e. g. following the stellar mass density.

Though the small sample of localized FRBs suggest the missing baryons are in the ionized IGM, the error margin does not yet allow for unambiguous confirmation of their detection.

[3] github.com/shackste/PreFRBLE

ACKNOWLEDGEMENTS

This work was funded by the Deutsche Forschungsgemeinschaft (DFG) under grant BR2026/25.

SH thanks Rainer Beck, Laura Spitler and Charles Walker for interesting and fruitful discussions on many aspects of this work.

Our cosmological simulations were performed with the ENZO code (http://enzo-project.org), under project HHH38 and HHH42 at the Jülich Supercomputing Centre (P.I. F. Vazza). FV acknowledges financial support from the ERC Starting Grant "MAGCOW", no. 714196.

We further acknowledge the use of computational resources at the Rechenzentrum of the University of Hamburg.

REFERENCES

Ade P. A., et al., 2016, Astronomy & Astrophysics, 594, A13
Amiri M., et al., 2018, The Astrophysical Journal, 863, 48
Amiri M., et al., 2019, arXiv preprint arXiv:1901.04525
Andersen B., et al., 2019, The Astrophysical Journal Letters, 885, L24
Bannister K. W., et al., 2019, Science, 365, 565
Bera A., Bhattacharyya S., Bharadwaj S., Bhat N. R., Chengalur J. N., 2016, Monthly Notices of the Royal Astronomical Society, 457, 2530
Bhandari S., et al., 2020, The Astrophysical Journal Letters, 895, L37
Bryan G. L., et al., 2014, ApJS, 211, 19
Caleb M., Flynn C., Bailes M., Barr E., Hunstead R., Keane E., Ravi V., van Straten W., 2016, Monthly Notices of the Royal Astronomical Society, 458, 708
Cen R., Ostriker J. P., 1999, The Astrophysical Journal Letters, 519, L109
Chawla P., et al., 2017, The Astrophysical Journal, 844, 140
Connor L., et al., 2020, arXiv preprint arXiv:2002.01399
Cordes J. M., Lazio T. J. W., 2002, arXiv preprint astro-ph/0207156
Dai J.-P., Xia J.-Q., 2020, Reconstruction of Reionization History through Dispersion Measure of Fast Radio Bursts (arXiv:2004.11276)
Dave R., et al., 2001, The Astrophysical Journal, 552, 473
Deng W., Zhang B., 2014, The Astrophysical Journal Letters, 783, L35
Dolag K., Gaensler B. M., Beck A. M., Beck M. C., 2015, MNRAS, 451, 4277
Eftekhari T., Berger E., 2017, ApJ, 849, 162
Fonseca E., et al., 2020, arXiv preprint arXiv:2001.03595
Gardenier D., van Leeuwen J., Connor L., Petroff E., 2019, arXiv preprint arXiv:1910.08365
Hackstein S., 2020, PrEFRBLE, doi:10.5281/zenodo.3862636
Hackstein S., Vazza F., Brüggen M., Sorce J. G., Gottlöber S., 2018, MNRAS, 475, 2519
Hackstein S., Brüggen M., Vazza F., Gaensler B. M., Heesen V., 2019, Monthly Notices of the Royal Astronomical Society, 488, 4220
Hackstein S., Rodrigues L. F. S., Brüggen M., Vazza F., 2020, in subm
Josephy A., et al., 2019, The Astrophysical Journal Letters, 882, L18
Keane E., et al., 2016, Nature, 530, 453
Li B., Li L.-B., Zhang Z.-B., Geng J.-J., Song L.-M., Huang Y.-F., Yang Y.-P., 2019, arXiv preprint arXiv:1901.03484
Li Z., Gao H., Wei J.-J., Yang Y.-P., Zhang B., Zhu Z.-H., 2020, Cosmology-insensitive estimate of IGM baryon mass fraction from five localized fast radio bursts (arXiv:2004.08393)
Linder E. V., 2020, arXiv preprint arXiv:2001.11517
Locatelli N., Ronchi M., Ghirlanda G., Ghisellini G., 2018, arXiv e-prints, p. arXiv:1811.10641
Luo R., Lee K., Lorimer D. R., Zhang B., 2018, MNRAS, 481, 2320
Macquart J.-P., Ekers R., 2018, Monthly Notices of the Royal Astronomical Society, 480, 4211
Macquart J.-P., et al., 2010, Publications of the Astronomical Society of Australia, 27, 272
Macquart J.-P., et al., 2020, Nature, 581, 391–395
Mahony E. K., et al., 2018, The Astrophysical Journal Letters, 867, L10
Manchester R. N., Hobbs G. B., Teoh A., Hobbs M., 2005, The Astronomical Journal, 129, 1993
Marcote B., Paragi Z., 2019, arXiv preprint arXiv:1901.08541
Marcote B., et al., 2020, Nature, 577, 190
McQuinn M., 2013, The Astrophysical Journal Letters, 780, L33
Metzger B. D., Berger E., Margalit B., 2017, The Astrophysical Journal, 841, 14
Muñoz J. B., Loeb A., 2018, Physical Review D, 98, 103518
Nicastro F., Mathur S., Elvis M., 2008, Science, 319, 55
Niino Y., 2018, ApJ, 858, 4
Petroff E., et al., 2016, arXiv
Piro A. L., Gaensler B. M., 2018, ApJ, 861, 150
Planck Collaboration et al., 2014, A&A, 571
Pol N., Lam M. T., McLaughlin M. A., Lazio T. J. W., Cordes J. M., 2019, arXiv e-prints, p. arXiv:1903.07630
Prochaska J. X., et al., 2019a, HST Proposal
Prochaska J. X., et al., 2019b, Science, 366, 231
Qiang D.-C., Wei H., 2020, Reconstructing the Fraction of Baryons in the Intergalactic Medium with Fast Radio Bursts via Gaussian Processes (arXiv:2002.10189)
Ravi V., et al., 2019, Nature, 572, 352
Shull J. M., Smith B. D., Danforth C. W., 2012, The Astrophysical Journal, 759, 23
Sorce J. G., et al., 2016, MNRAS, 455, 2078
Staveley-Smith L., et al., 1996, Publications of the Astronomical Society of Australia, 13, 243
Tanimura H., et al., 2018, Monthly Notices of the Royal Astronomical Society, 483, 223
Tendulkar S. P., et al., 2017, The Astrophysical Journal Letters, 834, L7
The CHIME/FRB Collaboration et al., 2018, ApJ, 863, 48
Walker C. R. H., Ma Y.-Z., Breton R. P., 2018, preprint, (arXiv:1804.01548)
Wei J.-J., Li Z., Gao H., Wu X.-F., 2019, Journal of Cosmology and Astroparticle Physics, 2019, 039
Yang Y.-P., Li Q.-C., Zhang B., 2020, arXiv preprint arXiv:2001.10761
de Graaff A., Cai Y.-C., Heymans C., Peacock J. A., 2019, Astronomy & Astrophysics, 624, A48

Chapter 3

Conclusions

In my thesis, I investigate the potential use of extreme astrophysical messengers to measure extragalactic magnetic fields and to infer their cosmic origin. I use sophisticated simulations to estimate the influence of these fields on the propagation of UHECRs and FRBs and compare the expected signal to observations. By probing different possible scenarios of magneto-genesis, the results presented in this work can be used to infer the strength of IGMFs in the foreseeable future as well as to constrain models for the cosmic origin of magnetic fields.

Using simulations to investigate the extragalactic propagation of UHECRs, for the first time, I compare implications of different scenarios of magneto-genesis in models of the IGM that resemble the local Universe. These constrained simulations were produced using the cosmological MHD code ENZO (Bryan et al., 2014) together with initial conditions obtained following Sorce et al. (2016). Starting with identical distribution of matter at redshift $z = 60$, these simulations probe different possible setups for the PMF, comparing implications of strong seed field with several topologies to implications of a weak initial field and formerly astrophysical magnetization. I combine these different models for the IGMF in the local Universe with possible source catalogues of UHECRs and simulate their propagation in order to match the recent observation of large-scale anisotropy reported by PAO (Aab et al., 2018a). I conclude that the observed large-scale anisotropy and its energy-dependence potentially contains information about the composition ejected by the sources and show that the **observed anisotropy in the arrival directions of UHECRs requires a heavy source composition**. The heavy particles at highest energies quickly dissolve into numerous Hydrogen and Helium nuclei, thus increasing the number of UHECRs from nearby sources that enter the MW. This causes a strong increase of flux in direction of these sources, mostly immediately below the maximum injection energy of nucleons and quickly decreasing at lower energies. This can explain the anisotropy above 8 EeV, while none is observed between 4 EeV and 8 EeV (Aab et al., 2018a).

I further investigate the angular power spectrum of spherical harmonics decomposition of the full-sky of arrival directions of UHECRs. I found that conclusions about the IGMF and magneto-genesis from the angular power spectrum are presently not possible, unless the sources of UHECRs can be localized. However, with the use of approximate Bayesian computation, competing source catalogues can be used together with models of the IGMF as well as the Galactic magnetic field. The results can be tested to reproduce the PAO dipole as well as the excess observed around Centaurus A in order to quantify and compare the likelihood of competing models to account for the observed data. Reasonable conclusions would require to investigate a large number of different scenarios. However, this procedure would potentially allow us to identify the sources of UHECRs as well as to measure strength and shape of intergalactic and Galactic magnetic fields. Once established, this framework can be used to further constrain the Galactic magnetic field models obtained by the procedure proposed in Boulanger et al. (2018).

After publication of Hackstein et al. (2018), Bray and Scaife (2018) attempt to derive a limit on the IGMF strength from the large-scale anisotropy reported by PAO, Fig. 1.9. They compare the inferred direction of the dipole to that of potential source catalogues, comparing the disposition to the average deflection angle of UHECRs as a function of IGMF strength. To derive the typical deflection angle, they assume a turbulent magnetic field, where the particles crossed several coherence lengths. In this propagation mode, however, small differences in the initial momentum of the particle

lead to completely uncorrelated propagation paths. Thus, turbulent magnetic fields do not cause a systematic shift in arrival directions, which is required to create a difference in the apparent and physical position of the source. They rather cause the average deviation from the original direction, similar to the random-walk problem, causing an increase of the apparent size of the object, while the position remains the same. Therefore, the angle derived in their work, describing the apparent size, cannot be compared to the disposition of apparent and actual direction of sources. Their inferred limits are thus invalid.

The dipole magnetic field of the Earth induces a quadrupole anisotropy in the flux of CRs, manifest e. g. in the van-Allen belts, where CRs oscillate between the magnetic poles, causing an increase in the flux that arrives at Earth's surface. At first glance, this seems to violate Liouville's principle for CRs, which states that deflections by magnetic fields cannot induce anisotropy in a flux of charged particles with uniform source density, as the integral that defines this flux would not depend on the path. However, since the sources of CRs are outside Earth's magnetic field, the assumption of uniform source density breaks down and the dipole magnetic field introduces an anisotropy, e. g. by unpopulated field lines. The same is true for UHECRs of extragalactic origin in the Galactic magnetic field. The potential existence of a strong poloidal magnetic field component that extends far into the halo of the MW would thus induce quadrupole anisotropy in the flux of UHECRs that reaches Earth. Non-observation of such an anisotropy in EeV protons suggests an upper limit on the characteristic strength of a poloidal magnetic field in the Galactic halo of the order of $\sim 10\ \mu$G.

However, the composition of UHECRs is changed on a smaller time scale, thus is more sensitive to systematically increased travel time. Thus, a future identification of individual nuclei (Aab et al., 2016) and subsequent observation of anisotropy or lack thereof in the composition of arriving particles potentially provides stronger limits on the magnetic field in the MW halo.

I used several models of IGMF to simulate the propagation of UHECRs with CRPropa, some of which I made publicly available at crpropa.desy.de. Batista et al. (2017) further compare the implications of models used in Hackstein et al. (2016) with other models of the IGMF and investigate their influence on identification of UHECR sources. They conclude that even the strongest fields allowed by observations of the CMB account only for weak deflection of protons in a significant part of the sky, thus potentially enabling UHECR astronomy. Further, they find that deflection in IGMFs can wash out features in the energy spectrum of UHECRs, especially at high energies, caused by inhomogeneities in the local distribution of sources. Eichmann (2019) used the *Hackstein* models (Hackstein et al., 2018) to show that even the strongest possible IGMFs cannot isotropize the flux of UHECRs from a source at only a few Mpc distance, e. g. Centaurus A. Rachen (2019) used the *Hackstein* models together with a sophisticated catalogue of radio sources as possible UHECR sources, based on a complete theoretical description of the source physics. For example, he considers blazars - active radio galaxies with a jet pointing in our direction - to eject increased amounts of UHECRs as compared to other radio galaxies, due to collimated stream of particles emitted by the jet. He concludes that radio galaxies can explain the observed properties of UHECRs in astrophysical models for the origin of IGMFs, where weak fields in voids, $B < 10^{-6}$ nG account only for small amounts of extragalactic deflection of UHECRs.

In conclusion, the **IGMF models I made publicly available** during my work **allow other researchers to obtain a realistic estimate for the extragalactic deflection of charged particles** as well as uncertainties due to unknown field strength in voids. Using this tool, the large-scale anisotropy reported by PAO together with sophisticated models for the sources of UHECRs as well as for the Galactic deflection can help to identify the origin of UHECRs as well as the injected composition. The unknown extragalactic deflection plays a significant role in this process and the results of my work contribute to a realistic estimate of the influence of IGMFs.

In addition to that, I investigate the possibility to measure properties of the IGM and infer information about magneto-genesis by comparing observations of FRBs to expectations. For the first time, I combine predictions for the most dominant regions along the LoS of FRBs, including the IGM, local source environment, the host as well as intervening galaxies, using sophisticated models that resemble our current knowledge. Using Bayesian tools, such as Monte-Carlo simulations, I derive likelihood functions for the individual contribution to DM, RM, and temporal broadening τ and combine the different regions to realistic scenarios for the full LoS. I compare statistical predictions to FRBs observed by different instruments in order to infer likelihood estimates for competing models. To this end, I have created the open-source python software package PREFRBLE[1], "Probability Estimates for Fast Radio Bursts to obtain model Likelihood Estimates" (Hackstein, 2020).

Most papers require localized FRBs or associations with other events, e. g. γ-ray bursts of superluminous supernovae. Using only the sample of six well-localized FRBs with decent redshift $z > 0.1$, I infer a **baryon content in the IGM of** $f_{\mathrm{IGM}} = 0.84^{+0.06}_{-0.24}$, where a value of 1 indicates that all baryons are part of the ionized IGM. This fits well with estimates from Li et al. (2020), who made a cosmology-independent inference using luminosity distance of Ia supernovae. The rather high value of f_{IGM} suggests that the missing baryons are indeed localized in the WHIM, although the high error margin requires further investigation. Thus the current sample of localized FRBs is not sufficient to unambiguously locate the missing baryons (Macquart et al., 2020).

Furthermore, I show how the DM of unlocalized FRBs together with assumptions on their intrinsic redshift distribution can be used to infer both, the amount of ionized baryons in the IGM fIGM as well as the redshift distribution of FRB sources. By applying Bayes theorem, I **provide lower limits for the host redshift of more than** 30 **FRBs**. For this, I work out a **statistical treatment of unidentified intervening galaxies** along the LoS, which I show cannot be excluded entirely based upon observed τ. I show that observations by different instruments, especially CHIME and ASKAP, strongly differ in their implications, either calling for too low or too high values of f_{IGM}. In order to allow for reasonable conclusions, this discrepancy has to be resolved on a theoretical level, e. g. by a different subset of sources observed by those instruments, thus a systematically stronger source environment for ASKAP events, or a lower average redshift for sources detected by CHIME. Still, by comparing detailed and constrained simulations of cosmic evolution and the local Universe that consider different scenarios for ionized gas in the IGM, the enigma of missing baryons can be solved using unlocalized FRBs in the framework presented in this thesis.

[1] github.com/shackste/PreFRBLE

Moreover, I show that the **strength of IGMFs determines the amount and likelihood of FRBs observed with extragalactic** RM ≈ 1 rad m^{-2}. An amount of $\gtrsim 10^3$ unlocalized FRBs potentially allows to put first constraints on the slope α of the relation between magnetic field strength B and gas density ρ in the IGM (cf. Fig. 1.3), idealized to $B \propto \rho^{\alpha}$, and thus to constrain scenarios of magneto-genesis. By using the combined likelihood of DM and RM I make use of the full information entailed in these measures, rather than to reduce to their ratio RM/DM (Akahori et al., 2016; Vazza et al., 2018; Piro and Gaensler, 2018). The required amount of FRBs will likely be made available by CHIME and ASKAP observations in the near future, which are able to observe few FRBs every day together with their polarization properties. However, the challenge is to correctly estimate the contribution to RM of all other regions along the LoS, since they can all provide RM on similar scale.

Finally, I show that a number of 10^5 FRBs can deliver sufficient information to infer an upper limit on the IGMF strength which is seven orders of magnitude lower than the current limit, thus **allowing to measure the whole range of possible field strengths** allowed by current constraints. The results of my work thus enable us to answer the long-standing question for the magnetization of the IGM. Though currently operating observatories cannot provide such an extensive basis, the fact that about 10^3 FRBs are visible in the sky every day (Champion et al., 2016) allows to acquire the required data in the foreseeable future with the use of huge arrays of radio telescopes, e. g. the SKA.

In the future, the framework established in PrEFRBLE can be used to compare competing models for the sources of FRBs and their host galaxies and thus allow for an automatized identification of FRB progenitors, also on an individual basis. However, especially the identification of the sources would benefit from consideration of other observables that are not affected during propagation, such as bandwidth, pulse width and fluence, which can easily be implemented in the presented framework.

In conclusion, my work on FRBs enables us to measure the IGMF to high precision and certainty, once sufficient observational data has been acquired. Thus, this work contributes an important step towards solving one of the most fascinating and challenging questions in modern astronomy: "What is the cosmic origin of magnetic fields?" Furthermore, the framework established during my thesis can be used to confirm the location of missing baryons in the WHIM as well as to answer many pressing questions of FRB astronomy, regarding the sources, their host galaxy and their population properties.

Bibliography

Aab, A., Abreu, P., Aglietta, M., Ahn, E., Samarai, I. A., Albuquerque, I., Allekotte, I., Allison, P., Almela, A., Castillo, J. A., et al. (2016). The pierre auger observatory upgrade-preliminary design report. *arXiv preprint arXiv:1604.03637*.

Aab, A., Abreu, P., Aglietta, M., Al Samarai, I., Albuquerque, I., Allekotte, I., Almela, A., Castillo, J. A., Alvarez-Muñiz, J., Anastasi, G., et al. (2017). Combined fit of spectrum and composition data as measured by the pierre auger observatory. *Journal of Cosmology and Astroparticle Physics*, 2017(04):038.

Aab, A., Abreu, P., Aglietta, M., Albuquerque, I. F. M., Albury, J. M., Allekotte, I., Almela, A., Castillo, J. A., Alvarez-Muñiz, J., Anastasi, G. A., et al. (2018a). Large-scale cosmic-ray anisotropies above 4 eev measured by the pierre auger observatory. *The Astrophysical Journal*, 868(1):4.

Aab, A., Abreu, P., Aglietta, M., Albuquerque, I. F. M., Allekotte, I., Almela, A., Castillo, J. A., Alvarez-Muñiz, J., Anastasi, G. A., Anchordoqui, L., Andrada, B., Andringa, S., Aramo, C., Arsene, N., Asorey, H., Assis, P., Avila, G., Badescu, A. M., Balaceanu, A., Barbato, F., Luz, R. J. B., Beatty, J. J., Becker, K. H., Bellido, J. A., Berat, C., Bertaina, M. E., Bertou, X., Biermann, P. L., Biteau, J., Blaess, S. G., Blanco, A., Blazek, J., Bleve, C., Boháčová, M., Bonifazi, C., Borodai, N., Botti, A. M., Brack, J., Brancus, I., Bretz, T., Bridgeman, A., Briechle, F. L., Buchholz, P., Bueno, A., Buitink, S., Buscemi, M., Caballero-Mora, K. S., Caccianiga, L., Cancio, A., Canfora, F., Caruso, R., Castellina, A., Catalani, F., Cataldi, G., Cazon, L., Chavez, A. G., Chinellato, J. A., Chudoba, J., Clay, R. W., Cerutti, A. C. C., Colalillo, R., Coleman, A., Collica, L., Coluccia, M. R., Conceição, R., Consolati, G., Contreras, F., Cooper, M. J., Coutu, S., Covault, C. E., Cronin, J., D'Amico, S., Daniel, B., Dasso, S., Daumiller, K., Dawson, B. R., de Almeida, R. M., de Jong, S. J., Mauro, G. D., de Mello Neto, J. R. T., Mitri, I. D., de Oliveira, J., de Souza, V., Debatin, J., Deligny, O., Castro, M. L. D., Diogo, F., Dobrigkeit, C., D'Olivo, J. C., Dorosti, Q., dos Anjos, R. C., Dova, M. T., Dundovic, A., Ebr, J., Engel, R., Erdmann, M., Erfani, M., Escobar, C. O., Espadanal, J., Etchegoyen, A., Falcke, H., Farmer, J., Farrar, G., Fauth, A. C., Fazzini, N., Fenu, F., Fick, B., Figueira, J. M., Filipčič, A., Freire, M. M., Fujii, T., Fuster, A., Gaïor, R., García, B., Gaté, F., Gemmeke, H., Gherghel-Lascu, A., Ghia, P. L., Giaccari, U., Giammarchi, M., Giller, M., Głas, D., Glaser, C., Golup, G., Berisso, M. G., Vitale, P. F. G., González, N., Gorgi, A., Grillo, A. F., Grubb, T. D., Guarino, F., Guedes, G. P., Halliday, R., Hampel, M. R., Hansen, P., Harari, D., Harrison, T. A., Haungs, A., Hebbeker, T., Heck, D., Heimann, P., Herve, A. E., Hill, G. C., Hojvat, C., Holt, E., Homola, P., Hörandel, J. R., Horvath, P., Hrabovský, M., Huege, T., Hulsman, J., Insolia, A., Isar, P. G., Jandt, I., Johnsen, J. A., Josebachuili, M., Jurysek, J., Kääpä, A., Kambeitz, O., Kampert, K. H., Keilhauer, B., Kemmerich, N., Kemp, E., Kemp, J., Kieckhafer, R. M., Klages, H. O., Kleifges, M., Kleinfeller, J., Krause, R., Krohm, N., Kuempel, D., Mezek, G. K., Kunka, N., Awad, A. K., Lago, B. L., LaHurd, D., Lang, R. G., Lauscher,

M., Legumina, R., de Oliveira, M. A. L., Letessier-Selvon, A., Lhenry-Yvon, I., Link, K., Presti, D. L., Lopes, L., López, R., Casado, A. L., Lorek, R., Luce, Q., Lucero, A., Malacari, M., Mallamaci, M., Mandat, D., Mantsch, P., Mariazzi, A. G., Mariş, I. C., Marsella, G., Martello, D., Martinez, H., Bravo, O. M., Meza, J. J. M., Mathes, H. J., Mathys, S., Matthews, J., Matthiae, G., Mayotte, E., Mazur, P. O., Medina, C., Medina-Tanco, G., Melo, D., Menshikov, A., Merenda, K.-D., Michal, S., Micheletti, M. I., Middendorf, L., Miramonti, L., Mitrica, B., Mockler, D., Mollerach, S., Montanet, F., Morello, C., Morlino, G., Mostafá, M., Müller, A. L., Müller, G., Muller, M. A., Müller, S., Mussa, R., Naranjo, I., Nellen, L., Nguyen, P. H., Niculescu-Oglinzanu, M., Niechciol, M., Niemietz, L., Niggemann, T., Nitz, D., Nosek, D., Novotny, V., Nožka, L., Núñez, L. A., Oikonomou, F., Olinto, A., Palatka, M., Pallotta, J., Papenbreer, P., Parente, G., Parra, A., Paul, T., Pech, M., Pedreira, F., Pekala, J., Pelayo, R., Peña-Rodriguez, J., Pereira, L. A. S., Perlin, M., Perrone, L., Peters, C., Petrera, S., Phuntsok, J., Pierog, T., Pimenta, M., Pirronello, V., Platino, M., Plum, M., Poh, J., Porowski, C., Prado, R. R., Privitera, P., Prouza, M., Quel, E. J., Querchfeld, S., Quinn, S., Ramos-Pollan, R., Rautenberg, J., Ravignani, D., Ridky, J., Riehn, F., Risse, M., Ristori, P., Rizi, V., de Carvalho, W. R., Fernandez, G. R., Rojo, J. R., Roncoroni, M. J., Roth, M., Roulet, E., Rovero, A. C., Ruehl, P., Saffi, S. J., Saftoiu, A., Salamida, F., Salazar, H., Saleh, A., Salina, G., Sánchez, F., Sanchez-Lucas, P., Santos, E. M., Santos, E., Sarazin, F., Sarmento, R., Sarmiento-Cano, C., Sato, R., Schauer, M., Scherini, V., Schieler, H., Schimp, M., Schmidt, D., Scholten, O., Schovánek, P., Schröder, F. G., Schröder, S., Schulz, A., Schumacher, J., Sciutto, S. J., Segreto, A., Shadkam, A., Shellard, R. C., Sigl, G., Silli, G., Šmída, R., Snow, G. R., Sommers, P., Sonntag, S., Soriano, J. F., Squartini, R., Stanca, D., Stanič, S., Stasielak, J., Stassi, P., Stolpovskiy, M., Strafella, F., Streich, A., Suarez, F., Durán, M. S., Sudholz, T., Suomijärvi, T., Supanitsky, A. D., Šupík, J., Swain, J., Szadkowski, Z., Taboada, A., Taborda, O. A., Theodoro, V. M., Timmermans, C., Peixoto, C. J. T., Tomankova, L., Tomé, B., Elipe, G. T., Travnicek, P., Trini, M., Ulrich, R., Unger, M., Urban, M., Galicia, J. F. V., Valiño, I., Valore, L., van Aar, G., van Bodegom, P., van den Berg, A. M., van Vliet, A., Varela, E., Cárdenas, B. V., Vázquez, R. A., Veberič, D., Ventura, C., Quispe, I. D. V., Verzi, V., Vicha, J., Villaseñor, L., Vorobiov, S., Wahlberg, H., Wainberg, O., Walz, D., Watson, A. A., Weber, M., Weindl, A., Wiedeński, M., Wiencke, L., Wilczyński, H., Wirtz, M., Wittkowski, D., Wundheiler, B., Yang, L., Yushkov, A., Zas, E., Zavrtanik, D., Zavrtanik, M., Zepeda, A., Zimmermann, B., Ziolkowski, M., Zong, Z., and and, F. Z. (2018b). An indication of anisotropy in arrival directions of ultra-high-energy cosmic rays through comparison to the flux pattern of extragalactic gamma-ray sources. *The Astrophysical Journal*, 853(2):L29.

Abbasi, R., Abe, M., Abu-Zayyad, T., Allen, M., Anderson, R., Azuma, R., Barcikowski, E., Belz, J., Bergman, D., Blake, S., et al. (2014). Indications of intermediate-scale anisotropy of cosmic rays with energy greater than 57 eev in the northern sky measured with the surface detector of the telescope array experiment. *The Astrophysical Journal Letters*, 790(2):L21.

Abbasi, R., Abe, M., Abu-Zayyad, T., Allen, M., Azuma, R., Barcikowski, E., Belz, J., Bergman, D., Blake, S., Cady, R., et al. (2019). Mass composition of ultrahigh-energy cosmic rays with the telescope array surface detector data. *Physical Review D*, 99(2):022002.

Abbott, B. P., Abbott, R., Abbott, T., Acernese, F., Ackley, K., Adams, C., Adams, T., Addesso, P., Adhikari, R., Adya, V., et al. (2017). Estimating the contribution of dynamical ejecta in the kilonova associated with gw170817. *arXiv preprint arXiv:1710.05836*.

Abu-Zayyad, T., Aida, R., Allen, M., Anderson, R., Azuma, R., Barcikowski, E., Belz, J., Bergman, D., Blake, S., Cady, R., Cheon, B., Chiba, J., Chikawa, M., Cho, E., Cho, W., Fujii, H., Fujii, T., Fukuda, T., Fukushima, M., Gorbunov, D., Hanlon, W., Hayashi, K., Hayashi, Y., Hayashida, N., Hibino, K., Hiyama, K., Honda, K., Iguchi, T., Ikeda, D., Ikuta, K., Inoue, N., Ishii, T., Ishimori, R., Ivanov, D., Iwamoto, S., Jui, C., Kadota, K., Kakimoto, F., Kalashev, O., Kanbe, T., Kasahara, K., Kawai, H., Kawakami, S., Kawana, S., Kido, E., Kim, H., Kim, H., Kim, J., Kim, J., Kitamoto, K., Kobayashi, K., Kobayashi, Y., Kondo, Y., Kuramoto, K., Kuzmin, V., Kwon, Y., Lim, S., Machida, S., Martens, K., Martineau, J., Matsuda, T., Matsuura, T., Matsuyama, T., Matthews, J., Myers, I., Minamino, M., Miyata, K., Miyauchi, H., Murano, Y., Nakamura, T., Nam, S., Nonaka, T., Ogio, S., Ohnishi, M., Ohoka, H., Oki, K., Oku, D., Okuda, T., Oshima, A., Ozawa, S., Park, I., Pshirkov, M., Rodriguez, D., Roh, S., Rubtsov, G., Ryu, D., Sagawa, H., Sakurai, N., Sampson, A., Scott, L., Shah, P., Shibata, F., Shibata, T., Shimodaira, H., Shin, B., Shin, J., Shirahama, T., Smith, J., Sokolsky, P., Sonley, T., Springer, R., Stokes, B., Stratton, S., Stroman, T., Suzuki, S., Takahashi, Y., Takeda, M., Taketa, A., Takita, M., Tameda, Y., Tanaka, H., Tanaka, K., Tanaka, M., Thomas, S., Thomson, G., Tinyakov, P., Tkachev, I., Tokuno, H., Tomida, T., Troitsky, S., Tsunesada, Y., Tsutsumi, K., Tsuyuguchi, Y., Uchihori, Y., Udo, S., Ukai, H., Vasiloff, G., Wada, Y., Wong, T., Wood, M., Yamakawa, Y., Yamaoka, H., Yamazaki, K., Yang, J., Yoshida, S., Yoshii, H., Zollinger, R., and Zundel, Z. (2012). The surface detector array of the telescope array experiment. *Nuclear Instruments and Methods in Physics Research Section A: Accelerators, Spectrometers, Detectors and Associated Equipment*, 689:87 – 97.

Ade, P., Aghanim, N., Arnaud, M., Arroja, F., Ashdown, M., Aumont, J., Baccigalupi, C., Ballardini, M., Banday, A., Barreiro, R., et al. (2016a). Planck 2015 results-xix. constraints on primordial magnetic fields. *A&A*, 594:A19.

Ade, P. A., Aghanim, N., Arnaud, M., Ashdown, M., Aumont, J., Baccigalupi, C., Banday, A., Barreiro, R., Bartlett, J., Bartolo, N., et al. (2016b). Planck 2015 results-xiii. cosmological parameters. *Astronomy & Astrophysics*, 594:A13.

Aharonian, F., Bykov, A., Parizot, E., Ptuskin, V., and Watson, A. (2011). Cosmic rays in galactic and extragalactic magnetic fields. *Space Science Reviews - SPACE SCI REV*, 166.

Akahori, T., Ryu, D., and Gaensler, B. (2016). Fast radio bursts as probes of magnetic fields in the intergalactic medium. *The Astrophysical Journal*, 824(2):105.

Allard, D. (2012). Extragalactic propagation of ultrahigh energy cosmic-rays. *Astroparticle Physics*, 39:33–43.

Amiri, M., Andersen, B., Bandura, K., Bhardwaj, M., Boyle, P., Brar, C., Chawla, P., Chen, T., Cliche, J., Cubranic, D., et al. (2020). Periodic activity from a fast radio burst source. *arXiv preprint arXiv:2001.10275*.

Amiri, M., Bandura, K., Berger, P., Bhardwaj, M., Boyce, M., Boyle, P., Brar, C., Burhanpurkar, M., Chawla, P., Chowdhury, J., et al. (2018). The chime fast radio burst project: system overview. *The Astrophysical Journal*, 863(1):48.

Amiri, M., Bandura, K., Bhardwaj, M., Boubel, P., Boyce, M. M., Boyle, P. J., Brar, C., Burhanpurkar, M., Chawla, P., Cliche, J. F., et al. (2019). Observations of fast radio bursts at frequencies down to 400 megahertz. *arXiv preprint arXiv:1901.04524*.

Andersen, B., Bandura, K., Bhardwaj, M., Boubel, P., Boyce, M., Boyle, P., Brar, C., Cassanelli, T., Chawla, P., Cubranic, D., et al. (2019). Chime/frb discovery of eight new repeating fast radio burst sources. *The Astrophysical Journal Letters*, 885(1):L24.

Arlen, T. C., Vassilev, V. V., Weisgarber, T., Wakely, S. P., and Shafi, S. Y. (2014). Intergalactic magnetic fields and gamma-ray observations of extreme tev blazars. *The Astrophysical Journal*, 796(1):18.

Athreya, R., Kapahi, V., McCarthy, P., and Van Breugel, W. (1998). Large rotation measures in radio galaxies at z¿ 2. *Astronomy and Astrophysics*, 329:809–820.

Batista, R. A., Biteau, J., Bustamante, M., Dolag, K., Engel, R., Fang, K., Kampert, K.-H., Kostunin, D., Mostafa, M., Murase, K., et al. (2019). Open questions in cosmic-ray research at ultrahigh energies. *arXiv preprint arXiv:1903.06714*.

Batista, R. A., Shin, M.-S., Devriendt, J., Semikoz, D., and Sigl, G. (2017). Implications of strong intergalactic magnetic fields for ultrahigh-energy cosmic-ray astronomy. *Physical Review D*, 96(2):023010.

Beck, R. (2009). Galactic and extragalactic magnetic fields–a concise review. *Astrophysics and Space Sciences Transactions*, 5(1):43–47.

Beloborodov, A. M. (2017). A Flaring Magnetar in FRB 121102? *ApJL*, 843(2):L26.

Bernet, M. L., Miniati, F., Lilly, S. J., Kronberg, P. P., and Dessauges-Zavadsky, M. (2008). Strong magnetic fields in normal galaxies at high redshift. *Nature*, 454(7202):302–304.

Bhandari, S., Keane, E., Barr, E., Jameson, A., Petroff, E., Johnston, S., Bailes, M., Bhat, N., Burgay, M., Burke-Spolaor, S., et al. (2017). The survey for pulsars and extragalactic radio bursts–ii. new frb discoveries and their follow-up. *MNRAS*, 475(2):1427–1446.

Bhandari, S., Sadler, E. M., Prochaska, J. X., Simha, S., Ryder, S. D., Marnoch, L., Bannister, K. W., Macquart, J.-P., Flynn, C., Shannon, R. M., et al. (2020). The host galaxies and progenitors of fast radio bursts localized with the australian square kilometre array pathfinder. *The Astrophysical Journal Letters*, 895(2):L37.

Biermann, L. (1950). Uber den ursprung der magnetfelder auf sternen und im interstellaren raum (mit einem anhang von a. schluter). *Zs. Naturforschung, 5a*, 65.

Blasi, P. (2013). The origin of galactic cosmic rays. *The Astronomy and Astrophysics Review*, 21(1):70.

Blasi, P., Burles, S., and Olinto, A. V. (1999). Cosmological magnetic field limits in an inhomogeneous universe. *The Astrophysical Journal Letters*, 514(2):L79.

Blümer, J., Engel, R., and Hörandel, J. R. (2009). Cosmic rays from the knee to the highest energies. *Progress in Particle and Nuclear Physics*, 63(2):293–338.

Bochenek, C. D., Ravi, V., Belov, K. V., Hallinan, G., Kocz, J., Kulkarni, S. R., and McKenna, D. L. (2020). A fast radio burst associated with a galactic magnetar. *arXiv preprint arXiv:2005.10828*.

Boulanger, F., Enßlin, T., Fletcher, A., Girichides, P., Hackstein, S., Haverkorn, M., Hörandel, J. R., Jaffe, T., Jasche, J., Kachelrieß, M., Kotera, K., Pfrommer, C., Rachen, J. P., Rodrigues, L. F. S., Ruiz-Granados, B., Seta, A., Shukurov, A., Sigl, G., Steininger, T., Vacca, V., van der Velden, E., van Vliet, A., and Wang, J. (2018). IMAGINE: a comprehensive view of the interstellar medium, Galactic magnetic fields and cosmic rays. *Journal of Cosmology and Astro-Particle Physics*, 2018:049.

Bouwhuis, M., Bannister, K. W., Macquart, J.-P., Shannon, R. M., Kaplan, D. L., Bunton, J. D., Koribalski, B. S., and Whiting, M. T. (2020). A search for fast radio burst-like emission from fermi gamma-ray bursts.

Bray, J. and Scaife, A. (2018). An upper limit on the strength of the extragalactic magnetic field from ultra-high-energy cosmic-ray anisotropy. *The Astrophysical Journal*, 861(1):3.

Brown, S., Vernstrom, T., Carretti, E., Dolag, K., Gaensler, B., Staveley-Smith, L., Bernardi, G., Haverkorn, M., Kesteven, M., and Poppi, S. (2017). Limiting magnetic fields in the cosmic web with diffuse radio emission. *Monthly Notices of the Royal Astronomical Society*, 468(4):4246–4253.

Bryan, G. L., Norman, M. L., O'Shea, B. W., Abel, T., Wise, J. H., Turk, M. J., Reynolds, D. R., Collins, D. C., Wang, P., Skillman, S. W., et al. (2014). Enzo: An adaptive mesh refinement code for astrophysics. *The Astrophysical Journal Supplement Series*, 211(2):19.

Caleb, M., Stappers, B., Rajwade, K., and Flynn, C. (2019). Are all fast radio bursts repeating sources? *Monthly Notices of the Royal Astronomical Society*, 484(4):5500–5508.

Cameron, R., Dikpati, M., and Brandenburg, A. (2017). The global solar dynamo. *Space Science Reviews*, 210(1-4):367–395.

Camilo, F., Ransom, S. M., Halpern, J. P., Reynolds, J., Helfand, D. J., Zimmerman, N., and Sarkissian, J. (2006). Transient pulsed radio emission from a magnetar. *Nature*, 442(7105):892–895.

Champion, D., Petroff, E., Kramer, M., Keith, M., Bailes, M., Barr, E., Bates, S., Bhat, N., Burgay, M., Burke-Spolaor, S., et al. (2016). Five new fast radio bursts from the htru high-latitude survey at parkes: first evidence for two-component bursts. *Monthly Notices of the Royal Astronomical Society: Letters*, 460(1):L30–L34.

Chawla, P., Andersen, B. C., Bhardwaj, M., Fonseca, E., Josephy, A., Kaspi, V. M., Michilli, D., Pleunis, Z., Bandura, K. M., Bassa, C. G., Boyle, P. J., Cassanelli, T., Cubranic, D., Dobbs, M., Dong, F. Q., Gaensler, B. M., Good, D. C., Hessels, J. W. T., Landecker, T. L., Leung, C., Li, D. Z., Lin, H. . H., Masui, K., Mckinven, R., Mena-Parra, J., Merryfield, M., Meyers, B. W., Naidu, A., Patel, C., Rafiei-Ravandi, M., Rahman, M., Sanghavi, P., Scholz, P., Shin, K., Smith, K. M., Stairs, I. H., Tendulkar, S. P., and Vanderlinde, K. (2020). Detection of repeating frb 180916.j0158+65 down to frequencies of 300 mhz.

Cho, H., Macquart, J.-P., Shannon, R. M., Deller, A. T., Morrison, I. S., Ekers, R. D., Bannister, K. W., Farah, W., Qiu, H., Sammons, M. W., Bailes, M., Bhandari, S., Day, C. K., James, C. W., Phillips, C. J., Prochaska, J. X., and Tuthill, J. (2020). Spectropolarimetric analysis of frb 181112 at microsecond resolution: Implications for fast radio burst emission mechanism.

Cirkel-Bartelt, V. (2008). History of astroparticle physics and its components. *Living reviews in relativity*, 11(1):2.

Coenen, T., van Leeuwen, J., Hessels, J. W. T., Stappers, B. W., Kondratiev, V. I., Alexov, A., Breton, R. P., Bilous, A., Cooper, S., Falcke, H., Fallows, R. A., Gajjar, V., Grießmeier, J. M., Hassall, T. E., Karastergiou, A., Keane, E. F., Kramer, M., Kuniyoshi, M., Noutsos, A., Osłowski, S., Pilia, M., Serylak, M., Schrijvers, C., Sobey, C., ter Veen, S., Verbiest, J., Weltevrede, P., Wijnholds, S., Zagkouris, K., van Amesfoort, A. S., Anderson, J., Asgekar, A., Avruch, I. M., Bell, M. E., Bentum, M. J., Bernardi, G., Best, P., Bonafede, A., Breitling, F., Broderick, J., Brüggen, M., Butcher, H. R., Ciardi, B., Corstanje, A., Deller, A., Duscha, S., Eislöffel, J., Fender, R., Ferrari, C., Frieswijk, W., Garrett, M. A., de Gasperin, F., de Geus, E., Gunst, A. W., Hamaker, J. P., Heald, G., Hoeft, M., van der Horst, A., Juette, E., Kuper, G., Law, C., Mann, G., McFadden, R., McKay-Bukowski, D., McKean, J. P., Munk, H., Orru, E., Paas, H., Pand ey-Pommier, M., Polatidis, A. G., Reich, W., Renting, A., Röttgering, H., Rowlinson, A., Scaife, A. M. M., Schwarz, D., Sluman, J., Smirnov, O., Swinbank, J., Tagger, M., Tang, Y., Tasse, C., Thoudam, S., Toribio, C., Vermeulen, R., Vocks, C., van Weeren, R. J., Wucknitz, O., Zarka, P., and Zensus, A. (2014). The LOFAR pilot surveys for pulsars and fast radio transients. *A&A*, 570:A60.

Collaboration, P. A. et al. (2007). Correlation of the highest-energy cosmic rays with nearby extragalactic objects. *Science*, 318(5852):938–943.

Collaboration, P. A. et al. (2015). The pierre auger cosmic ray observatory. *Nuclear Instruments and Methods in Physics Research Section A: Accelerators, Spectrometers, Detectors and Associated Equipment*, 798:172–213.

Collaboration, T. C., :, Andersen, B. C., Bandura, K. M., Bhardwaj, M., Bij, A., Boyce, M. M., Boyle, P. J., Brar, C., Cassanelli, T., Chawla, P., Chen, T., Cliche, J. F., Cook, A., Cubranic, D., Curtin, A. P., Denman, N. T., Dobbs, M., Dong, F. Q., Fandino, M., Fonseca, E., Gaensler, B. M., Giri, U., Good, D. C., Halpern, M., Hill, A. S., Hinshaw, G. F., Höfer, C., Josephy, A., Kania, J. W., Kaspi, V. M., Landecker, T. L., Leung, C., Li, D. Z., Lin, H. H., Masui, K. W., Mckinven, R., Mena-Parra, J., Merryfield, M., Meyers, B. W., Michilli, D., Milutinovic, N., Mirhosseini, A., Münchmeyer, M., Naidu, A., Newburgh, L. B., Ng, C., Patel, C., Pen, U. L., Pinsonneault-Marotte, T., Pleunis, Z., Quine, B. M., Rafiei-Ravandi, M., Rahman, M., Ransom, S. M., Renard, A., Sanghavi, P., Scholz, P., Shaw, J. R., Shin, K., Siegel, S. R., Singh, S., Smegal, R. J., Smith, K. M., Stairs, I. H., Tan, C. M., Tendulkar, S. P., Tretyakov, I., Vanderlinde, K., Wang, H., Wulf, D., and Zwaniga, A. V. (2020). A bright millisecond-duration radio burst from a galactic magnetar.

Cordes, J. M. and Lazio, T. J. W. (2002). Ne2001. i. a new model for the galactic distribution of free electrons and its fluctuations. *arXiv preprint astro-ph/0207156*.

de Gouveia Dal Pino, E. M. (2006). Cosmic magnetic fields. In *AIP Conference Proceedings*, volume 875, pages 289–295. American Institute of Physics.

DeLaunay, J., Fox, D. B., Murase, K., Mészáros, P., Keivani, A., Messick, C., Mostafá, M. A., Oikonomou, F., Tešić, G., and Turley, C. (2016). Discovery of a transient gamma-ray counterpart to frb 131104. *The Astrophysical Journal Letters*, 832(1):L1.

Dolag, K., Gaensler, B. M., Beck, A. M., and Beck, M. C. (2015). Constraints on the distribution and energetics of fast radio bursts using cosmological hydrodynamic simulations. *MNRAS*, 451(4):4277–4289.

Dolag, K., Grasso, D., Springel, V., and Tkachev, I. (2005). Constrained simulations of the magnetic field in the local universe and the propagation of ultrahigh energy cosmic rays. *Journal of Cosmology and Astroparticle Physics*, 2005(01):009–009.

Domínguez-Fernández, P., Vazza, F., Brüggen, M., and Brunetti, G. (2019). Dynamical evolution of magnetic fields in the intracluster medium. *Monthly Notices of the Royal Astronomical Society*, 486(1):623–638.

Durrer, R. and Neronov, A. (2013). Cosmological magnetic fields: their generation, evolution and observation. *The Astronomy and Astrophysics Review*, 21(1):62.

Eftekhari, T. and Berger, E. (2017). Associating Fast Radio Bursts with Their Host Galaxies. *APJ*, 849(2):162. [Astrophys. J.849,162(2017)].

Eichmann, B. (2019). Ultra-high-energy cosmic rays by cygnus a or the bulk of non-local radio galaxies? In *36th International Cosmic Ray Conference (ICRC2019)*, volume 36.

Farah, W., Bailes, M., Jameson, A., Flynn, C., Andreoni, I., Bateman, T., Barr, E. D., Bhandari, S., Caleb, M., Campbell-Wilson, D., Deller, A., Green, A. J., Hunstead, R. W., Jankowski, F., Keane, E. F., Krishnan, V. V., O'Neill, M., Oslowski, S., Parthasarathy, A., Plant, K., Ravi, V., and Temby, D. (2017). Detection of a highly scattered Fast Radio Burst at the Molonglo Radio Telescope. *The Astronomer's Telegram*, 10867:1.

Farrar, G. R. and Sutherland, M. S. (2019). Deflections of uhecrs in the galactic magnetic field. *Journal of Cosmology and Astroparticle Physics*, 2019(05):004.

Feretti, L., Giovannini, G., Govoni, F., and Murgia, M. (2012). Clusters of galaxies: observational properties of the diffuse radio emission. *A&ARv*, 20(1):54.

Fermi, E. (1949). On the Origin of the Cosmic Radiation. *Physical Review*, 75(8):1169–1174.

Fermi, E. (1954). Galactic magnetic fields and the origin of cosmic radiation. *The Astrophysical Journal*, 119:1.

Fonseca, E., Andersen, B., Bhardwaj, M., Chawla, P., Good, D., Josephy, A., Kaspi, V., Masui, K., Mckinven, R., Michilli, D., et al. (2020). Nine new repeating fast radio burst sources from chime/frb. *arXiv preprint arXiv:2001.03595*.

Foster, G., Karastergiou, A., Geyer, M., Surnis, M., Golpayegani, G., Lee, K., Lorimer, D., Price, D. C., and Rajwade, K. (2018). Verifying and reporting fast radio bursts. *Monthly Notices of the Royal Astronomical Society*, 481(2):2612–2627.

Fuller, J. and Ott, C. D. (2015). Dark matter-induced collapse of neutron stars: a possible link between fast radio bursts and the missing pulsar problem. *MNRAS*, 450:L71–L75.

Gajjar, V., Siemion, A., Price, D., Law, C., Michilli, D., Hessels, J., Chatterjee, S., Archibald, A., Bower, G., Brinkman, C., et al. (2018). Highest frequency detection of frb 121102 at 4–8 ghz using the breakthrough listen digital backend at the green bank telescope. *The Astrophysical Journal*, 863(1):2.

Gao, H., Li, Z., and Zhang, B. (2014). Fast radio burst/gamma-ray burst cosmography. *The Astrophysical Journal*, 788(2):189.

Ginzburg, V. L. (1996). Cosmic ray astrophysics (history and general review). *Physics-Uspekhi*, 39(2):155.

Giovannini, G., Feretti, L., and Stanghellini, C. (1991). The coma cluster radio source 1253+ 275, revisited. *Astronomy and Astrophysics*, 252:528–537.

Giovannini, G., Feretti, L., Venturi, T., Kim, K.-T., and Kronberg, P. (1993). The halo radio source coma c and the origin of halo sources. *The Astrophysical Journal*, 406:399–406.

Grasso, D. and Rubinstein, H. R. (2001). Magnetic fields in the early universe. *Physics Reports*, 348(3):163–266.

Greisen, K. (1966). End to the cosmic-ray spectrum? *Physical Review Letters*, 16(17):748.

Hackstein, S. (2020). Prefrble.

Hackstein, S., Rodrigues, L. F. S., Brüggen, M., and Vazza, F. (2020). Prefrble method paper. *in subm.*

Hackstein, S., Vazza, F., Brüggen, M., Sigl, G., and Dundovic, A. (2016). Propagation of ultrahigh energy cosmic rays in extragalactic magnetic fields: a view from cosmological simulations. *Monthly Notices of the Royal Astronomical Society*, 462(4):3660–3671.

Hackstein, S., Vazza, F., Brüggen, M., Sorce, J. G., and Gottlöber, S. (2018). Simulations of ultra-high energy cosmic rays in the local Universe and the origin of cosmic magnetic fields. *MNRAS*, 475:2519–2529.

Hamilton, P., Hall, P., and Costa, M. (1985). Changing parameters along the path to the vela pulsar. *Monthly Notices of the Royal Astronomical Society*, 214(1):5P–8P.

Harrison, E. R. (1970). Generation of Magnetic Fields in the Radiation ERA. *Monthly Notices of the Royal Astronomical Society*, 147(3):279–286.

Haverkorn, M. (2015). Magnetic fields in the milky way. In *Magnetic fields in diffuse media*, pages 483–506. Springer.

Hess, V. F. (1912). Über beobachtungen der durchdringenden strahlung bei sieben freiballonfahrten. *Phys. Z.*, 13:1084–1091.

Hillas, A. M. (1984). The origin of ultra-high-energy cosmic rays. *Annual review of astronomy and astrophysics*, 22(1):425–444.

Hutschenreuter, S., Dorn, S., Jasche, J., Vazza, F., Paoletti, D., Lavaux, G., and Enßlin, T. A. (2018). The primordial magnetic field in our cosmic backyard. *Classical and Quantum Gravity*, 35(15):154001.

Jansson, R. and Farrar, G. R. (2012). A new model of the galactic magnetic field. *APJ*, 757(1):14.

Jaroszynski, M. (2019). Fast radio bursts and cosmological tests. *Monthly Notices of the Royal Astronomical Society*, 484(2):1637–1644.

Jedamzik, K., Katalinić, V., and Olinto, A. V. (1998). Damping of cosmic magnetic fields. *Physical Review D*, 57(6):3264.

Jedamzik, K. and Saveliev, A. (2019). Stringent limit on primordial magnetic fields from the cosmic microwave background radiation. *Physical review letters*, 123(2):021301.

Kachelriess, M., Parizot, E., and Semikoz, D. (2008). The gzk horizon and constraints on the cosmic ray source spectrum from observations in the gzk regime. *JETP letters*, 88(9):553–557.

Kampert, K.-H. and Watson, A. A. (2012). Extensive air showers and ultra high-energy cosmic rays: a historical review. *The European Physical Journal H*, 37(3):359–412.

Karastergiou, A., Chennamangalam, J., Armour, W., Williams, C., Mort, B., Dulwich, F., Salvini, S., Magro, A., Roberts, S., Serylak, M., et al. (2015). Limits on fast radio bursts at 145 mhz with artemis, a real-time software backend. *Monthly Notices of the Royal Astronomical Society*, 452(2):1254–1262.

Katz, J. (2016). Fast radio bursts—a brief review: Some questions, fewer answers. *Modern Physics Letters A*, 31(14):1630013.

Kim, J., Ryu, D., Kang, H., Kim, S., and Rey, S.-C. (2019). Filaments of galaxies as a clue to the origin of ultrahigh-energy cosmic rays. *Science Advances*, 5(1):eaau8227.

Kolmogorov, A. N. (1991a). Dissipation of energy in the locally isotropic turbulence. *Proceedings of the Royal Society of London. Series A: Mathematical and Physical Sciences*, 434(1890):15–17.

Kolmogorov, A. N. (1991b). The local structure of turbulence in incompressible viscous fluid for very large reynolds numbers. *Proceedings of the Royal Society of London. Series A: Mathematical and Physical Sciences*, 434(1890):9–13.

Kulsrud, R. M. (1999). A critical review of galactic dynamos. *Annual Review of Astronomy and Astrophysics*, 37(1):37–64.

Letessier-Selvon, A. and Stanev, T. (2011). Ultrahigh energy cosmic rays. *Reviews of Modern Physics*, 83.

Li, Z., Gao, H., Wei, J.-J., Yang, Y.-P., Zhang, B., and Zhu, Z.-H. (2020). Cosmology-insensitive estimate of igm baryon mass fraction from five localized fast radio bursts.

Li, Z.-X., Gao, H., Ding, X.-H., Wang, G.-J., and Zhang, B. (2018). Strongly lensed repeating fast radio bursts as precision probes of the universe. *Nature communications*, 9(1):1–8.

Lorimer, D., Bailes, M., McLaughlin, M., Narkevic, D., and Crawford, F. (2007). A bright millisecond radio burst of extragalactic origin. *Science*, 318(5851):777–780.

Lorimer, D. R. and Kramer, M. (2012). *Handbook of Pulsar Astronomy*. Cambridge University Press.

Luo, R., Lee, K., Lorimer, D. R., and Zhang, B. (2018). On the normalized frb luminosity function. *MNRAS*, 481(2):2320–2337.

Lyne, A., Pritchard, R., and Graham-Smith, F. (2001). Pulsar reflections within the crab nebula. *Monthly Notices of the Royal Astronomical Society*, 321(1):67–70.

Lyubarsky, Y. (2014). A model for fast extragalactic radio bursts. *MNRAS*, 442:L9–L13.

Macquart, J.-P., Bailes, M., Bhat, N., Bower, G., Bunton, J., Chatterjee, S., Colegate, T., Cordes, J., D'Addario, L., Deller, A., et al. (2010). The commensal real-time askap fast-transients (craft) survey. *Publications of the Astronomical Society of Australia*, 27(3):272–282.

Macquart, J.-P., Bower, G. C., Wright, M. C., Backer, D. C., and Falcke, H. (2006). The rotation measure and 3.5 millimeter polarization of sagittarius a. *The Astrophysical Journal Letters*, 646(2):L111.

Macquart, J.-P., Prochaska, J. X., McQuinn, M., Bannister, K. W., Bhandari, S., Day, C. K., Deller, A. T., Ekers, R. D., James, C. W., Marnoch, L., and et al. (2020). A census of baryons in the universe from localized fast radio bursts. *Nature*, 581(7809):391–395.

Mao, S., Carilli, C., Gaensler, B., Wucknitz, O., Keeton, C., Basu, A., Beck, R., Kronberg, P., and Zweibel, E. (2017). Detection of microgauss coherent magnetic fields in a galaxy five billion years ago. *Nature Astronomy*, 1(9):621.

Margalit, B. and Metzger, B. D. (2018). A concordance picture of frb 121102 as a flaring magnetar embedded in a magnetized ion–electron wind nebula. *The Astrophysical Journal Letters*, 868(1):L4.

Marnoch, L., Ryder, S. D., Bannister, K. W., Bhandari, S., Day, C. K., Deller, A. T., Macquart, J.-P., McDermid, R. M., Prochaska, J. X., Qiu, H., and et al. (2020). A search for sn-like optical counterparts to askap-localised fast radio bursts. *Astronomy & Astrophysics*.

Marrone, D. P., Moran, J. M., Zhao, J.-H., and Rao, R. (2006). An unambiguous detection of faraday rotation in sagittarius a. *The Astrophysical Journal Letters*, 654(1):L57.

Mereghetti, S., Savchenko, V., Ferrigno, C., Götz, D., Rigoselli, M., Tiengo, A., Bazzano, A., Bozzo, E., Coleiro, A., Courvoisier, T. J. L., Doyle, M., Goldwurm, A., Hanlon, L., Jourdain, E., von Kienlin, A., Lutovinov, A., Martin-Carrillo, A., Molkov, S., Natalucci, L., Onori, F., Panessa, F., Rodi, J., Rodriguez, J., Sánchez-Fernández, C., Sunyaev, R., and Ubertini, P. (2020). Integral discovery of a burst with associated radio emission from the magnetar sgr 1935+2154.

Metzger, B. D., Berger, E., and Margalit, B. (2017). Millisecond magnetar birth connects frb 121102 to superluminous supernovae and long-duration gamma-ray bursts. *The Astrophysical Journal*, 841(1):14.

Metzger, B. D., Margalit, B., and Sironi, L. (2019). Fast radio bursts as synchrotron maser emission from decelerating relativistic blast waves. *MNRAS*, 485(3):4091–4106.

Michilli, D., Seymour, A., Hessels, J., Spitler, L., Gajjar, V., Archibald, A., Bower, G., Chatterjee, S., Cordes, J., Gourdji, K., et al. (2018). An extreme magneto-ionic environment associated with the fast radio burst source frb 121102. *Nature*, 553(7687):182–185.

Mollerach, S. and Roulet, E. (2013). Magnetic diffusion effects on the ultra-high energy cosmic ray spectrum and composition. *Journal of Cosmology and Astroparticle Physics*, 2013(10):013.

Muñoz, J. B., Kovetz, E. D., Dai, L., and Kamionkowski, M. (2016). Lensing of fast radio bursts as a probe of compact dark matter. *Physical Review Letters*, 117(9):091301.

Murase, K., Kashiyama, K., and Mészáros, P. (2016). A burst in a wind bubble and the impact on baryonic ejecta: high-energy gamma-ray flashes and afterglows from fast radio bursts and pulsar-driven supernova remnants. *Monthly Notices of the Royal Astronomical Society*, 461(2):1498–1511.

Neronov, A. and Semikoz, D. (2009). Sensitivity of γ-ray telescopes for detection of magnetic fields in the intergalactic medium. *Physical Review D*, 80(12):123012.

Neronov, A. and Vovk, I. (2010). Evidence for strong extragalactic magnetic fields from fermi observations of tev blazars. *Science*, 328(5974):73–75.

Nicastro, F. (2016). A Decade of WHIM search: Where do We Stand and Where do We Go. In *XMM-Newton: The Next Decade*, page 27.

Nicastro, F., Kaastra, J., Krongold, Y., Borgani, S., Branchini, E., Cen, R., Dadina, M., Danforth, C. W., Elvis, M., Fiore, F., and et al. (2018). Observations of the missing baryons in the warm–hot intergalactic medium. *Nature*, 558(7710):406–409.

Niino, Y. (2018). Fast Radio Bursts Recipes for the Distributions of Dispersion Measures, Flux Densities, and Fluences. *APJ*, 858:4.

Oppermann, N., Yu, H.-R., and Pen, U.-L. (2018). On the non-poissonian repetition pattern of frb121102. *Monthly Notices of the Royal Astronomical Society*, 475(4):5109–5115.

Ostapchenko, S. (2004). Qgsjet-ii: towards reliable description of very high energy hadronic interactions. *arXiv preprint hep-ph/0412332*.

Parker, E. (1971). The generation of magnetic fields in astrophysical bodies. iii. turbulent diffusion of fields and efficient dynamos. *The Astrophysical Journal*, 163:279.

Parker, E. N. (1979). *Cosmical magnetic fields. Their origin and their activity*.

Petroff, E., Barr, E. D., Jameson, A., Keane, E. F., Bailes, M., Kramer, M., Morello, V., Tabbara, D., and van Straten, W. (2016). FRBCAT: The Fast Radio Burst Catalogue. *arXiv*.

Petroff, E., Hessels, J., and Lorimer, D. (2019). Fast radio bursts. *The Astronomy and Astrophysics Review*, 27(1):4.

Piddington, J. H. (1981). Turbulent diffusion of magnetic fields in astrophysical plasmas. *APJ*, 247:293–299.

Pierog, T., Karpenko, I., Katzy, J. M., Yatsenko, E., and Werner, K. (2015). Epos lhc: Test of collective hadronization with data measured at the cern large hadron collider. *Physical Review C*, 92(3).

Pilia, M., Burgay, M., Possenti, A., Ridolfi, A., Gajjar, V., Corongiu, A., Perrodin, D., Bernardi, G., Naldi, G., Pupillo, G., and et al. (2020). The lowest-frequency fast radio bursts: Sardinia radio telescope detection of the periodic frb 180916 at 328 mhz. *The Astrophysical Journal*, 896(2):L40.

Piro, A. L. and Gaensler, B. M. (2018). The dispersion and rotation measure of supernova remnants and magnetized stellar winds: Application to fast radio bursts. *APJ*, 861(2):150.

Platts, E., Prochaska, J. X., and Law, C. J. (2019). Constraining the dispersion measure of the galactic halo using frbs and density estimation.

Platts, E., Prochaska, J. X., and Law, C. J. (2020). A data-driven technique using millisecond transients to measure the milky way halo. *arXiv preprint arXiv:2005.06256*.

Platts, E., Weltman, A., Walters, A., Tendulkar, S., Gordin, J., and Kandhai, S. (2018). A living theory catalogue for fast radio bursts. *arXiv preprint arXiv:1810.05836*.

Pol, N., Lam, M. T., McLaughlin, M. A., Lazio, T. J. W., and Cordes, J. M. (2019). Estimates of Fast Radio Burst Dispersion Measures from Cosmological Simulations. *arXiv e-prints*, page arXiv:1903.07630.

Popov, S. B. and Postnov, K. A. (2010). Hyperflares of SGRs as an engine for millisecond extragalactic radio bursts. *Evolution of Cosmic Objects through their Physical Activity*, pages 129–132.

Price, D., Foster, G., Geyer, M., van Straten, W., Gajjar, V., Hellbourg, G., Karastergiou, A., Keane, E., Siemion, A., Arcavi, I., et al. (2019). A fast radio burst with frequency-dependent polarization detected during breakthrough listen observations. *Monthly Notices of the Royal Astronomical Society*, 486(3):3636–3646.

Price, D. J. (2004). *Magnetic fields in Astrophysics*. PhD thesis, University of Cambridge Cambridge, UK.

Rachen, J. P. (2019). A parametrized catalog of radio galaxies as uhecr sources. In *36th International Cosmic Ray Conference*, volume 358, page 396. SISSA Medialab.

Rajwade, K. M., Mickaliger, M. B., Stappers, B. W., Bassa, C. G., Breton, R. P., Karastergiou, A., and Keane, E. F. (2020a). Limits on absorption from a 332-mhz survey for fast radio bursts.

Rajwade, K. M., Mickaliger, M. B., Stappers, B. W., Morello, V., Agarwal, D., Bassa, C. G., Breton, R. P., Caleb, M., Karastergiou, A., Keane, E. F., and Lorimer, D. R. (2020b). Possible periodic activity in the repeating frb 121102.

Rane, A., Lorimer, D., Bates, S., McMann, N., McLaughlin, M., and Rajwade, K. (2016). A search for rotating radio transients and fast radio bursts in the parkes high-latitude pulsar survey. *Monthly Notices of the Royal Astronomical Society*, 455(2):2207–2215.

Rincon, F. (2019). Dynamo theories. *Journal of Plasma Physics*, 85(4).

Scholz, P., Bogdanov, S., Hessels, J., Lynch, R., Spitler, L., Bassa, C., Bower, G., Burke-Spolaor, S., Butler, B., Chatterjee, S., et al. (2017). Simultaneous x-ray, gamma-ray, and radio observations of the repeating fast radio burst frb 121102. *The Astrophysical Journal*, 846(1):80.

Scholz, P., Cook, A., Cruces, M., Hessels, J. W. T., Kaspi, V. M., Majid, W. A., Naidu, A., Pearlman, A. B., Spitler, L., Bandura, K. M., Bhardwaj, M., Cassanelli, T., Chawla, P., Gaensler, B. M., Good, D. C., Josephy, A., Karuppusamy, R., Keimpema, A., Kirichenko, A. Y., Kirsten, F., Kocz, J., Leung, C., Marcote, B., Masui, K., Mena-Parra, J., Merryfield, M., Michilli, D., Naudet, C. J., Nimmo, K., Pleunis, Z., Prince, T. A., Rafiei-Ravandi, M., Rahman, M., Shin, K., Smith, K. M., Stairs, I. H., Tendulkar, S. P., and Vanderlinde, K. (2020). Simultaneous x-ray and radio observations of the repeating fast radio burst frb 180916.j0158+65.

Scholz, P., Spitler, L., Hessels, J., Chatterjee, S., Cordes, J., Kaspi, V., Wharton, R., Bassa, C., Bogdanov, S., Camilo, F., et al. (2016). The repeating fast radio burst frb 121102: multi-wavelength observations and additional bursts. *APJ*, 833(2):177.

Schröder, F. G. (2017). Radio detection of extensive air showers (ecrs 2016). *arXiv preprint arXiv:1701.05496*.

Shukurov, A. (2004). Introduction to galactic dynamos. *arXiv preprint astro-ph/0411739*.

Sorce, J. G., Gottlöber, S., Yepes, G., Hoffman, Y., Courtois, H. M., Steinmetz, M., Tully, R. B., Pomarède, D., and Carlesi, E. (2016). Cosmicflows Constrained Local UniversE Simulations. *MNRAS*, 455:2078–2090.

Spitler, L., Cordes, J., Hessels, J., Lorimer, D., McLaughlin, M., Chatterjee, S., Crawford, F., Deneva, J., Kaspi, V., Wharton, R., et al. (2014). Fast radio burst discovered in the arecibo pulsar alfa survey. *APJ*, 790(2):101.

Steenbeck, M., Krause, F., and Rädler, K.-H. (1966). Berechnung der mittleren lorentz-feldstärke für ein elektrisch leitendes medium in turbulenter, durch coriolis-kräfte beeinflußter bewegung. *Zeitschrift für Naturforschung A*, 21(4):369–376.

Subramanian, K. (2019). From primordial seed magnetic fields to the galactic dynamo. *Galaxies*, 7(2):47.

Tanimura, H., Hinshaw, G., McCarthy, I. G., Van Waerbeke, L., Aghanim, N., Ma, Y.-Z., Mead, A., Hojjati, A., and Tröster, T. (2018). A search for warm/hot gas filaments between pairs of sdss luminous red galaxies. *Monthly Notices of the Royal Astronomical Society*, 483(1):223–234.

Tavani, M., Verrecchia, F., Casentini, C., Perri, M., Ursi, A., Pacciani, L., Pittori, C., Bulgarelli, A., Piano, G., Pilia, M., Bernardi, G., Addis, A., Antonelli, L. A., Argan, A., Baroncelli, L., Caraveo, P., Cattaneo, P. W., Chen, A., Costa, E., Persio, G. D., Donnarumma, I., Evangelista, Y., Feroci, M., Ferrari, A., Fioretti, V., Lazzarotto,

F., Longo, F., Morselli, A., Paoletti, F., Parmiggiani, N., Trois, A., Vercellone, S., Naldi, G., Pupillo, G., Bianchi, G., and Puccetti, S. (2020). Gamma-ray and x-ray observations of the periodic-repeater frb 180916 during active phases.

Tendulkar, S. P., Bassa, C., Cordes, J. M., Bower, G. C., Law, C. J., Chatterjee, S., Adams, E. A., Bogdanov, S., Burke-Spolaor, S., Butler, B. J., et al. (2017). The host galaxy and redshift of the repeating fast radio burst frb 121102. *The Astrophysical Journal Letters*, 834(2):L7.

Tingay, S. J. and Kaplan, D. L. (2016). Limits on einstein's equivalence principle from the first localized fast radio burst frb 150418. *The Astrophysical Journal Letters*, 820(2):L31.

Trivedi, P., Subramanian, K., and Seshadri, T. (2014). Primordial magnetic field limits from the cmb trispectrum: Scalar modes and planck constraints. *Physical Review D*, 89(4):043523.

Trotta, R. (2008). Bayes in the sky: Bayesian inference and model selection in cosmology. *Contemporary Physics*, 49(2):71–104.

Vallée, J. P. (1997). Observations of the magnetic fields inside and outside the milky way, starting with globules (1 parsec), filaments, clouds, superbubbles, spiral arms, galaxies, superclusters, and ending with the cosmological universe's background surface (at 8 teraparsecs). *Fundamentals of Cosmic Physics*, 19:1–89.

van Weeren, R., de Gasperin, F., Akamatsu, H., Brüggen, M., Feretti, L., Kang, H., Stroe, A., and Zandanel, F. (2019). Diffuse radio emission from galaxy clusters. *Space Science Reviews*, 215(1):16.

Vazza, F., Brüggen, M., Gheller, C., Hackstein, S., Wittor, D., and Hinz, P. (2017). Simulations of extragalactic magnetic fields and of their observables. *Classical and Quantum Gravity*, 34(23):234001.

Vazza, F., Brüggen, M., Hinz, P., Wittor, D., Locatelli, N., and Gheller, C. (2018). Probing the origin of extragalactic magnetic fields with fast radio bursts. *Monthly Notices of the Royal Astronomical Society*, 480(3):3907–3915.

Vieyro, F. L., Romero, G. E., Bosch-Ramon, V., Marcote, B., and del Valle, M. V. (2017). A model for the repeating frb 121102 in the agn scenario. *Astronomy & Astrophysics*, 602:A64.

Walker, C. R. H., Ma, Y.-Z., and Breton, R. P. (2018). Constraining Redshifts of Unlocalised Fast Radio Bursts. *ArXiv e-prints*.

Walters, A., Weltman, A., Gaensler, B. M., Ma, Y.-Z., and Witzemann, A. (2018). Future cosmological constraints from fast radio bursts. *The Astrophysical Journal*, 856(1):65.

Wang, J.-S., Yang, Y.-P., Wu, X.-F., Dai, Z.-G., and Wang, F.-Y. (2016). Fast Radio Bursts from the Inspiral of Double Neutron Stars. *ApJL*, 822(1):L7.

Wang, X.-G., Li, L., Yang, Y.-P., Luo, J.-W., Zhang, B., Lin, D.-B., Liang, E.-W., and Qin, S.-M. (2020). Is grb 110715a the progenitor of frb 171209?

Wei, J.-J., Gao, H., Wu, X.-F., and Mészáros, P. (2015). Testing einstein's equivalence principle with fast radio bursts. *Physical review letters*, 115(26):261101.

Wei, J.-J., Wu, X.-F., and Gao, H. (2018). Cosmology with gravitational wave/fast radio burst associations. *The Astrophysical Journal Letters*, 860(1):L7.

Widrow, L. M. (2002). Origin of galactic and extragalactic magnetic fields. *Reviews of Modern Physics*, 74(3):775.

Wu, X.-F., Zhang, S.-B., Gao, H., Wei, J.-J., Zou, Y.-C., Lei, W.-H., Zhang, B., Dai, Z.-G., and Mészáros, P. (2016). Constraints on the photon mass with fast radio bursts. *The Astrophysical Journal Letters*, 822(1):L15.

Xi, S.-Q., Tam, P.-H. T., Peng, F.-K., and Wang, X.-Y. (2017). Search for gev counterparts to fast radio bursts with fermi. *The Astrophysical Journal Letters*, 842(1):L8.

Yang, Y.-P. and Zhang, B. (2016). Extracting host galaxy dispersion measure and constraining cosmological parameters using fast radio burst data. *The Astrophysical Journal Letters*, 830(2):L31.

Yao, J., Manchester, R., and Wang, N. (2017). A new electron-density model for estimation of pulsar and frb distances. *The Astrophysical Journal*, 835(1):29.

Yüksel, H., Stanev, T., Kistler, M. D., and Kronberg, P. P. (2012). The centaurus a ultrahigh-energy cosmic-ray excess and the local extragalactic magnetic field. *The Astrophysical Journal*, 758(1):16.

Zatsepin, G. T. and Kuzmin, V. A. (1966). Upper limit of the spectrum of cosmic rays. *Journal of Experimental and Theoretical Physics Letters (JETP Letters)*, 4(3):78–80.

Zhou, B., Li, X., Wang, T., Fan, Y.-Z., and Wei, D.-M. (2014). Fast radio bursts as a cosmic probe? *Physical Review D*, 89(10):107303.

Zwaan, C. (1987). Elements and patterns in the solar magnetic field. *Annual review of astronomy and astrophysics*, 25(1):83–111.